An Experimental and Computational Study of Flow Behaviour in Bubbling Fluidized Beds

by

Britt Halvorsen

Department of Technology
Telemark University College (HiT-TF)
Kjølnes Ring, N-3914 Porsgrunn
Norway

Thesis submitted to
The Norwegian University of Science and Technology (NTNU)
for the degree of Dr. Ing.

Porsgrunn, April 2005

Abstract

Experimental and computational studies of bubble behaviour in gas/solid fluidized beds have been performed. Bubble behaviour depends on particle density, particle size and size distribution and emphasis is given to study these effects. Bubble behaviour is also influenced by the superficial gas velocity, excess gas velocity and the relation between particle diameter and bed dimensions. These effects and their influence on flow behaviour are studied as well.

Measurements have been performed on a two-dimensional fluidized bed with a central jet. Experiments were performed with two different groups of powders A video camera was used to detect bubble behaviour. The purpose was to verify the calculation of bubble formations on a simple well-defined model.

A three dimensional fluidized bed has been constructed and built. A fibre optical probe was used to detect bubbles and their properties. A Labview program has been developed to calculate bubble frequencies, velocities and sizes from the detected signals. Powders with different particle size distributions were used to study its influence on flow behaviour. It was found that bubble behaviour is highly dependent on particle size distribution and that this has to be taken into consideration in the modelling of gas/particle systems.

A three-dimensional computational fluid dynamic (CFD) model developed by previous studies at Telemark University College was modified to improve its use in dense particle systems like bubbling fluidized beds. A computational routine was developed to calculate bubble frequencies, velocities and sizes. To obtain realistic bubble shapes and bubble velocities, second order upwind schemes and different flux limiters were included in the code.

The code has been modified to prevent unphysically dense packing of solids. A ‘switch’ to plastic regime at critical packing has been included in the code. Frictional stresses substitute the kinetic and collisional stresses above a specified critical packing. The solid pressure is defined as a function of the solid volume fraction. A routine for solid volume fraction correction was included in the code to stabilize the computations in closed packed regions. An alternative equation for the radial distribution function has been included.

Simulations of bubble behaviour in two and three dimensional beds have been performed with different types of powders and different superficial gas velocities. The influence of drag models, coefficient of restitution and number of particle phases has been studied. The numerical results correlate fairly well with experimental data for most of the cases.

A computational study of bubble behaviour in fluidized beds with different diameters has been performed by using a CFD code developed at National Energy Technology Laboratory (NETL). The computational results are compared to experimental data presented in literature. Some connections between bubble behaviour and bed dimensions were observed and can be used for further work on the scaling of industrial fluidized beds. Scaling was also performed by using scaling parameters.

Acknowledgements

First of all I would like to thank my supervisor Vidar Mathiesen for his encouragement and excellent guidance during this work. His knowledge and his capability of disseminating knowledge within multiphase flow have been very useful for me. I will also thank him for his friendship and for his patience with the stubborn part of me.

Secondly I will thank Thomas O'Brien and his co-workers at National Energy Technology Laboratory and Fluent Incorporated for giving me an interesting and exciting stay in Morgantown, West Virginia. I am proud of having been a member of their excellent group. I also want to thank Tom for introducing me to American folk music and for all the social time he spent with me, Ted and Gwen for giving me an experience of American Halloween and Thanks Giving celebration, Mike for introducing me to American football and Maria and Sofiane for doing my days in Morgantown enjoyable.

A special thank to Haavard Aakre for his valuable help with developing a Labview program for analysing data. Without his support I would have had to spend a lot more time on the experimental work.

Thanks also to professor Prieur du Plessis from the University of Stellenbosch for his support and for useful discussions about drag models.

I would also like to thank Telemark University College and all my colleagues and former colleagues, in particular Hildegunn Haugen, Magnar Ottøy and all the nice people participating the '10.00-coffee-break', for making the days enjoyable. I also want to thank Talleiv Skredtveit, Eivind Fjelddalen and Morten Pedersen for their contribution with construction and instrumentation of the experimental equipment.

This work has been sponsored by Telemark Technological Research and Development Centre (Tel-Tek).

Finally, special thanks to Tore for his patience and moral support. I would also like to thank Torbjørn, Eirik and Friid for not complaining about lack of attention during the last year. Thanks also to my mother and the rest of my family for their support.

April, 2005 Britt Halvorsen

Contents

Nomenclature

a	coefficient in the discretised algebraic equation
b	collection term in the discretised algebraic equation
C	fluctuation component of particle velocity [m/s]
C_D	friction coefficient [-]
C_f	factor, bubble diameter to bubble height [-]
c_t	constant in Sub Grid Scale model [-]
D_b	diameter of bubble [m]
D_t	bed diameter [m]
d_f	distance between optic fibres [m]
d_p	particle diameter [m]
d_{sn}	mean particle diameter=$0.5(d_s+d_n)$ [m]
E	error, velocity [m/s]
e	coefficient of restitution [-]
e_{sn}	mean coefficient of restitution = $0.5(e_s+e_n)$ [-]
f	gradient of g_0 [-]
f	sampling frequency [s^{-1}]
G_s	net solid flux [kg/m^2s]
g_i	i-direction component of gravity [m/s^2]
g_0	radial distribution function for a single solid phase [-]
g_{sn}	binary radial distribution function [-]
H	height above distributor [m]
H_t	bed height [m]
L	height from distributor to exit [m]
L	bed dimension [m]
l	mean free path [m]
M	number of phases [-]
M	position of the cross correlation maximum [-]
m	mass of a particle [kg]
m_0	binary mass =m_s+m_n [kg]
N	number of solid phases [-]
n	number of particles [-]
P	fluid pressure [Pa]
P^*	empirical solid phase pressure [Pa]
P_C	collisional pressure [Pa]
P_s	solid phase pressure [Pa]
q_w	rate of dissipation per unit area of wall by collision [kg/s^3]
R	radius of bubble [m]
Re_s	particle Reynolds number [-]
$R_{V_1V_2}$	cross-correlation [ ]
r	radius of bubble [m]
S_Φ	source term in general equation [ ]
S_{ij}	rate of deformation tensor [m/s^2]
t	Time [s]
U_i, U_j	i and j components of velocity [m/s]
u_0	superficial velocity [m/s]

u_b	bubble velocity [m/s]
u_{br}	rise velocity to a bubble with respect to the emulsion phase [m/s]
u_{mf}	minimum fluidisation velocity [m/s]
V_b	volume of bubble [m^3]
$V_1(t)$, $V_2(t)$	signal from fibre 1 and 2 [V]
x	coordinate in x-direction
y	coordinate in y-direction
z	coordinate in z-direction
$\underline{z}$	height of bubble [m]
$\bar{z}$	mean bubble height [m]

Greek symbols

β	angle of internal friction [º]
Γ	diffusion coefficient [kg/m·s]
Δ	length scale of resolved eddies [m]
ε_g	void fraction [-]
ε_m	Volume fraction of phase m [-]
ε_s	solid volume fraction [-]
$\varepsilon_{s,max}$	maximum solid volume fraction [-]
γ	collisional energy dissipation [$kg/m \cdot s^3$]
δ_{ij}	Kroenecker delta [-]
θ	granular temperature $=1/3\langle C \cdot C \rangle$ [m^2/s^2]
κ	conductivity of granular temperature [kg/m·s]
μ	shear viscosity [kg/m·s]
ξ	bulk viscosity [kg/m·s]
Π_{ij}	total stress tensor [$kg/m \cdot s^2$]
ρ	density [kg/m^3]
Φ_{sg}	total gas/particle drag coefficient [$kg/m^3 \cdot s$]
Φ_{sn}	particle/particle drag coefficient [$kg/m^3 \cdot s$]
τ	time step [s]
τ	viscous stresses [$kg/m \cdot s^2$]
τ_w	rate of transfer of momentum to the wall by collisions [$kg/m \cdot s^2$]
Ψ	flux limiter [-]
ψ	particle form factor [-]
ω	specularity factor [-]

Subscripts

av	average
C	collisional
col	collisional
dil	dilute
eff	effective
g	gas phase
i,j,k	i, j and k directions
lam	laminar
m	phase number
n	phase number
s	solid

1. Introduction

Fluidized beds are widely used in industrial operations. Several applications can be found in the chemical, petroleum, pharmaceutical, agricultural, biochemical, food, electronic and power generation industries. In a fluidized bed gas is passing upwards through a bed of particles. The earliest applications of fluidisation were for the purpose of carrying out chemical reactions. Since that time there have been a number of successful chemical processes involving fluidized bed reactors. Fluidized beds in chemical industry include two main types of reactions, catalytic gas phase reactions and gas-solid reactions. In catalytic gas phase reactions the particles are not undergoing any chemical reaction. This is the principal of oil cracking for manufacturing of various chemical substances. In gas-solid reactions the fluidized particles are involved in the reactions and undergo a phase change. An example of this type of process is combustion or gasification of coal. Other application of fluidized beds are drying and coating of solids.

Fluidized beds are applied in industry due to their large contact area between phases, which enhances chemical reactions, heat transfer and mass transfer. The efficiency of fluidized beds is highly dependent of flow behaviour and knowledge about flow behaviour is essentially for scaling, design and optimisation. Computational fluid dynamics (CFD) has during the last decades become a useful tool in predicting flow behaviour in fluidized bed processes. However, further model development and verification of the model and the numeric are still needed.

1.1 Previous work

This section gives a short overview of previous work within bubbling fluidized beds. Much work has been performed on both experimental and computational studies of bubbling fluidized bed. The experimental work discussed here are concentrated on optical methods used for measuring bubble behaviour. Gas/solid systems can be modelled by using either Eulerian or Lagrangian approaches for the solid phases. In this work focus will be on the Eulerian approach.

1.1.1 Experimental work

A lot of work has been done to study bubbles in a fluidized bed. Of practical reasons the experimental studies of bubble behaviour have most often been performed on cold beds. Both two dimensional and three dimensional beds have been constructed and used in experimental research. Gidaspow et. al., (1983), Gidaspow et. al. (1986), Kuipers et. al. (1992), Halvorsen and Mathiesen (2002a), Bokkers et al. (2004), Patil et. al. (2005a) studied bubbles in two dimensional beds with a jet. The advantage of studies of fluidization with a jet is that the jet establishes the flow pattern, and this problem is easier to model than uniform fluidisation. In these studies photographic techniques as movie camera or digital video camera were used to measure bubble sizes and bubble velocities. Bokkers et. al. (2004) used particle image velocimetry (PIV) to study bubble behaviour and particle mixing and concluded that PIV was successfully applied to obtain the ensemble averaged particle velocity profile in the vicinity of a bubble.

Different measurement systems have been developed and used for studying bubble behaviour in fluidized beds. Werther and Molerus (1973a) used a miniaturised capacitance probe for measuring parameters characterising local state of fluidization in cylindrical beds of different sizes. Werther and Molerus (1973b) reported experimental results on bubble behaviour for fluidized beds with different diameters. The diameters of these beds were 0.10, 0.20, 0.45 and 1.00 m, and particles with different sizes and densities were used. They found that close to the distributor a zone of increasing bubble formation exist in an annulus close to the wall. This zone moves towards the centre of the bed with increasing height above the distributor. This was different from what was reported in earlier studies. Kunii et al. (1967) concluded from measurements taken with a capacitive probe that bubbles rise uniformly distributed over the cross-section from the distributor to a height about equal to the bed diameter.

Halow et al. (1990) developed a unique rapid imaging system based on measurement of capacitance. The imaging system was incorporated into a 0.1524 m diameter fluidized bed, and was used by Halow and Nicoletti (1992) and Halow et al. (1993) to study bubble behaviour in fluidized beds. The experiments were performed with particles with different sizes and densities. The measurement technique provided detailed information and increased the understanding of the void distributions in fluidized beds.

Militzer and Shakourzadeh (1991) developed a measurement system to measure particle velocities in fluidized beds. The system was a fibre optical system based on light reflection. The system was capable to measure bubble velocity and bubble pierced length in fluidized beds. Saberi et al. (1995) used the fibre optical probe to measure bubble behaviour and discussed how the data should be treated and analysed to obtain a statistical mean value for bubble volume and bubble diameter.

Pugsley et al. (2003) used fibre optical probe for verification of electrical capacitance tomography (ECT) measurements in bubbling fluidized bed. They observed rather good agreement between the two measuring methods. Off-line iterative reconstruction of the ECT images is necessary.

In this work a digital video camera is used to detect bubble size and bubble velocity in a two dimensional fluidized bed with a jet. Measurements of bubble behaviour in three dimensional bubbling bed is performed with a fibre optical probe based on light reflection. The measurement system is developed by Militzer (1991). A program for acquisition, validation and analysis of raw data is developed in this work.

1.1.2 Numerical modelling

In the last decades considerable progress has been made in hydrodynamic modelling of gas/particle systems. Two different classes of models can be distinguished, the Lagrangian models and the Eulerian models. In the Lagrangian approach the dynamics of each particle or parcels of particles are solved. The effects of particle collisions and particle/fluid interactions are taken into account. In the Eulerian approach all the phases are considered to be continuous. The presence of each phase is defined by a volume fraction. All phases are described in terms of separate conservation equations. Eulerian methods are faster for large number of particles than Lagrangian methods, but require the formulation of constitutive equations.

The focus in this thesis is on Eulerian models. In most recent Eulerian models equations according to the kinetic theory of granular flow are incorporated. This theory describes the dependence of rheological properties of the fluidized particles on local particle concentration and the fluctuating motion of the particles owing to particle-particle collisions. The kinetic theory of granular flow is based on the kinetic theory of non-uniform gases presented by Chapman and Cowling (1970). Jenkins and Savage (1983) introduced the granular temperature. Granular temperature is defined as one-third the mean square fluctuation velocity. Ding and Gidaspow (1990), Kuipers et al. (1993), van Wachem et al. (1998), Pain et al. (2001a), Pain et al. (2001b), Halvorsen and Mathiesen (2002a) and Halvorsen and Mathiesen (2002b) have shown that Eulerian models including granular temperature, predicted well bubble behaviour in bubbling fluidized beds. Gidaspow (1994), Samuelsberg and Hjertager (1996), Crowe et al. (1998), Aguillónet al. (1996), Mathiesen et al. (1999), Mathiesen et al. (2000b), Zevenhoven et al. (2001), Ibsen (2002) achieved good results in simulation of circulating fluidized beds.

Particle size, particle size distribution and particle density are important parameters in gas/particle systems that influence the flow behaviour in fluidized beds. Geldart (1973) classified particles into four groups. He focused on the characteristics of the particles that made them fluidized in one way or another. Geldart's classification is based on particle size and density difference between particles and fluid. The classification is clear and easy to use.

Two-phase gas/particle models assume that all particles have the same diameter and densities. In the last years progress has been done in including more than one particle phase in the models and thereby be able to simulate a more realistic mixture of particles with different diameters and/or different densities. Gidaspow et al. (1996) and Manger (1996), Huilin et al. (2000) extended the kinetic theory of dense gases to binary mixtures of particles. The approach included kinetic theory with unequal granular temperatures between the particle phases. Gidaspow et al. (1996), Mathiesen et al. (2000a), van Wachem et al. (2001a), Huilin et al. (2000), Huilin et al. (2003a,b,c), Gera et al. (2004) have developed and used multi-fluid models in flow simulations of fluidized beds.

In modelling of bubbling fluidized bed it is important to prevent solids from reaching unphysical large solid volume fractions, and solid pressure function are used for this objective. Lun et al. (1984) and Lun et Savage (1987) obtained a relation between solid pressure and granular temperature using the methods of dense phase kinetic theory. Gidaspow (1994) reviewed this derivation by using Chapman and Cowling's (1970) method. Gidaspow and Huilin (1998) showed by experiments that a relation exists between solid pressure, temperature and density analogous to the ideal gas law. Solid phase pressure is described by solid volume fraction, solid density, granular temperature, coefficient of restitution and a radial distribution function. In addition to a kinetic and a collisional term, Gidaspow and Huilin (1998) also included a cohesion term in the solid pressure equation. This term is close to zero in dilute flow and increases rapidly with increasing solid volume fraction. The cohesive term is not included in this work.

In the kinetic theory of granular flow the radial distribution function is applied to correct the probability of a collision for the effect of the volume occupied by the particles. Different radial distribution functions have been proposed by Bagnold (1954), Carnahan and Starling (1969) Ma and Ahmadi (1986), Ding and Gidaspow (1990). Mathiesen et al. (1999) proposed a binary radial distribution function based on Bagnold's equation. Another binary function

was derived by Lebowitz (1964). Goldschmidt et al. (2001a) demonstrated that hard-sphere discrete particle models can be applied to identify which radial distribution function is best suitable in continuum simulations. He concluded that the radial distribution function proposed by Carnahan and Starling (1969) gave a good agreement with the results obtained from the hard-sphere discrete particle model.

Goldschmidt et al. (2001b) studied the effect of coefficient of restitution on bed dynamics. They used kinetic theory of granular flow in the numerical model. The simulations did not show extreme sensitivity with respect to the coefficient of restitution. These results are consistent with those obtained from discrete particle simulations of dense beds performed by Hoomans et al. (1998). Earlier works by Pita and Sundaresan (1993), Nieuwland et al. (1996), Hrenya and Sinclair (1997) reported an extreme, unrealistic sensitivity of Eulerian models due to inelastic particle-particle collisions.

Van Wachem et al. (2001b) compared different Eulerian CFD models. Experimental data were used to quantitatively assess the various treatments. The conclusion of the comparison was that flow predictions were not sensitive to the use of different solid stress models or radial distribution functions. In dense gas-solid flow, the different approaches in the kinetic theory modelling predicted similar values for the solid phase. Frictional stress was found to be an important contributing force in the dense gas-solid modelling. The various frictional stress models predicted an order of magnitude difference in the normal stress. Patil et al. (2005a,b) compared different models of frictional stresses. They concluded that frictional stresses have a significant influence on bubble behaviour.

Gravity and drag are the most dominating terms in the solid phase momentum equation. The application of different drag models significantly impacted the flow of the solid phase by influencing the predicted bed expansion and the solid concentration in the dense phase regions of the bed. Yasuna et al. (1995), Halvorsen and Mathiesen (2002a), Ibsen (2002), Bokkers (2004) showed that the solution of their model is sensitive to drag coefficient. In general, the performance of most current models depends on the accuracy of the drag formulation.

A number of different drag models have been proposed in modelling of fluidized beds. Ergun (1952) developed a drag model that was valid for high particle concentration. Gidaspow (1994) combined Ergun's equation with drag equations developed by Rowe (1961) and Wen and Yu (1966) and got a model that was valid for both dilute and dense particle phases. Gibilaro et al. (1985) proposed a model for the friction coefficient that was included in the total gas/particle drag coefficient. This model was valid for the whole range of particle concentrations. Other drag models have been proposed by e.g. Syamlal and O'Brian (1987), Di Felice (1994) and Zhang and Reese (2003).

Gera et al. (1998) compared predicted bubble behaviour from distinct element method (DEM) with simulations with two fluid model. It was inferred that the inter-particle frictions that is included in the Eulerian approach through the solid pressure and viscosity are the very sensitive key parameters. Inaccurate determination of solid pressure will hinder the true bubble characteristics. Bingham plastic model was assumed to predict the more realistic bubble shapes. Chiesa et al. (2004) compared computational results obtained from DEM and Eulerian approach with experimental results. The study was performed on bubble behaviour in a 2-D fluidized bed with a jet. They found that the results from both approaches agreed well with the experimental results. The DEM gave the best agreement with the experiments,

but this approach requires four orders of magnitude higher CPU time than the Eulerian approach.

Patankar and Joseph (2001a,b) presented a new Eulerian-Lagrangian numerical simulation model for particular flows. The numerical method was verified by comparing results with test cases and experiments. They found that simulations performed on a 3-D fluidized bed with a central jet, gave about the same results as similar simulations using an Eulerian approach. Pain et al. (2001a) studied a bubbling and slugging bed using the two-fluid granular temperature model. The simulations showed that the results are sensitive to material-particles parameters to various degrees. They are sensitive to wall friction coefficient but less sensitive to the coefficients of restitution. A number of phenomenons as formation, coalescence, elongation and eruption of bubbles were discussed and it was shown that in some cases, bubbles are created by the centrifugal force on the particles.

In numerical flow modelling of fluidized beds it is important to study how numerical schemes influence the results. In bubbling fluidized bed it has been shown that first order upwind (FOU) differencing schemes can give unphysical pointed bubbles. Syamlal (1998) included higher order discretisation schemes in the multiphase flow model and compared the exact solution of a moving plug with the results from FOU and different higher order schemes. It was found that a second order scheme, including the flux limiter Superbee, predicted physically realistic rounded bubbles. Guenther and Syamlal (2001) studied the effect of numerical diffusion on simulation of isolated bubbles in a two dimensional fluidized bed with a central jet. They implemented higher order discretisation schemes into two-fluid codes and found that the pointed shape of the bubble using FOU was determined by the discretisation scheme used for solving the solid momentum equations. Higher order schemes predicted rounded bubbles. It was also found that FOU predicted rounded bubbles provided there are sufficient grid resolutions to reduce numerical diffusion. Higher order schemes with different flux limiters were studied and compared. Corresponding studies have been performed by Witt et al. (1996) and Halvorsen and Mathiesen (2002b).

1.2 Objective

The scope of this study is to improve the CFD mode proposed by Mathiesen et al. (2000a) with special emphasis on dense bubbling fluidized bed. The model has been tested and verified in previous studies for circulating fluidized beds with rather low concentration of particles. The aim of this work is to modify the model to improve its use in dense particle systems like bubbling fluidized beds. The purpose is to study bubble behaviour and increase the knowledge of the complex gas/solid flow in such systems. In order to obtain good foundation for evaluating the CFD model experimental studies are performed on laboratory scale bubbling fluidized beds. Experimental studies are carried out on two and three dimensional fluidized beds. The measurements are performed with fibre optical probe, digital video camera and pressure detectors.

Simulation using the CFD model, MFIX, presented by Syamlal et al. (1998) is also included in this thesis. The aim of this part of the work is to study flow behaviour of fluidized beds with different diameters and to use the results in scaling of bubbling fluidized beds.

1.3 Outline of thesis

This first chapter gives a short introduction to fluidized systems with focus on previous experimental and computational work on bubbling fluidized beds.

Chapter 2 starts with a description of expected bubble behaviour in the different particle groups that are used in this work. Further the principle of fibre optical measurement technique is described. This chapter also gives a description of the program that is developed and used for analysis of raw data.

Chapter 3 describes the governing equations in gas/particle systems. Focus in this chapter is put on dense packing of solids. In chapter 4 numerical solution procedures are presented. Differencing schemes and a routine for solid volume fraction correction are discussed.

Experimental and computational study of two dimensional fluidized bed with a central jet is presented in chapter 5. Comparison of experimental and computational results is performed. The influence of drag models, coefficient of restitution, particle size distribution and differensing schemes on bubble behaviour is discussed.

A grid resolution test is performed in chapter 6. For these simulation a CFD code, MFIX, is used. The chapter also include simulations of fluidized beds with different diameters and the results are compared with experimental data found in literature. The simulations are performed using three dimensional cylindrical coordinates and two dimensional axis symmetrical and Cartesian coordinates.

In chapter 7 and 8 experimental and computational studies of a three dimensional bubbling fluidized bed are presented. Fibre optical probe are used to study bubble behaviour. The simulations are performed with three dimensional Cartesian coordinates. Glass particles with different particle size distribution are used. Experimental and computational results have been compared.

The thesis is ended with a conclusion and recommendations to further work in chapter 9.

2. Experimental techniques and analysis

2.1 Bubble behaviour

A gas/solid fluidized bed is formed by forcing gas upwards through a bed of particles supported on a distributor. In a fluidized bed the friction between particles are small, such that the gas/particle assembly behaves like a liquid with a density equal to the bulk density. The behaviour of particles in fluidized beds depends on a combination of their mean particle size and density. Geldart (1973) fluidization diagram, shown in Figure 2.1, is used to identify characteristics associated with fluidization of particular powders at ambient conditions.

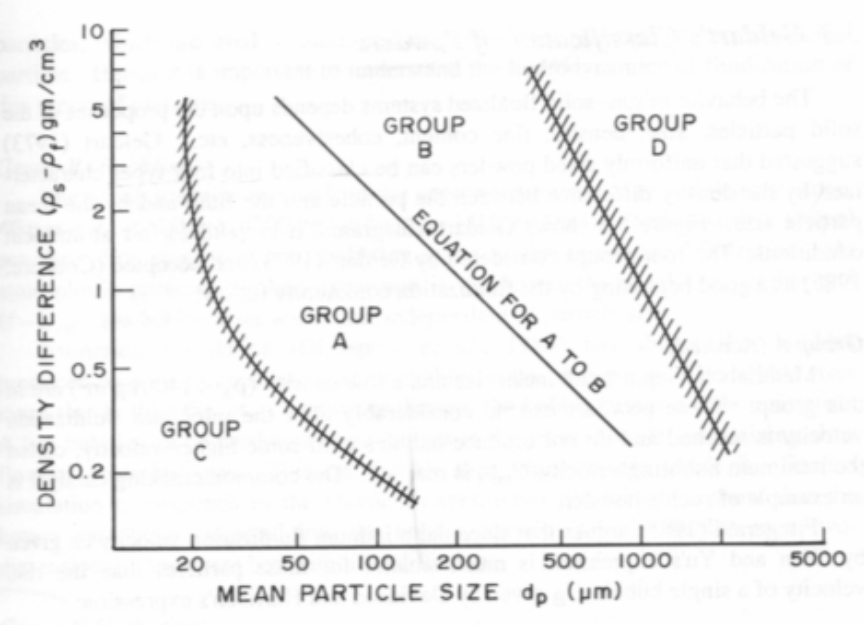

Figure 2.1: Geldart (1973) classification of particles according to their fluidization behaviour.

Group C powders are cohesive. Fluidization of these powders is extremely difficult and bubble formation will not occur. Geldart group D describes large and/or dense particle powders. Large particle beds are usually undesirable for physical and chemical operations. Large gas flows are needed to get these particles fluidized, Kunii and Levenspiel (1991). Both Geldart C and D powders give a low degree of solid mixing and gas back-mixing compared to group A and B powders. In this work group A and group B particles are used and the bubble formation and bubble behaviour of these two groups are described below.

Most commercial fluidized bed catalytic reactors use Geldart group A powders. Particles characterized in this group are easily fluidized and the bed expands considerably before bubbles appear. This is due to inter-particle forces that are present in this group of powder, Geldart (1986). Inter-particle forces are due to particle wetness, electrostatic charges and van der Waals forces. Bubble formation will occur when the gas velocity exceeds the minimum bubble velocity. The bubbles rice faster than the gas percolating through the emulsion. According to Kunii and Levenspiel (1991) maximum bubble size is usually less than 10 cm and independent of the bed size.

For group B particles the inter-particle forces are negligible and bubbles are formed as the gas velocity reaches the minimum fluidization velocity. The bed expansion is small compared to group A particles. Small bubbles are formed close to the air distributor and the bubble size increase with distance above the distributor. The bubble size also increases with the excess gas velocity which is defined as the difference between the gas velocity and the minimum fluidization velocity, Geldart (1986). Coalescence is the dominating phenomena for group B powders and bubble size is roughly independent of mean particle size. Most bubbles rise faster than the interstitial gas velocity.

2.2 Fibre optical probe measurement technique

Measurement systems based on fibre optical probes have been used in various configurations by different research scientists to perform local measurements of bubble velocity, size and concentration in particle/gas flows, Crowe et al. (1998). An optical fibre probe system consists of a probe head, a light source, a photo detector and the signal processing unit. Two different measurement principles may be used, the light attention method and the light reflection method. The probe in the light reflection method can consist of two parallel fibres, one transmitting and one receiving fibre. This method has been used by Rice et al. (2003). Instead of separate transmitting and receiving fibres, a single fibre that both transmits and receives light can be used. Single fibre reflection probes have been used by Lischer and Louge (1991) and Resner and Werther (1992) for measurements in dense two-phase flows. Tayebi et. al. (1999) developed a multi-fibre optical probe. They used tracer particles together with uncoated particles and distinguished the reflected signals by using optical filters. The method can be used to measure local movement of a single tracer particle, local bubble properties and local solid volume fraction in different positions in the bed.

In the light attenuation method the transmitting and receiving fibres are arranged opposite to each other. The method is used for particle concentration measurements and is based on Lambert-Beer law for light attenuation or on counting individual particles, Crowe et al. (1998).

The measuring system that is used in this work is based on the principle of light reflection. The system, VECTOR, is developed by Militzer and Shakourzadeh (1991) and is composed of an electronic circuit box, a fibre optic probe, a data acquisition card and a computer program to control the data acquisition. The circuit box contains two light emitting diodes (LED), two photocells and the amplification circuits. The vector system is shown in Figure 2.2.

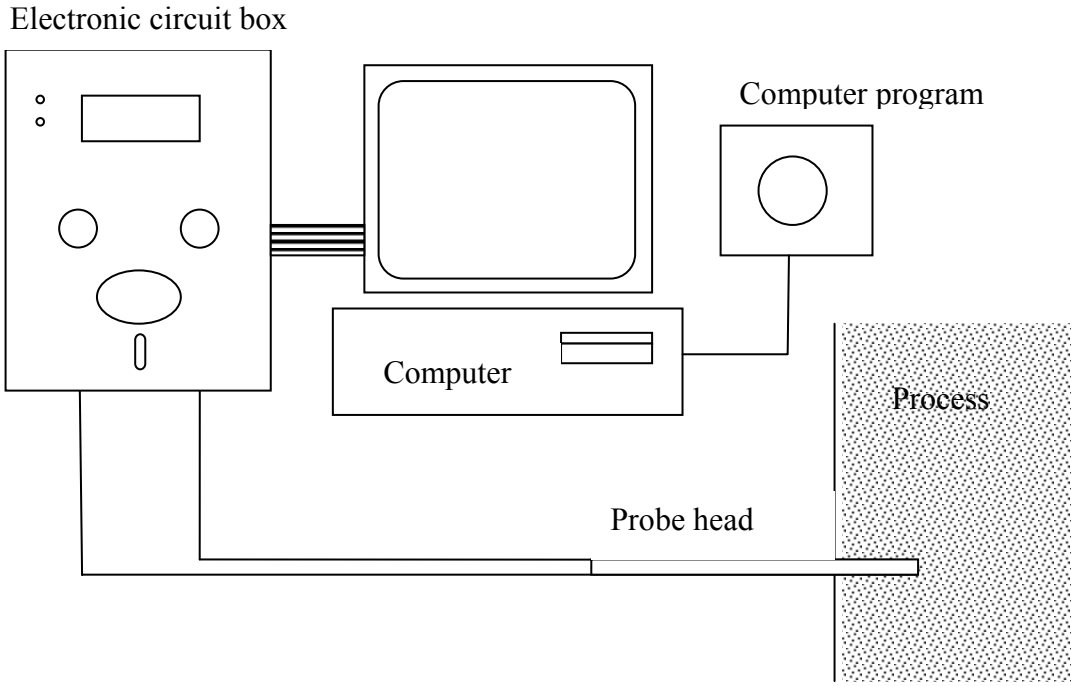

Figure 2.2: A sketch of the VECTOR kit

The probe head contains two single plastic fibres that both transmit and receive light. The vertical distance between the fibres is 2.7 mm. Each of the fibres is connected to a LED and to a photocell. When the probe is inserted into a flow of particles, the light emitted by the two LEDs is partly reflected back by the solid particles and received by the same two fibres. The fibres transmit the light to the photocells, which converts it to voltage. The intensity of the signal reflected by the solids passing in front of the fibres depends on the material, the particle shape, the particle size distribution and the concentration of particles. The reflected light produces two delayed signals where the delay time corresponds to the mean time of passage of particles between the fibres. Particle velocities are calculated from the time delay. The shape of the voltage versus time curve is essentially a function of the velocity and the concentration of the particles.

Bubble detection is based on the variations of the intensity of the light reflected back across the flow. The passage of a bubble gives a special form of a descending peak followed by an ascending peak. These two peaks correspond to the head and tail detection of the bubble.

The signal can be affected of dilute particle streams passing through a void and of particles carried up by the wakes behind the bubbles. Both of these can give positive peaks. Figure 2.3 shows the raw data from typical bubble detection. The positive peak caused by particles in the wake behind the bubble can be seen. The experimental data shown in Figure 2.3 is performed with a group B powder. Rice et al. (2003) showed that different particles may give different curves.

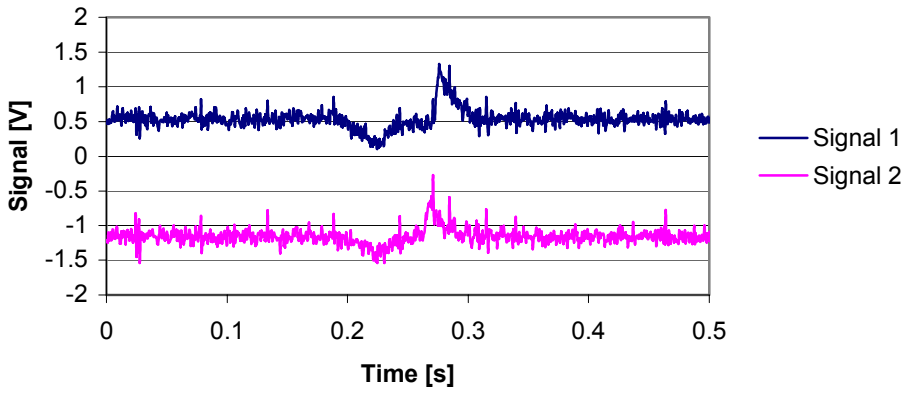

Figure 2.3: Typical voltage versus time signals obtained from a bubble detection.

2.3 Method of analysis

A data processing program is developed in Labview to analyse the raw data from the photocell is developed in this work. The raw data are given as voltage versus time signals. The raw data file consists of a specified number of data series and each of the series contains 1024 samples. The Labview program integrates the raw data curve, and use the integrated curve to detect bubbles. Criteria for a peak to be accepted as a bubble are specified. The intensity of the detected signal is dependent on the particle properties and on the initial gas velocity and the criteria have to be specified for each case. The calculated bubble frequency includes all bubbles detected.

After detecting the bubbles from the integrated curves, a cross-correlation between the two raw data curves is performed to calculate the time delay between the bubble peaks. The cross-correlation is performed for each of the validated bubbles. The bubble velocity is determined by dividing the distance between the fibres by the time delay between the two peaks.

Some of the peaks that are accepted as bubbles are difficult to analyse with respect to bubble velocity and bubble height. After the cross-correlation, the program again integrates the detected bubble peaks, and criteria are set for the bubbles to use in the calculation of bubble velocity and bubble height. When a bubble is accepted, the bubble velocity and the bubble height for actual bubble are calculated. The peak width from each signal indicates the time interval between the passage of the bubble front and the bubble rear, and is proportional to the bubble height. Thus, by knowing the bubble velocity, the bubble height can be determined. Figure 2.4 shows a screen picture of a bubble detection and calculation by the Labview program. In the upper left window the raw data of a bubble is shown and the integrated bubble peak is shown in the lower window. One criterion for accepting a peak as a bubble is that the integrals of the two raw data curves overlap each other. The windows to the right show the cross-correlation curve and a plot of the bubble velocity versus the bubble height.

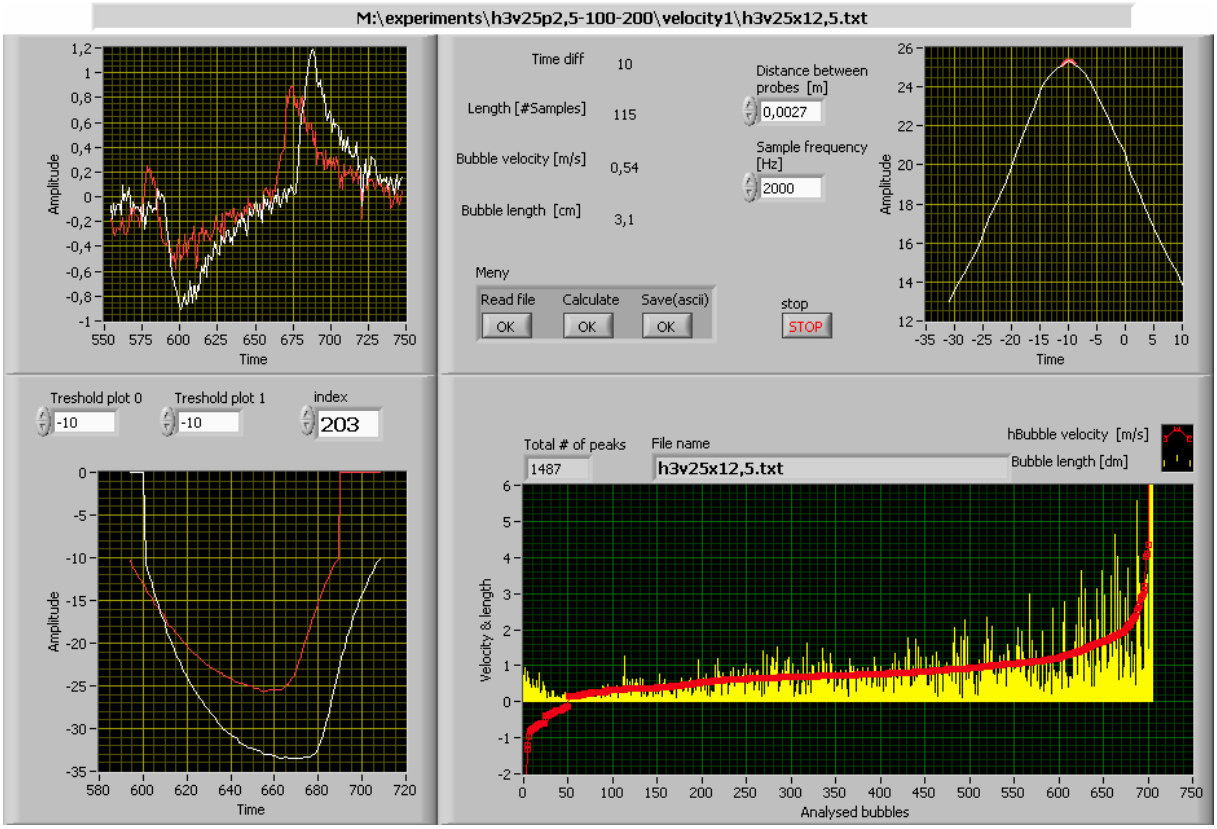

Figure 2.4: A screen picture from the Labview program.

2.3.1 The cross-correlation function

Correlation is a statistical concept describing the similarity between two signals. The extent of similarity can be determined by a mathematical method, Weber (1995). The cross-correlation is a discrete function of the time lag at multiples of the sampling interval and therefore a significant error is introduced in the velocity calculation when there are only a few points sampled during a particle's passage between two fibres. Militzer et al. (1992) propose fitting a second degree curve around the maximum in order to define a new maximum between the points and thus try to diminish the error. This implies the use of interpolation between two sampled points. The cross-correlation function is a direct consequence of the fact that it is based on signals that have been sampled at finite intervals. Herbert et al. (1994) emphasised that the use of an interpolation method will not eliminate the inherent uncertainty. Weber (1995) compared the result of using Militzer cross-correlation function, and the cross-correlation function used in the program Matlab, and he concluded that the functions give significantly different results if the quality of the data is bad and a good agreement if the quality of the data is good.

In the Labview program, developed for this work, the second degree curve around the maximum is included. The maximum is found by adjusting a second degree curve to the three sampled points around the maximum. The interpolation routine can be switch on and off. It is possible to check how the second degree curve fits with the maximum of the cross-correlation curve.

When measuring bubble velocity and bubble height, the accuracy of the measurements depends on the sampling frequency that is used. Herbert et al. (1994) defined the error, E, as the difference in velocity calculated from two neighbouring points M and M+1:

$$E = f \cdot d_f \left(\frac{1}{M} - \frac{1}{M+1} \right) \tag{2.1}$$

where f is the sampling frequency, d_f is the distance between the fibres and M is the position of the cross correlation maximum. M is directly proportional to the frequency, and by increasing the sampling frequency for a given particle velocity the value of M is also increased and the error or prevarication, E, will be reduced. There is a significant source of error in the velocity measurements and this error may be quantified using equation (2.1). Figure 2.5 shows the error in particle velocity as a function of expected particle velocities for the sampling frequencies 2000 and 4000 Hz.

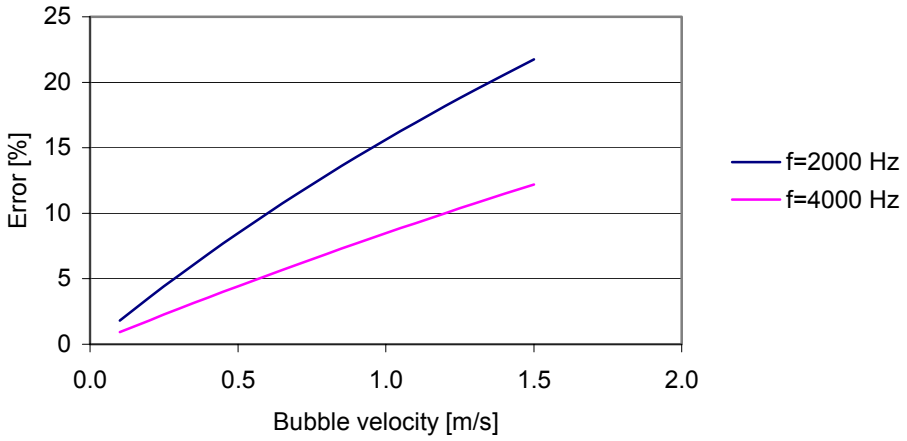

Figure 2.5: Error in particle velocity (calculated from equation (2.1)) as a function of particle velocity for the sampling frequencies 2000 and 4000 Hz.

2.3.2 Bubble velocity calculation

Bubble velocities are calculated by performing the cross-correlation between the signals, $V_1(t)$ and $V_2(t)$, from the two fibres respectively. The cross-correlation is defined as:

$$R_{V_1V_2}(t) = V_1(t) \otimes V_2(t) = \int_{-\infty}^{\infty} V_1(\tau) V_2(t+\tau) d\tau \tag{2.2}$$

where τ is the time step. The maximum of the cross-correlation curve corresponds to the time by which one of the signals is to be displaced so that it superposes the other. This time is considered as the time needed for the bubble to traverse the distance between the two fibres (Δt), and the bubble velocity is calculated by dividing the distance between the fibres by Δt, Saberi et al. (1995).

2.3.3 Bubble size calculation

The height of a bubble is calculated by multiplying the length of the signal corresponding to the passage of a bubble by the calculated bubble velocity. A bubble may contact the fibre in different positions, and therefore the measured bubble height for bubbles of the same size will have a statistical distribution, Saberi et al. (1995). A typical shape of a bubble detected is shown in Figure 2.6.

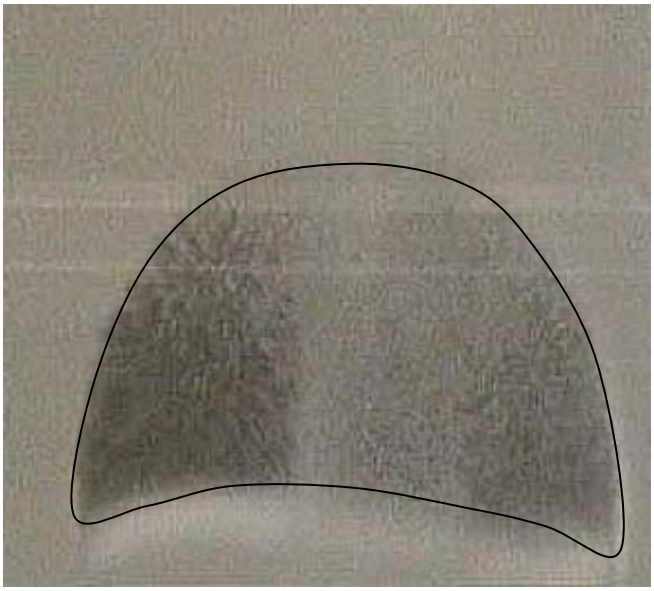

Figure 2.6: A typical bubble shape in a fluidized bed. This is a bubble observed in a bubbling fluidized bed with glass particles with diameter 400-600 μm.

The volume of the bubble can be expressed by:

$$V_b = \int_0^R 2\pi rzdr \tag{2.3}$$

where r and z is the bubble radius and height respectively. The theoretical mean height of the bubble, viewed by the probe, can be calculated by the following integral:

$$\bar{z} = \frac{\int_0^R 2\pi rzdr}{\int_0^R 2\pi rdr} = \frac{V_b}{2\pi \int_0^R rdr} = \frac{V_b}{\pi R^2} \tag{2.4}$$

Thus

$$V_b = \pi R^2 \bar{z} = \frac{\pi^2 D_b}{4} \cdot \bar{z} \tag{2.5}$$

The probability of a bubble probe contact in the horizontal area $2\pi r\Delta r$ depends on the shape of the bubble. For a bubble of the same shape as shown in Figure 2.6, the probability of measuring the mean bubble height ± 20% is about 80%. In a small area in the peripheral region of the bubble, the measured bubble height differs considerably from the mean bubble

height. The probability for measuring in this area is less than 10 %. This is a roughly calculation performed by integrating over the bubble diameter, calculating the mean bubble height from the integrated area and calculating in which positions the bubble heights will differ significantly from the mean bubble height.

For the bubble shown in Figure 2.6, the relationship between the bubble diameter, D_b, and the mean height is about 2. This relationship can be expressed by a factor, C_f:

$$C_f = \frac{D_b}{\bar{z}} \tag{2.6}$$

Bubbles with the same shape will have the same factor independent of the bubble size. Thus when the mean bubble height is calculated, the diameter of the bubble and the volume of the bubble can be calculated from equations (2.6) and (2.5) respectively. This method for statistical calculation of mean bubble sizes is applicable for systems where all the bubbles are expected to have the same size.

In a bubbling fluidized bed the size of the bubbles will differ rather much, and it is difficult to find a precise method for treating all data and calculate mean bubble height. The heights detected at one location may for instance be from the centre of a small bubble or from periphery of a large bubble. Figure 2.7 shows the measured height distribution for bubbles detected in the centre of the bed. This cannot be treated as the bubble height distribution at one location, but as the distribution of local bubble pierced length.

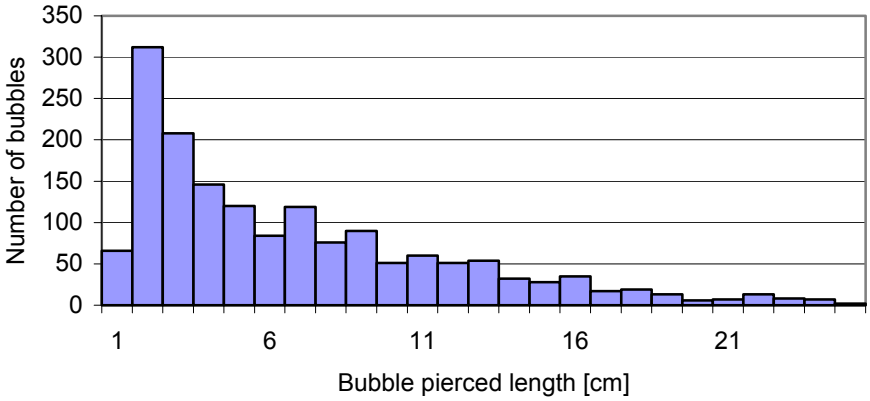

Figure 2.7: Typical bubble pierced length distribution in a bubbling fluidized bed.

In this work mean bubble pierced length, mean bubble frequency and mean bubble velocity are calculated for each location. These data can be used to calculate the local mean bubble gas flow which is defined as local mean bubble pierced length times mean bubble frequency. Mean bubble gas flow might be compared to the total gas flow to find how much of the inserted gas that leave the bed through the bubbles.

3. Governing equations in gas/particle flow

This work includes simulations performed using the CFD models (FLOTRACS-MP-3D) and MFIX. Both these CFD codes are based on a multi-fluid Eulerian description of the phases. The kinetic theory for granular flow forms the basis for the turbulence modelling of the solid phases. The MFIX code is described by Syamlal (1998) and a detailed description will not be given here. This chapter will concentrate on the CFD model (FLOTRACS-MP-3D) proposed by Mathiesen et al. (2000a,b) and emphasis the modifications that have been done in this work.

FLOTRACS-MP-3D is a gas/solid flow model, which is generalized for one gas phase and N number of solid phases. Inclusion of more than one particle phase in the model describes a more realistic particle size distribution. Based on Ding and Gidaspow (1994), Manger (1996) gave an extension from one solid phase to binary mixtures of solid phases and derived conservation equations for each solid phase. Mathiesen et al. (2000a) gave a detailed description of the model, including a discussion of the consistency of the multiphase gas/particle model. The model was verified and good results on simulations of circulating fluidized beds with relative low concentration of particles were observed. In this work the model is modified to improve its use in dense particle systems like bubbling fluidized beds.

Each solid phase is characterized by a diameter, form factor, density and coefficient of restitution. The presence of each phase is described by a volume fraction varying from zero to unity. The laws of conservation of mass, momentum and granular temperature are satisfied for each phase individually. All the phases share a fluid pressure. The gas phase turbulence is modelled by a sub-grid scale (SGS) model proposed by Deardorff (1971). The largest scales are simulated directly, whereas the small scales are modelled with the SGS turbulence model. In order to model the fluctuations in the solid phases a conservation equation for granular temperature is solved for each solid phase.

3.1 Transport equations

3.1.1 Continuity equations

The continuity equation for phase m is given by:

$$\frac{\partial}{\partial t}\left(\varepsilon_m \rho_m\right) + \frac{\partial}{\partial x_i}\left(\varepsilon_m \rho_m U_{i,m}\right) = 0 \tag{3.1}$$

where ε_m, ρ_m and $U_{i,m}$ are the phase volume fraction, the density and the i-th direction velocity component for phase m respectively. No mass transfer is allowed between the phases.

3.1.2 Momentum equations

The momentum equation in the *j* direction for phase *m* may be expressed as:

$$\frac{\partial}{\partial t}\left(\varepsilon_m \rho_m U_{j,m}\right)+\frac{\partial}{\partial x_i}\left(\varepsilon_m \rho_m U_{i,m} U_{j,m}\right)= -\varepsilon_m \frac{\partial P}{\partial x_j}+\frac{\partial \Pi_{ij,m}}{\partial x_j}+\varepsilon_m \rho_m g_j+\sum_{k=l,k\neq m}^{M}\Phi_{mk}\left(U_{j,k}-U_{j,m}\right) \tag{3.2}$$

where P is the fluid pressure, Π_{ij} the total stress tensor, g_j the j-direction component of gravity and Φ_{mk} the drag coefficient between the phases m and k. The terms on the right hand side represent pressure forces, viscous forces, mass forces and drag forces respectively. These terms are described in Table 3.1. The solid phase pressure, P_s, the solid phase bulk viscosity, ξ_s, and the solid phase shear viscosity, μ_s, are derived from the kinetic theory of granular flow.

Table 3.1: Stress tensor for gas and solid phases. Equations for gas and solid viscosity, solid pressure and averaged granular temperature.

Gas phase stress tensor:

$$\Pi_{ij,g}=\mu_{eff,g}\left[\left(\frac{\partial U_j}{\partial x_i}+\frac{\partial U_i}{\partial x_j}\right)-\frac{2}{3}\mu_s\delta_{ij}\left(\frac{\partial U_k}{\partial x_k}\right)\right]_g \tag{T3.1}$$

The effective viscosity:

$$\mu_{eff,g}=\varepsilon_g\mu_{lam,g}+\varepsilon_g\rho_g\left(c_t\Delta\right)^2\sqrt{S_{ij,g}:S_{ij,g}} \tag{T3.2}$$

$$S_{ij,g}=\frac{1}{2}\left[\frac{\partial U_j}{\partial x_i}+\frac{\partial U_i}{\partial x_j}\right]_g$$

Characteristic length scale of resolved eddies:

3D: $\Delta=\sqrt[3]{\Delta x\Delta y\Delta z}$

2D: $\Delta=\sqrt[2]{\Delta x\Delta y}$

The total stress tensor for each solid phase s:

$$\Pi_{ij,s}=-P_s\delta_{ij}+\mu_s\left(\frac{\partial U_j}{\partial x_i}+\frac{\partial U_i}{\partial x_j}\right)_s+\left(\xi_s-\frac{2}{3}\mu_s\right)\delta_{ij}\left(\frac{\partial U_k}{\partial x_k}\right)_s \tag{T3.3}$$

Solid phase bulk viscosity:

$$\xi_s=\sum_{n=1}^{N}P_{C,sn}\frac{d_{sn}}{3}\left(\theta_s+\left(m_n/m_s\right)\theta_n\right)\sqrt{\frac{2}{\pi\theta_s\theta_n\left(\theta_s+\left(m_n/m_s\right)^2\theta_n\right)}} \tag{T3.4}$$

Table 3.1 continued

Solid phase shear viscosity, collision term:

$$\mu_{col,s} = \sum_{n=1}^{N} P_{C,sn} \frac{d_{sn}}{5}\left(\theta_s + (m_n/m_s)\theta_n\right)\sqrt{\frac{2}{\pi\theta_s\theta_n\left(\theta_s + (m_n/m_s)^2\,\theta_n\right)}} \qquad \text{(T3.5)}$$

Solid phase shear viscosity, kinetic term:

$$\mu_{kin,s} = \frac{2\mu_{dil,s}}{\frac{1}{N}\sum_{n=1}^{N}(1+e_{sn})g_{sn}}\left\{1 + \frac{4}{5}\sum_{n=1}^{N} g_{sn}\varepsilon_n(1+e_{sn})\right\}^2 \qquad \text{(T3.6)}$$

Dilute viscosity:

$$\mu_{dil,s} = \frac{15}{8d_s^3}\varepsilon_s l_s\sqrt{\frac{2m_s\theta_{s,av}}{\pi}} \qquad \Lambda \qquad l_s = \frac{1}{6\sqrt{2}}\frac{d_s}{\varepsilon_s} \qquad \text{(T3.7)}$$

Average granular temperature $\theta_{s,av}$:

$$\theta_{s,av} = \frac{2m_s\theta_s}{\left\{\sum_{n=1}^{N}\left(\frac{n_n}{n_s}\right)\left(\frac{d_{sn}}{d_s}\right)^2\sqrt{\frac{(m_0/m_s)^2\,\theta_n}{\left(\theta_s + (m_n/m_s)^2\,\theta_n\right)}}S^{3/2}\right\}^2} \qquad \text{(T3.8)}$$

$$S = \frac{(m_0/m_s)^2\,\theta_n\theta_s}{\left(\theta_s + (m_n/m_s)^2\,\theta_n\right)(\theta_n + \theta_s)}$$

Solid phase pressure:

$$P_s = \sum_{n=1}^{N} P_{C,sn} + \varepsilon_s\rho_s\theta_s \qquad \text{(T3.9)}$$

Pressure caused by collisions between the solid phases s and n:

$$P_{C,sn} = \frac{\pi}{3}(1+e_{sn})d_{sn}^3 g_{sn} n_s n_n \left\{\frac{m_0\theta_s\theta_n}{((m_s/m_n)\theta_s + (m_n/m_s)\theta_n)}\right\}\left\{\frac{(m_0/m_s)^2\,\theta_s\theta_n}{\left(\theta_s + (m_n/m_s)^2\,\theta_n\right)_n(\theta_s+\theta_n)}\right\}^{3/2} \qquad \text{(T3.10)}$$

$$e_{sn} = \frac{1}{2}(e_s + e_n) \qquad d_{sn} = \frac{1}{2}(d_s + d_n) \qquad m_0 = (m_s + m_n)$$

Assumption; spherical particles:

Number of particles: $n_s = \frac{6\cdot\varepsilon_s}{\pi\cdot d_s^{\,3}}$, Mass of one particle: $m_s = \frac{\pi\cdot d_s^{\,3}\cdot\rho_s}{6}$ (T3.11)

Gas-particle drag and particle-particle drag are included in the total drag. The equations used for describing the drag are shown in Table 3.2.

Many different gas/particle drag models can be found in the literature. In this work the drag model proposed by Gibilaro et al. (1985), Syamlal and O'Brien (1987) and Erguns model in combination with Wen and Yu (1966) are used. Erguns drag model is developed for fixed bed, and is only valid for high particle concentration. Wen and Yu (1966) derived an expression for pressure drop in a particle bed, where the drag coefficient, C_D, is related to Reynolds number by Rowe (1961). Gidaspow (1994) used Ergun in combination with Wen and Yu and got a drag model that covered the whole range of particle concentrations.

Table 3.2: Equations for gas/particle and particle/particle drag

Total gas/particle drag:

$$\Phi_{sg} = \frac{3}{4} C_D \frac{\varepsilon_s \varepsilon_g}{d_s \psi_s} \rho_g \left| \vec{U}_g - \vec{U}_s \right| \qquad \text{(T3.12)}$$

Friction coefficient, Gibilaro et al. (1985):

$$C_D = \frac{4}{3}\left(\frac{17.3}{Re_s} + 0.336 \right) \varepsilon_g^{-2.80} \qquad \text{(T3.13)}$$

Particle Reynolds number:

$$Re_s = \frac{d_s \psi_s \rho_g \left| \vec{U}_g - \vec{U}_s \right| \varepsilon_s}{\mu_g} \qquad \text{(T3.14)}$$

Ergun equation, Ergun (1952):

$$\Phi_{sg} = 150 \frac{(1-\varepsilon_g)^2 \mu_s}{\varepsilon_g (d_s \psi_s)^2} + 1.75 \frac{\rho_s \left| \vec{U}_g - \vec{U}_s \right| \varepsilon_s}{d_s \psi_s}, \text{ for } \varepsilon_g \le 0.8 \qquad \text{(T3.15)}$$

Rowe (1961) and Wen and Yu (1966):

$$\Phi_{sg} = \frac{3}{4} C_D \frac{\varepsilon_s \varepsilon_g}{d_s \psi_s} \rho_g \left| \vec{U}_g - \vec{U}_s \right| \varepsilon_g^{-2.65}, \quad \text{for } \varepsilon_g > 0.8 \qquad \text{(T3.16)}$$

Friction coefficient related to Reynolds number:

$$C_D = \frac{24}{Re_s}\left(1 + 0.15 Re^{0.687}\right), \quad Re_s \le 1000 \qquad \text{(T3.17)}$$

$$C_D = 0.44, \quad Re_s > 1000$$

Table 3.2 continued

Syamlal and O'Brian (1987):

$$\Phi_{sg} = \frac{3}{4 d_s} C_D \rho_g \frac{1}{R_t^{\,2}} \varepsilon_g (1-\varepsilon_g) \left| \vec{U}_g - \vec{U}_s \right| \tag{T3.18}$$

$$R_t = 0.5\left(A - 0.06 Re_s + \sqrt{0.0036 Re_s^2 + 0.12 Re_s (2B - A) + A^2}\right) \tag{T3.19}$$

$$A = \varepsilon_g^{4.14}$$

$$B = 0.8 \varepsilon_g^{1.28}, \quad \text{for } \varepsilon_g < 0.85$$

$$B = \varepsilon_g^{2.65}, \quad \text{for } \varepsilon_g > 0.85$$

$$C_D = \left(0.63 + 4.8 \sqrt{\frac{R_t}{Re_s}}\right) \tag{T3.20}$$

Particle/particle drag coefficient, Manger (1996):

$$\Phi_{sn} = P_{C,sn} \left\{ \frac{3}{d_{sn}} \sqrt{\frac{2\left(m_s^2 \theta_s + m_n^2 \theta_n\right)}{\pi m_0^2 \theta_s \theta_n}} + \frac{1}{\left| \vec{U}_g - \vec{U}_s \right|} \left[\nabla \left| \ln \frac{\varepsilon_s}{\varepsilon_n} \right| + \frac{\theta_s \theta_n}{\theta_s + \theta_n} \left| \frac{\nabla \theta_n}{\theta_n^2} - \frac{\nabla \theta_s}{\theta_s^2} \right| + 3 \nabla \left| \frac{\ln(m_n \theta_n)}{\ln(m_s \theta_s)} \right| \right] \right\} \tag{T3.21}$$

3.1.3 Granular temperature equation

Kinetic theory of granular flow describes the dependence of the rheologic properties of the fluidized particles on local particle concentration and the random fluctuating motion of particles due to particle-particle collisions. The granular temperature for a particle is defined as:

$$\theta = \frac{1}{3} \langle C \cdot C \rangle \tag{3.3}$$

where C is the fluctuating component of the particle velocity. The variation of particle velocity fluctuation is described with a separate conservation equation, the granular temperature equation. The transport equation for granular temperature is solved for each solid phase, and is given by:

$$\frac{3}{2}\left[\frac{\partial}{\partial t}\left(\varepsilon_s \rho_s \theta_s\right) + \frac{\partial}{\partial x_i}\left(\varepsilon_s \rho_s U_{i,s} \theta_s\right) \right] = \left(\Pi_{ij,s} : \frac{\partial U_{j,s}}{\partial x_i} \right) + \frac{\partial}{\partial x_i}\left(\kappa_s \frac{\partial \theta_s}{\partial x_i} \right) - \gamma_{sn} - 3 \Phi_{sg} \theta_s \tag{3.4}$$

The terms on the right hand side represent granular temperature production, conductivity of granular temperature, dissipation due to particle-particle collisions and dissipation due to fluid-particle interaction. The conductivity and dissipation of granular temperature are given in Table 3.3.

Table 3.3: Conductivity and the dissipation of granular temperature

Conductivity of granular temperature, dense part:

$$\kappa_s = \frac{2\kappa_{dil,s}}{\frac{1}{N}\sum_{n=1}^{N}(1+e_{sn})g_{sn}}\left\{1+\frac{6}{5}\sum_{n=1}^{N}\varepsilon_n g_{sn}(1+e_{sn})\right\}^2 + 2\varepsilon_s\rho_s d_s\sqrt{\frac{\theta_s}{\pi}}\sum_{n=1}^{N}\varepsilon_n g_{sn}(1-e_{sn}) \qquad \text{(T3.22)}$$

Conductivity of granular temperature, dilute part:

$$\kappa_{dil,s} = \frac{225}{32}\varepsilon_s l_s\sqrt{\frac{2m_s\theta_{s,av}}{\pi}} \qquad \text{(T3.23)}$$

The dissipation of granular temperature due to inelastic collisions:

$$\gamma_{sn} = \sum_{n=1}^{N}\frac{3}{4}P_{C,sn}\frac{(1-e_{sn})}{d_{sn}}\left[4\sqrt{\frac{2\theta_s\theta_n}{\pi\left((m_s/m_0)^2\theta_s+(m_n/m_0)^2\theta_n\right)}} - d_{sn}\left(\frac{(m_s/m_0)\theta_s+(m_n/m_0)\theta_n}{(m_s/m_0)^2\theta_s+(m_n/m_0)^2\theta_n}\right)\right]\frac{\partial U_{k,s}}{\partial x_k} \qquad \text{(T3.24)}$$

3.2 Dense packing of solids

The success of numerical computation of bubbling fluidized beds critically depends upon the ability to handle dense packing of solids. Granular materials display a variety of behaviours that are in many ways different from those of other substances. They cannot be easily classified as either solids or fluids.

3.2.1 Solid phase pressure and frictional stresses

At high solid volume fraction, sustained contacts between particles occur and the resulting frictional stresses must be accounted for in the description of the solid phase stress. Granular flows can be classified into two flow regimes, a viscous regime and a plastic regime. In a viscous or rapidly shearing regime, the stresses arise because of collisional or translational transfer of momentum, whereas in a plastic or slowly shearing regime, the stresses arise because of Coulomb friction between grains in enduring contact, Jenkins and Cowin (1979).

Different approaches are used to describe the stresses in these flow regimes. E.g. Johnson and Jackson (1987) combined the theories of the two regimes by adding the formulas of the regimes. Syamlal et al. (1993) combined these theories in the MFIX code by introducing a "switch" between the viscous and the plastic regime at a critical void fraction. The critical

packing is the packed bed void fraction at which a granular flow regime transition is assumed to occur. In fluidized bed simulations the critical void fraction is usually set to the void fraction at minimum fluidization. Laux (1998) assumed that long-term particle contacts only contribute to the stress tensor above a certain particle volume fraction. The effective stresses are then given by the maximum of the viscosity obtained from the kinetic and collisional stresses and the frictional stresses. The frictional stresses are not included below the specified critical particle volume fraction.

The same "switch" that is used by Syamlal (1993), has been incorporated in FLOTRACS. The stress tensor for the solid phase s, is given by:

$$\Pi_{ij,s} = \begin{cases} -P_s^{P}\delta_{ij} + \bar{\tau}_s^{P} & \text{if } \varepsilon \le \varepsilon^* \\ -P_s^{V}\delta_{ij} + \bar{\tau}_s^{V} & \text{if } \varepsilon > \varepsilon^* \end{cases} \tag{3.5}$$

where P_s is the solid phase pressure, τ is the viscous stress of the solid phase s and ε^* is the void fraction at minimum fluidization. The superscripts P and V describe the plastic and the viscous regimes respectively.

The stress tensor for the viscous regime is given in Table 3.1, equations T3.3-T3.8. The stress tensor for the plastic regime is described below.

The frictional stress of the plastic regime is given by Schaeffer (1987):

$$\tau_{ij,s}^{p} = \mu_s^{P}\left(\frac{\partial U_j}{\partial x_i} + \frac{\partial U_i}{\partial x_j}\right)_s \tag{3.6}$$

where μ_s^p is the plastic viscosity and is given by:

$$\mu_s^p = \frac{P^* \sin\Phi}{2\sqrt{I_{SD}}}$$

$$I_{SD} = \frac{1}{6}\left[\left(\frac{\partial U_i}{\partial x} - \frac{\partial U_j}{\partial y}\right)_s^2 + \left(\frac{\partial U_j}{\partial y} - \frac{\partial U_k}{\partial z}\right)_s^2 + \left(\frac{\partial U_k}{\partial z} - \frac{\partial U_i}{\partial x}\right)_s^2\right] + \left(\frac{\partial U_i}{\partial y}\right)_s^2 + \left(\frac{\partial U_j}{\partial z}\right)_s^2 + \left(\frac{\partial U_k}{\partial x}\right)_s^2 \tag{3.7}$$

I_{SD} is the second invariant of the deviator of the strain rate tensor and Φ is the angle of internal friction. In MFIX the solid stresses of the plastic regime are calculated for only one particle phase even when multiple particle phases are included, Syamlal et al. (1993). In this work simulations have been performed by calculating the solid stresses of the plastic regime for all the solid phases.

Prichett et al. (1978) described the solid phase pressure for the plastic flow regime by an arbitrary function that allows a certain amount of compressibility in the solid phase:

$$P_{sn}^{P} = \varepsilon_{sn} P^{*} \tag{3.8}$$

where P^{*} is represented by an empirical power law developed by Jenike (1987):

$$P^{*} = A(\varepsilon^{*} - \varepsilon)^{n} \tag{3.9}$$

The values $A=10^{25}$ and $n=10$ are most commonly used, and these values are used in MFIX. In this work different values of A have been tested in FLOTRACS. These studies show that using $A=10^{25}$ give a very abrupt transition in bubble behaviour when switching from the viscous to the plastic regime. $A=10^{9}$ gives a very smooth transition between the regimes. This value of A is used in the simulations in this work.

3.2.2 Radial distribution function

The radial distribution function, g_0, influences the calculation of the solid phase pressure, caused by the collisions between particles, and g_0 is also included in the equation for the granular temperature and in the wall functions. The radial distribution function is close to one when the flow is dilute and becomes infinite when the flow is so dense that motion is impossible. Different expressions for g_0 are proposed by different scientists.

In FLOTRACS the radial distribution function derived by Bagnold (1954) is an alternative. This equation works well for dilute suspensions and is expressed by:

$$g_0 = \left[1 - \left(\frac{\varepsilon_s}{\varepsilon_{s,max}} \right)^{1/3} \right]^{-1} \tag{3.10}$$

For uniform spheres, Bagnold (1954) showed:

$$\varepsilon_{s,max} = \frac{\pi}{3\sqrt{2}} = 0.7405 \tag{3.11}$$

The radial distribution function estimated by the model proposed by Ma and Ahmadi (1986) is included in FLOTRACS. The function is given by:

$$g_0 = 1 + 4\varepsilon_s \frac{1 + 2.5000\varepsilon_s + 4.5904\varepsilon_s^2 + 4.515439\varepsilon_s^3}{\left[1 - \left(\frac{\varepsilon_s}{\varepsilon_{s,max}} \right)^{3} \right]^{0.67802}} \tag{3.12}$$

with $\varepsilon_{s,max} = 0.64356$.

When the void fraction is lower than the minimum void fraction the radial distribution function is calculated for a void fraction, ε_0, close to the minimum void fraction and $g_0(\varepsilon_0)$ is corrected by a term developed from two points close to ε_0.

When $\varepsilon<\varepsilon_{min}$, g_0 is expressed by the following equation:

$$g_0(\varepsilon) = f\cdot(\varepsilon-\varepsilon_0)+g_0(\varepsilon_0)$$

$$f = \frac{(g_0(\varepsilon_+)-g_0(\varepsilon_-))}{\varepsilon_+-\varepsilon_-} \qquad (3.13)$$

where f is the gradient of g_0 in ε_0, $f\cdot(\varepsilon-\varepsilon_0)$ is the correction term, ε_+ and ε_- are void fractions higher and lower than ε_0 respectively. Figure 3.1 shows a calculation of radial distribution function in a case where the void fractions ε_0, ε_+ and ε_- are 0.36, 0.36001 and 0.35999 respectively.

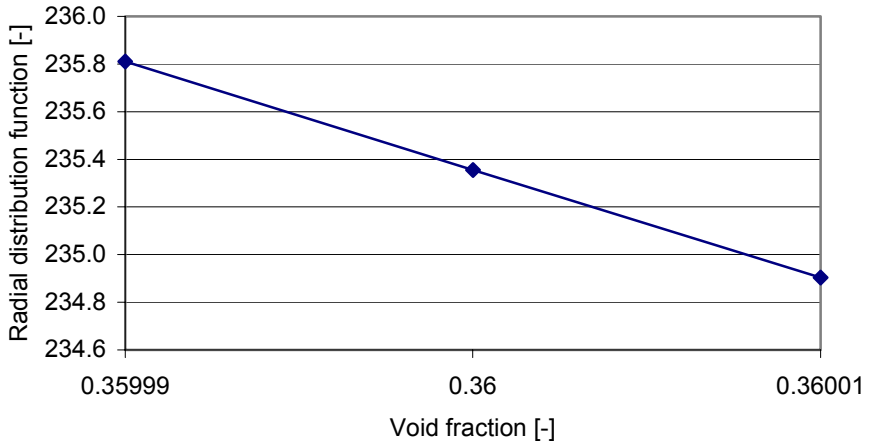

Figure 3.1 Radial distribution function calculated for different void fraction

In MFIX the function of Carnahan & Starling (1969) is included. This equation can be used if the calculations are performed with only one particle phase.

$$g_0 = \frac{1}{1-\varepsilon_s}+1.5\varepsilon_s\left(\frac{1}{1-\varepsilon_s}\right)^2+0.5\varepsilon_s^{\,2}\left(\frac{1}{1-\varepsilon_s}\right)^3 \qquad (3.14)$$

When more than one particle phase is included, the radial distribution function may be expressed by Mathiesen et al (2000a):

$$g_{0,sn} = \frac{N}{2}\frac{g_0}{(1-\varepsilon)}(\varepsilon_s+\varepsilon_n) \qquad (3.15)$$

where N is the total number of solid phases ε_s and and ε_n is the volume fraction for the solid phases s and n.

MFIX use the radial distribution function, $g_{0,sn}$, derived by Lebowitz (1964):

$$g_{0,sn} = \frac{1}{\varepsilon} + \frac{3 d_n d_s}{\varepsilon^2 (d_n + d_s)} \sum_{m=1}^{N} \frac{\varepsilon_{sm}}{d_m} \tag{3.16}$$

N is the number of solid phases, d_n and d_s is the particle diameter of solid phase s and n respectively and ε_{sm} is the volume fraction of solid phase m. This radial distribution function is derived for a mixture of spheres.

4. Numerical solution procedure

The governing equations given in chapter 3 are solved by a finite volume method, where the calculation domain is divided into a finite number of non-overlapping control volumes. Physical parameters are stored at main grid points placed in centre of the control volumes. Staggered grid arrangements are used for the velocity components that are stored at the main control volume surfaces. Figure 4.1 shows a scalar control volume for a two-dimensional Cartesian situation and in Figure 4.2 velocity control volumes are shown.

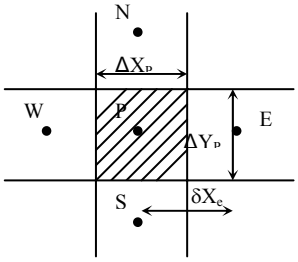

Figure 4.1: Control volume for scalar variables

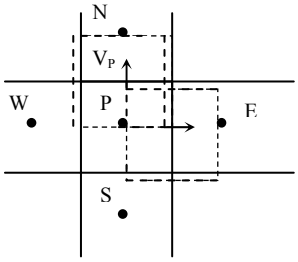

Figure 4.2: Control volume for velocities

The conservation equations are integrated in space and time. This integration is performed using first or second order upwind differencing in space and fully implicit in time. The set of algebraic equations is solved by a tri-diagonal matrix algorithm (TDMA), except for the volume fraction where a point iteration method is used. Partial elimination algorithm (PEA) generalized to multiple phases is used to decouple the drag forces. The interphase-slip algorithm (IPSA) is used to take care of the coupling between the continuity and the velocity equations.

4.1 Differencing schemes

First and second order upwind schemes are included in FLOTRACS. Upwind differencing schemes take into account the flow direction.

First order upwind scheme (FOU) may produce erroneous results when the flow is not aligned with the grid lines and can cause flow parameters to become smeared. This error is referred to as false diffusion. In this work second order upwind scheme (SOU) is introduced in FLOTRACS (MP-3D) to avoid the problem with false diffusion. SOU is less computationally stable and can generate oscillations around discontinuities. Hence total variation dimishing (TVD) is included to avoid this unphysical behaviour.

4.1.1 First order upwind scheme (FOU)

A general differential equation can be written as:

$$\frac{\partial}{\partial t}(\rho\Phi)+\frac{\partial}{\partial x_i}(\rho U_i\Phi)=\frac{\partial}{\partial x_i}\left(\Gamma\frac{\partial\Phi}{\partial x_i}\right)+S_\Phi \tag{4.1}$$

where S_Φ is the source term. The discretisation equation for the dependent variable Φ for a one-dimensional system is obtained.

$$a_P\Phi_P = a_E\Phi_E + a_W\Phi_W + b \tag{4.2}$$

where the constant part of the source term is included in b. The value of Φ in point P becomes a linear combination of Φ in the neighbour points W and E. The coefficients in the neighbour points depend on how Φ varies between the main grid nodes, and include convection and diffusion. For the FOU difference scheme the coefficients of the neighbouring points can be written as, Patankar (1980):

$$a_W = \max(F_w,0)+D_W \qquad a_E = \max(-F_e,0)+D_E \tag{4.3}$$

The variables, F and D, represent the convective and the diffusive fluxes at cell faces and are defined according to:

$$F_e=(\rho U)_e\Delta y \qquad F_w=(\rho U)_w\Delta y \qquad D_e=\frac{\Gamma_e\Delta y}{\delta x_e} \qquad D_w=\frac{\Gamma_w\Delta y}{\delta x_w} \tag{4.4}$$

The transport coefficient, Γ, at the east control volume surface is expressed as:

$$\Gamma_{\Phi,e}=\frac{2\Gamma_P\Gamma_E\delta x_e}{\Gamma_P\Delta x_E+\Gamma_E\Delta x_P} \tag{4.5}$$

4.1.2 Second order upwind scheme (SOU)

The principle of the SOU scheme is illustrated in Figure 4.3. The cell face value of Φ is estimated from the two upstream neighbouring nodes by linear extrapolation.

The value of Φ_e can be expressed by:

$$\begin{aligned}\Phi_e &= \Phi_P+(\Phi_P-\Phi_W)\frac{(\delta x)_{Pe}}{(\delta x)_{WP}} \qquad \text{if } F_e>0\\ \Phi_e &= \Phi_E+(\Phi_E-\Phi_{EE})\frac{(\delta x)_{eE}}{(\delta x)_{EEE}} \qquad \text{if } F_e<0\end{aligned} \tag{4.6}$$

and the one-dimensional discretization equation for Φ becomes:

$$a_P\Phi_P = a_E\Phi_E + a_W\Phi_W + a_{EE}\Phi_{EE} + a_{WW}\Phi_{WW} + b \tag{4.7}$$

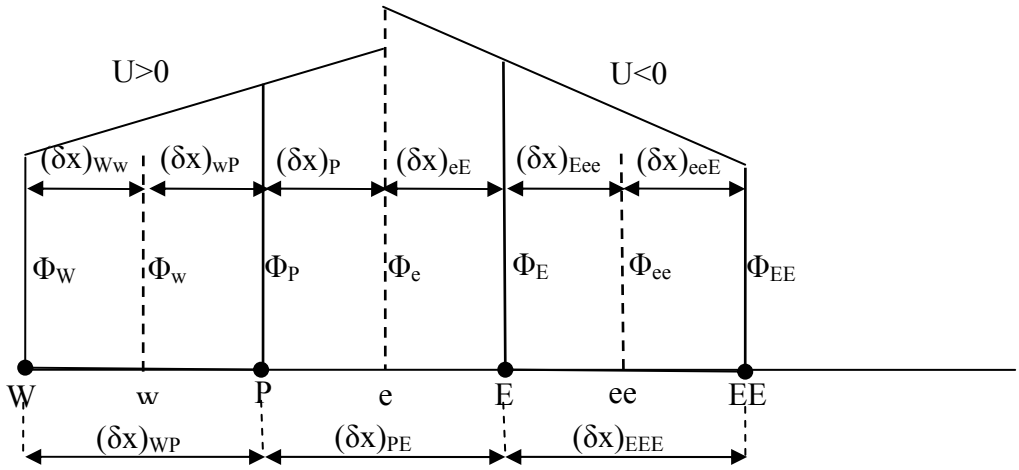

Figure 4.3: The principle of second order upwind scheme.

For uniform grid size the coefficients of the neighbouring points become:

$$\begin{aligned} a_E &= D_e + \frac{3}{2}\max(-F_e,0) + \frac{1}{2}\max(-F_w,0) \\ a_W &= D_w + \frac{3}{2}\max(F_w,0) + \frac{1}{2}\max(F_e,0) \\ a_{EE} &= -\frac{1}{2}\max(-F_e,0) \\ a_{WW} &= -\frac{1}{2}\max(F_w,0) \end{aligned} \tag{4.8}$$

The SOU scheme is unbounded and may generate oscillations around sharp gradients, Hirsch (1990). Introduction of non-linear flux limiters into the scheme solves this problem. Such limiters are derived on the basis of TVD conditions, which ensure that no new local extrema are created and that the value of an existing local minimum/maximum must be non-decreasing/non-increasing. The SOU-scheme for Φ_e with TVD limiters can be written as:

$$\Phi_e = \Phi_P + \frac{1}{2}\Psi_e(r_e)(\Phi_P - \Phi_W) \qquad \text{if } F_e > 0 \tag{4.9}$$

where $\Psi_e(r_e)$ is the flux limiter and r_e is the limiter argument.

$$r_e = \frac{\Phi_E - \Phi_P}{\Phi_P - \Phi_W} \tag{4.10}$$

Several different flux limiters are proposed to ensure the TVD conditions. The following flux limiters have been included in FLOTRACS:

Van Leer limiter:

$$\Psi_e(r_e) = \frac{r_e + |r_e|}{(1 + r_e)} \tag{4.11}$$

Superbee limiter:

$$\Psi_e(r_e) = \max(0, \min(2r_e, 1), \min(r_e, 2)) \tag{4.12}$$

Minmod limiter:

$$\Psi_e(r_e) = \max(0, \min(r_e, 1)) \tag{4.13}$$

Second order accuracy is ensured by the condition $\Psi(1)=1$, and $\Psi=0$ reduces the scheme to first order accuracy.

4.2 Solid volume fraction correction

In gas/particles flow calculations it is important to prevent unphysically dense packing of solids. As discussed in Chapter 3, the solid pressure is influencing the solid packing. The solid pressure is defined for the viscous regime and for the plastic regime. In both regimes the solid pressure is defined as a function of solid volume fraction. In MFIX the calculations are stabilized by including the effect of solids pressure, P_S, in the discretized solids continuity equation. MFIX uses a solid volume fraction correction. The solid volume fraction correction equation accounts for the effect of solids pressure so that the computations are stabilized in closed packed regions. For this method to work, a state equation that relates solids pressure to solids volume fraction is needed, Syamlal (1998):

$$P_S = P_S(\varepsilon_S) \tag{4.14}$$

and the derivate of solids pressure with respect to solids volume fraction, K_S, is defined as:

$$K_S = \frac{\partial P_S}{\partial \varepsilon_S} \tag{4.15}$$

A small change in solids pressure, P_S', can be calculated as a function of the change in solids volume fraction, ε_S':

$$P_S' = K_S \varepsilon_S' \tag{4.16}$$

An equation for volume fraction correction can then be written as:

$$a_P\left(\varepsilon_S'\right)_P = \sum_{nb} a_{nb}\left(\varepsilon_S'\right)_{nb} + b \tag{4.17}$$

where the terms on the right hand are the convective terms and the source term respectively.

The coefficient on the east neighbouring point can be expressed as:

$$a_E = \max\left(-F_{S,e}, 0\right) + D_E \tag{4.18}$$

$F_{S,e}$ and D_E are expressed as:

$$F_{S,e} = \left(\rho_S\right)_E \left(U_S\right)_e^* A_e \quad \text{and} \quad D_E = \left(\rho_S \varepsilon_S\right)_e^* e_e \left(K_S\right)_E A_e \tag{4.19}$$

The velocity field $\left(U_S\right)_e^*$ is the velocity field after correcting for the fluid pressure correction. The actual solid velocity can be represented as:

$$\left(U_S\right)_e = \left(U_S^*\right)_e + \left(U_S^{'}\right)_e \tag{4.20}$$

where the velocity correction, $\left(U_S^{'}\right)_e$, is related to the solids pressure field as, Syamlal (1998):

$$\left(U_S^{'}\right)_e = e_e \left[\left(P_S^{'}\right)_P - \left(P_S^{'}\right)_E\right] \tag{4.21}$$

P_S' is the solid pressure correction and e_e is the coefficient linking velocity correction to the solid pressure correction. Substituting from (4.16) gives the following equation for the solid velocity correction:

$$\left(U_S^{'}\right)_e = e_e \left[\left(K_S\right)_P \left(\varepsilon_S^{'}\right)_P - \left(K_S\right)_E \left(\varepsilon_S^{'}\right)_E\right] \tag{4.22}$$

The source term, b, in eq. 4.17 can be expressed as, Syamlal (1998):

$$\begin{aligned} b = & -\left(\rho_S \varepsilon_S^*\right)_e \left(U_S^*\right)_e A_e + \left(\rho_S \varepsilon_S^*\right)_w \left(U_S^*\right)_w A_w - \left(\rho_S \varepsilon_S^*\right)_n \left(V_S^*\right)_n A_n \\ & + \left(\rho_S \varepsilon_S^*\right)_s \left(V_S^*\right)_s A_s - \left(\rho_S \varepsilon_S^*\right)_t \left(W_S^*\right)_t A_t + \left(\rho_S \varepsilon_S^*\right)_b \left(W_S^*\right)_b A_b \\ & - \left[\left(\rho_S \varepsilon_S^*\right)_P - \left(\rho_S \varepsilon_S^*\right)_P^0\right] \frac{\Delta V}{\Delta t} \end{aligned} \tag{4.23}$$

After calculating the solids volume fraction correction, $\varepsilon_S^{'}$, the solid volume fraction is updated:

$$\varepsilon_S = \varepsilon_S^* + \varepsilon_S^{'} \tag{4.24}$$

In regions where the solid volume fraction is close to maximum packing, a small increase in the solid volume fraction will cause a large increase in the solid pressure. Such rapid changes in the solids pressure leads to numerical instability. Selective under relaxation is applied in densely packed regions to avoid these rapid changes. The equation of solid volume fraction under dense packed condition is expressed as:

$$\varepsilon_S = \varepsilon_S^* + \omega_{PS} \varepsilon_S^{'} \tag{4.25}$$

$$\text{when} \quad \varepsilon_S > \varepsilon_{S,max} \quad \text{and} \quad \varepsilon_S^{'} > 0$$

ω_{PS} is the relaxation factor for the solid volume fraction correction.

The velocity corrections for the solids phases are calculated and the solids velocity field is updated according to equation (4.20). The void fraction is calculated from:

$$\varepsilon = 1.0 - \sum \varepsilon_S \tag{4.26}$$

The solid phase pressure is calculated from the state equation. The procedure for the calculations is shown in Figure 4.4.

4.3 Initial and boundary conditions

4.3.1 Initial conditions

Initial conditions are specified for the dependent variables. The velocity field is set to zero in the whole calculation domain. Initial volume fractions are specified for the multiphase part of the bed. The initial volume fraction for solids is set closed to the solid fraction at maximum packing. In the rest of the calculation domain the void fraction are set to one.
The granular temperature for the solid phases is set to:

$$\theta_s = 5 \cdot 10^{-6}\, \varepsilon_s \tag{4.27}$$

4.3.2 Wall boundaries

For the gas phase a non slip boundary condition is used at the wall. For the solid phases wall conditions as proposed by Sinclair and Jackson (1989) are adopted:

$$\tau_w = \mu_s \frac{\partial U_{j,s}}{\partial x_i} = \frac{\varepsilon_s}{\varepsilon_{smax}} \frac{\pi}{6} \rho_s \omega_s \sqrt{3\theta_s}\, U_{j,s} g_{ss,w} \tag{4.28}$$

where $g_{ss,w}$ is the radial distribution function at the wall and ω_s is the specularity factor. The specularity factor is one for diffusely scattered collisions and zero for completely specular collisions.

The flux of the granular temperature at the wall is also expressed by Sinclair and Jackson (1989). The granular temperature flux at the wall is given as the generation of turbulent kinetic energy by slip and dissipation by inelasticity of collisions between particles and wall:

$$q_w = \frac{\varepsilon_s (1-\varepsilon_s)}{\varepsilon_{smax}} g_{ss,w} \pi \rho_s \sqrt{3} \left[\frac{\omega_s}{6} \sqrt{\theta_s}\, U_{j,s}^2 - \frac{1}{4} \left(1 - e_{sw}^2\right) \theta_s \sqrt{\theta_s} \right] \tag{4.29}$$

where e_{sw} is the coefficient of restitution for collisions between particles and wall. Zero flux is used for the volume fractions and pressure. The velocity component perpendicular to the wall is set to zero.

4.3.3 Inlet and outlet boundaries

Inlet flux is specified at the boundaries. Granular temperature at inlet is set by equation (4.27). At the outlet, volume fractions, pressure, granular temperatures and velocities of the solid phases are extrapolated upstream. The velocity at the outlet of the continuous phase is calculated from the total mass balance.

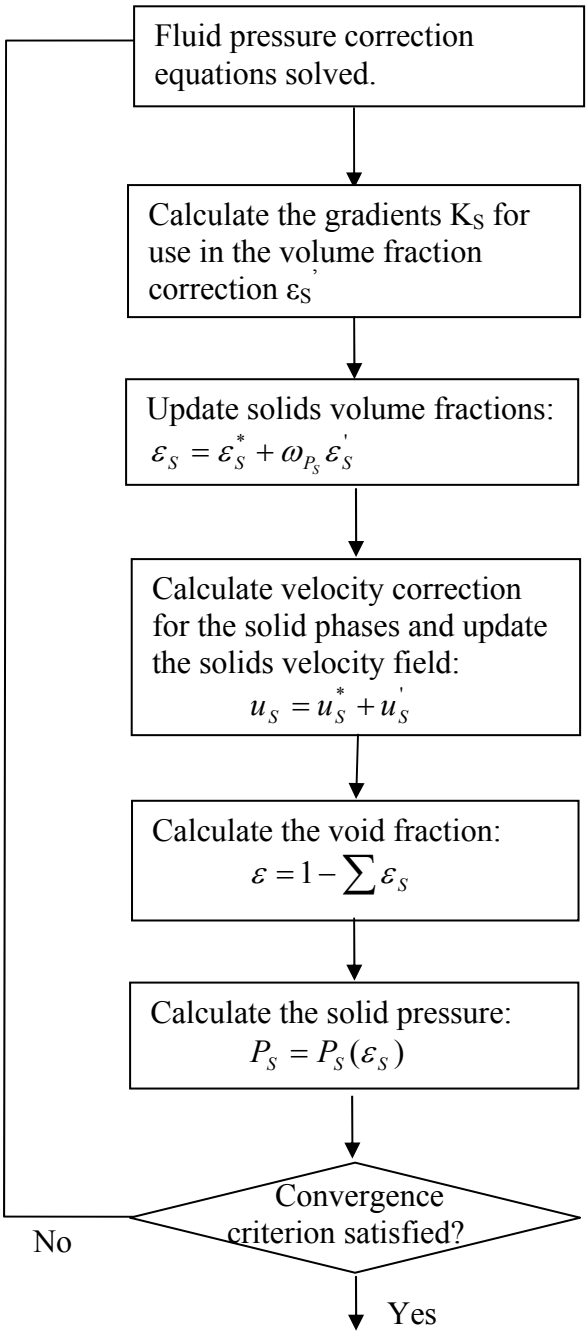

Figure 4.4: Flow chart of solid volume fraction correction procedure.

5. Experimental and computational study of a 2-D fluidized bed with a jet

Bubble formation in a two dimensional bed with a central jet is studied experimentally and computationally. The purpose of this study is to verify the calculation of bubble formations on a simple well-defined model.

5.1 Experimental set-up

The fluidized bed is constructed with a cross-sectional area of 19.5x2.5 cm and a height of 63 cm. The central jet is a 0.5x2.5 cm rectangular slit. The pressure drop through the distribution section is about 15 % of the bed weight. The experimental set-up is shown in Figure 5.1.

1. 2D-bed
2. Flowmeter, jet
3. Flowmeter, fluidization
4. Pressure reduction valve for jet
5. Pressure reduction valve for fluidization

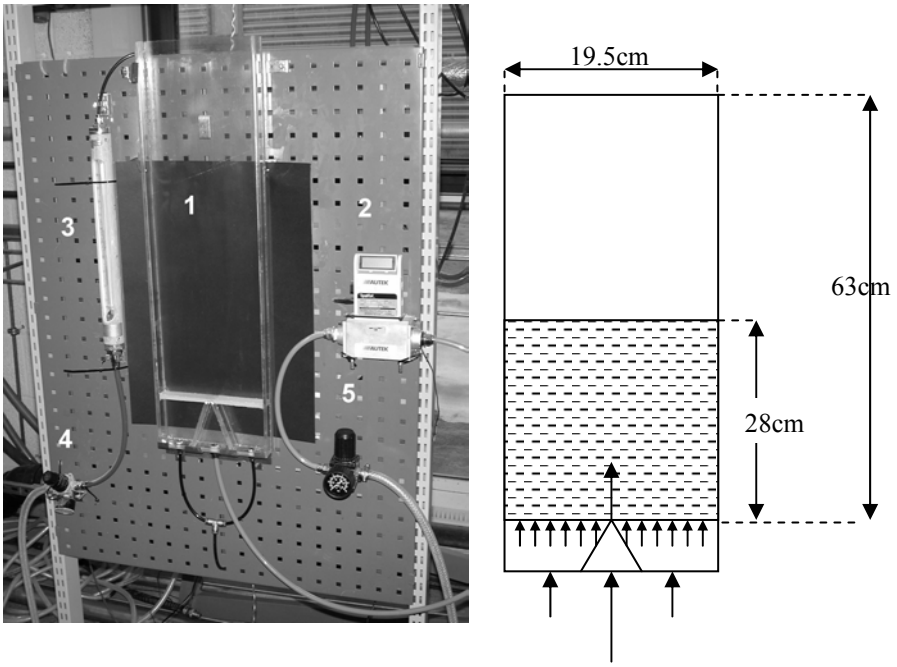

Figure 5.1: Experimental set-up.

Two different powders are used in this study. Spherical glass particles with a particle density of 2485 kg/m^3 and a volume averaged diameter of 491 μm are applied in the first series. These particles are Geldart group B particles. In the second series PMMA (poly methyl meta acrylat) particles with a particle density of 1100 kg/m^3 and a volume averaged diameter of 128 μm are used. PMMA particles are characterized as Geldart group A particles. The experimental conditions are given in Table 5.1. A digital video camera is applied to measure bubble formation and velocity.

Table 5.1: Experimental set-up and conditions.

Design			
Height	63.0 cm	Depth	2.50 cm
Width	19.5 cm	Jet area	0.5x2.5 cm^2
Glass particles			
Mean particle diameter	491 μm	Jet velocity	4.9 m/s
Solid density	2485 kg/m^3	Fluidization velocity	0.29 m/s
Bulk density	1500 kg/m^3	Initial bed height	28.0 cm
PMMA particles			
Mean particle diameter	128 μm	Jet velocity	1.5 m/s
Solid density	1100 kg/m^3	Fluidization velocity	0.02 m/s
Bulk density	500 kg/m^3	Initial bed height	25.0 cm

5.2 Computational set-up

A two-dimensional Cartesian co-ordinate system is used to describe the geometry. The grid is uniform in both horizontal and vertical direction. Computational set-up for glass particles and PMMA particles are given in Table 5.2 and 5.3 respectively. Simulations have been run with both one and three solid phases in order to discuss possible improvement obtainable by using several solid phases.

Table 5.2: Computational set-up and conditions, glass particles.

Design:			
Height	63.0 cm	Horizontal grid size	5.0 mm
Width	19.5 cm	Vertical grid size	10.0 mm
Initial bed height	28.0 cm	Gas phase shear viscosity	$1.8 \cdot 10^{-5}$ Pa s
Glass particles			
One phase			
Particle mean diameter	491 μm	Jet velocity	4.9 m/s
Three phases:		Fluidization velocity	0.29 m/s
Particle mean diameter	630 μm (18%)	Freeboard pressure	101325 Pa
	500 μm (50%)	Solid density	2485 kg/m^3
	400 μm (32%)	Initial void fraction	0.40
		Maximum volume fraction of solids	0.64356
		Initial bed height	28.0 cm
PMMA particles			
Three phases			
Particle mean diameter	85 μm (26%)	Jet velocity	1.5 m/s
	120 μm (47%)	Fluidization velocity	0.02 m/s
	170 μm (27%)	Freeboard pressure	101325 Pa
		Solid density	1100 kg/m^3
		Initial void fraction	0.50
		Maximum volume fraction of solids	0.60
		Initial bed height	25.0 cm

5.3 Experimental results of glass particles

An experimental study of bubble formation for spherical glass particles with mean diameter 491 μm is performed. A movie sequence of the experimental results is shown in Figure 5.2. Between 0 and 120 ms the bubble size increases, but is located at the approximate same vertical position. At time 120 ms the bubble diameter is 4.2 cm, and the bubble starts to rise. The bubble is circular, and the diameter increases to 6.5 cm during the next 200 ms. During the time interval 320 ms to 740 ms the bubble moves from bed height 12 to 28 cm.

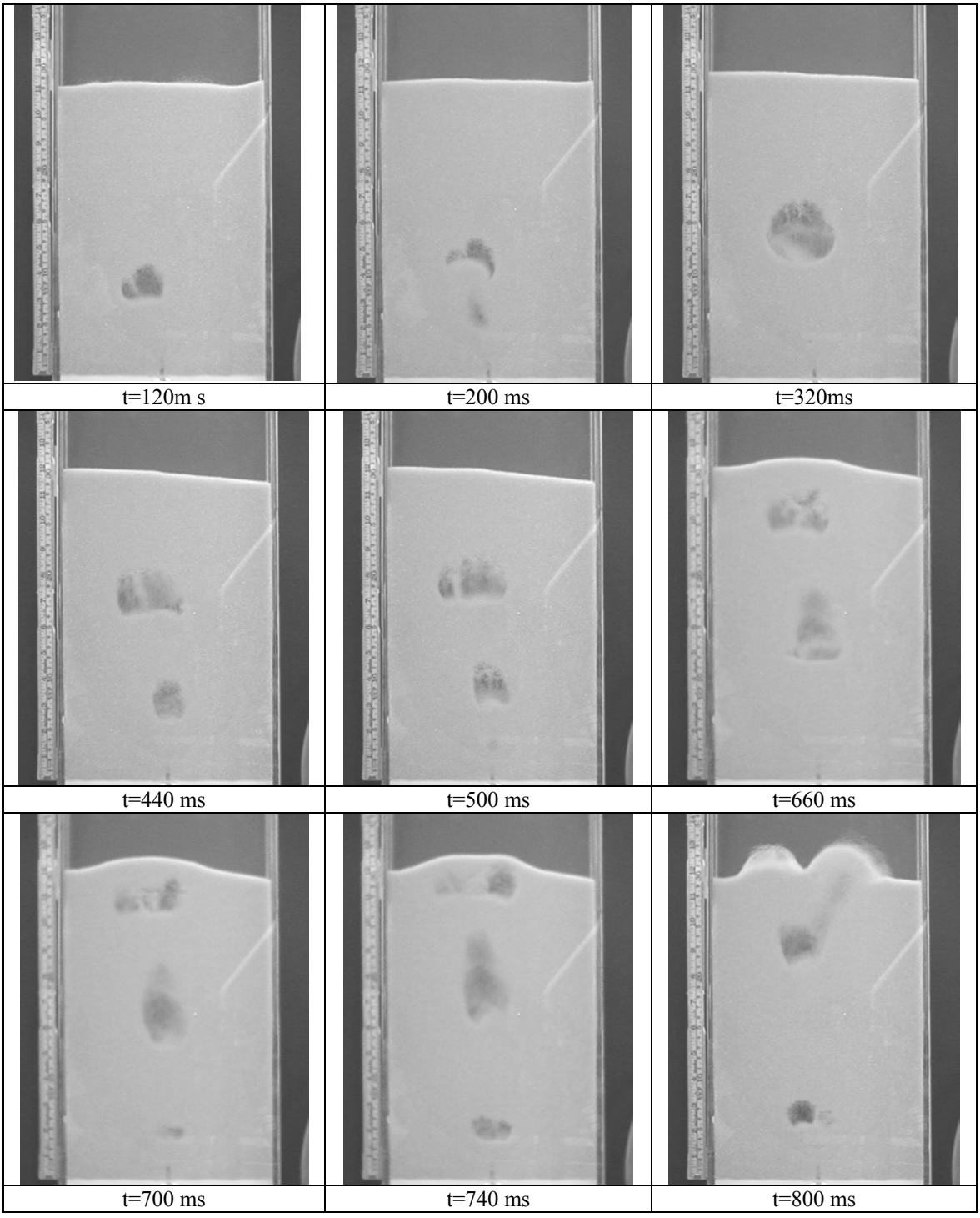

Figure 5.2: A movie sequence of experimental results.

During this rise, the shape of the bubble changes and bubble break-up is observed. The vertical diameter decreases from 6.5 cm to about 2 cm and the horizontal diameter increases from 6.5 to 8.5 cm. After 800 ms the first bubble has erupted.

A new bubble is formed and starts to rise after 440 ms. This bubble moves faster and differs significantly in shape from the first one. At time 740 ms the lower part of the bubble has reached a height of 14 cm. The horizontal diameter is 3.6 cm and the vertical diameter is 5.5 cm. At this same position the first bubble was already split and had a horizontal and vertical diameter of 6.7 cm and 3.6 cm respectively. During the bubble rise the bed expands from 28 to 32 cm.

5.4 Computationals results of glass particles

In this section a computational study of bubble behaviour in a Geldart B particle bed is performed. A bubble is assumed to be a region of void fraction larger than 0.85. Kuipers et al. (1991) used this definition of a bubble. Gidaspow (1994) defined the bubble contour as a void fraction of 0.80.

5.4.1 The influence of number of particle phases

In the multi-fluid Eulerian model the particle mixture can be divided into a discrete number of phases, whereby different physical properties can be specified for each particle class. In this study three particle phases are included in the simulations. Each of these phases has its own particle size, whereas the particle density and the coefficient of restitution remain the same for the three phases. A corresponding case with one particle phase is simulated and the numerical results compared. Figures 5.3 and 5.4 show the results from the simulations with one and three particle phases respectively. Ergun's drag model is used in these simulations and the coefficient of restitution is 0.80.

Comparisons of the simulations with one and three particle phases show that three particle phases yield somewhat flatter bubbles. The velocities of the first bubble in these two cases are about the same. The shape and velocities of the subsequent bubbles differ significantly. Simulation with one particle phase gives higher bubble velocities for the subsequent bubbles than is obtained during the simulation with three phases. It can also be seen from the Figure 5.3 that the bubbles split up before they reach the bed surface. Simulations with three particle phases give the best agreement to the experiments according to subsequent bubbles, and three particle phases are used in the further simulations.

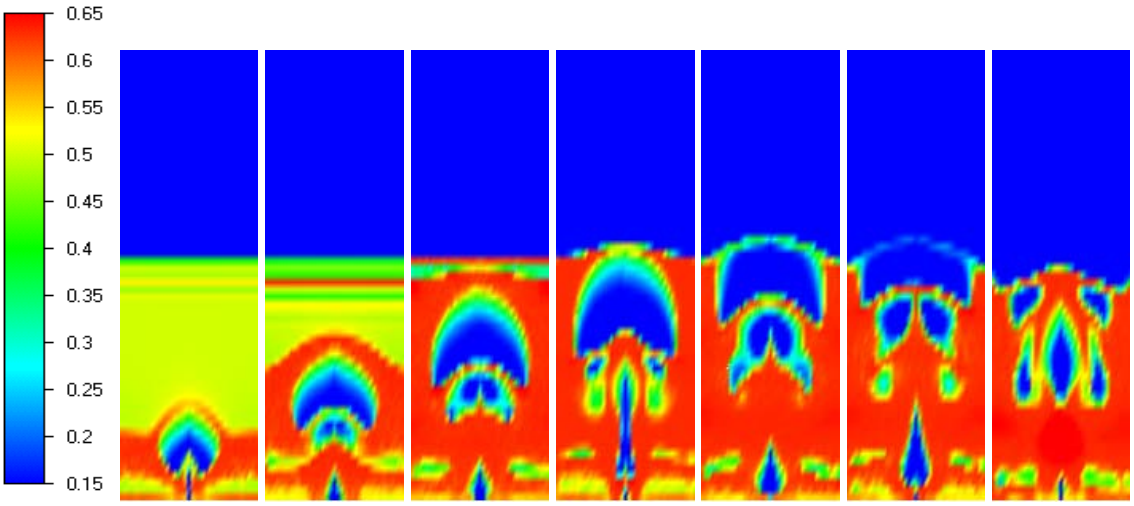

Figure 5.3: Volume fraction of solids, simulation with one particle phase.

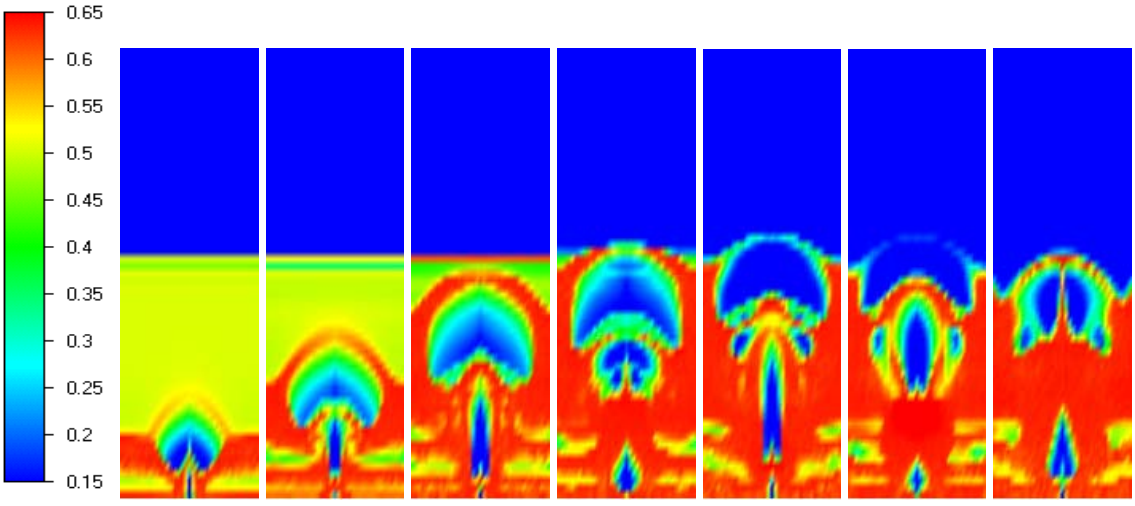

Figure 5.4: Volume fraction of solids, simulation with three particle phases.

5.4.2 Simulations with different drag models

Figures 5.4, 5.5 and 5.6 show the results from the simulations with the Ergun/Wen and Yu, the Gibilaro et al. and the Syamlal & O'Brien drag model respectively. The drag models are described in Table 3.2.

The figures show that the results from simulations with the Ergun, Gibilaro and Syamlal & O'Brien drag models differ considerably from each other. A comparison of the three drag models shows that the Ergun drag model gives the largest bubble size and the lowest bubble velocity for the first bubble. The Syamlal & O'Brien drag model gives an unsymmetrical first bubble and for this model no continuous bubble formation can be observed. Comparison of Ergun's and Gibilaro's drag models shows that the subsequent bubbles differ rather much in shape, but minor in size and velocities, for the two cases. Ergun's drag model gives higher bed expansion and a more stable bed and bubble formation.

It seems that the Ergun model calculates the most realistic bubble formation and bubble velocity for the actual particles and flow conditions. Hence, the Ergun drag model is used in the further simulations.

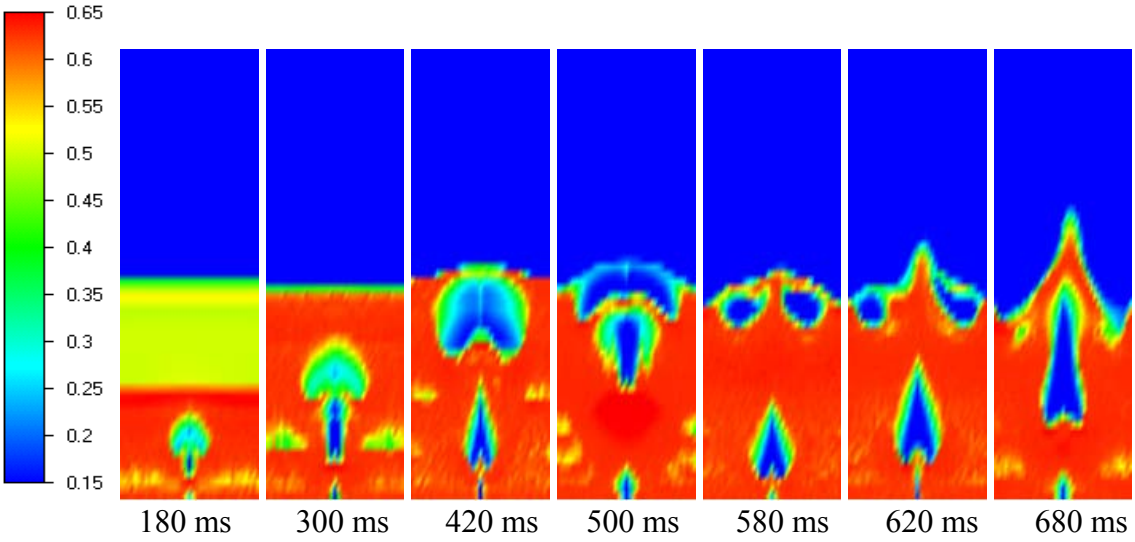

Figure 5.5: Simulation with Gibilaro drag model.

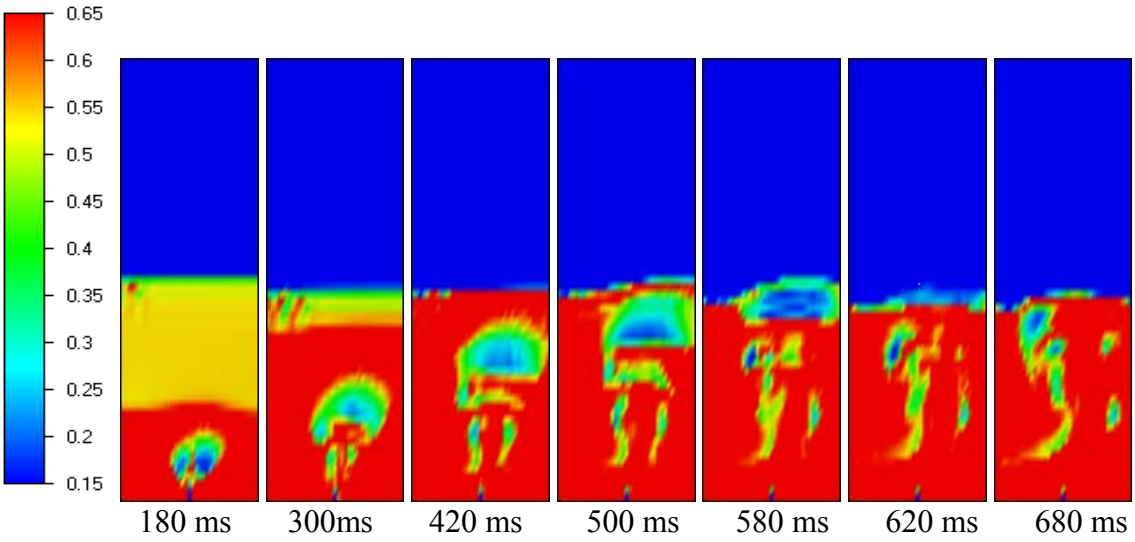

Figure 5.6: Simulation with Syamlal & O'Brien drag model.

5.3.4 Simulations with different coefficients of restitution

The coefficient of restitution will influence the hydrodynamics of dense fluidized beds especially when the solid volume fraction is close to maximum packing. Halvorsen and Mathiesen (2002a) performed two-dimensional simulations with various values of the coefficient of restitution and concluded that the bubble behaviour is rather sensitive for the value of the coefficient of restitution. The simulations were performed with a first order upwind scheme (FOU) and a viscous regime was used to describe the stresses in the solid phases. Figure 5.7 shows the results of the simulations. It can be seen from the figure that as the coefficient of restitution decreases and collisions become less ideal, particles become

closer packed in the densest regions and the bubble size increases. The concentration gradient of solids increases significantly when the coefficient of restitution is decreased from 1 to 0.95. The simulation using FOU did not converge for coefficient of restitution lower than 0.95. This may be due to unphysical high packing.

In the present work the same cases have been studied, but now with a second order upwind scheme (SOU) and with a plastic regime included in the code. The 'switch' from viscous to plastic regime occurs when the void fraction reaches about the void fraction at minimum fluidization. The solid pressure and the stresses for the plastic regime are not functions of the coefficient of restitution and the bubble behaviour is therefore less influenced by the coefficient of restitution. This is shown in Figure 5.8. The coefficient of restitution, e, is varied from 0.99 to 0.70, and no differences in bubble size and bubble velocity are observed.

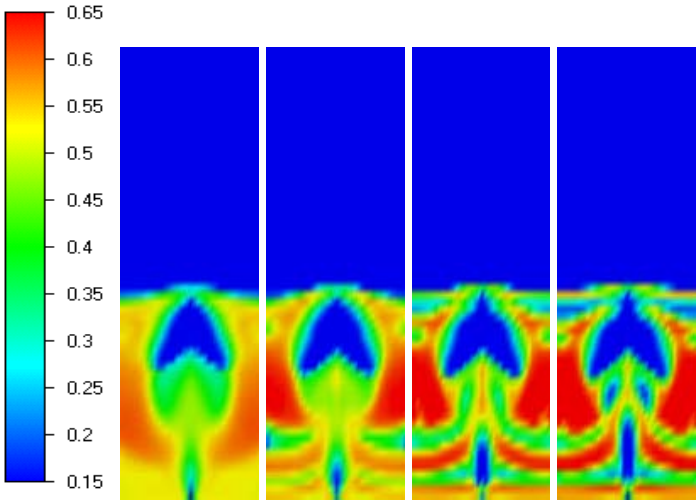

Figure 5.7: Volume fraction of solids, simulations with various values of the coefficient of restitution at time t=380 ms.

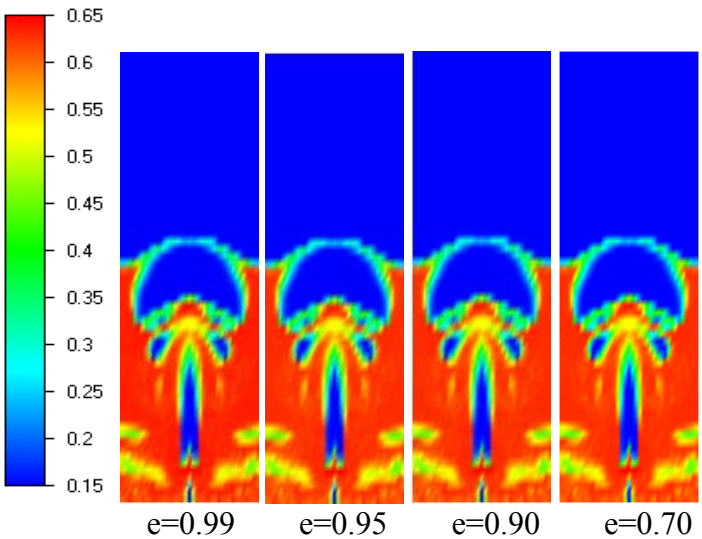

Figure 5.8: Volume fraction of solids at time t=580 ms. Switch from viscous to plastic regime close to minimum fluidization.

5.4.3 Comparison between computational and experimental results

Figures 5.9 shows a comparison between experimental and computational bubbles calculated by using the Ergun, Gibilaro and Syamlal & O'Brien drag models. The bubbles are shown at position 12 cm above the air inlet. Discrepancies in shape between the experimental and computational bubbles are observed at this level. Ergun's drag model gives a bubble with a higher radial diameter and lower vertical diameter than the experimental bubble. The shape of the computational bubble using Gibilaro's drag model differs less from the experimental bubble, but a rather high concentration of particles within the bubble is observed. The Syamlal & O'Brien drag model gives an unsymmetrical bubble. The Ergun and Syamlal & O'Brien drag models give the most realistic bubble velocities. The Gibilaro and Syamlal & O'Brien drag models give the best agreement to the experiments regarding bed expansion.

Figure 5.10 shows a comparison between experiments and simulations at the time when the first bubbles erupt. Both the computational and the experimental bubbles have changed in shape. The computed bubbles are somewhat larger than the experimental bubble. The numerical bubble velocity is higher than the experimental one. The Gibilaro drag model gives the highest bubble velocity. The Ergun and Syamlal & O'Brien drag models give bubble velocities that agree well with the experimental bubble velocity. This can be seen from difference in time at comparable levels. The simulations and the experiment give about the same bed expansion.

It can also be seen from Figure 5.10 that simulations with Ergun's and Gibilaro's drag models agree well with experiment regarding the shape and the position of the second bubble.

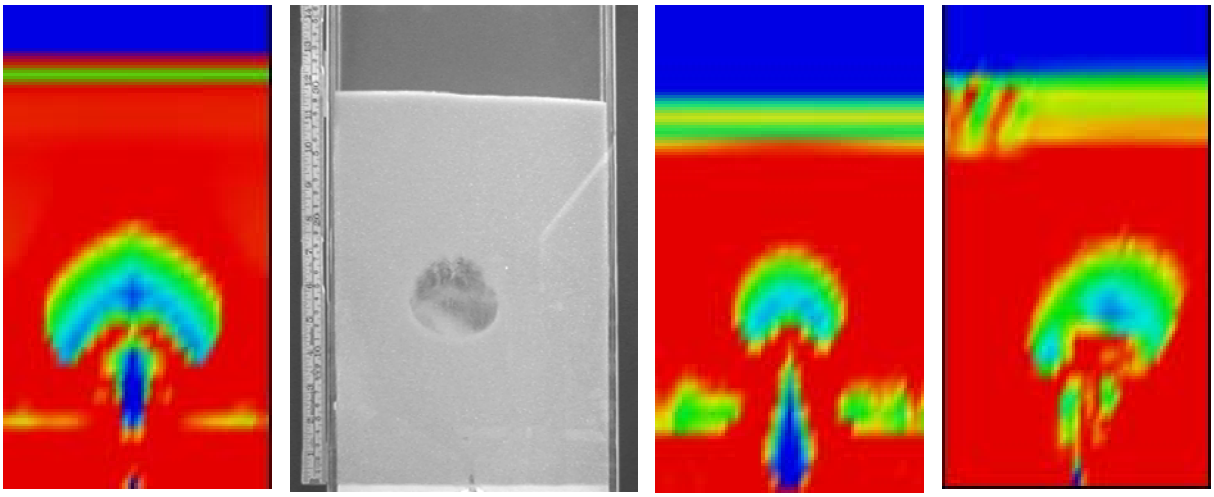

t=300 ms (Ergun) | t=320 ms (experimental) | t=260 ms (Gibilaro) | t=300 ms (Syamlal &O'Brien)

Figure 5.9: Computational vs. experimental bubble at bed height 12 cm.

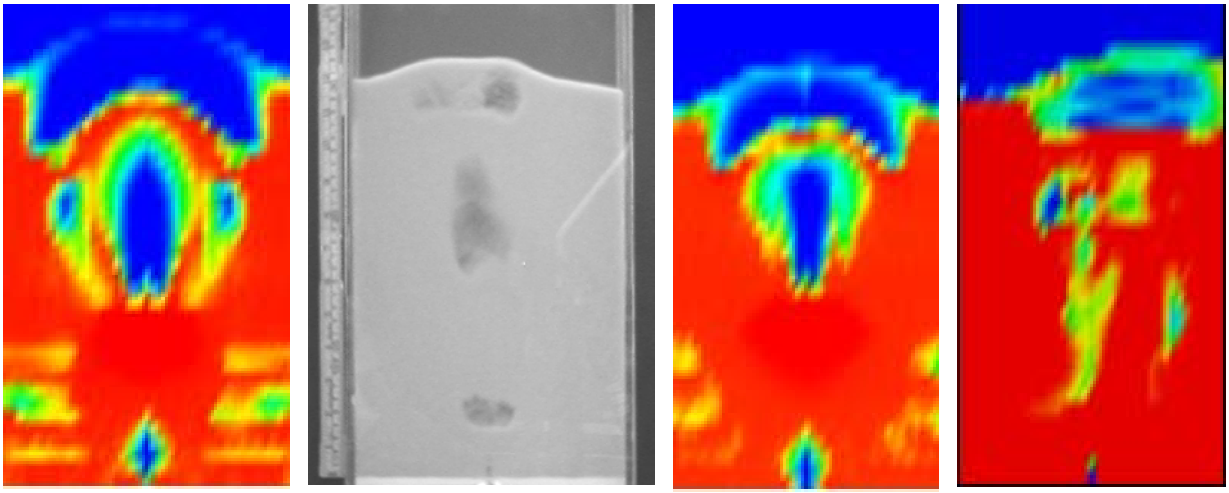

t=0620 ms (Ergun) | t=740 ms (experimental) | t=500 ms (Gibilaro) | t=580 ms (Syamlal &O'Brien)

Figure 5.10: Computational vs. experimental bubble near the top of the bed.

5.5 Experimental results of PMMA particles

Figure 5.11 shows some photographs from the experimental study of PMMA particles. PMMA particles are characterized in group A and are slightly cohesive. Hence the particles also adhere to the walls and it is difficult to get clear photographs of the bubble behaviour. It can be seen from the photographs that the bubble is rounded and that the shape and the size of the bubble change during the rise through the bed. Presence of particles within the bubbles is observed. At some location this make the bubbles appear like splitting up. The bubble erupts after about 900 ms.

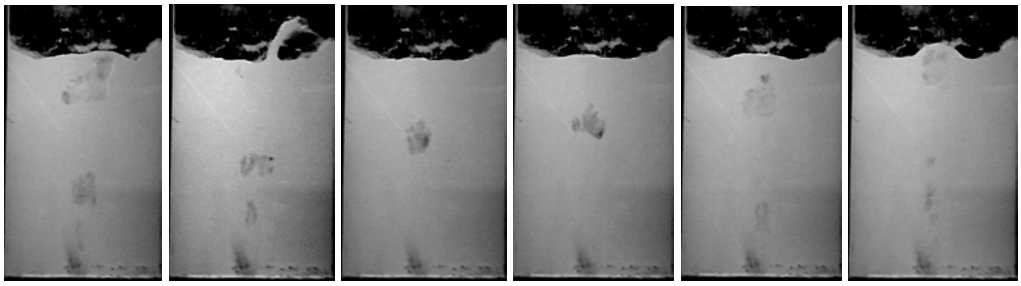

t=320 ms t=480 ms t=600 ms t=680 ms t=800 ms t=880 ms

Figure 5.11: Photographs from experimental study of PMMA particles.

5.6 Computational results of PMMA particles

In this chapter a computational study of the Geldart group A particles, PMMA, is performed. This study is an extension of the computational study of spherical PMMA particles in a 2D fluidized bed performed by Halvorsen and Mathiesen (2002b).

Group A particles expand considerably before bubbles appears. Due to the high expansion, dense packing is not a problem in simulations of Group A fluidized beds, and drag models

and values of coefficient of restitution may not affect the calculation of bubble behaviour significantly. The computational study of PMMA particles is performed with three particle phases.

5.6.1 Simulations with different drag models

Figures 5.12 and 5.13 show time series of solid volume fractions for the simulations with the Ergun drag model and the Gibilaro drag model respectively. The simulations are performed with second order upwind scheme (SOU) and the coefficient of restitution is set to 0.80 for both cases. The two drag models give about the same bubble shape and bubble size. The Gibilaro drag model gives a lower bubble velocity. The bubble erupts after about 0.800 s. The Gibilaro drag model is used in the further simulations.

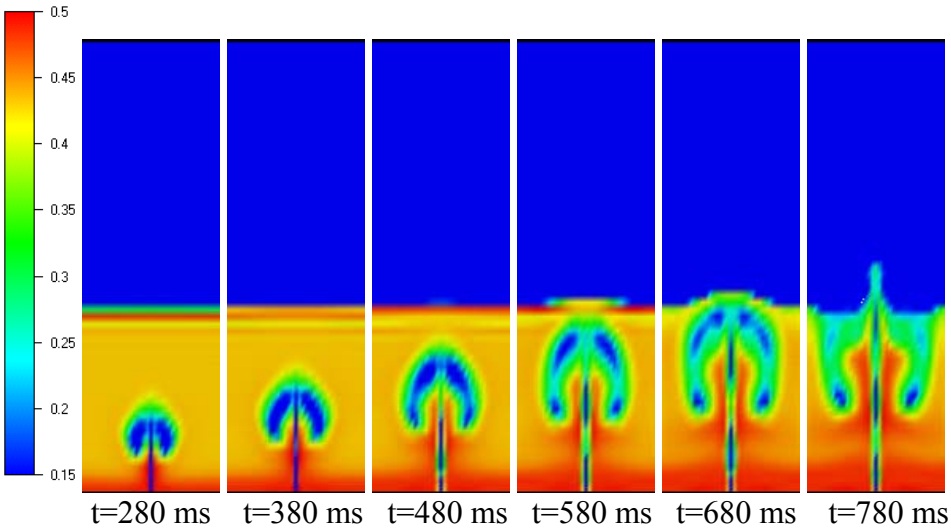

Figure 5.12: Volume fraction of solids, Ergun drag model.

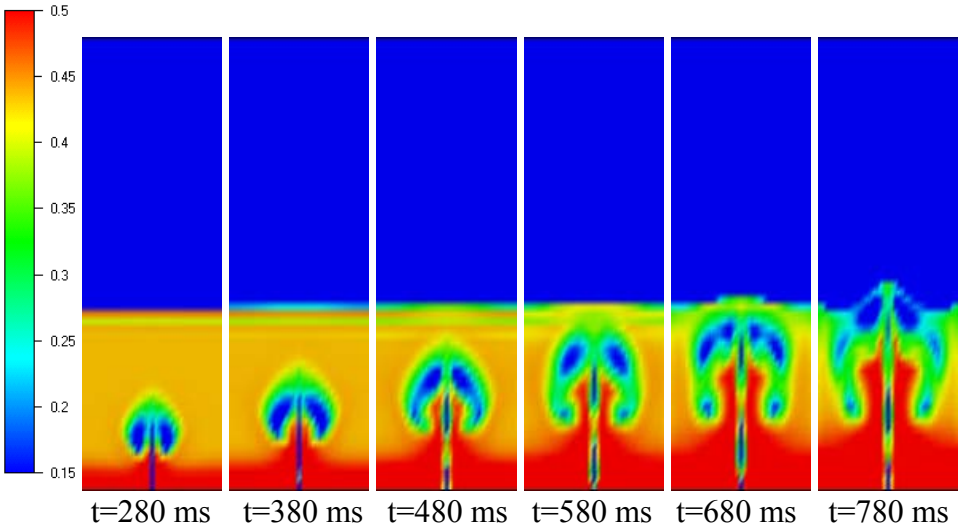

Figure 5.13: Volume fraction of solids, Gibilaro drag model.

5.6.2 Comparison of first and second order upwind schemes

In this work second order spatial scheme (SOU) and different flux limiters are implemented in FLOTRACS-MP-3D. The schemes and the flux limiters are described in chapter 4.1. Simulations have been performed with first order upwind scheme (FOU), second order upwind scheme (SOU) and second order upwind schemes with the flux limiters Van Leer, Superbee and Minmod.

Figure 5.14 shows the results from the simulation with FOU. The bubble shape is elliptical and it can be seen that FOU scheme gives an unphysical pointed bubble. This is assumed to be due to numerical diffusion. The bubble erupted after about 600 ms.

In Figure 5.15, 5.16, 5.17 and 5.18 the results from the simulations with second order schemes are shown. Figure 5.15 confirms that the shape of the bubble becomes rounded and more spherical when the SOU scheme with Superbee flux limiter is used. Another effect of using the second order scheme is that the bubble velocity decreases. Figure 5.16 shows that simulation with Van Leer flux limiter also gives a rounded bubble. A comparison of these two flux limiters shows that the bubble shape differs insignificantly and that the Superbee flux limiter gives the lowest bubble velocity. The simulation with the Minmod flux limiter is presented in Figure 5.17. This simulation gives almost the same result as the simulation with the Van Leer flux limiter but the bubble velocity becomes somewhat higher by using the Minmod flux limiter.

A simulation with SOU without a flux limiter is shown in Figure 5.18. This simulation gives the lowest bubble velocity and the most realistic bubble shape. The bubble erupts after 800 ms. SOU without flux limiter gives second order accuracy, whereas the limiters can give a locally reduced accuracy. However, SOU without a flux limiter can generate oscillations around sharp gradients and may give unphysical solutions after some time.

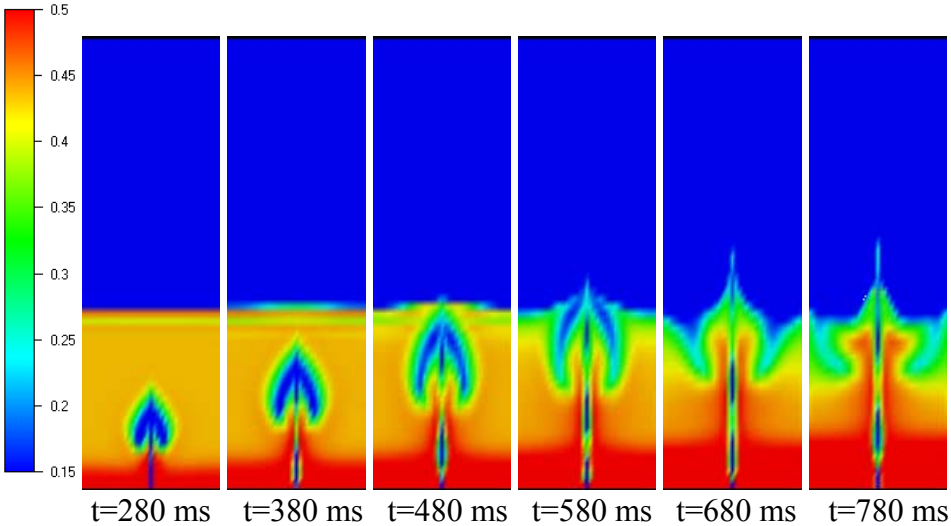

Figure 5.14: Volume fraction of solids, FOU.

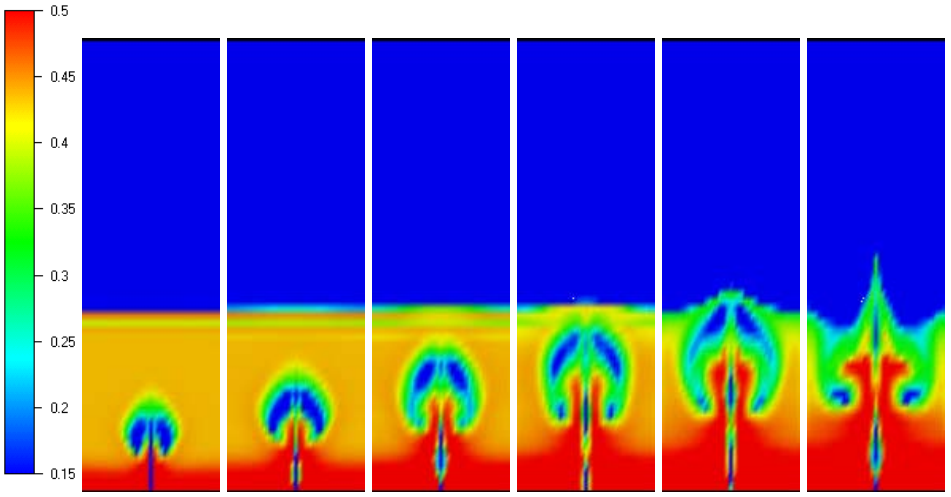

Figure 5.15: Volume fraction of solids, Superbee flux limiter.

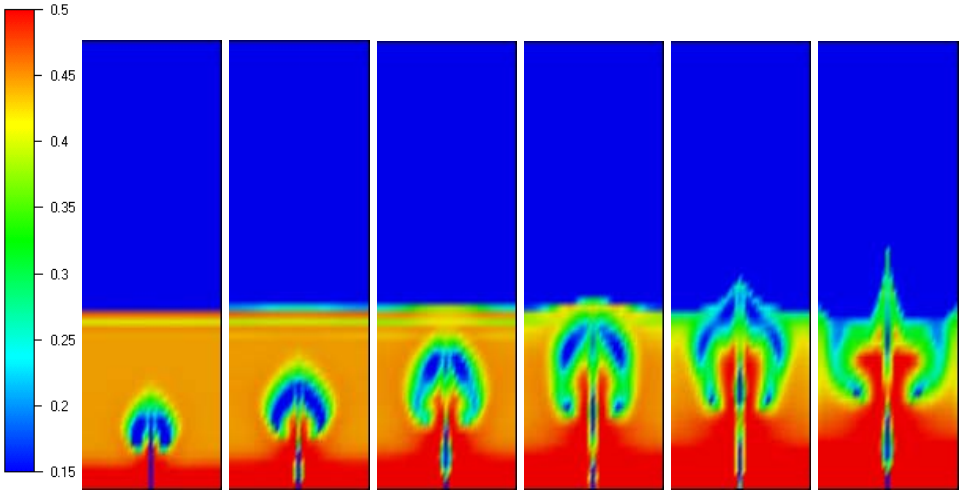

Figure 5.16: Volume fraction of solids, Van Leer flux limiter.

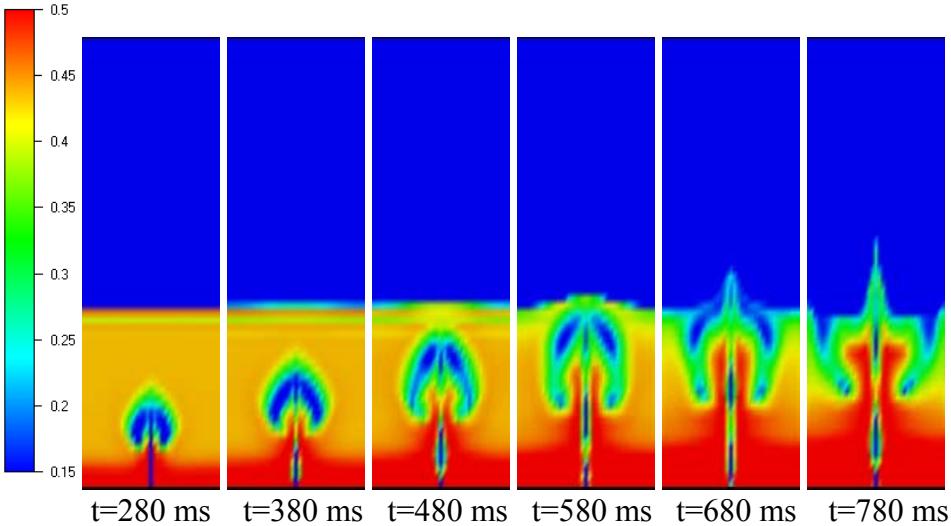

Figure 5.17: Volume fraction of solids, Minmod flux limiter.

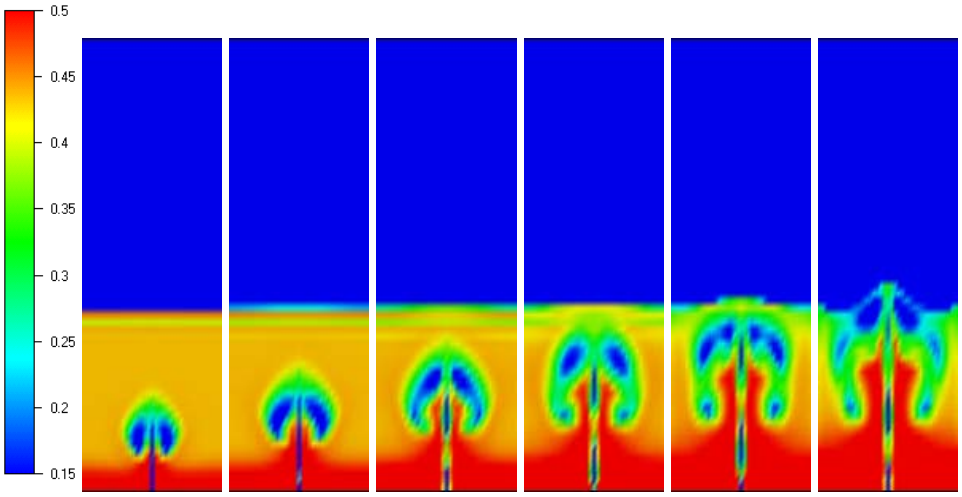

Figure 5.18: Volume fraction of solids, SOU.

5.6.3 Comparison between computational and experimental results

Figure 5.19 shows a comparison between experiment and simulations with FOU and SOU at two levels in the bed. Simulation with FOU gives a pointed bubble that differs significantly from the experimental bubble both in shape and in velocity. Simulation with SOU gives a rounded bubble. The simulated bubble has a higher horizontal diameter than the experimental bubble whereas the vertical diameter differ less. Within both the computational and the experimental bubbles the presence of particles can be seen. Hence, the bubbles look like they are splitted. Simulation with SOU gives a bubble velocity that differs slightly from the experimental bubble velocity. The experimental bubble velocity is about 0.35 m/s, whereas the computational bubble velocities are about 0.39 m/s and 0.52 m/s for simulations with SOU and FOU respectively. The experimental bed has a higher bed expansion than the simulated beds. Simulation with SOU gives good agreement with the experimental bubble behaviour. However, SOU without flux limiter may give unphysical solutions and a flux limiter should be used. Comparison of the flux limiters shows that Superbee gives the lowest bubble velocity.

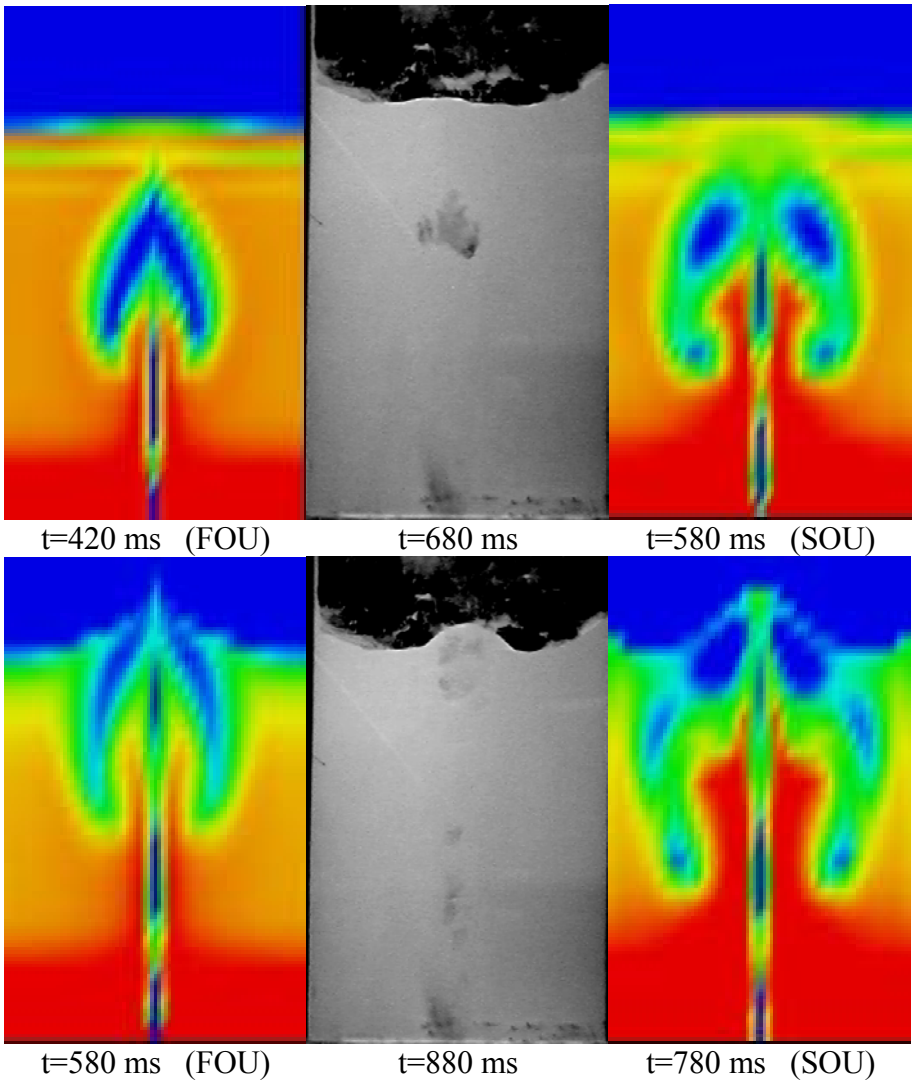

Figure 5.19: Experimental and computational bubbles.

5.7 Summary

Experimental and computational studies of a two-dimensional lab scale fluidized bed with a central jet are performed. The studies are performed with glass particles and PMMA particles, which are classified as Geldart group B and A particles respectively.

The simulations with glass particles are performed with one and three particle phases, with three different drag models and with various values for the coefficients of restitution. The computational results with different simulations conditions are compared. Simulation with one and three particle phases give no significant differences in bubble formations. Thus the simulations with three particle phases gave slightly lower bubble velocities, especially for the second bubble. The further simulations were performed with three particle phases.

It is shown that simulations with the Ergun/Wen and Yu, the Gibilaro et al. and the Syamlal & O'Brien drag models gave significant different bubble formation, bubble velocity and bed

expansion. Ergun's drag model gave the largest bubbles, the lowest bubble velocities and the highest bed expansion.

The coefficient of restitution has an important effect on bubble behaviour when the solid volume fraction is close to the maximum solid volume fraction. However the effect of varying the coefficient of restitution was insignificant when plastic regime was included. When the solid concentration was close to maximum packing, the plastic regime was controlling the flow.

A selection of the experimental data has been compared to computational results performed by using the Ergun, Gibilaro and Syamlal & O'Brien drag models. The Ergun and Syamlal & O'Brien drag models agree well with the experiments according to bubble velocity. The Gibilaro drag model give a rather good agreement with the experiments according to bubble size and bubble shape, but the model gave significantly higher bubble velocities than the experiment.

Simulations with PMMA particles are performed with two different drag models. It is found that simulations with Geldart A particles are less dependent on the particular drag model used than Geldart B particles. For the PMMA particles, simulations with the Gibilaro model gave a lower bubble velocity than simulations with the Ergun model. The Gibilaro model was therefore used in the further simulations.

PMMA particles are also used in order to study how different discretization schemes influence bubble behaviour. Second order upwind scheme and the flux limiters Superbee, Van Leer and Minmod are included in the model. Simulations of the two-dimensional fluidized bed are performed with first and second order discretization schemes. It is shown that the second order scheme reduces the numerical diffusion significantly and the simulations give physically more realistic rounded bubbles. Second order schemes also give a lower bubble velocity. A comparison of the results from experiments and simulations shows that SOU without flux limiter give the most realistic bubble shape and bubble velocity, but SOU without a flux limiter can generate oscillations around sharp gradients and may give unphysical solutions after some time. The comparison of different flux limiters shows that all the flux limiters give rounded bubbles and that the simulations with Superbee give the most realistic bubble velocity.

6. CFD calculations for scaling of bubbling fluidized beds

The operation of a gas/solid fluidized bed is influenced by the spatial distribution of bubbles within the bed. Werther and Molerus (1973a) performed an experimental study of the spatial distribution of bubbles in gas fluidized beds.

In order to be able to calculate complex industrial bed reactors with CFD, the bubble distribution, bubble velocities and bubble sizes have to be calculated correctly.

This chapter shows the results of a grid resolution test that is performed for a fluidized bed with diameter 0.1 m. The intension is to find an optimum mesh that can be used in computational studies of larger fluidized beds. The primary objective is to find a connection between bed diameter and bubble behaviour and how the grid resolution influences the calculated results, Halvorsen et al. (2003). This information can be used in scaling of bubbling fluidized beds. Simulations on large industrial beds require a large number of control volumes and large CPU time. Scaling down from large to smaller beds include use of dimensionless numbers which are kept constant during the scaling. Scaling down is a way of reducing mesh and the CPU time.

6.1 Computational set-up

All simulations in this study are performed with the MFIX code described by Syamlal et al. (1993). Cylindrical bubbling fluidized beds with diameters 0.10, 0.20, 0.45 and 1.0 m and height 1.0 m are modelled. The simulations of the 0.10 m bed are performed with different grid resolutions in angular, radial and axial direction in order to perform grid resolution studies. Simulations are performed with 3-D cylindrical, 2-D Cartesian and 2D axis-symmetrical coordinates. The applied resolutions are given in Tables 6.1 and 6.2 for the 0.1 m bed and in Table 6.3 for the other bed sizes. The numerical flow parameters and computational set-up are given in Table 6.4.

Table 6.1: Grid resolution in 3-D simulations of a fluidized bed with a 0.10 m diameter.

Direction	*3-D cylindrical*											
Radial	10	15	20	25	30	20	20	20	20	20	20	20
Axial	100	100	100	100	100	150	250	200	200	200	200	200
Angular	6	6	6	6	6	6	6	6	12	18	24	30

Table 6.2: Grid resolution in 2-D simulations of a fluidized bed with a 0.10 m diameter.

Direction	*2-D axis symmetrical*	*2-D Cartesian*
Radial	20	40
Axial	200	200
Angular	1	1

Table 6.3: Number of grid nodes used in the simulations of the fluidized beds with diameters 0.20, 0.45 and 1.0 m.

Directions	*0.20 m 3D cylindrical*	*0.20 m 2-D Cartesian*	*0.45 m 2-D Cartesian*	*1.0 m 2-D Cartesian*
Radial	40	80	180	400
Axial	200	200	200	200
Angular	18	1	1	1

Table 6.4: Computational configuration and numerical flow parameters.

Height	1.0 m	Mean particle diameter	83 μm
Diameter	0.1, 0.2, 0.45, 1.0 m	Particle density	2640 kg/m^3
Initial bed height	0.50 m	Shape factor	0.8
Superficial gas velocity	0.09 m/s	Coefficient of restitution	0.8
Initial void fraction	0.4	Simulation time	13.5, 20 s

6.2 Grid resolution test

Simulations using different grid resolutions are performed for the bubbling fluidized bed with diameter of 0.10 m. The void fractions are averaged with respect to time and space in radial and angular directions. The averaging procedure has been performed for three radial rings in the bed. These radial regions are shown as shaded areas in Figure 6.1. The grid resolution test is divided into regions in order to find possible regions in the bed where the numerical results are less dependent of the grid sizes than in other regions. Calculations have been performed for three sectors in the angular direction.

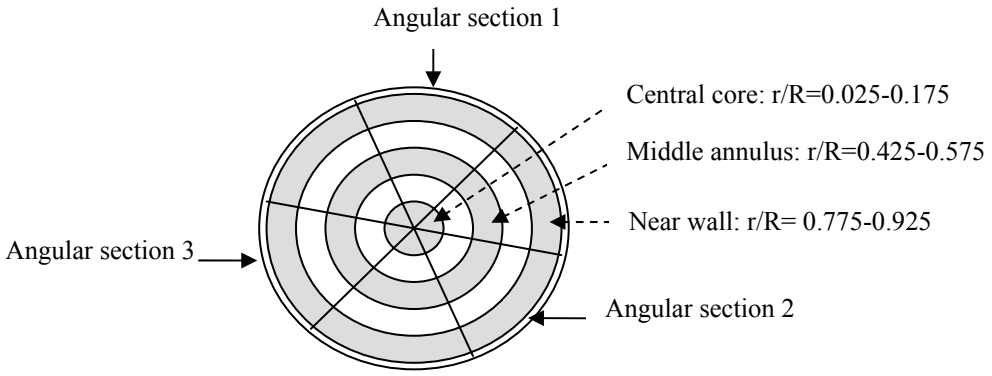

Figure 6.1: The cross-sectional areas of the bed. Calculations have been performed for the three sections in the angular direction.

6.2.1 Time averaging periods

For transient CFD calculations it is important to find minimum sufficient simulation times and time periods necessary for the averaging. The first seconds of the simulations are not included in the time averaging periods. Void fractions as a function of bed height are compared for the different time averaging periods. This is shown in Figure 6.2. There are just minor differences between the void fractions as a function of bed height for the time

averaging period 6-10 s and 6-13.5 s. However, results from the time averaging period 5-8 s show some discrepancies from the two other time periods. This shows that 6-10 s is sufficient time interval for the time averaging. However, the time averaging period 6-13.5 s is used in further simulations to ensure that the time averaging period is sufficient.

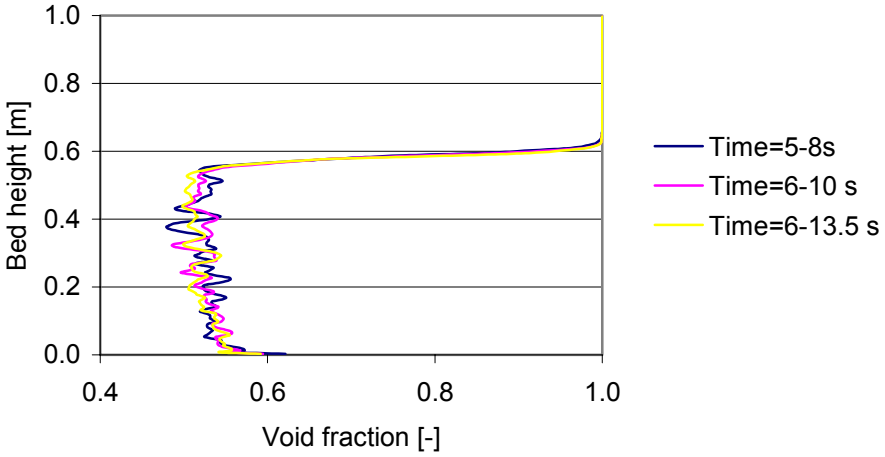

Figure 6.2: Different time averaging periods for grid size 20x200x30, radial position is middle annulus.

6.2.2 Spatial grid size

Figure 6.3 shows void fraction as a function of bed height for five different radial resolutions. The comparison is performed with coarse grids in the angular direction and in height. The void fraction as a function of bed height changes minimally when the number of control volumes is increased from 20 to 30 in the radial direction. The two coarsest meshes give a higher void fraction than the other meshes at most axial positions. The comparison is shown for the middle annulus of the bed. The same comparison is also performed for the central core and near the wall, and also in those positions the void fraction as a function of bed height changes insignificantly when grid is refined from 20 to 30 in the radial direction. At least 20 nodes should thus be used in radial direction.

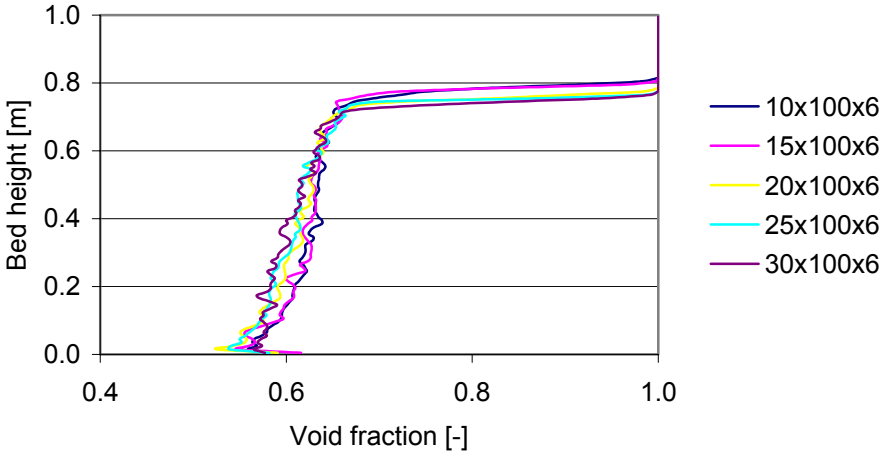

Figure 6.3: Comparison of void fraction in the middle annulus for different grid sizes in radial direction.

Figure 6.4 shows the comparison of the void fraction as a function of bed height for four different resolutions in height. The comparison is performed for 20 control volumes in the radial and 6 control volumes in the angular direction. The void fractions as a function of bed height decrease when the resolution is varied from 100 to 250 in axial direction. In most of the axial positions there is rather good agreement between the two finest grids. Hence 200 control volumes are used in the axial direction in the further calculations.

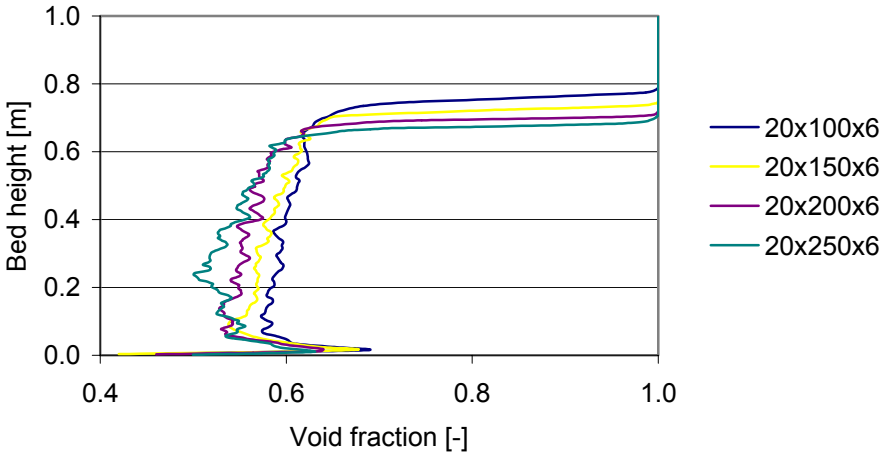

Figure 6.4: Comparison of void fraction near the wall of the bed for different grid sizes in height.

The void fraction for five different angular resolutions are calculated and compared. The comparison of the void fractions is performed in the central core, in the middle annulus and near the wall of the bed. Figure 6.5 shows the comparison of the void fraction in the middle annulus of the bed. The void fractions calculated from the simulations with the 20x200x6 and 20x200x12 control volumes differ considerably from the others from a height of about 0.10 m and throughout the bed. These grid resolutions are not of current interest, and will not be considered further.

Below a bed height of 0.10 m and above 0.30 m the void fractions are rather similar for the three finest grid sizes. Between 0.10 and 0.30 m, the simulation with grid 20x200x30 gives a lower void fraction than the two coarser meshes. The void fraction rises to unity at a lower bed height for the finest grid than for the two other grid sizes.

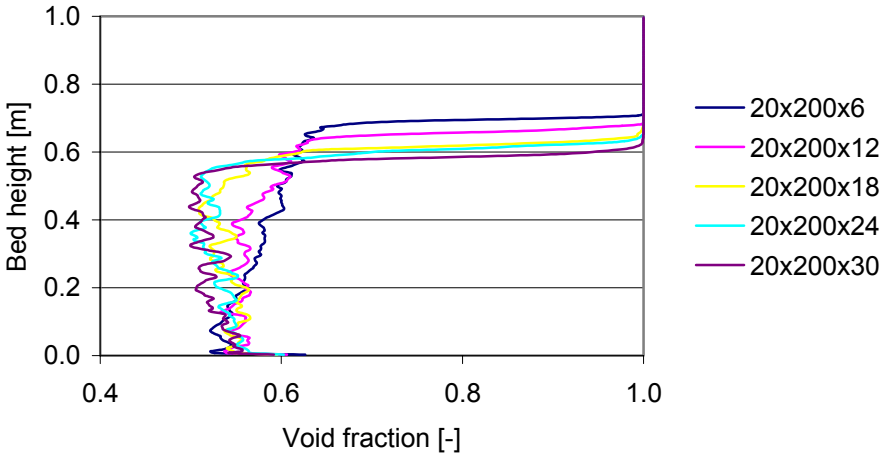

Figure 6.5: Comparison of void fraction in the middle annulus of the bed for different resolutions in angular direction.

The same comparison is also performed for the central core and near the wall, and also in those positions void fraction as a function of bed height changes significantly when the grid is reduced from 18 to 12 in the angular direction. The comparisons of the different resolutions show that 20x200x18 is the coarsest mesh that can be used without losing important information.

6.3 Void fraction variations

6.3.1 Angular variation

Figure 6.6 shows a comparison of void fraction as a function of bed height for the three angular sectors. The averaged void fractions in the different circular sectors differ only randomly from each other. This result shows that the void distribution is independent of angular position when averaging over 7.5 seconds.

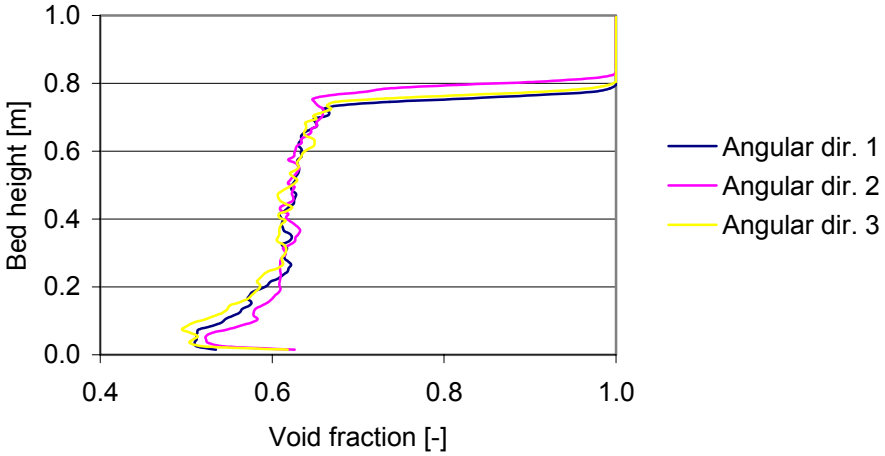

Figure 6.6: Comparison of void fraction in the middle annulus of the bed for three different angular sections.

6.3.2 Radial variation

In Figure 6.7 a comparison of void fractions in the central core, middle annulus and near wall is performed. The void fraction as a function of height depends significantly on the radial position. Between heights of 0.05 and 0.25 m the void fractions in the middle annulus is higher than in the central core. Higher up in the bed the void fraction in the centre is higher than in the middle annular section of the bed. From the height 0.05 m to the top of the bed, the void fraction near the wall is considerably lower than in the other areas. Close to the gas distributor the void fractions near the wall and in the middle annulus are higher than in the central core.

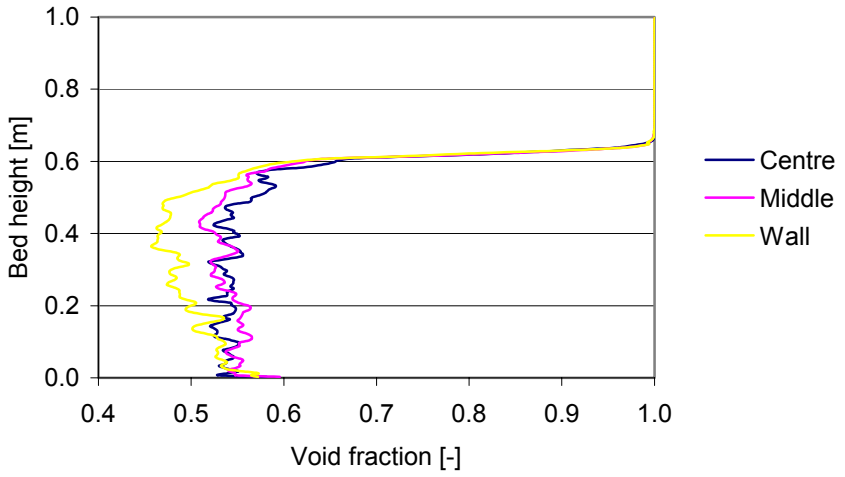

Figure 6.7: Void fractions at three different radial positions.

6.3.3 Comparison of 2-D and 3-D coordinate systems

Figure 6.8 shows the comparison of void fractions as a function of bed height for the simulations with grid 20x200x18 in cylindrical coordinates, 20x200 in 2-D Cartesian coordinates and 20x200 in axis-symmetrical coordinates. The comparison of the simulations is performed near the wall of the bed. In this region it seems that simulation with 2-D Cartesian coordinates agree rather well with the 3-D simulations. The results from the simulation 2-D axis-symmetrical coordinates differ considerably from the others over the entire bed height. This is probably caused by the axis which will significantly damp the bubble formation and oscillation in the centre of the bed.

The comparison between the 2-D simulation and the 3-D simulation shows that 2-D Cartesian coordinates can be used to simulate most parts of the bed without losing information.

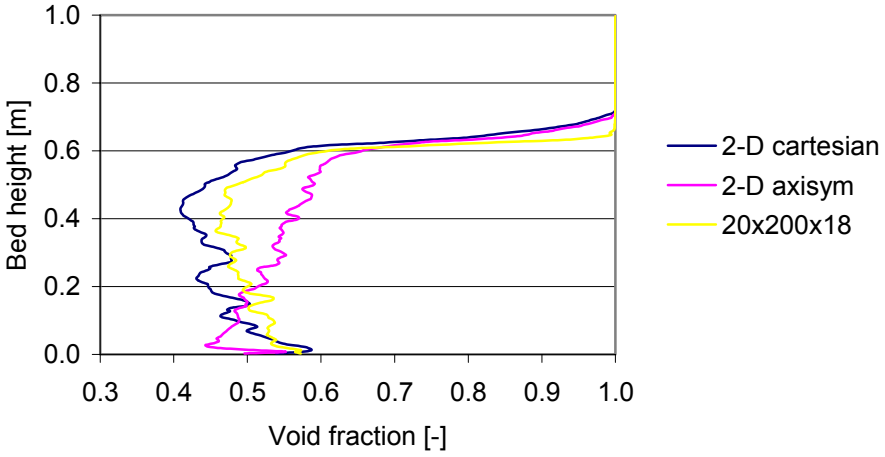

Figure 6.8: Comparison of the results of 2-D and 3-D simulations near the wall in the bed.

6.4 Calculations for scaling of a bubbling fluidized bed

Calculations of bubble behaviour in large beds in 3-D coordinates require large CPU time. In the grid resolution test it was found that the results from simulations with 2-D Cartesian coordinates differ rather little from simulations with 3-D cylindrical coordinates. In order to study bubble behaviour in a large bed a fine grid is needed also in the angular direction to avoid a smeared solution. The grid width near the wall for the 1.0 m diameter bed is about 0.17 m if 18 nodes are used in the angular direction. Such a mesh will be too coarse to satisfactorily capture information about bubble behaviour. In this work beds with diameter 0.45 and 1.0 m are calculated in 2D Cartesian coordinates only. The beds with diameter 0.10 and 0.20 m are calculated both in 2D Cartesian coordinates and in 3D cylindrical coordinates.

Application of scaling laws is useful in this type of studies. Different scaling models are suggested in the literature. Johnsson et al. (1999) used simplified scaling laws for fluid dynamics proposed by Glickman (1993) in his experimental study of 1/9 scale model of an industrial circulating bed. Ibsen (2002) did an experimental and computational study of the same CFB by using same scaling laws. The scaling laws proposed by Glickman are yielding the following dimensionless numbers which are kept constant during scaling:

$$\frac{u_0^2}{gL}, \frac{\rho_s}{\rho_f}, \frac{u_0}{u_{mf}}, \frac{L_1}{L_2}, \frac{G_s}{\rho_s u_0}, \Phi, \text{ size distribution} \tag{6.1}$$

Here L is the height from distributor to exit and G_s is the net solid flux.

Horio et al. (1986) stated that the similarity between a large bed and its model is achieved if the following scaling parameters are matched:

$$\frac{u-u_{mf}}{(gd_p)^{0.5}} \quad \text{and} \quad \frac{u_{mf}}{(gd_p)^{0.5}} \tag{6.2}$$

Fitzergald and Crane (1980) proposed using the scaling parameters:

$$\frac{d_p u \rho_g}{\mu}, \frac{\rho_s}{\rho_g}, \frac{u}{(g d_p)^{0.5}} \text{ and } \frac{L}{d_p} \tag{6.3}$$

These terms represent the Reynolds number, the density ratio, the Froude number and the geometrical similarity expressed by bed particle ratio respectively.

6.4.1 Simulations with 2-D Cartesian coordinates

Bubbling fluidized beds with diameters of 0.10, 0.20, 0.45 and 1.0 m are simulated using 2-D Cartesian coordinates. The simulations are performed with a constant control volume size of 2.5 mm and 5 mm in radial and axial direction respectively. The computational set-up is given in Table 6.4.

Figures 6.9, 6.10, 6.11 and 6.12 show the void fraction as a function of height above the air distributor at three radial positions for the fluidized beds with diameters of 0.10, 0.20, 0.45 and 1.0 m respectively. The calculations are performed using time averaging between 5-15 seconds and space averaging over 4, 8, 18 and 40 nodes in the radial direction.

The void fraction increases considerably from the wall to the centre of the beds with diameter 0.10 and 0.20 m. This can be seen from Figures 6.10 and 6.11. However, in a small zone close to the air distributor the void fraction is highest near the wall. For the 0.45 m bed shown in Figure 6.12 the void fraction increases less with radial position. The zone of high void fraction near the wall is observed at height 0-0.10 m for this case. For the 1.0 m bed the void fraction is higher in the middle of the bed than in the centre. Near the wall there is a zone of high void fraction close to the air distributor. The void fraction changes rather much as a function of height for the 0.20 and 0.45 m beds, less for the 0.10 m bed and insignificantly for the 1.0 m vessel. The void fraction is most uniformly distributed in the axial direction in the centre of the vessels

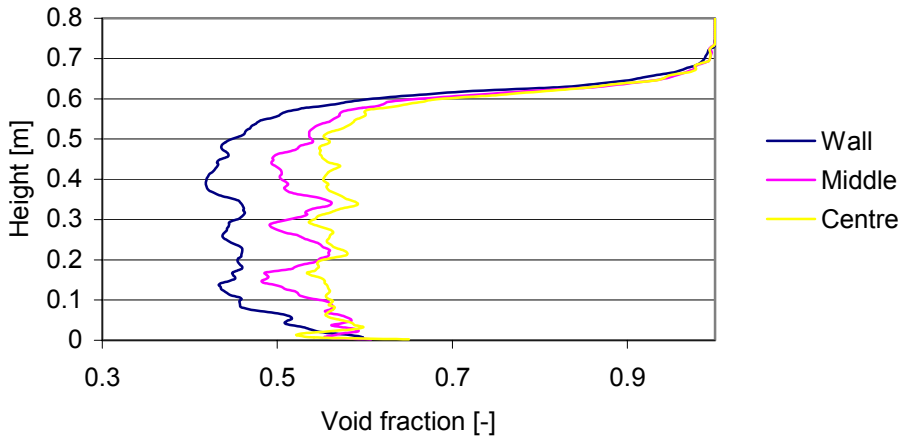

Figure 6.9: Void fraction as a function of height at different radial positions for a bed with diameter 0.10 m.

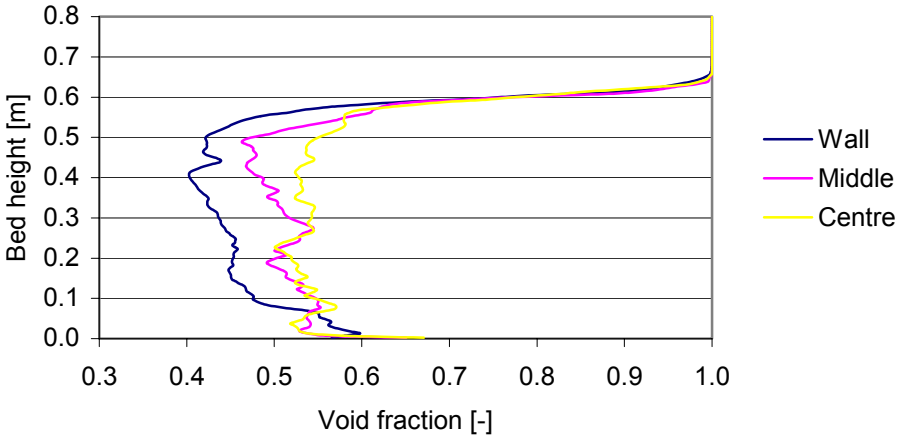

Figure 6.10: Void fraction as a function of height at different radial positions for a bed with diameter 0.20 m.

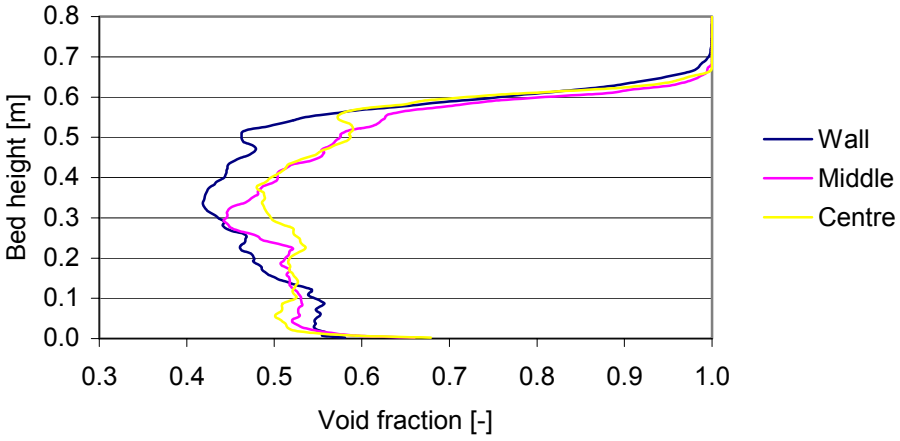

Figure 6.11: Void fraction as a function of height at different radial positions for a bed with diameter 0.45 m.

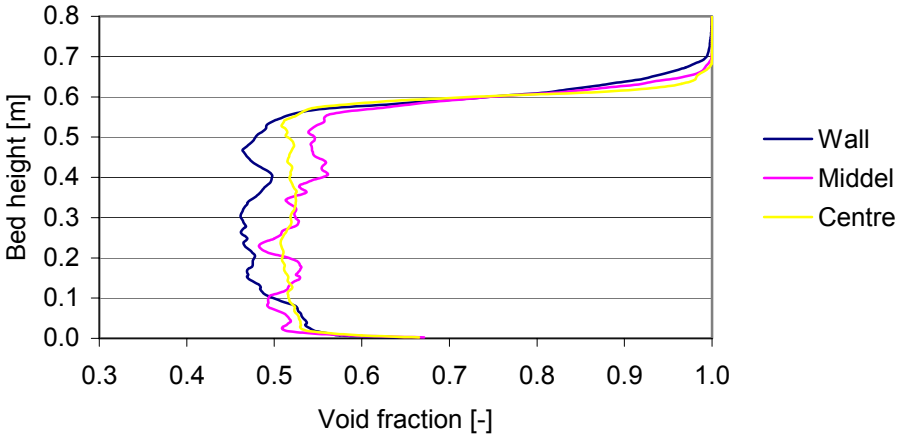

Figure 6.12: Void fraction as a function of height at different radial positions for a bed with diameter 1.0 m.

The void fraction as a function of radial position is studied next. Figure 6.13 shows that for the 0.10 m bed the void fraction profile changes significantly from height 0.05 m to 0.40 m. Close to the distributor, at height 0.05 m, the void fraction is highest in the middle annulus, but it is rather high in most of the radial positions. At height 0.40 m the void fraction is highest in the centre core and decreases towards the walls. In Figure 6.14 corresponding void fraction profiles can be seen for the 0.2 m bed. Both these beds are defined as deep beds, and it is expected that the bubbles are located mainly in centre at height 0.40 m. The void fraction profiles for these beds are approximately laminar.

Figure 6.15 shows void fraction as a function of radial position for the 0.45 m bed. At height 0.05 m the void fraction profile is rather flat. Highest void fractions are located close to the walls. At level 0.40 m the areas of highest void fractions have moved from near the walls to the middle annulus. The void fractions in the centre are low at both the levels. For the 1.0 m bed shown in Figure 6.16, the void fraction profile is rather flat at both the axial levels, but also for this case it can be seen that the bubbles have moved a little from the walls towards the centre.

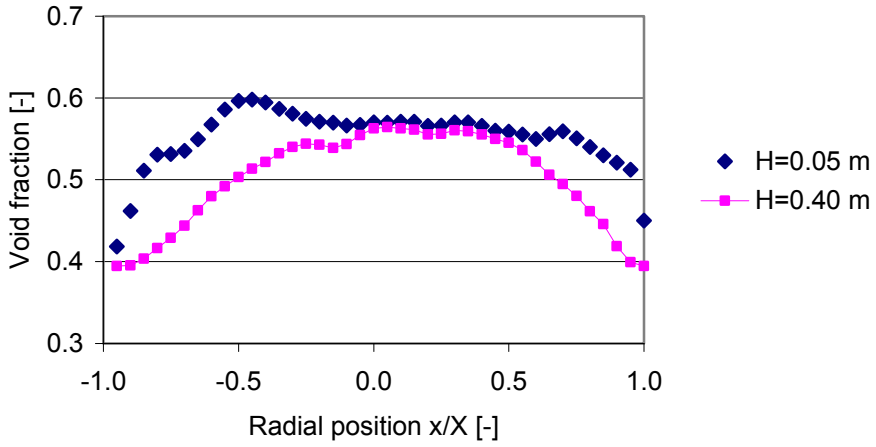

Figure 6.13: Void fraction as a function of radial position, bed diameter 0.10 m.

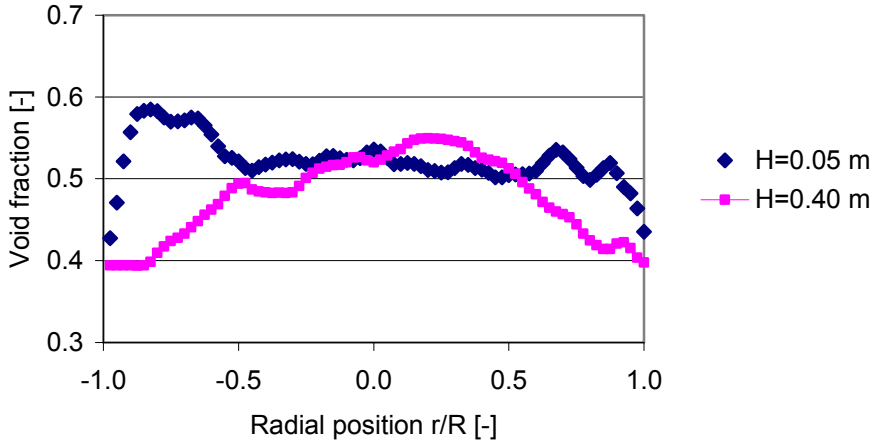

Figure 6.14: Void fraction as a function of radial position, bed diameter 0.20 m.

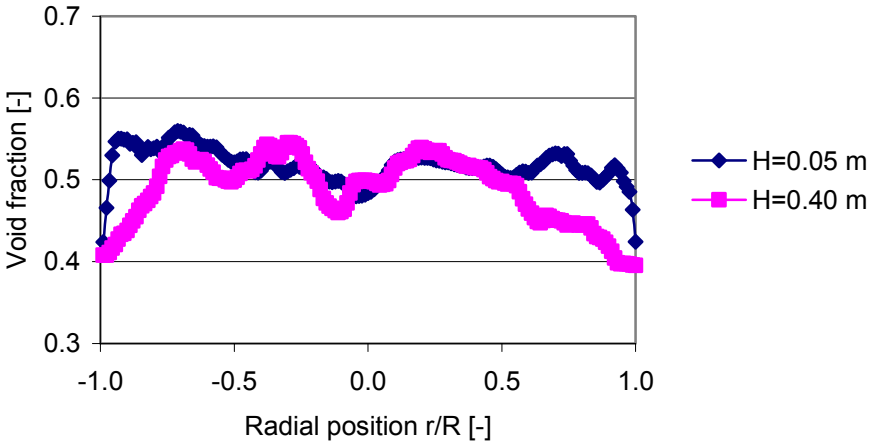

Figure 6.15: Void fraction as a function of radial position, bed diameter is 0.45 m.

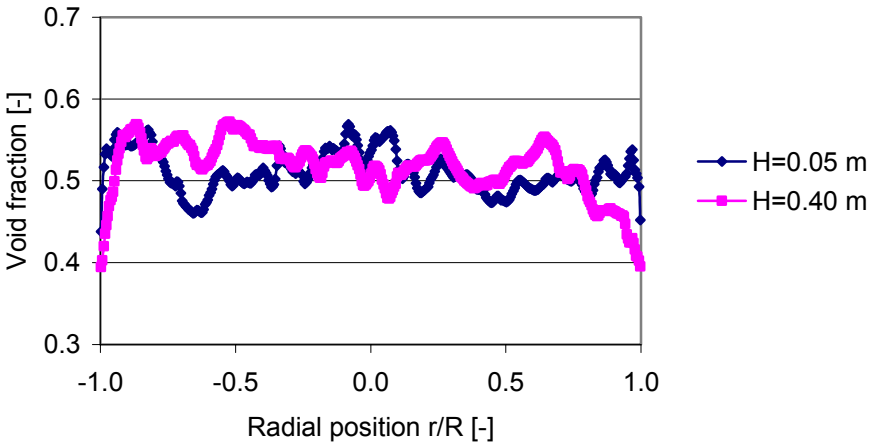

Figure 6.16: Void fraction as a function of radial position, bed diameter is 1.0 m.

The bubble frequency has been calculated at different radial positions at height 0.30 m. Figure 6.17 shows the bubble frequency in a point. A bubble is defined where the void fraction is greater than 0.8, Gidaspow (1994).

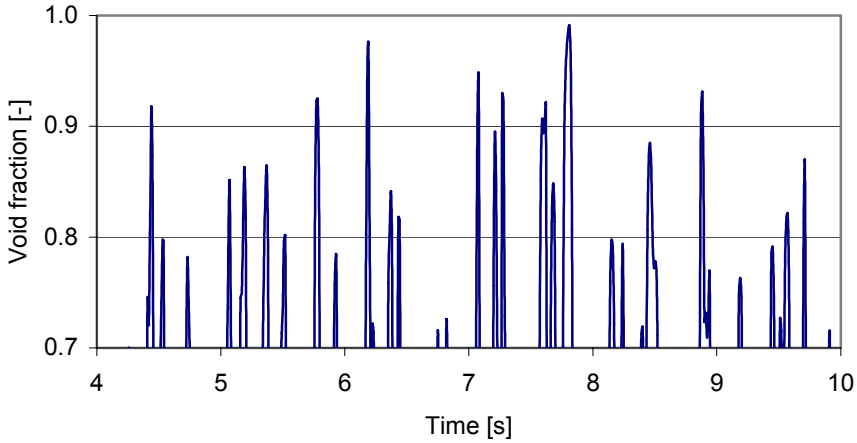

Figure 6.17: Bubble frequency in one point.

Figures 6.18, 6.19, 6.20 and 6.21 show the bubble frequencies as a function of radial position for the beds of diameter 0.10, 0.20, 0.45 and 1.0 m respectively. In the 0.10 m bed the bubble frequency is about 3.7 s^{-1} in the centre and decreases towards the walls. Close to the walls, no bubbles are detected. The bubble frequency for the 0.20 m bed is also highest in the centre, but for this case the area of high bubble frequencies is wider. In the 0.45 m bed there is a wide region where the bubble frequency is about 3.5 s^{-1}. From this region the frequency decrease rather steep, and in a 0.10 m annulus near the wall, the bubble frequency is low. The region of high frequency is located to the right of the centre. This may be due to a too short time interval used for the frequency calculations. Figure 6.22 shows that for the 1.0 m bed the frequency varies between 3 and 4 in the area with radius 0-0.30 m and decrease to 0 close to the wall.

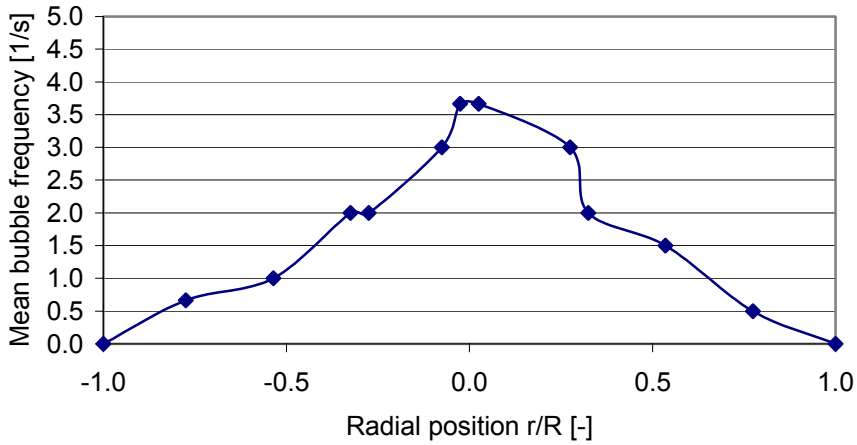

Figure 6.18: Bubble frequency as a function of radial position at height 0.30 m, bed diameter 0.10 m.

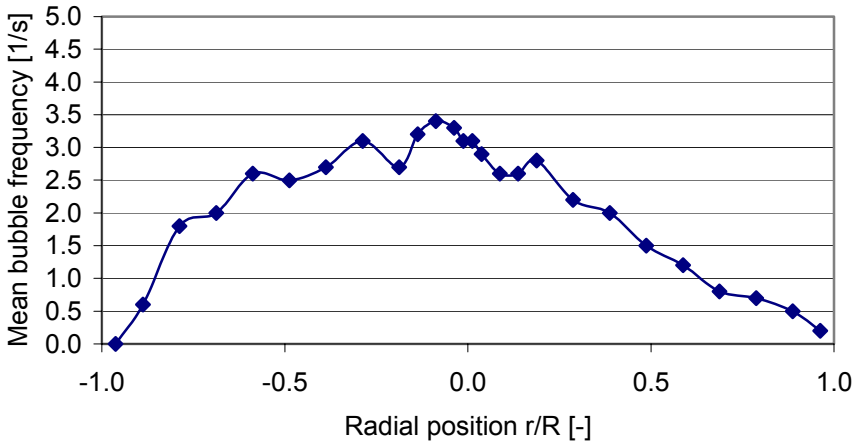

Figure 6.19: Bubble frequency as a function of radial position at height 0.30 m, bed diameter 0.20 m.

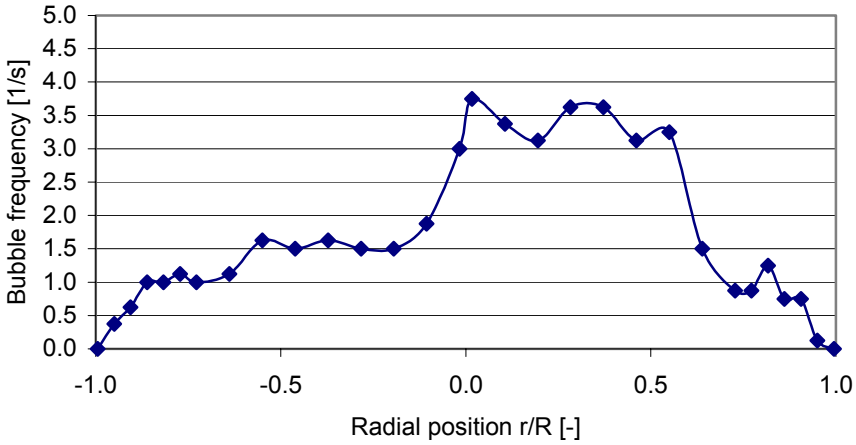

Figure 6.20: Bubble frequency as a function of radial position at height 0.30 m, bed diameter 0.45 m.

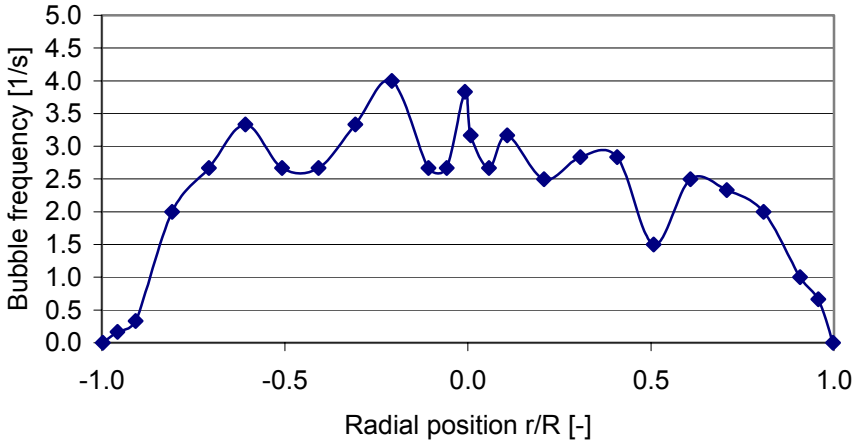

Figure 6.21: Bubble frequency as a function of radial position at height 0.30 m, bed diameter 1.0 m.

The simulations are performed with a bed height of 0.5 m for all the four bed diameters. The ratio between bed diameter (D_t) and bed height (H_t) influences the bubble behaviour in a fluidized bed. In shallow beds ($H_t/D_t<0.5$) solid down-flow in the centre is deflecting bubbles towards the walls. In deep beds ($H_t/D_t>1$) the same flow pattern can be observed in the lower part of the bed, but it changes to solid up-flow in the centre and down-flow near walls, which cause bubbles move to the centre of the bed. According to Werther and Molerus (1973b) bubbles break the surface preferentially at the centre of bed in beds deeper than two bed diameters. This is the case for the 0.10 and 0.20 m diameter beds but not for the two larger beds. Based on this it is expected that the radial distribution of bubbles and void fraction will differ for the four cases studied here.

The bubble behaviour is also influenced by the ratio of bed diameter and particle diameter. Bubble diameter divided by bed diameter (D_b/D_t) is approximately the same for different bed sizes at equal ratio H_t/D_t and the same difference between superficial gas velocity and minimum fluidization velocity (u_0-u_{mf}), Geldart (1980). In this study, the bed height is kept constant whereas the diameter is varied. Bubbles grow with height in the bed, so it can be expected that the bubble diameter is about the same for the four cases. From Figure 6.18 and Figure 6.21 it can be seen that in the 0.10 m bed the bubbles are concentrated in centre of the bed, whereas in the 1.0 m bed the bubbles are distributed over the diameter. This can be used for scaling.

Because of wall effects and how the walls and the coalescence effects influence the flow pattern in a fluidized bed, it cannot be assumed that bubble behaviour measured or simulated in a two dimensional bed is the same as that existing in a three dimensional bed with the same particles, Geldart (1986).

6.4.2 Simulations with 3-D cylindrical coordinates

The fluidized beds with diameters 0.10 m and 0.20 m have been simulated using 3-D cylindrical coordinates. The simulations have been performed for 10 s real simulation time and with a grid resolution of 0.25 cm in the radial and 0.5 cm in the axial direction. 18 control volumes have been used in the angular direction for both cases.

Bubble detection has been performed in the time interval 4-10 s. Bubble frequency as a function of radial position is calculated. Figure 6.22 shows bubble frequency at heights 0.15 and 0.30 m for the 0.10 m bed. The calculations give no uniform peak in the centre of the bed, as was observed for the 2-D calculations. According to theory and experimental research, the bubbles are formed close to the distributor and near the wall. The bubbles will move towards the centre with increasing height and will be located in centre when they reach a bed height of about 2 times the bed diameter, which means at height 0.20 m for the case shown here. It can be seen from Figure 6.23 that the bubble frequency near the centre increases significantly from height 0.15 to 0.30 m.

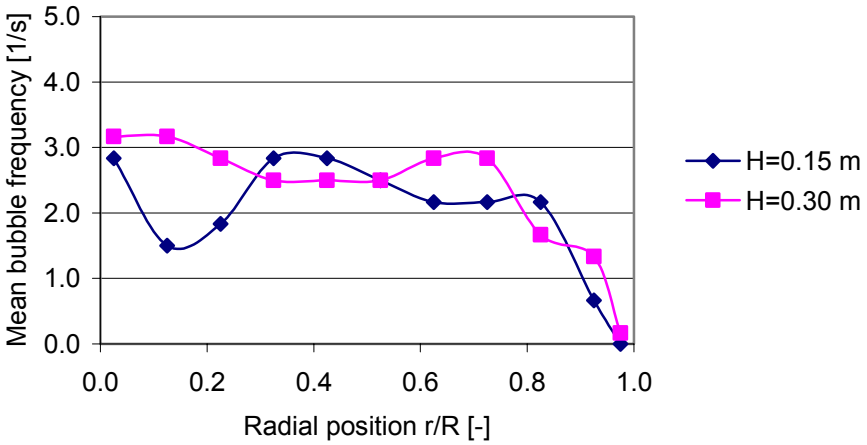

Figure 6.22: Bubble frequency as a function of radial position, 0.10 m diameter bed.

The bubble frequency as a function of radius for the 0.20 m bed is shown in Figure 6.23. For this case the bubble frequency is low in the centre and near the wall, and highest about 1.5 cm from the wall. In the centre the frequency increases with increasing height. Both the bed heights used for the calculations are less than two times the bed diameter.

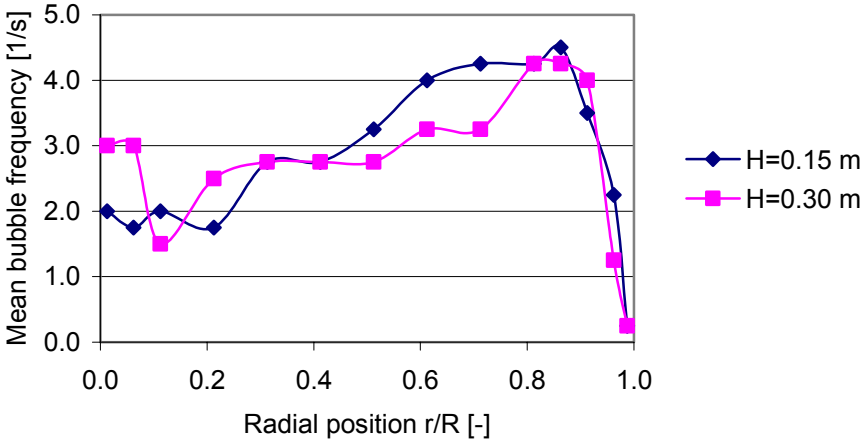

Figure 6.23: Bubble frequency as a function of radius, 0.20 m diameter bed.

6.4.3 Scaling using scaling parameters

The parameters of the 0.20 and 0.45 m diameter beds are scaled down to perform the simulations on a 0.10 m diameter bed. Scaling down from 1.0 m to 0.1 m will give unrealistic low values for gas viscosity and this scaling and simulations are not performed. The scaling parameters proposed by Fitzergald and Crane and shown in Table 6.5 are used. The simulations are performed with 3D cylindrical coordinates.

Table 6.5: Scaling parameters

Parameters	Parameters used without scaling	Scaling from 0.20 m to 0.10 m	Scaling from 0.45 m to 0.10 m
Particle mean diameter	83 μm	41.5 μm	18.4 μm
Particle density	2640 kg/m^3	4475 kg/m^3	8660 kg/m^3
Bed geometry	D, H	D/2, H/2	D/4.5, H/4.5
Initial bed height	0.5 m	0.25 m	0.11 m
Superficial velocity	0.09 m/s	0.028 m/s	0.042 m/s
Gas density	1.2 kg/m^3	1.8 kg/m^3	3.52 kg/m^3
Gas viscosity	$1.8 \cdot 10^{-5}$ kg/m·s	$0.96 \cdot 10^{-5}$ kg/m·s	$0.55 \cdot 10^{-5}$ kg/m·s
Mesh		20x200x18	20x200x18

Figure 6.24 a. and b. shows a comparison of the results obtained from scaling down the 0.20 m diameter bed to 0.10 m bed and the results obtained from simulation of the 0.20 m bed respectively. The simulations are performed with 3-D cylindrical co-ordinates. Werther and Molerus used sand particles with a mean diameter of 83 μm and density 2640 kg/m^3 in their experimental research. These particles are classified as Geldart A particles, but are situated close to Geldart B particles. When scaling down from 0.20 m to 0.10 m bed, the particle diameter and density becomes 41.5 μm and 4475 kg/m^3 respectively. The particles are still classified as Geldart A particles, but now not so close to Geldart B particles. When Geldart A particles are fluidized, the bed expands considerably before bubbles appear. It can be seen from the figure that simulation using 0.20 m bed give a high bed expansion whereas the result from the scaled bed show considerably lower bed expansion. The figure also shows that simulation of the 0.20 m bed gives increase in void fraction with increasing height, especially near the centre. The scaled case gives a flat void fraction profile at both heights, and the increase in void fraction with height is insignificant. An analysis that is performed of the bubble frequency for the scaled bed shows no bubbles at all.

In Figure 6.25 are shown the result of scaling down the 0.45 m diameter bed to a 0.10m bed. 3-D simulation of this case has not been performed on a 0.45 m bed. The particle diameter is scaled down from 83 μm to 18.4 μm. The density is changed to 8660 kg/m^3. These particles are classified at the limit between Geldart C and A particles. Group C particles are cohesive or very fine powders and normal fluidization is extremely difficult for these solids, because inter-particle forces are greater than forces resulting from the action of gas, Kunii and Levenspiel (1991). The results from the scaling simulation of the 0.45 m bed show that the bed expands considerably. The void fraction profile is flat, and the void fraction increase from about 0.60 to about 0.63 between the two heights.

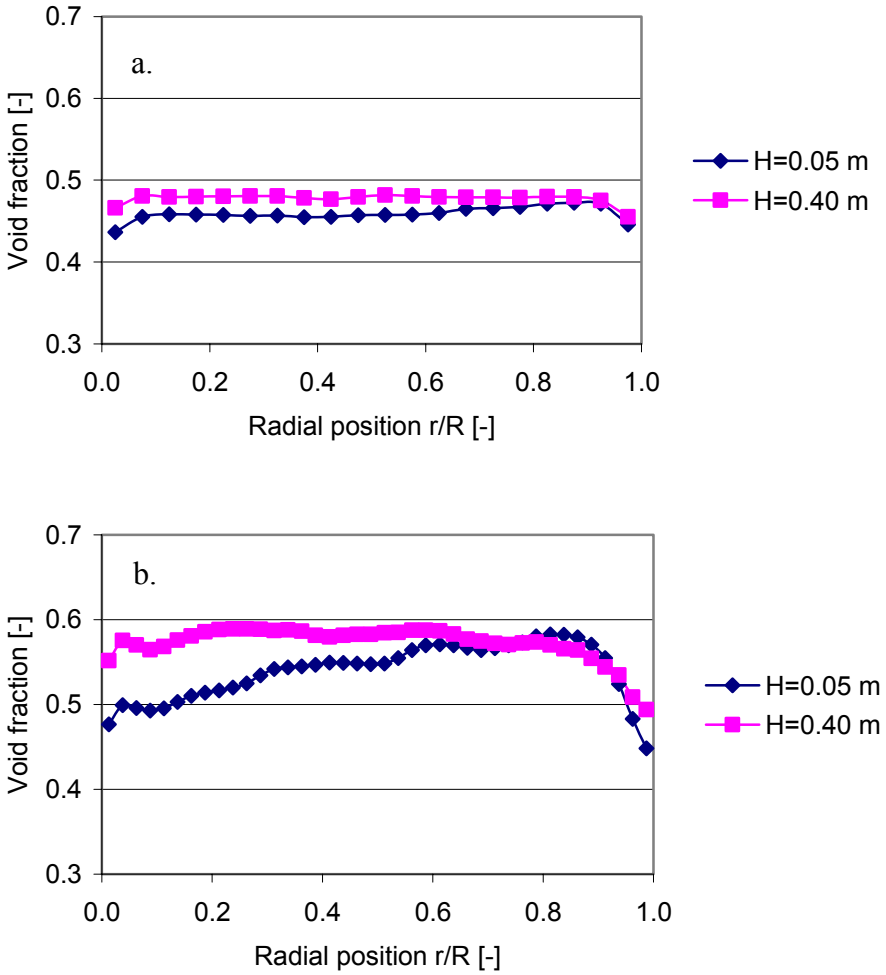

Figure 6.24: Void fraction as a function of radial position r/R [-]. Comparison of a) 0.20 m bed scaled down to 0.10 m b) 0.20 m full size bed.

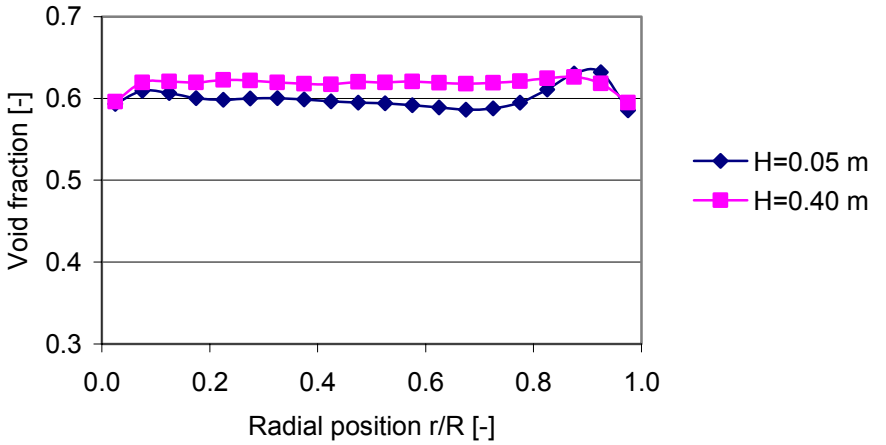

Figure 6.25: Void fraction as a function of radial position r/R [-]. 0.45 m bed scaled down to 0.10 m.

The simulations performed by using the scaling parameters proposed by Fitzergald and Crane give results that differ considerably from corresponding results from full scale simulations and from experimental and predicted results. This may be due to the size of the control volume compared to the particle size. It seems that when scaling down the beds, the results can be smeared and information is lost. The same tendency is observed in the in the grid resolution test. Information is lost when grid becomes too coarse. Another reason might be that by scaling down the particle size the particle density has to be changed and the particle properties and characterisation may change. Flow conditions and bubble behaviour change significantly with powder properties.

6.4.4 Comparison of experimental and computational results

Werther and Molerus (1973b) performed an experimental study of the spatial distribution of bubbles in these gas fluidized beds with diameters 0.10, 0.20, 0.45 and 1.0 m. Their measurement system consisted of a miniaturized capacitance probe which did not disturb the local state of fluidization. Based on the statistical analysis of the signal, the mean bubble pulse duration, the number of bubbles striking the probe per unit time and the local mean bubble rise velocity were measured. The local mean pierced bubble length was derived from these measured parameters.

Comparisons of experimental and computational data for bubble frequency as a function of radial position for the fluidized bed with diameter of 0.10 m are shown in Figure 6.26. The comparisons are performed at height 0.30 m above the air distributor. The agreement is good.

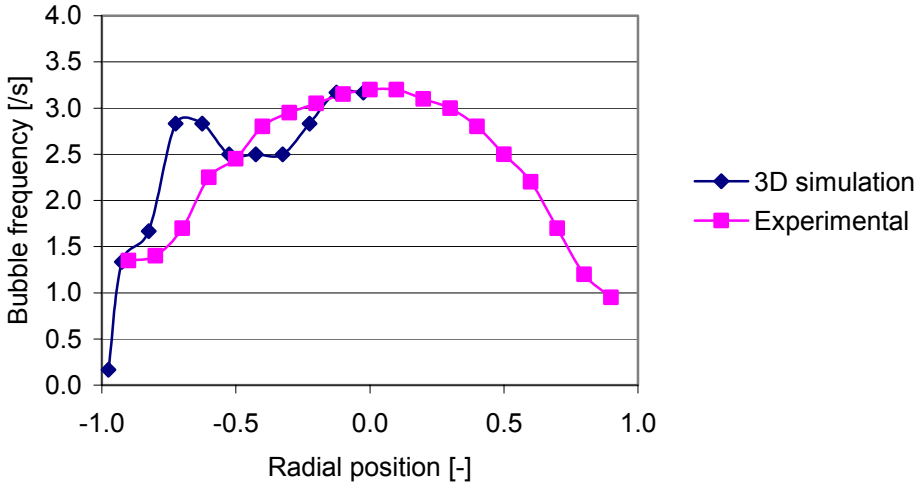

Figure 6.26: Bubble frequency as a function of radial position, height 30 cm, 0.10 m bed.

Figure 6.27 shows the comparison of experimental and computational data in the fluidized bed with diameter 0.20 m at height 0.15 m. Both the experimental and the calculated data show a low bubble frequency in the centre and the highest frequency in the middle annulus. However, the calculated frequencies are somewhat higher than the experimental ones. In the calculation of bubble frequencies, all bubbles equal to or larger than control volumes were used.

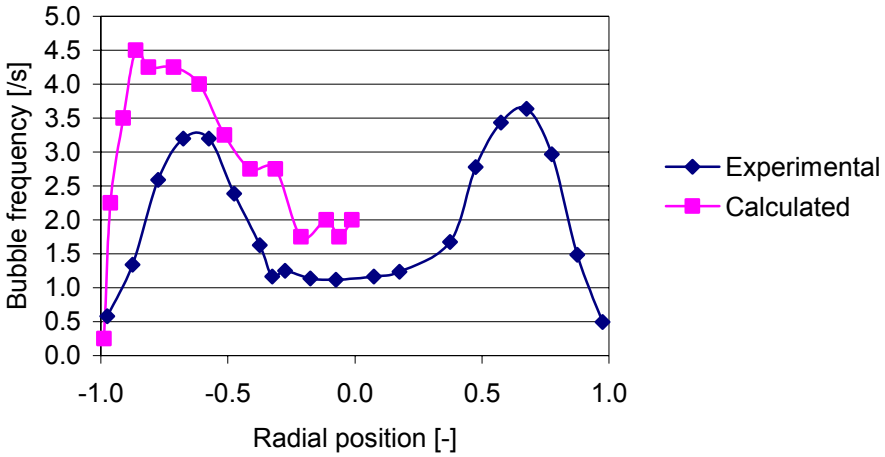

Figure 6.27: Bubble frequency as a function of radial position, height 0.15 m, 0.2 m bed.

Bubble frequency, mean piercing length and mean bubble velocity are calculated as a function of bed height. The calculations are performed at the axis for the 0.10 m bed. The calculations of mean bubble velocity and mean bubble pierced length are based on 6 bubbles at each point. These calculations were performed by locating the bubbles in time and calculate the height of the bubbles at the actual points in time. Comparison of computational and experimental data for mean bubble pierced length as a function of bed height is shown in Figure 6.28. At height 0-0.25 m above the distributor the calculations agree well with the experimental results. Above height 0.25 m the calculated mean bubble pierced length are considerable lower than the bubble pierced length observed in the experiments. The experimental data show that bubbles have been detected at bed heights up to 0.95 m above the air distributor. This means that the experiments give a very high bed expansion compared to the calculations where no bubbles where detected above 0.65 m.

Figure 6.29 shows the comparison of computational and experimental results of local mean bubble rise velocity with height above the distributor. This comparison shows that there are rather large discrepancies at heights above 0.40 m. Both the calculated and measured data give a velocity peak at height 0.20m. The calculated velocity at this height is about 0.9 m/s, whereas the measured velocity is 0.6 m/s.

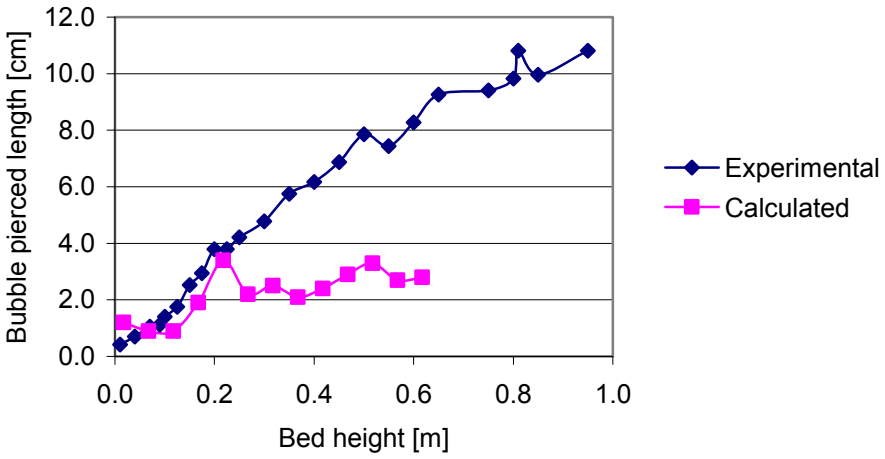

Figure 6.28: Local mean bubble pierced length as a function of height above the air distributor at the column axis.

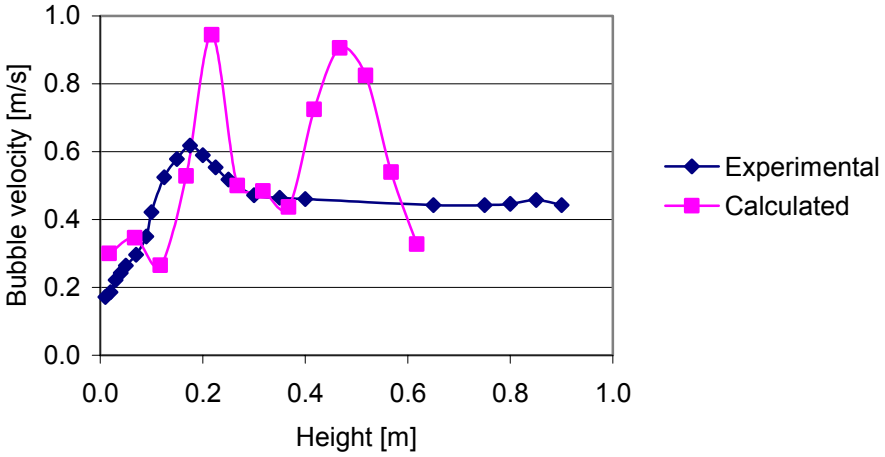

Figure 6.29: Mean bubble velocity as a function of height above the distributor at the column axis, 0.10 m bed.

The discrepancies between computational and experimental results that are observed for the local mean bubble rise velocity and local mean bubble pierced length with height above the distributor may be due to the number of bubbles that are used for the calculations. At most of the axial locations the calculations are based on 6 bubbles. At the axis the grids are very small and the discrepancies cannot be due to a smeared solution. However, the calculations are performed for a grid very close to the singular point and this may give some unexpected solutions.

6.5 Summary

Simulations of a bubbling fluidized bed with diameter 0.10 m are performed with 3-D cylindrical, 2-D Cartesian and 2-D axis symmetrical coordinates. A grid independency study was performed. This study showed that 20×200×18 is the coarsest mesh that can be used. The comparison between the 2-D simulations and the 3-D simulations shows that 2-D Cartesian coordinates can be used to model the bed with good accuracy in most regions.

Fluidized beds with diameters of 0.1, 0.2, 0.45 and 1.0 m have been simulated using 2-D Cartesian coordinates. The averaged void fractions change significantly as a function of height for the 0.2 and 0.45 m beds, less for the 0.10 m bed and just insignificantly for the 1.0 m bed. The void fraction changes rather much with radial position for the 0.10 and 0.20 m beds and less for the 0.45 and 1.0 m beds. For all beds the bubble frequency at height 0.30 m is lowest near the wall and highest in the centre. Wall and coalescence effects influence the flow pattern and it cannot be assumed that bubble behaviour in a two dimensional bed is the same as in a three dimensional bed with the same particles and superficial velocity.

Three dimensional simulations are performed for the 0.1 m and 0.2 m beds. Bubble frequencies as a function of radial position are compared to experimental data. Experimental and computational results agree well. Mean bubble pierced length and mean bubble rise velocity at the axis as a function of height above the distributor have been calculated and compared with experimental data. These comparisons are performed for the 0.10 m bed. The calculated mean local pierced length and local mean bubble rise velocity agree rather well with the experimental data in the lower part of the bed, whereas the discrepancies are significant in the top of the bed.

The 0.20 m and 0.45 m beds are scaled down and simulated on a 0.10 m bed. Scaling parameters proposed by Fitzergald and Crane (1980) are used in the simulations. The results of the simulations show that the scaling down performed in the way done here gives unrealistic and smeared results. This may be due to the control volume size compared to the particle sizes and to the fact that change of particle properties may change the bubble behaviour in the fluidized bed.

7. Experimental study of a 3-D bubbling fluidized bed

The efficiency of fluidized bed reactors depends on bubble distribution, bubble size and bubble velocity within the reactor. Different types, sizes and size distributions of solids used in the bed may lead to different bubble behaviour. Bubble behaviour is influenced by superficial gas velocity and the ratio between the cross-section area and the bed height as well. In chemical reactors the contact between gas and solid is controlling the reaction.

Boundaries of bubbles in fluidized beds are permeable, and gas circulates through the bubble, entering in the bottom and leaving through the upper surface. This phenomenon is called 'through-flow' and is important for the gas-solid contacting and the interface mass transfer in fluidized beds, Geldart (1986). 'Through-flow' occurs when the bubble velocity is higher than the dense phase (emulsion) gas velocity, Kunii and Levenspiel (1991). The region below the bubbles is the wake region. The wakes are formed because the pressure in the lower part of the bubbles is lower than in the dense phase nearby, and gas is drawn into the bubble. This causes instability, partially collapse of the bubble and turbulent mixing, Kunii and Levenspiel (1991). Solids are dragged up the bed behind the bubbles and drift downwards in the emulsion. The down flow of solids can be faster than the up flow of gas in the dense phase and causes a net down flow of emulsion gas in parts of the bed.

In this work glass particles of three different size distributions are used to study how particle size distributions influence on the bubble behaviour. In addition the influence of superficial gas velocity is studied. Studies of bubble size, velocity and frequency at different heights above the air distributor are performed.

7.1 Experimental setup

The fluidized bed is constructed from transparent plexiglass sheets. The bed has a square of 0.25 m x 0.25 m cross section and the height is 2 m. Air is fed through an air distributor in the bottom of the bed. A porous steel plate acts as distributor and the pressure drop over the distributor is about 15% of the expected bed pressure drop. The experimental set-up is shown in Figure 7.1.

Pressure sensors are installed at 10 different heights of the bed. The sensors are 0-2 psi (0-13.8 kPa) gauge sensors from Honeywell. The sensors are connected to a PC and a Labview program is used to log the data and convert the data from voltages to kPa.

The Vector fibre optical probe described in Chapter 2 is used to measure the bubble behaviour. The optical probe can be inserted at 5 different bed heights. The system was not able to detect validated bubbles at the two lowest heights, so only three heights are used for the bubble detections in this work.

Spherical glass particles with a particle density of 2485 kg/m^3 and with three different mean particle sizes are used in the experiments. The measurements have been performed with different superficial velocities. The experimental conditions are given in Table 7.1.

Table 7.1: Experimental conditions.

Design			
Height of vessel	2.0 m		
Cross section area	(0.25x0.25) m^2		
Pressure sensors:			
Heights above air distributor:	0.115 m, 0.155 m, 0.195 m, 0.275 m, 0.355 m, 0.425 m, 0.505 m, 0.605 m, 0.705 m, 1.820 m		
Fibre optical probe:			
Heights above air distributor:	0.39 m, 0.55 m, 0.71 m		
Glass particles	**d_p : 100-200 µm**	**d_p : 400-600 µm**	**Mixed powder:**
Mean diameter:	154 µm	480 µm	322 µm
Superficial velocites:	0.090 m/s 0.133 m/s	0.210 m/s	0.090 m/s 0.133 m/s
Particle density	2485 kg/m^3	2485 kg/m^3	2485 kg/m^3
Bulk density	1490 kg/m^3		1590 kg/m^3
Initial bed height	0.75 m	0.75 m	0.75 m

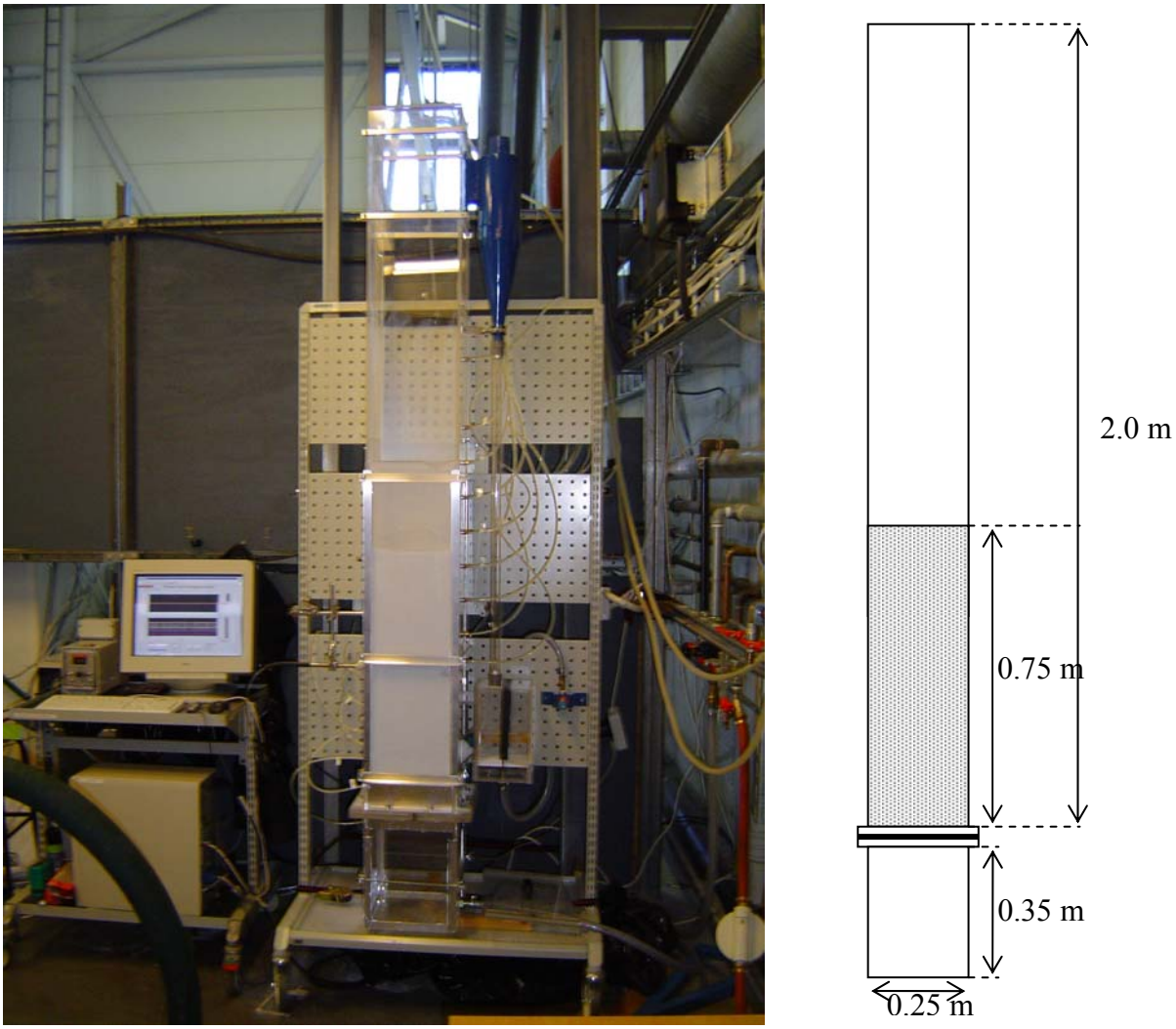

Figure 7.1: Experimental set-up.

The particle size distribution has an effect on the bulk density and may therefore also influence the flow conditions in the fluidized bed. The three powders, the small particle powder, the large particle powder and the mixed powder, have volume averaged particle diameters of 154 μm, 480 μm and 322 μm respectively. According to the mean diameters, the large particle powder and the mixed powder are clearly classified within Geldart group B particles whereas the small particle powder is classified close to Geldart group A particles. The cumulative particle size distributions for the three powders are shown in Figures 7.2, 7.3 and 7.4. These distributions are based on weight. The mixed powder is a mixture of 50 volume% of each of the two other powders. The sample that was used for the particle size analysis for the mixed powder was a random sample from the experimental bed.

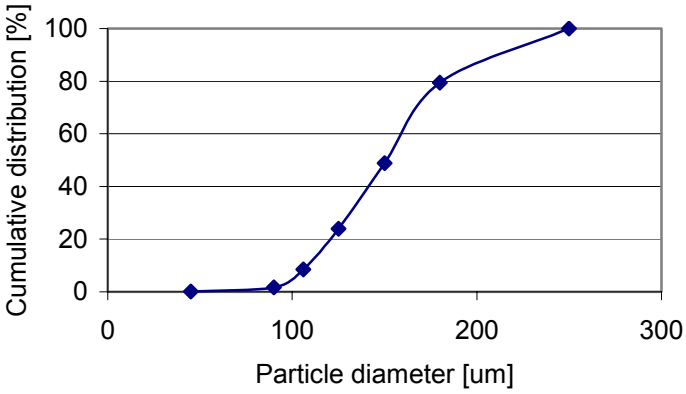

Figure 7.2: Cumulative particle size distribution for small particle powder.

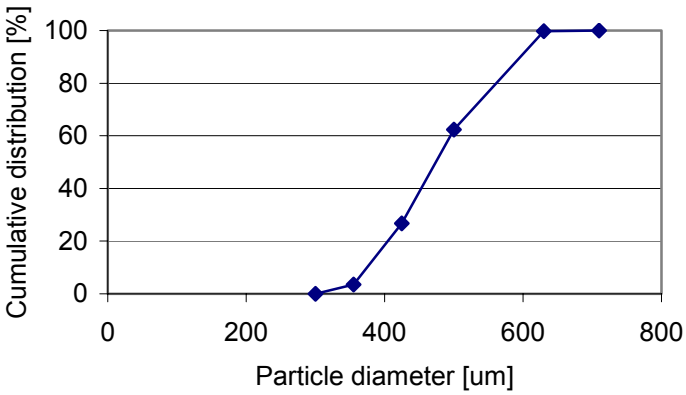

Figure 7.3: Cumulative particle size distribution for the large particle powder.

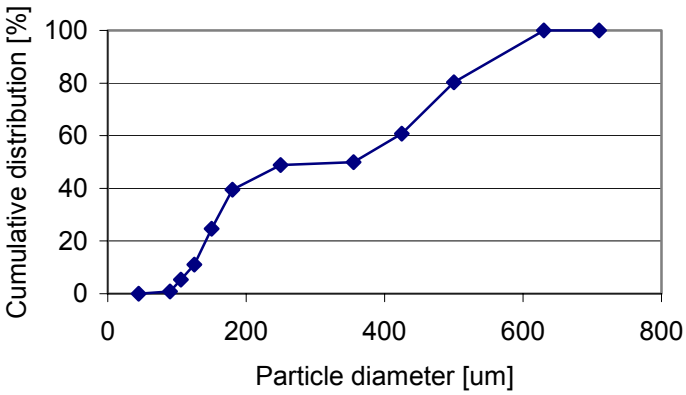

Figure 7.4: Cumulative particle size distribution for mixed powder.

7.1.1 Bubble velocity

Bubble rise velocity is a function of bubble size. The bubble velocity is also influenced by the geometry of the fluidized bed and the position of the bubble in the bed. Bubble velocities tend to increase with bubble size. When the bubble diameter increases, however, the wall effects on the bubbles will affect the bubble velocity and a decrease in velocity can be observed. Wall effects retard the bubble rise when the bubble diameter increases to more than 0.125 times the bed diameter.

Bubble velocities are measured at the heights 0.39 m, 0.55 m, and 0.71 m above the air distributor. The fibre optical probe is introduced from the wall at position x/X=-1. X is the distance from the centre of the bed to the wall and is equal to 0.125 m and x is the radial position in the bed and varies from -0.125 m to 0.125 m. The bubble velocities are measured for the three powders. The experiments have been performed with superficial gas velocity 0.090 m/s and 0.133 m/s for the small particle powder and the mixed powder, and with the superficial gas velocity 0.210 m/s for the large particle powder.

7.1.2 Bubble pierced length

Bubbles in a bubbling fluidized bed can be quite irregular in shape and can vary significantly in size. The shape and the size of bubbles depend on particle size and particle size distribution. In beds of fine Geldart A particles an equilibrium state between coalescence and splitting of bubbles will limit the bubble sizes to a few centimetres. In beds of Geldart B particles the bubbles grow with height in the bed and can become significant larger than the bubbles in the fine particle beds. Kunii and Levenspiel (1991) used experimental data from Werther (1978) to develop expressions for bubble velocity as a function of bubble diameter for Geldart A and B particles. The bubble velocity for Geldart A particles was expressed by:

$$u_b = 1.55\left[(u_0 - u_{mf}) + 14.1(D_b + 0.005)\right]D_t^{0.32} + u_{br} \tag{7.1}$$

$$u_{br} = 0.711(gD_b)^{0.5} \tag{7.2}$$

where u_b is the bubble velocity, u_0 is the superficial velocity, u_{mf} is the minimum fluidization velocity and u_{br} is the rise velocity to a bubble with respect to the emulsion phase. D_b and D_t is the bubble diameter and the bed diameter respectively. The corresponding equation for Geldart B particles is:

$$u_b = 1.6\left[(u_0 - u_{mf}) + (1.13 D_b^{0.5})\right] D_t^{1.35} + u_{br} \tag{7.3}$$

The experimental bubble pierced length is calculated from bubble velocities and the width of the signals corresponding to the passage of bubbles. The detected signal may for instance be from measurement in the centre of a small bubble or from the periphery of a large bubble. The mean bubble heights may therefore be somewhat higher than the mean bubble pierced length.

7.1.3 Bubble frequency

The mean number of bubbles striking the probe per second is used here as the bubble frequency. This frequency parameter is not the same as the local bubble frequency defined as the number of bubble centres passing a unit cross-sectional area around the probe per unit time, Werther (1973a). The bubble frequency calculations include all detected bubbles and not only the bubbles used for calculation of bubble velocities and bubble sizes.

Werther (1973a) found that close to the air distributor in a fluidized beds, a zone of increasing bubble development exist in an area near the walls. The zone of higher bubble activity moves towards the centre with increasing height above the distributor. At a height about twice the bed diameter maxima of the bubble frequency is found in the centre of the bed.

The bubble measurements in this work are performed at rather high levels in the bed and it can be expected that the highest bubble frequencies will be located in the centre of the bed.

Local mean bubble gas flow is calculated by multiplying mean bubble frequency by mean bubble pierced length. The calculations are performed for superficial velocity 0.133 m/s for the small particles and the mixed powder, and for superficial velocity 0.210 m/s for the large particles. The total bubble gas flow is calculated by multiplying the local mean bubble gas flow with the surface area. These calculations are performed to find the part of the total gas flow that leaves the bed within the bubbles.

7.2 Preliminary experiments

Initial experiments and analysis were performed to check out the repeatability of the measurement method. Figure 7.6 shows a comparison of two experimental series performed with the same initial conditions. Particles with a particle size distribution of 100-200 μm were used in these series. The probe was located at height 0.39 m above the distributor and in the centre of the bed. The superficial velocity was 0.133 m/s. The analysis was based on 503 and 576 validated bubbles for series 1 and series 2 respectively.

The bubble velocity and the bubble pierced length have been averaged for the bubble length intervals 0-5 cm, 5-10 cm, 10-15 cm, 15-20 cm and 20-30 cm. The two experimental series agree rather well. There are some discrepancies for the largest bubbles. This may be due to few bubbles detected and validated in the intervals of bubble pierced length larger than 15 cm. The bubble size distribution is shown in Figure 7.7.

Figure 7.8 shows the bubble pierced length as a function of bubble velocity for one of the experimental series. Most of the detected bubbles have a velocity less than 1.5 m/s and a piercing length less than 15 cm. The uncertainty connected to the largest bubbles can be considerable.

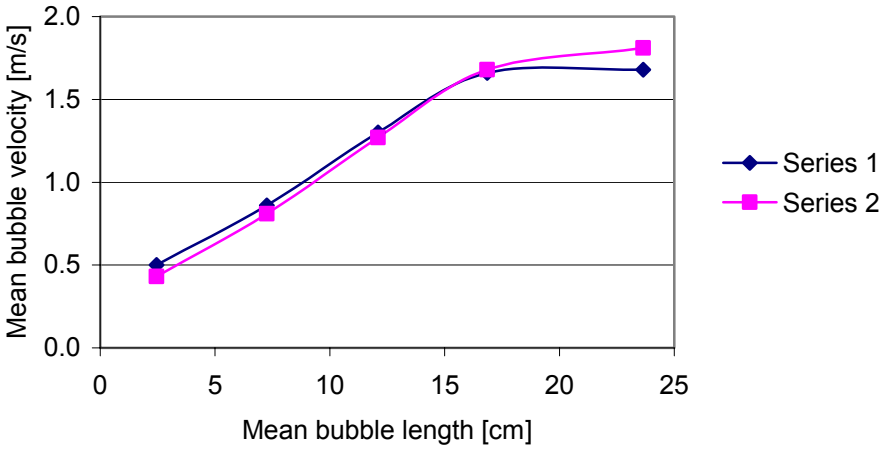

Figure 7.6: Mean bubble velocity as a function of mean bubble pierced length.

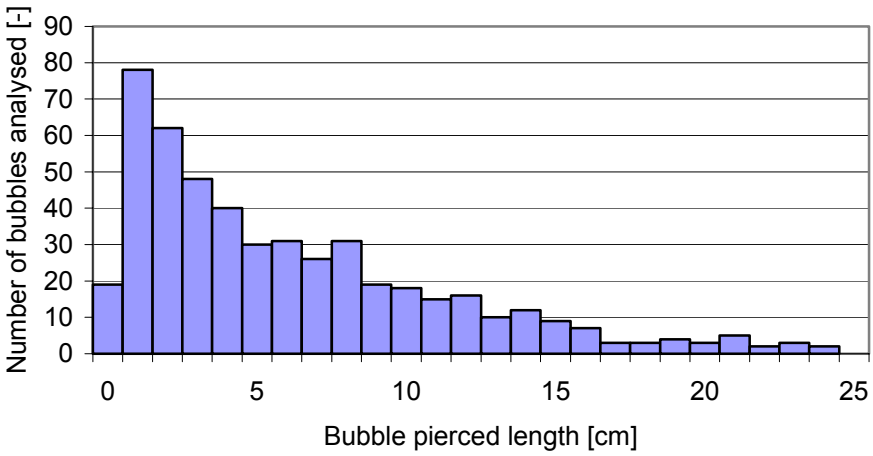

Figure 7.7: Bubble size distribution measured in centre of the bed at height 0.39 m. The superficial velocity is 0.133 m/s.

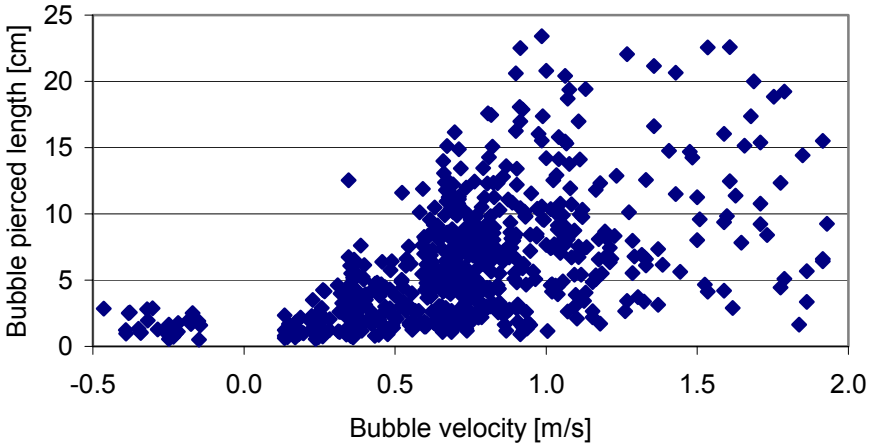

Figure 7.8: Bubble pierced length as a function of bubble velocity in centre of the bed at height 0.39 m. Superficial velocity is 0.133 m/s.

7.3 100-200 µm glass particles

The fluidized bed is initially filled up to a height of 0.75 m with particles of volume fraction about 0.6. When air is fed, the particle bed expands to about 0.82 m before bubbles appear. Bubbles start to appear at superficial gas velocities of about 0.07 m/s. The calculations of the bubble velocity and pierced length are based on about 500-600 bubbles in most positions. However, the number of bubbles decreases close to the walls and the calculations in these positions are mostly based on 50-200 bubbles.

7.3.1 Bubble velocity

Figure 7.9 shows the mean bubble velocity as a function of radial position. The superficial gas velocity is 0.09 m/s. At this velocity the mean level of the bubbling bed is about 0.82 m. The measurements show that there are some changes in bubble velocities with vertical position. At height 0.39 m above the distributor, the bubble velocity is lower than higher up in the bed in most of the radial positions. From height 0.55 m to 0.71 m the bubble velocities seems to decrease a little. The bubble velocities are highest near the centre of the bed, and decrease towards the walls. This can be seen at all three heights.

In Figure 7.10 bubble velocities as a function of radial position for the superficial velocity 0.133 m/s are shown. At this gas velocity the mean bed height is about 0.85 m. At height 0.39 m, the bubble velocities are about 0.7 m/s in the centre and decreases to about 0.4 m/s towards the walls. At heights 0.55 m and 0.71 m the maximum bubble velocities near the centre are 0.9 and 0.8 m/s respectively. At these two levels, the bubble velocities decrease to about 0.5-0.6 m/s towards the walls and increase again close to the walls.

For superficial velocities 0.09 and 0.133 m/s, the bubble velocities decrease from height 0.55 m to height 0.71 m. This may be due to the bubble diameters increase with height in the bed, and that at height 0.71 m the bubbles are so big that the influence of the wall effects reduces the bubble rise velocities.

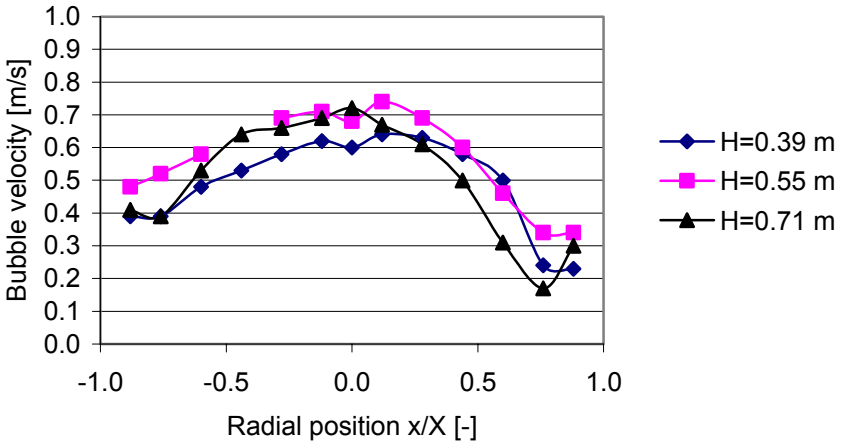

Figure 7.9: Mean bubble velocity as a function of radial position at three different heights. Superficial velocity is 0.09 m/s.

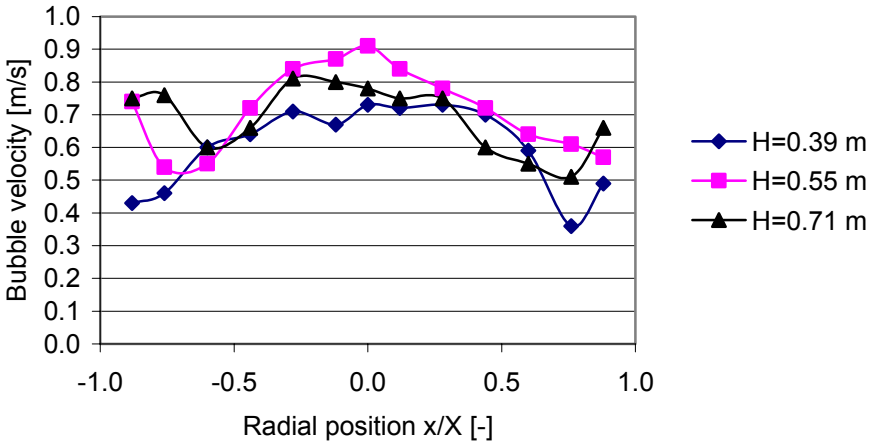

Figure 7.10: Mean bubble velocity as a function of radial position at three different heights. Superficial velocity is 0.133 m/s.

The measured bubble velocities do not give a precise symmetric velocity profile around the centre axis of the bed. This may partly be due to few bubbles detected near the walls. From visual study of the bubble behaviour in the bed, it was also observed that there was no obvious symmetry around the centre axis and that the path of the bubble rise could change during an experimental period.

Figure 7.11 shows a comparison between bubble velocities as a function of radial position for the superficial velocities 0.090 and 0.133 m/s. The measurements are performed at height 0.39 m above the air distributor. The bubble velocities increase significantly with increasing superficial velocity at all radial positions.

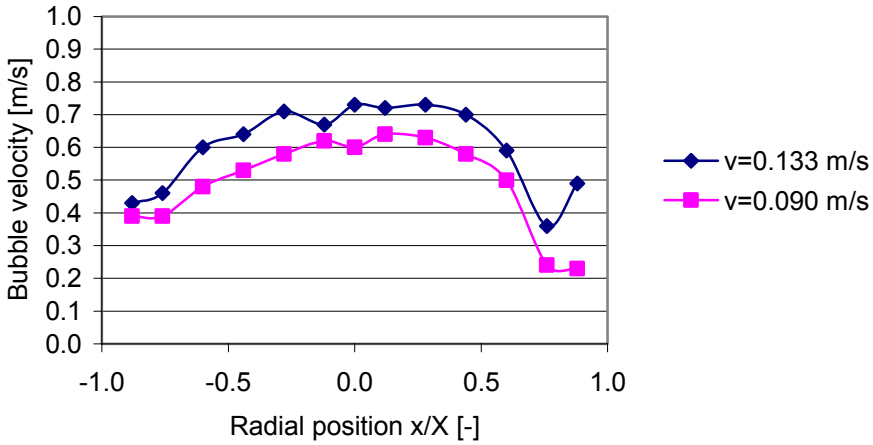

Figure 7.11: Comparison of mean bubble velocity for two different superficial velocities. The vertical position is 0.39 m above the distributor.

7.3.2 Bubble pierced length

In Figure 7.12 experimental data is compared to the expression of Kunii and Levenspiel (eq. 7.1-7.3). The figure shows the relation between bubble velocity and bubble size for superficial velocity 0.09 m/s. It can be seen that for Geldart A particles the bubble velocity increases

significantly with bubble diameter. For this powder, however, the bubble size is usually less than 10 cm. For Geldart B particles the bubble velocity increases less with bubble size.

The experimental data shows that the bubble velocities increase with increasing bubble size. There are, however, also some small bubbles with high velocities. These data might have been detected from the periphery of larger bubbles. The powder with mean particle diameter of 154 µm is classified as Geldart B particles, but is very close to Geldart A particles. The comparison of measured data and calculated curves shows that the measurements fit well with the Geldart B particles for the smaller bubbles but are located somewhere between the curves for Geldart A and B particles for the larger bubbles.

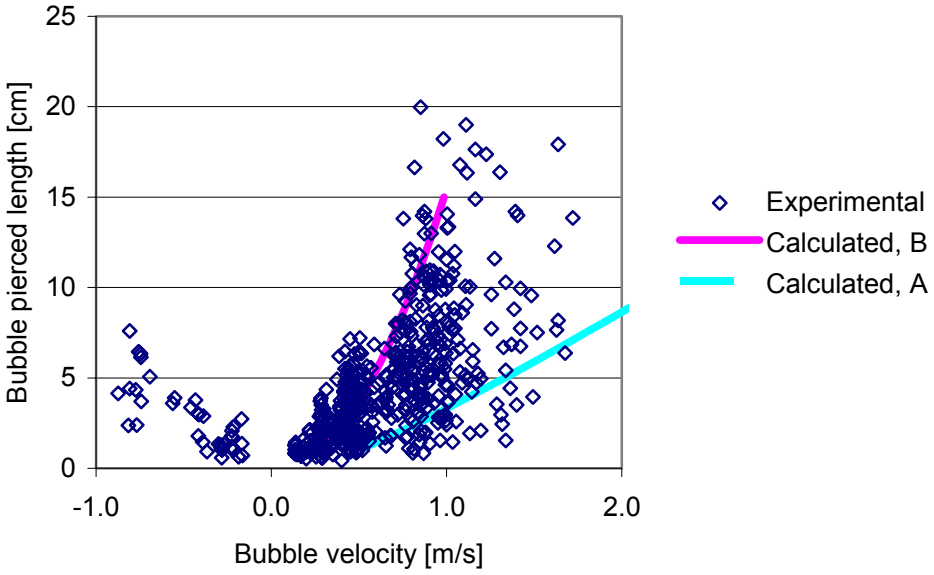

Figure 7.12: Bubble pierced length as a function of bubble velocity at height 0.39 m and superficial velocity 0.090 m/s.

Figure 7.13 shows the mean bubble pierced length as a function of radial position. The mean bubble size profile is obtained at a superficial gas velocity of 0.09 m/s and at heights 0.39 m, 0.55 m and 0.71 m above the air distributor. The mean bubble pierced length is lowest near the walls, and increases towards the centre. This is observed at all the three heights in the bed. The bubble size also increases with increasing height in the bed. Near the walls the bubble pierced length differ about 1 cm from height 0.39 to 0.71 m. In centre the bubble pierced lengths are about 5, 7 and 8 cm at heights 0.39 m, 0.55 m and 0.71 m respectively.

In Figure 7.14 the bubble size profiles for superficial velocity 0.133 m/s are shown. The bubble heights increase with height above the distributor. For this gas velocity the bubble size profile is rather flat at height 0.39 m. The bubble sizes at heights 0.55 m and 0.71 m differ rather little from each other near the wall. In centre the mean bubble pierced length increases from about 8 cm at height 0.55 m to 10 cm at height 0.71 m.

Comparison between bubble size profiles at height 0.39 m for different superficial gas velocities is shown in Figure 7.15. The profiles have the same shape and the bubble pierced lengths increase about 2 cm when the gas velocity increases from 0.09 m/s to 0.133 m/s.

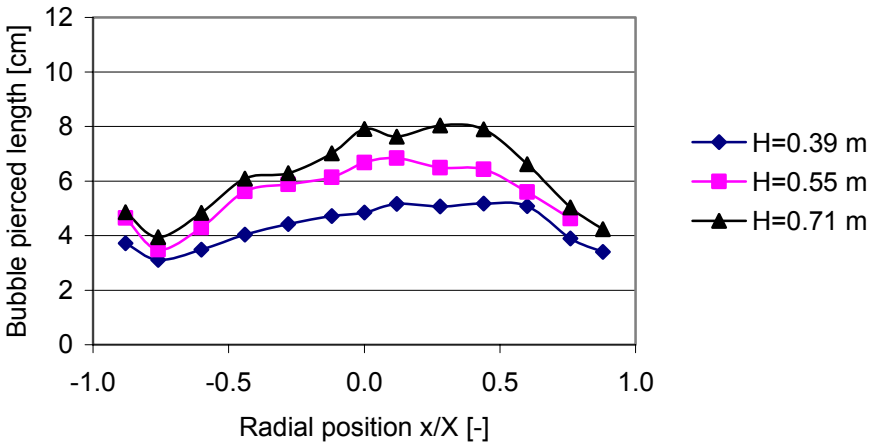

Figure 7.13: Mean bubble height at different vertical positions, v=0.09 m/s

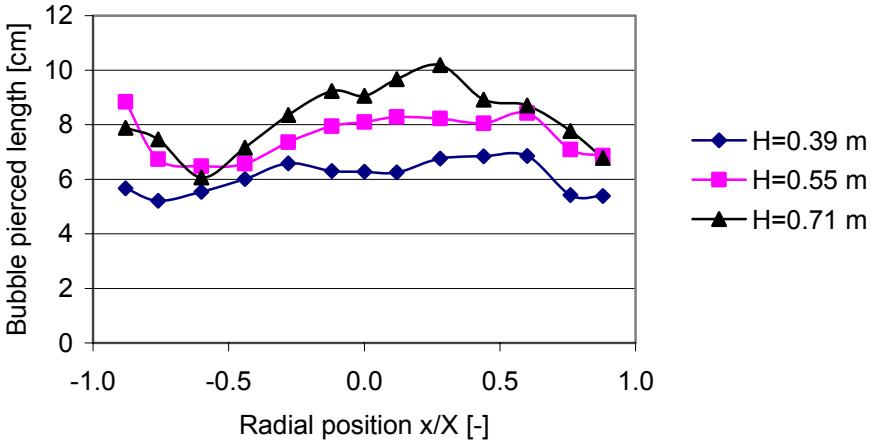

Figure 7.14: Mean bubble height at different vertical positions, v=0.133 m/s.

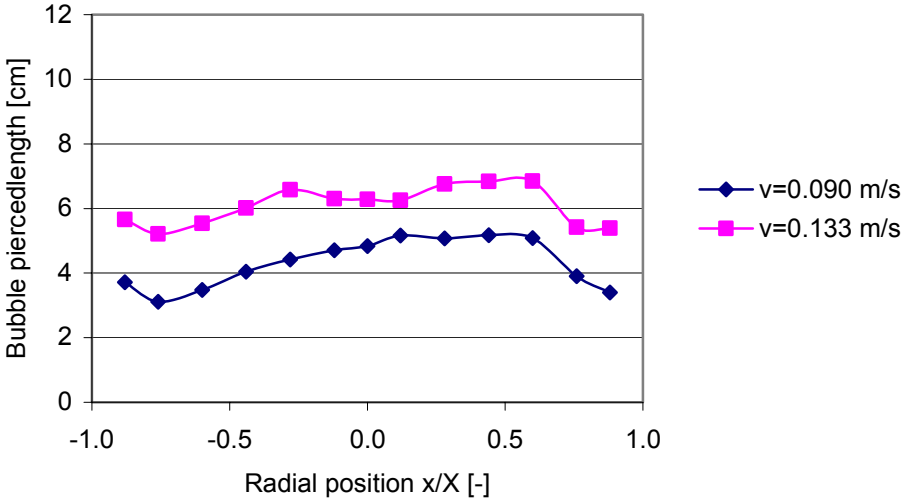

Figure 7.15: Comparison of mean bubble pierced length for different superficial velocities, H=0.39 m.

7.3.3 Bubble frequency

In Figures 7.16 and 7.17 bubble frequencies as a function of radial position are shown for superficial velocities of 0.090 m/s and 0.133 m/s respectively. For both cases the bubble frequency increases from the walls towards centre. For the lowest gas velocity, the frequency is highest at height 0.71 m. In the case with superficial velocity 0.133 m/s, the bubble frequency is highest at height 0.39 m and lowest at height 0.55 m at most of the radial positions. At height 0.71 m the bubble frequency profiles are more flat than at the other levels. This can be seen for both the cases. The reason for this may be that the bubble size increases with increasing height and in the top of the bed one bubble will occupy a rather large part of the radial positions.

In Figure 7.18 the bubble frequency for the two superficial velocities are compared at height 0.39 m. At this level the bubble frequency increases with increasing gas velocity. The frequency profiles have the same shape. This is also the case at the two other heights, but there the increase in bubble frequencies as a function of superficial velocity is less significant.

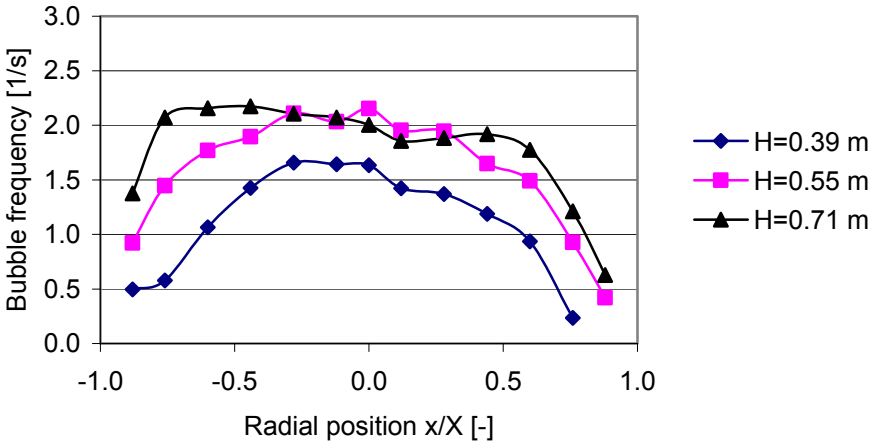

Figure 7.16: Bubble frequency as a function of radial position, superficial velocity 0.090 m/s

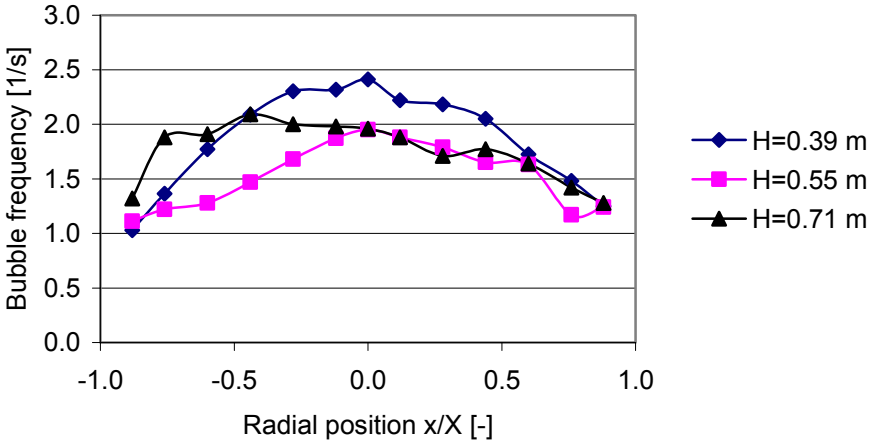

Figure 7.17: Bubble frequency as a function of radial position, superficial velocity 0.133 m/s.

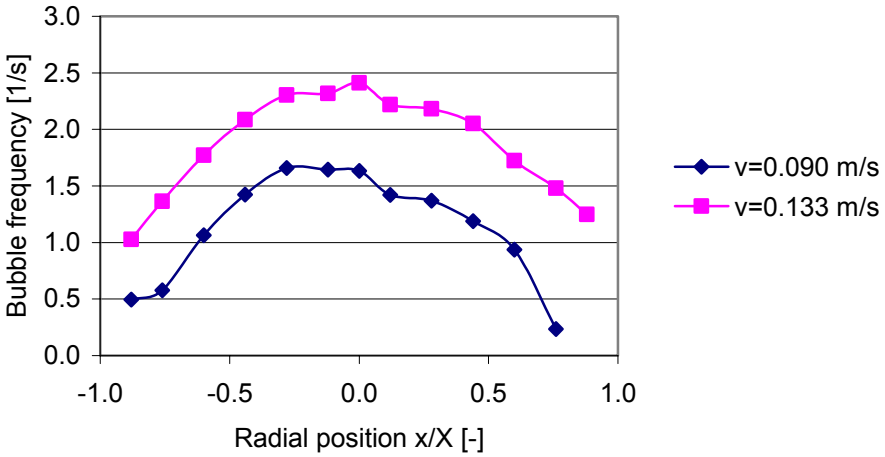

Figure 7.18: Comparison of bubble frequency at height 0.39 m for two superficial velocities.

Figure 7.19 shows the mean local bubble gas flow as a function of radial position at the three different heights in the bed. The superficial velocity is 0.133 m/s which gives an inserted gas flow of 0.0083 m^3/s. The total bubble gas flow is calculated to 0.0064 and 0.0079 m^3/s at height 0.55 m and 0.71 m respectively. This shows that the most of the inserted gas leaves the bed through the bubbles.

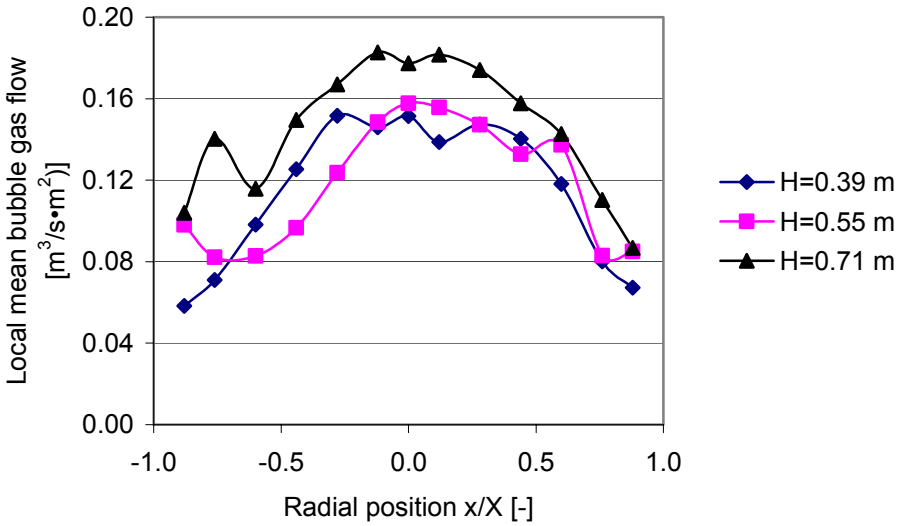

Figure 7.19: Local mean bubble gas flow as a function of radial position at different vertical positions. Superficial velocity is 0.133 m/s, small particles.

7.3.4 Pressure drop

In Figure 7.20 the mean pressure as a function of bed height is shown for different superficial velocities. The pressure drop over the bed for this powder is about 9 kPa for both superficial velocities. The standard deviation as a function of vertical position is shown in Figure 7.21. Whereas the mean pressure changed rather little with increased gas velocity, the standard deviation increases significantly with increasing gas velocity. The figure shows that the fluctuations change with height in the bed. The superficial velocity 0.09 m/s gives two peaks with a maximum of 0.20 and 0.13 kPa respectively. At superficial velocity 0.133 m/s the three peaks are observed and the maximum of these peaks are 0.35, 0.30 and 0.15 kPa respectively. The height of the peaks decreases with increasing height in the bed.

A spectral analysis is performed close to the air distributor and the results are shown in Figure 7.22. A high density of peaks is located at frequencies about 0.5 to 5 Hz. These peaks have high amplitudes and the frequencies are of the same magnitude as the bubble frequencies. The high frequent peaks located about 5 to 80 Hz are typically a result of numerical noise.

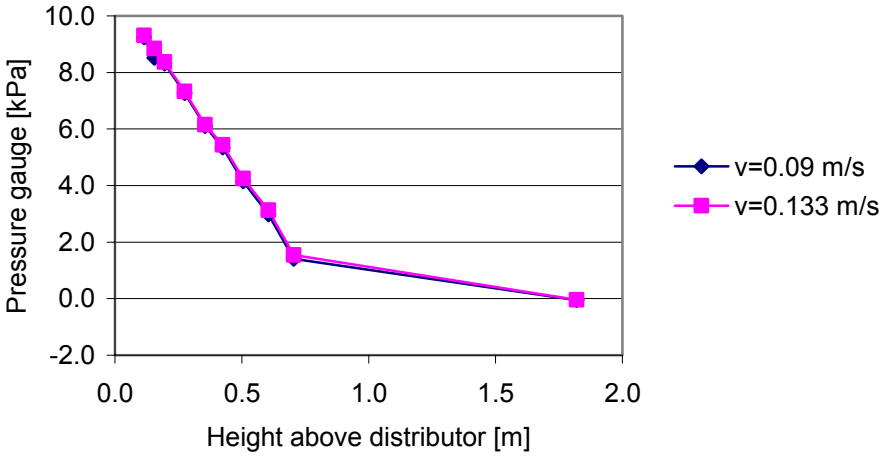

Figure7.20: Pressure gauge as a function of vertical position.

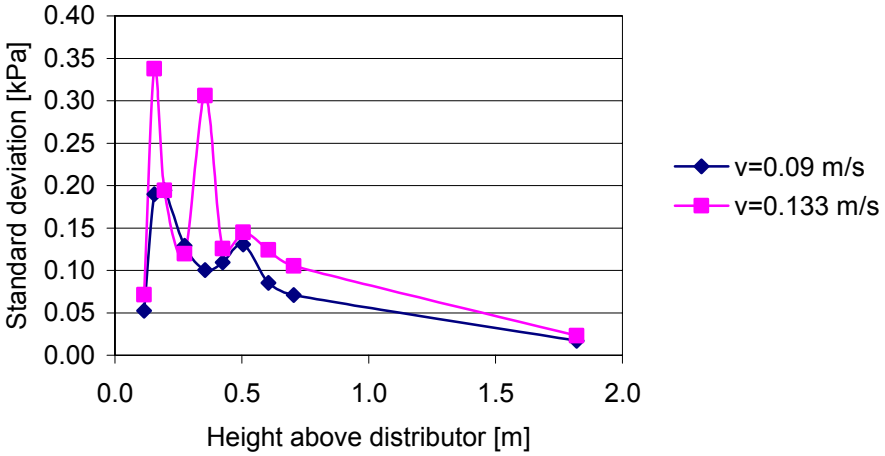

Figure7.21: Standard deviation as a function of vertical position.

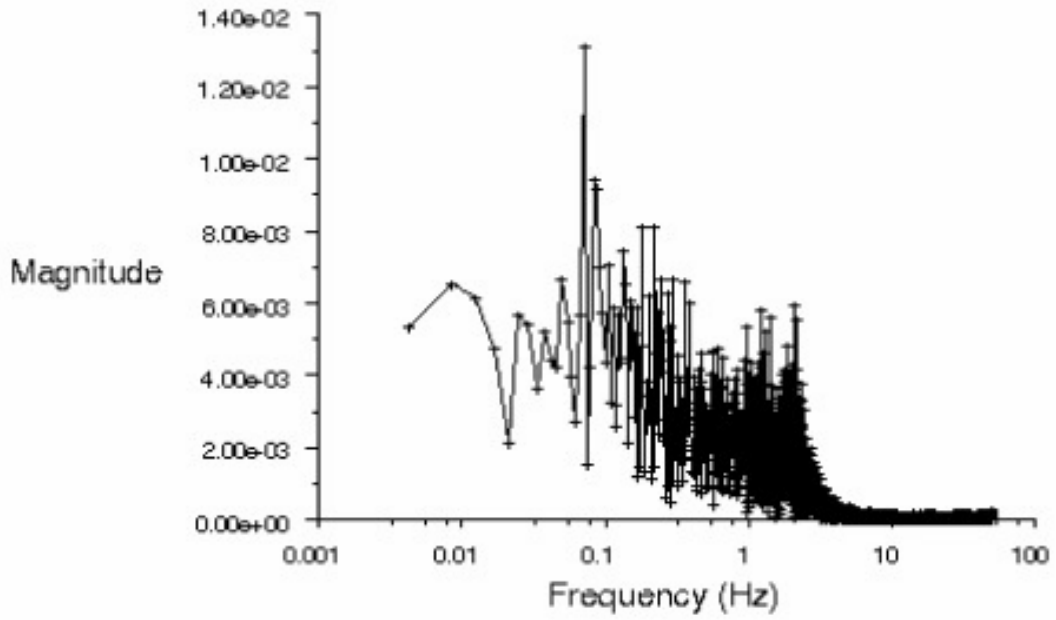

Figure 7.22: Spectral analysis of pressure measurements at height 0.115 m above the air distributor.

7.4 400-600 µm glass particles

When inserting air into the 400-600 µm powder the bed expands just minor. Bubbles did not appear at superficial velocities below about 0.20 m/s. The experiments are therefore performed with a superficial velocity of 0.21 m/s. The measurement system was not able to detect bubbles closer than 3 cm from the walls. In all the radial positions rather few bubbles are detected and validated for bubble velocity and size calculations. The experimental data are based on about 200-300 bubbles in centre 50-100 bubbles near the walls.

7.4.1 Bubble velocity

Bubble velocities as a function of radial position are presented in Figure 7.23. The bubble velocities at height 0.39 m are about 0.65 m/s in centre and decrease to 0.35 m/s towards the walls. At height 0.55 m the bubble velocities are about 0.8-0.9 m/s close to centre and about 0.5 m/s near the walls. The bubble velocities decrease from height 0.55 m to 0.71 m. The maximum bubble velocity at height 0.71 m is about 0.75 m/s and decreases towards the walls.

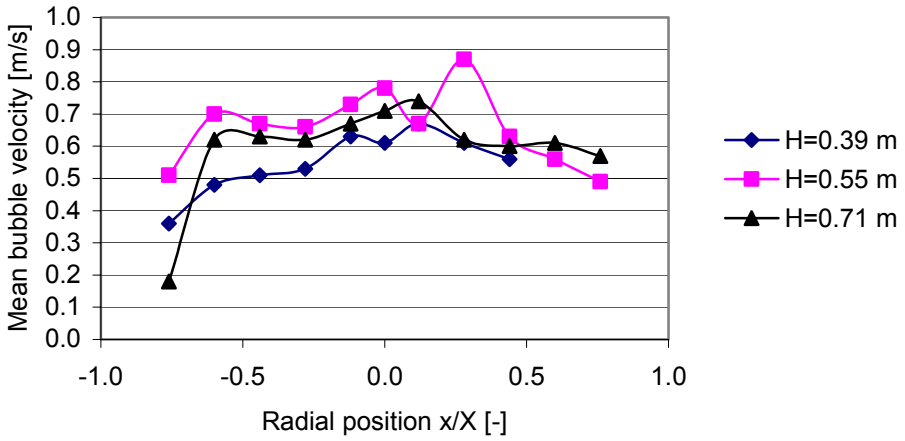

Figure 7.23: Bubble velocity as a function of radial position at different heights, v=0.21 m/s.

7.4.2 Bubble pierced length

Figure 7.24 shows the bubble pierced length as a function of bubble velocity. The experimental results are compared against the expression developed by Kunii and Levenspiel. The measurements are performed at radial position x/X=0 and at height 0.39 m. Also for this powder it can be seen from the experimental data that the bubble velocity increases with increasing bubble size. Very few bubbles have a velocity higher than 0.75 m/s. The experimental data agree rather well with the curve calculated from the equation of Kunii and Levenspiel (1991) for group B particles.

In Figure 7.25 the mean bubble pierced length as a function of radial position is shown at three vertical levels. The results from the experimental study of the large particle bed do not give a clear picture of how bubble size changes with radial and axial position. Visually it is observed that very few bubbles are rising near the walls. Rather few of the detected bubbles were validated for bubble velocity and bubble size calculations. The measuring time was 10 minutes for each radial position. Two additional experimental series are performed to try to get a more precise picture of the bubble behaviour. The results of those series are about the same as the first one, rather few bubbles are accepted for further calculations especially at radial positions near the walls. Figure 7.25 shows that the bubble length increases with increasing height in the bed in most of the radial positions. At height 0.55 m, the largest bubbles are located at each side of the centre.

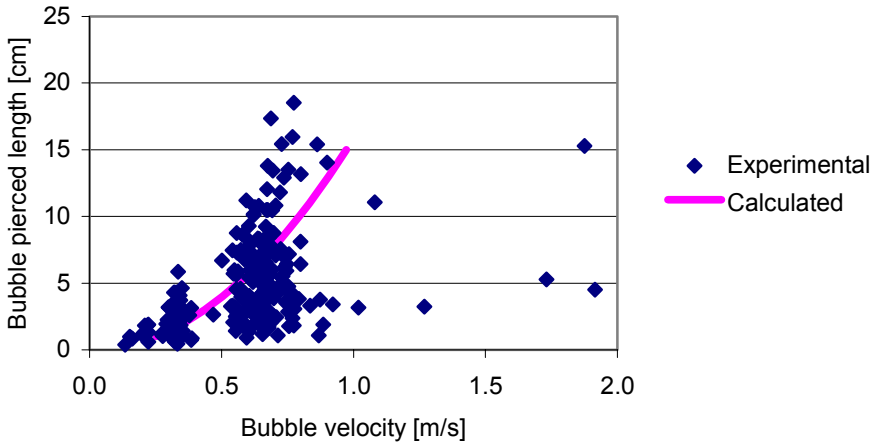

Figure 7.24: Bubble pierced length as a function of bubble velocity at height 0.39 m. The superficial velocity is 0.21 m/s.

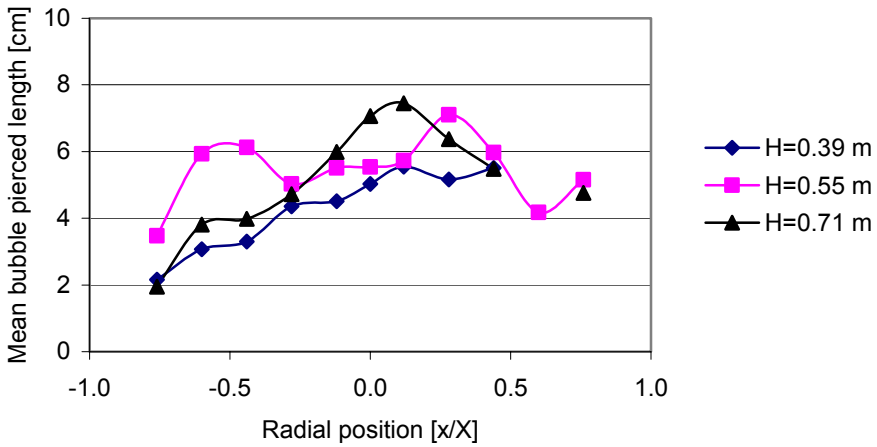

Figure 7.25: Mean bubble pierced length as a function of radial position at three different vertical positions. Superficial velocity is 0.21 m/s.

7.4.3 Bubble frequency

Figure 7.26 shows the bubble frequency profiles. At heights 0.55 m and 0.71 m the frequencies increase from the walls towards the centre. The frequency profiles at these two levels are rather flat, and they do not differ significantly from each other. Bubbles at these positions in the bed have a rather large horizontal diameter and it seems reasonable that the frequency profiles are flat.

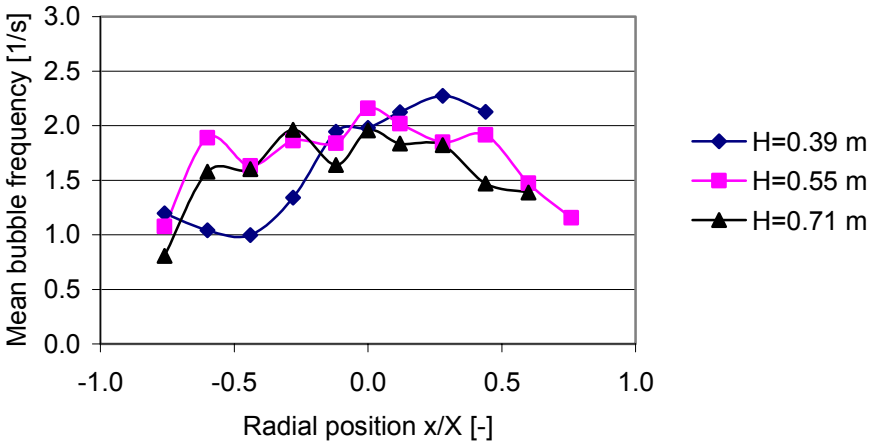

Figure 7.26: Bubble frequency as a function of radial position, superficial velocity 0.210 m/s.

Local mean bubble gas flow as a function of radial position is given in Figure 7.27. The inserted gas flow is 0.0131 m^3/s. The calculated mean bubble gas flow is 0.0045 and 0.0026 m^3/s at height 0.55 and 0.71 m respectively. This means that more than 60% of the total gas flow penetrates through the bed outside the bubbles. These experiments were performed with a low excess gas velocity, and the gas leaving in the bubbles are expected to be a rather small part of the inserted gas flow. It also seems like the bubble gas flow decreases with increasing height in the bed.

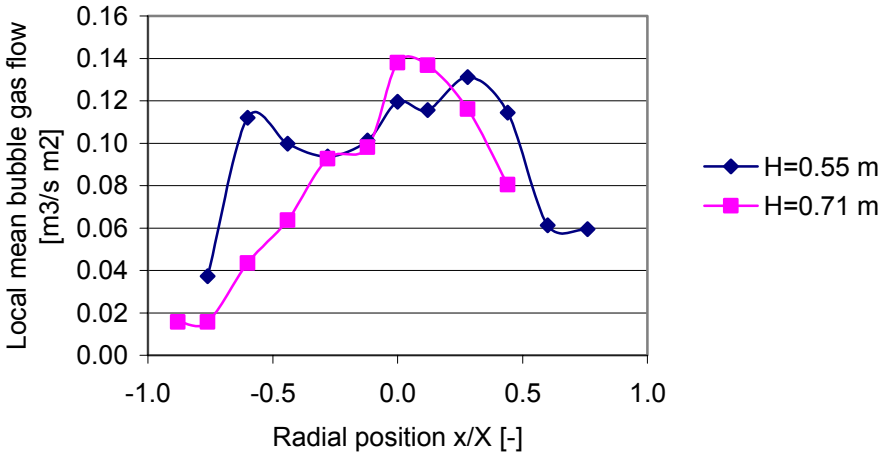

Figure 7.27: Local mean bubble gas flow as a function of radial position.

7.4.4 Pressure drop

Figures 7.28 and 7.29 show the pressure gauge and the pressure standard deviation as a function of vertical position respectively. The pressure drop over the bed is about 9.5 kPa. The pressure fluctuations, expressed as the standard deviation, change rather much with height in the bed. The standard deviation curve gives one wide peak which is located from about 0.155 m to about 0.710 m above the air distributor. The maximum of the peak is 0.30 kPa.

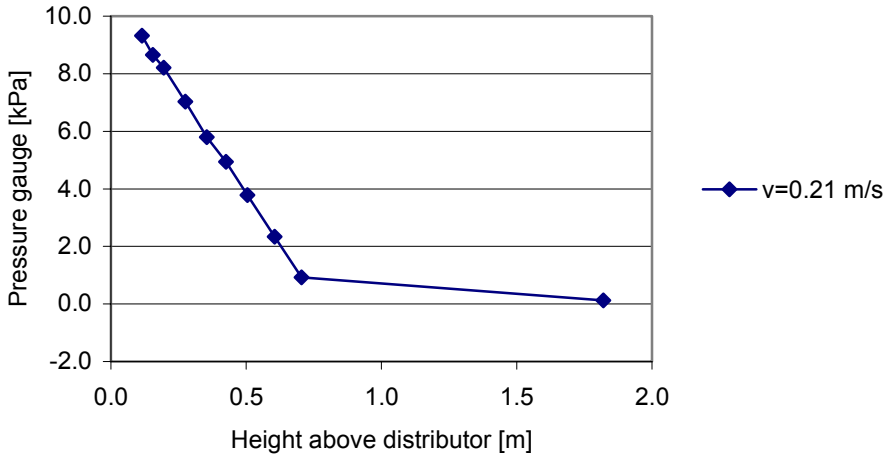

Figure 7.28: Pressure gauge as a function of vertical position.

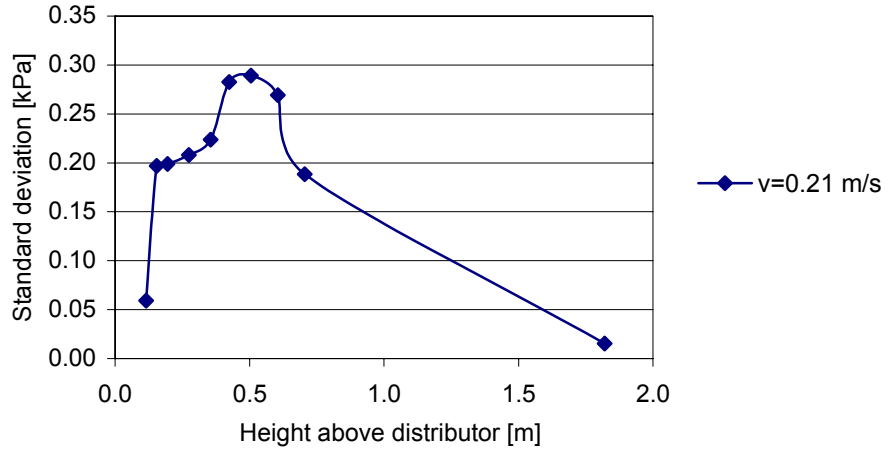

Figure 7.29: Pressure standard deviation as a function of vertical position.

7.5 Mixed glass particles

The mixed powder contains 50 volume % of the small particles and 50 volume % of the large particles. The bed was initially filled to 0.75 m, but when these two powders were completely mixed, the level in the bed decreased to 0.70 m, and had to be refilled. This indicates that the mixed powder has a lower void fraction than both the small particle powder and the large particle powder. According to Gera et al. (2004) a mixture of large and smaller spherical beads will have a maximum solid volume fraction greater than the maximum solid volume fraction of either of the particle types. Fedor and Landel (1979) proposed a maximum packing voidage for a binary mixture of two particle diameters as a function of mixture composition. The mixed powder seems to have about the same properties as the small particle powder. The minimum bubbling velocity turned out to be about 0.07 m/s and the bed expanded to about 0.82 m before bubbles appeared. These values are the same as for the small particle powder. The experiments with the mixed powder are therefore performed with the same superficial velocities as used in the experiments with the small particle powder.

7.5.1 Bubble velocity

Figure 7.30 shows the mean bubble velocities as a function of radial position at three different vertical positions. The superficial velocity is 0.09 m/s. At all the levels the bubble velocities increase considerably from the walls to the centre. At height 0.39 m the bubble velocity increases from 0.1 m/s near the walls to about 0.7 m/s in the centre. At heights 0.55 m and 0.71 m the velocities near the walls are about 0.4 m/s and increase to about 0.75 m/s near the centre. At height 0.55 m the velocity profile is almost symmetric around the centre axis. At height 0.39 m the highest velocity is displaced to the right side of the centre whereas at height 0.71 m the highest velocity is displaced to the left side of the centre.

Figure 7.31 shows the mean bubble velocities at three vertical levels when the superficial velocity is increased to 0.133 m/s. The bubble velocity profiles are more flat for this superficial velocity than for the lower one. At all the levels the bubble velocities increase from about 0.5 m/s near the walls to about 0.85 m/s towards the centre.

In Figure 7.32 the comparison between bubble velocities achieved at height 0.39 m with the superficial velocities 0.090 m/s and 0.133 m/s is shown. The bubble velocities increase significantly with increasing superficial velocity, especially towards the walls.

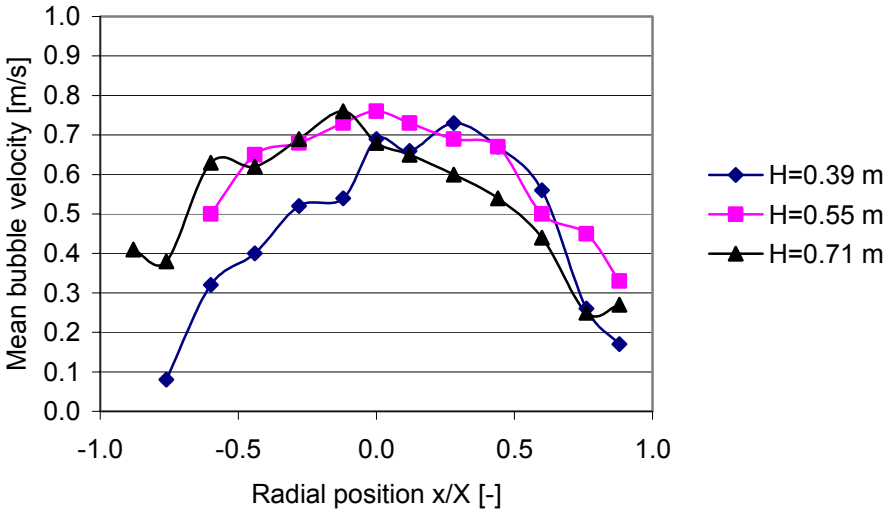

Figure 7.30: Mean bubble velocity as a function of radial position at three different vertical positions. Superficial velocity is 0.090 m/s.

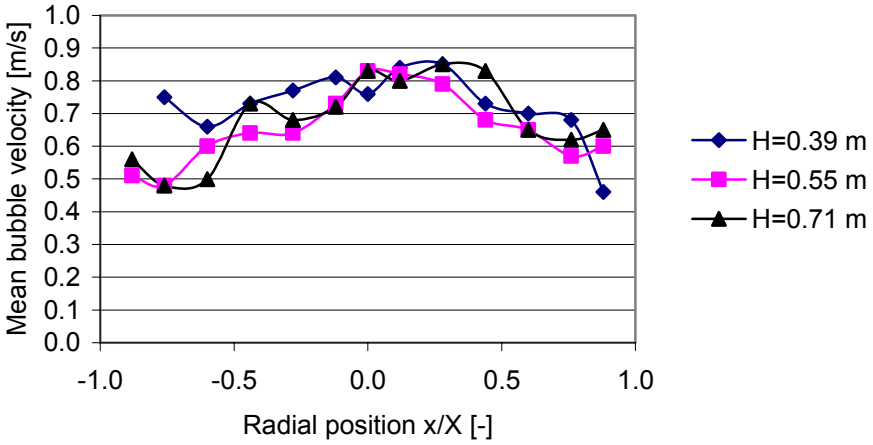

Figure 7.31: Mean bubble velocity as a function of radial position at three different vertical positions. Superficial velocity is 0.133 m/s.

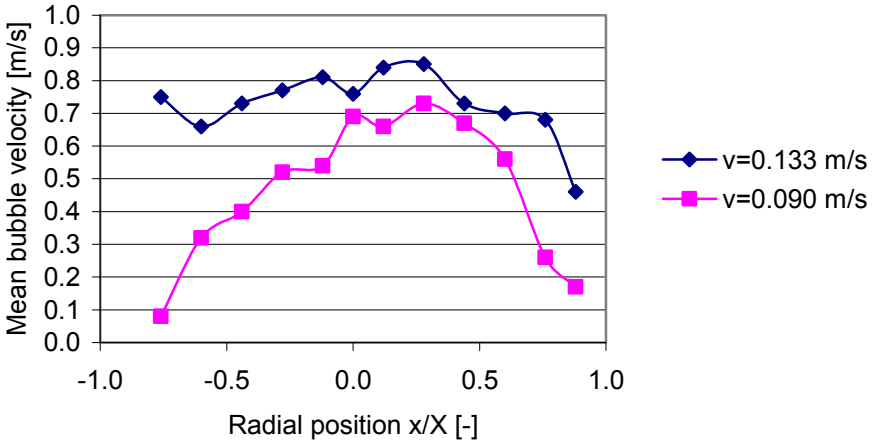

Figure 7.32: Comparison of mean bubble velocity for two different superficial velocities. The vertical position is 39 cm above the distributor.

7.5.2 Bubble pierced length

Figure 7.33 shows the bubble pierced length as a function of bubble velocity. The data are measured at height 0.39 m and in the centre of the bed. The superficial velocity is 0.090 m/s. The bubble velocities increase with increasing bubble length. Few of the bubbles are larger than 0.10 m. The experimental data is compared to the empirical equation developed by Kunii and Levenspiel (1991). The calculated curve for group B particles fits rather well to the experimental data for the smallest bubbles. For the larger bubbles the experimental results are located between the curves for group A and B particles. The same was observed for the small particles, and a possible explanation was that the small particles are classified as Geldart B particles but very close to Geldart A particles. The mixed powder has a mean particle size of 322 µm and a particle density of 2485 kg/m^3 and is very clearly classified as Geldart B particles. As mentioned above, the mixed powder behaves very much like the small particle powder and that the bulk density might influence the bubble behaviour rather much.

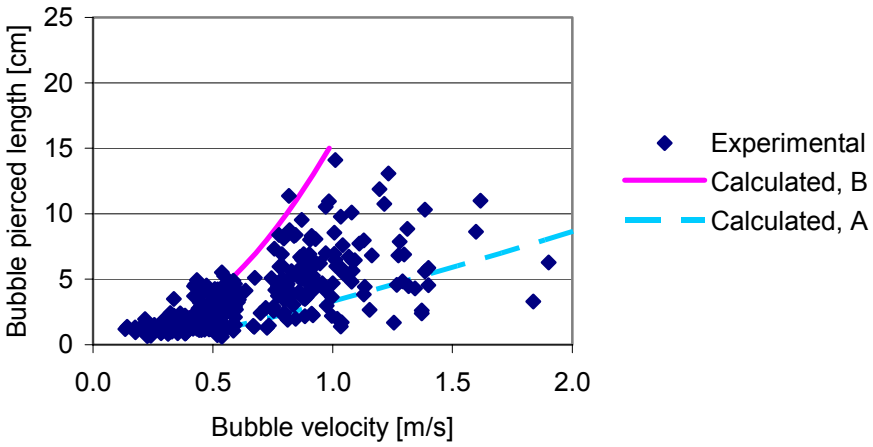

Figure 7.33: Bubble height as a function of bubble velocity at height 0.39 m and in centre of the bed. The superficial velocity is 0.09 m/s.

In Figure 7.34 the bubble pierced length as a function of radial position is shown for a superficial velocity of 0.090 m/s. It can be seen that the bubble size increases with increasing height in the bed. The experiments give rather smooth bubble height profiles and the profiles have about the same shape at all three levels. The smallest bubbles are measured near the walls and the bubble sizes increase towards the centre. The maximum bubble sizes are observed to the right of the centre. The mean bubble pierced length near the centre increases from about 5 cm at height 0.39 m to about 6 cm at height 0.71 m. Figure 7.35 shows the mean bubble pierced length as a function of radial position for superficial velocity 0.133 m/s. The bubble height profiles have different shapes at different levels, but the trend is increasing bubble size with increasing height in the bed. The maximum mean bubble size increases from about 7 cm at height 0.39 m to about 10 cm at height 0.71 m.

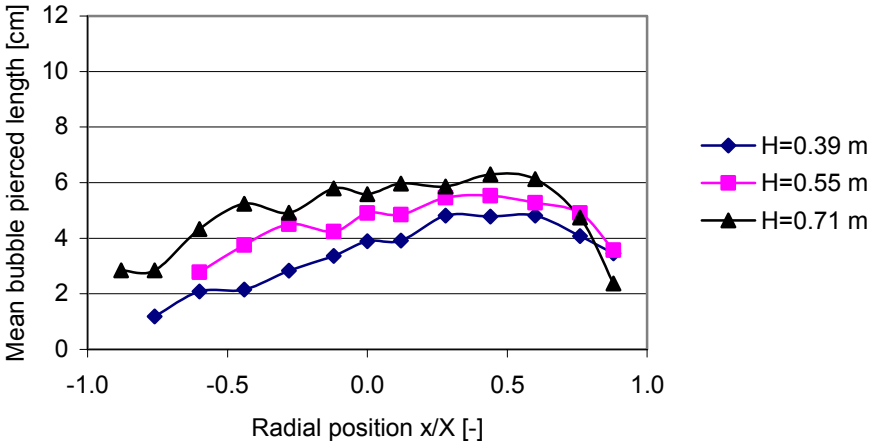

Figure 7.34: Mean bubble pierced length as a function of radial position at three different vertical positions. Superficial velocity is 0.09 m/s.

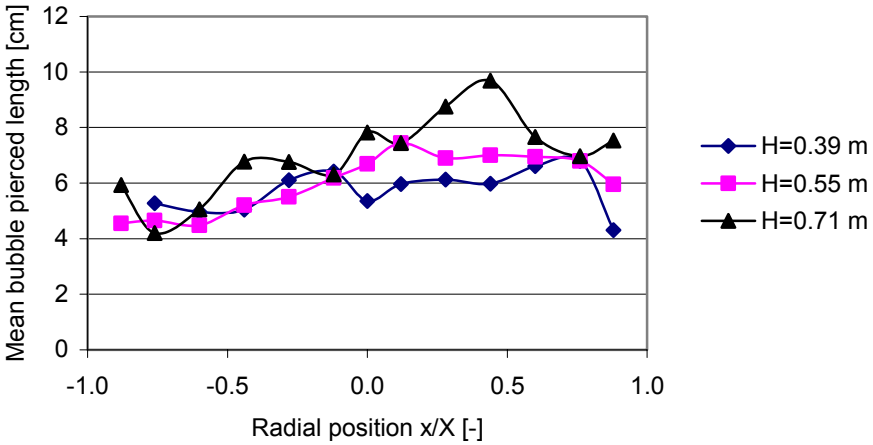

Figure 7.35: Mean bubble pierced length as a function of radial position at three different vertical positions. Superficial velocity is 0.133 m/s.

A comparison of mean bubble pierced length as a function of radial position for two superficial velocities is shown in Figure 7.36. The data are obtained from height 0.39 m. It can be seen that the mean bubble size increases significantly with increasing gas velocity at all radial positions.

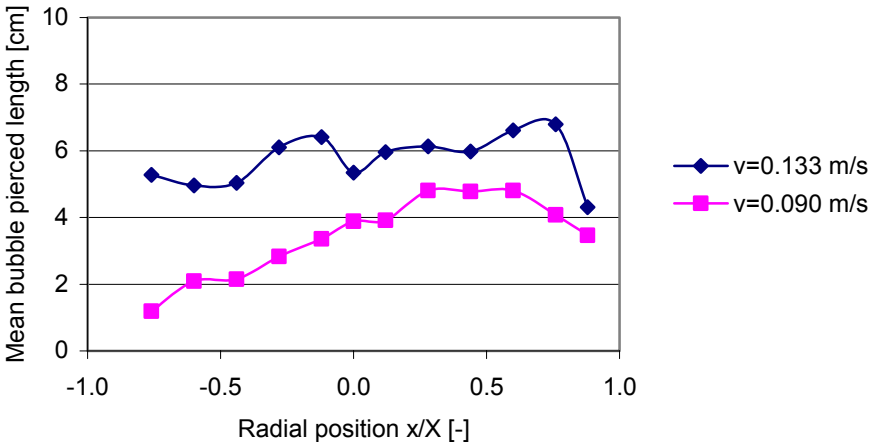

Figure 7.36: Comparison of mean bubble height at height 0.39 m for superficial velocity 0.090 m/s and 0.133 m/s.

7.5.3 Bubble frequency

Bubble frequency profiles for superficial gas velocity 0.090 m/s can be seen in Figure 7.37. The bubble frequencies are lowest near the walls and increase towards the centre. This is the case at heights 0.55 m and 0.71 m. At height 0.39 m the bubble frequency is somewhat lower in the centre than in the nearby regions. This indicates that most of the bubbles have not reached the centre line at this height in the bed. The bubble frequency is highest at level

height 0.55 m and lowest at level height 0.39 m. Bubble frequencies change rather little with radial position at height 0.71 m. At this level the frequency is about 1 near the wall and about 1.7 in the centre. In Figure 7.38 the bubble frequency profiles at gas velocity 0.133 m/s are shown. The frequency profiles at heights 0.55 m and 0.71 m differ rather little from each other. The bubble frequencies at height 0.39 m are somewhat lower than at the other levels at most of the radial positions.

A comparison of the bubble frequency at height 0.39 m for the two gas velocities is performed in Figure 7.39. There is no significant difference between the two profiles. This is also the case at height 0.71 m. At height 0.55 m the profiles differ somewhat more from each other, and the highest bubble frequencies are observed at the superficial gas velocity 0.090 m/s. This can be seen by comparing Figure 7.37 and 7.38.

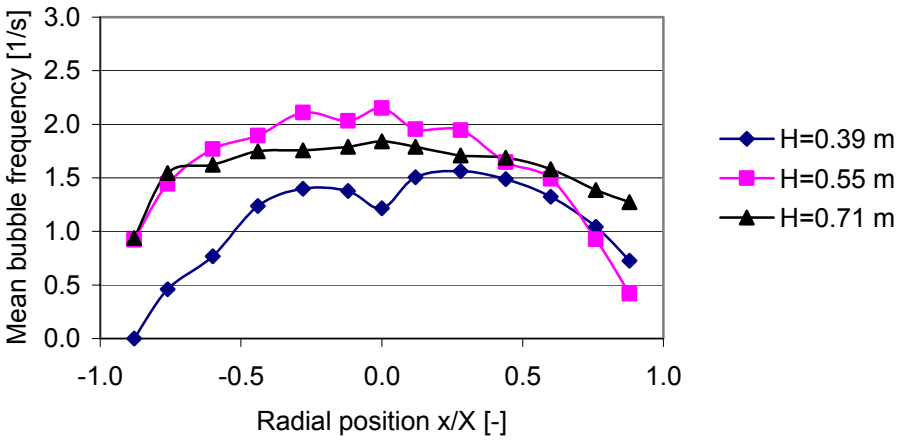

Figure 7.37: Bubble frequency as a function of radial position, superficial velocity 0.090 m/s.

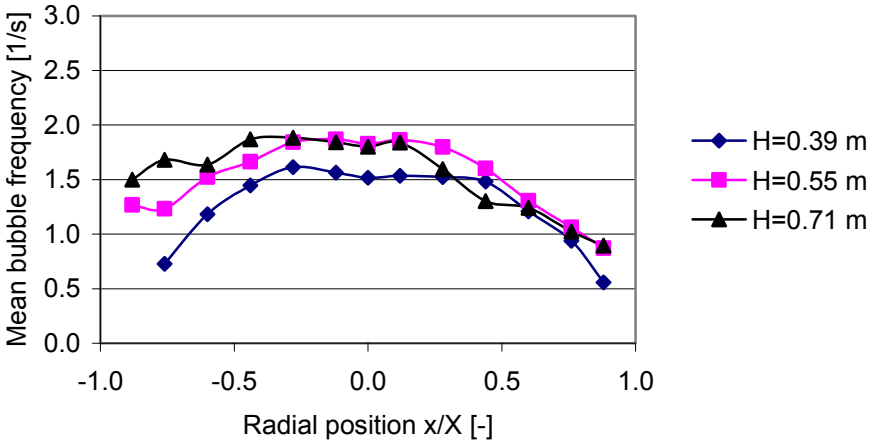

Figure 7.38: Bubble frequency as a function of radial position, superficial velocity 0.133 m/s.

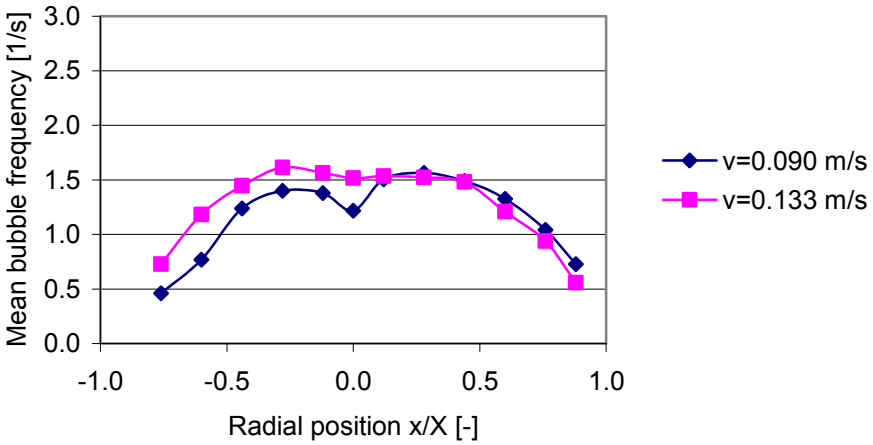

Figure 7.39: Comparison of bubble frequency for two superficial velocities at height 0.39 m.

Figure 7.40 shows the mean local bubble gas flow as a function of radial position at the three different heights in the bed. The superficial velocity is 0.133 m/s and the inserted gas flow is 0.0083 m^3/s. The total bubble gas flow is 0.0047 and 0.0055 m^3/s at height 0.55 m and 0.71 m respectively. The ratio between the bubble gas flow and the total inserted gas flow is 57% at height 0.55 m and 70% at height 0.71 m.

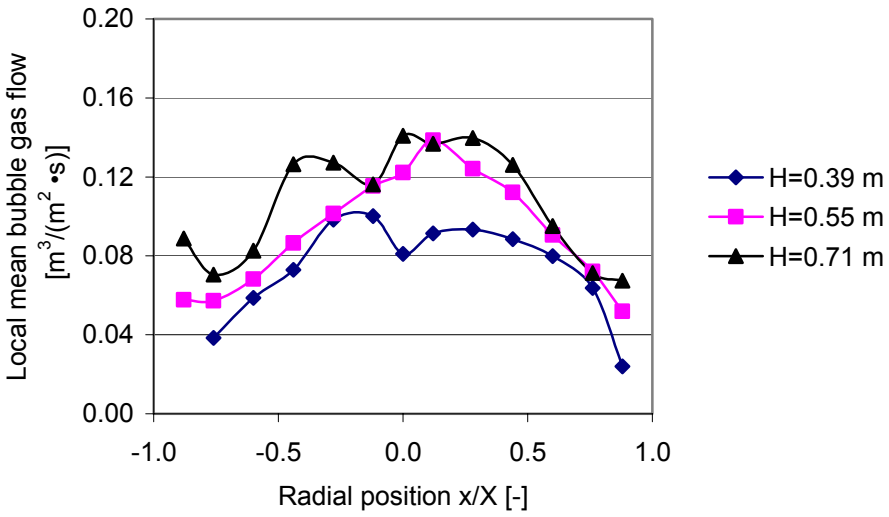

Figure 7.40: Local mean bubble gas flow as a function of radial position at different vertical positions. Superficial velocity is 0.133 m/s.

7.5.4 Pressure drop

Figure 7.41 shows the pressure gauge as a function of vertical position. The pressure drop is about 10.5 kPa and 11 kPa for the superficial velocities 0.090 m/s and 0.133 m/s respectively. The pressure standard deviation as a function of vertical position is shown in Figure 7.42. The standard deviation curves have the same shape for the two different velocities, but the standard deviation increases significantly with increasing superficial velocity. It can also be seen that the pressure fluctuations change with height in the bed. The highest fluctuations can be observed at height 0.115 m above the air distributor. The pressure fluctuations give three peaks. The maximum of the peaks are 0.16, 0.13 and 0.11 kPa for the lowest superficial velocity and 0.29, 0.23 and 0.19 kPa for the highest superficial velocity.

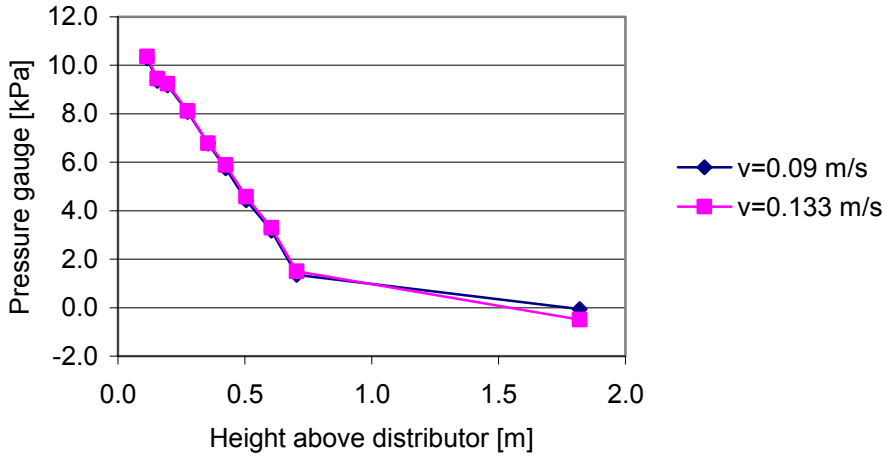

Figure 7.41: Pressure gauge as a function of vertical position.

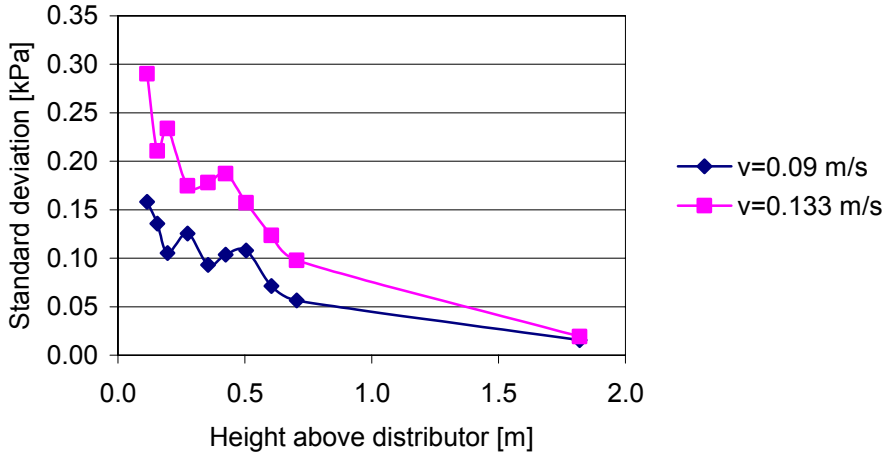

Figure 7.42: Pressure standard deviation as a function of vertical position.

7.6 Discussion

The difference between the small particle powder, the large particle powder and the mixed powder is the particle size distribution, and as a consequence of that also the bulk density of the settled bed. Particle size, particle size distribution, bulk density and excess gas velocity influence the flow behaviour in a bubbling bed.

7.6.1 Bubble velocity

The mixed powder has about the same fluidization velocity as the small particle powder. The small particle powder and the mixed powder beds also expand to about the same height before bubbles start to appear. The large particle powder, on the other hand, expands insignificantly before bubbles appear and bubbles are not created until the superficial velocity exceeded about 0.20 m/s.

Figure 7.43 shows a comparison between the bubble velocity profiles for the three powders. The comparison is performed at height 0.39 m and the superficial velocities are 0.133 m/s for the mixed and the small particle powders, and 0.210 m/s for the large particle powder. At this height the bubble velocities differ significantly for the three powders. The mixed powder gives the highest bubble velocities and the large particle powder gives the lowest bubble velocities. Higher up in the bed the differences in velocities are not so significant, but the trend is that the large particle powder gives the lowest velocities. Bubble velocities depend on excess air velocity, classification of powder and also the bulk density. The excess air velocity used for the large particles was low, and that can explain the relatively low bubble velocities. For the two other powders the same superficial velocities were used, and it could be expected that the smallest particles would give the highest bubble velocities. This was not the case, and that indicates that the particle size distribution and the bulk density influence the bubble velocities.

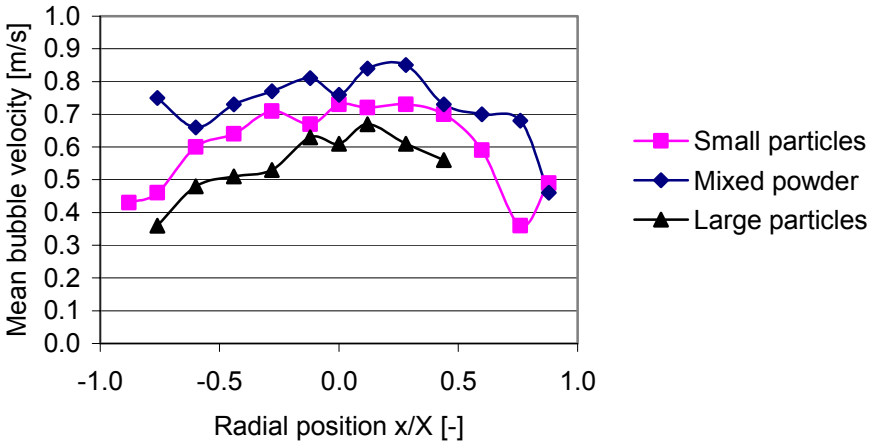

Figure 7.43: Comparison of bubble velocity profiles at height 0.39 m for the three different powders. The superficial velocity is 0.133 m/s for the small and the mixed particles and 0.210 for the large particles.

7.6.2 Bubble pierced length

Figure 7.44 shows a comparison between the bubble size profiles for the three different powders. The comparison is performed at height 0.39 m and the superficial velocities are 0.133 m/s for the small particle powder and the mixed powder, and 0.210 m/s for the large particle powder. The experimental results show that the mean bubble size for the small particles and the mixed powder differs rather little from each other in most of the radial positions. The small particle powder gives insignificantly larger bubbles. The experiment with the large particle powder gives significantly smaller bubbles than the two others. According to earlier experimental results and theory on bubble behaviour in fluidized beds, bubble sizes are expected to increase with increasing particle size. The bubble size also increases with increasing excess gas velocity. Excess gas velocity is defined as the difference between the superficial velocity and the minimum fluidization velocity. The large particle powder started to fluidize at a superficial velocity about 0.20 m/s. Minimum fluidization velocity can be calculated from the Ergun equation, and for particles with diameter 480 μm the minimum fluidization velocity is 0.19 m/s. This means that the excess gas velocity for the experiments with large particle powder is low, about 0.01-0.02 m/s. This might explain the rather low mean bubble pierced length for this powder. The calculated minimum fluidization velocities for the particles with diameter 154 μm and 322 μm are 0.019 m/s and 0.085 m/s respectively, and the excess gas velocity for these powders are higher. At equal bed heights and equal excess gas velocities, the bubble sizes are almost independent of particle size for group B particles, Gidaspow (1994). The fluidization velocities, however, do not depend on the mean particle diameter but on the particle size distribution and the bulk density. This is shown from the experimental study of the mixed powder. It is therefore reasonable that the bubbles obtained from the mixed powder have about the same mean bubble pierced length as the bubbles measured in the small particle bed.

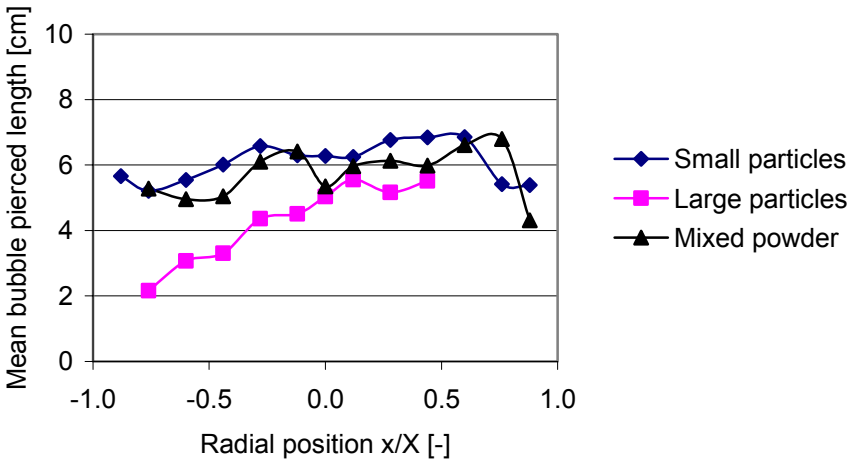

Figure 7.44: Comparison of bubble pierced length at height 0.39 m for different powders. Superficial velocity is 0.210 m/s for the large particle powder and 0.133 m/s for the two other powders.

Figure 7.45 shows photographs of bubbles at the wall for the three different powders. The superficial velocities are 0.133 m/s and 0.210 m/s. It is obvious that the different powders give rather different bubble shapes. The smallest particles and the mixed powder adhered to the wall which made it difficult to get clear photographs. It can however be seen that the small particles give rather irregular bubble shapes. This may be due to the rather high excess gas velocity. The mixed powder gives more rounded bubbles and the bubble seems to move rather diagonal upwards in the bed. The large particle bubble is regular and has a ratio between bubble diameter and bubble height of about two. The bubble seems to move in a straight vertical line towards the top of the bed. These photographs are only examples used to study the shapes of the bubbles. The photos from the small particles and the mixed powder are taken from height about 0.30 m whereas the photos of the large particles are taken near the top of the bed. The bubbles can vary very much in size for all the powders. The pictures of the bubbles show that particles are drawn upwards within the bubbles. This can disturb the measurement of bubble pierced length and can be a source of error in the measurements. In Figure 7.46 photos of bubbles in the small particle bed are shown. A high speed camera has been used to photograph these bubbles.

a. Small particle powder

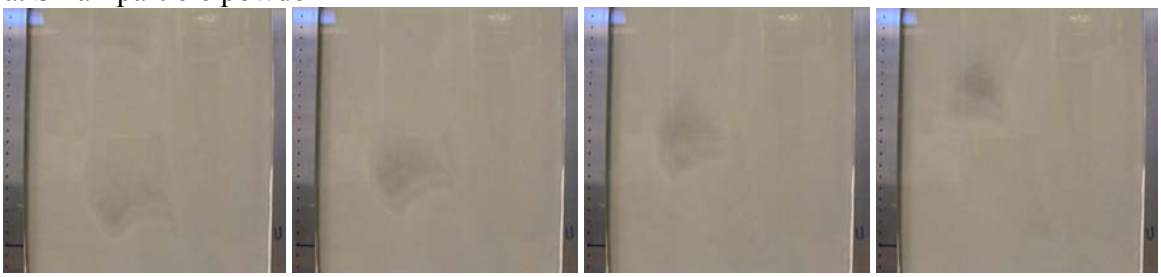

b. Mixed powder

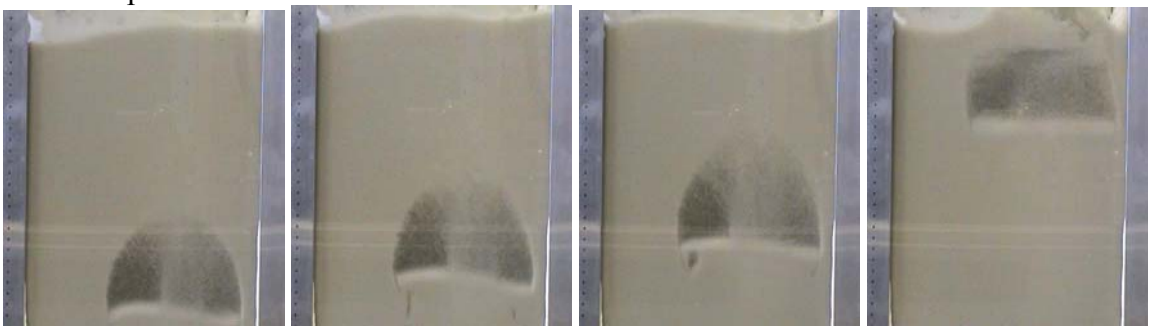

c. Large particle powder

Figure 7.45: Photographs of bubbles obtained by a) small particles and superficial velocity 0.133 m/s, b) mixed powder and superficial velocity 0.133 m/s and c) large particles and superficial velocity 0.210 m/s.

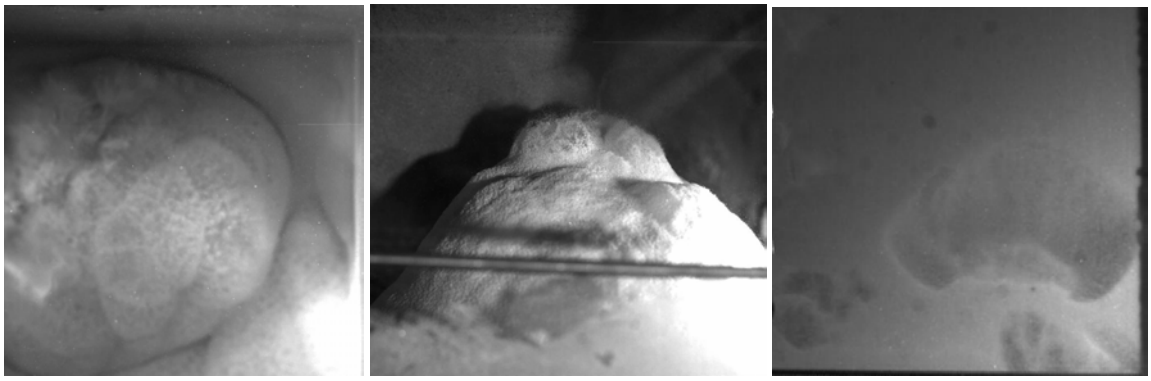

a. b. c.

Figure 7.46: Bubbles obtained from experiment with small particle powder. a) Bubble seen from the top of the bed. b) Bubble seen from the side at the top of the bed. c) Bubble seen from the side low in the bed. The superficial velocity is 0.133 m/s.

7.6.3 Bubble frequency and mean bubble gas flow

The most significant differences in frequencies between the small particle powder and the mixed powder are found at height 0.39 m for both the superficial velocities. For the lowest superficial velocity the frequency profiles also differ significantly from each other on the other levels. Comparison of frequency profiles for the higher superficial velocity shows that the bubble frequency for small particle powder and the mixed powder differs little from each other at height 0.55 m and 0.71 m. In Figure 7.47 a comparison at height 0.39 m is performed for superficial velocity 0.133 m/s. The large particle powder has about the same bubble frequency as the two other powders at height 0.55 m and 0.71 m. It has evidently to be taken into consideration that a higher superficial velocity is used in the experiments with the large particle powder.

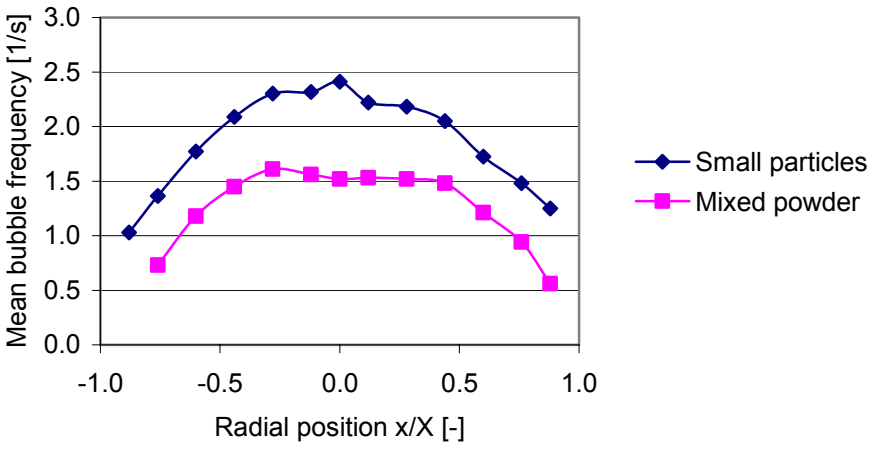

Figure 7.47: Comparison of bubble frequencies for the small particle powder and the mixed powder at height 0.39 m. The superficial velocity is 0.133 m/s.

The total bubble gas flow is calculated for the three powders. These calculations are performed to find the part of the total inserted gas flow that leaves the bed within the bubbles. Table 7.2 gives the values of the bubble gas flow for the three powders at heights 0.55 m and 0.71 m. The experiments with the small particles and the mixed powder show that most of the inserted gas flow leaves within the bubbles, and that the bubble flow increases with increasing height of the bed. This is not the case for the large particles. For this powder more than 60 % of the total gas flow penetrates through the bed outside the bubbles. For the large particles it also seems like the bubble gas flow decreases with increasing height in the bed. The gas leaving in the bubbles are expected to increase with increasing excess gas velocity.

Table 7.2: Bubble gas flow and total gas flow.

	Small particles		Large particles		Mixed powder	
Height above air distributor	0.55 m	0.71 m	0.55 m	0.71 m	0.55 m	0.71 m
Total bubble gas flow [m^3/s]	0.0064	0.0079	0.0045	0.0026	0.0047	0.0058
Total gas flow inserted [m^3/s]	0.0083	0.0083	0.0131	0.0131	0.0083	0.0083
Gas leaving with the bubbles in % of the inserted gas flow [%]	77	95	34	20	57	70

7.6.4 Pressure drop

Pressure drop increases with increasing drag. The drag increases with decreasing void fraction, decreasing particle diameter and increasing superficial velocity. The mixed powder has the highest pressure drop over the bed. The pressure drop for this powder is about 10.5 and 11 kPa at superficial gas velocity 0.09 and 0.133 m/s respectively. The small particle powder has a pressure drop of about 9 kPa at both the superficial velocity. The experiment with the large particles gives about the same total pressure drop over the bed as the small particles, but the pressure curve of the large particle bed is a somewhat steeper in parts of the bed. This is due to the difference in bed expansion for these two powders. The superficial velocity for the large particles is higher than for the other powders, and this will influence on the pressure drop. The mixed powder has the lowest minimum void fraction and the highest pressure drop over the bed. Figure 7.48 shows a comparison of the mean pressure gauge as a function of bed height for the three different powders. The superficial velocities are 0.133 m/s for the small particles and the mixed powder and 0.21 m/s for the large particles.

In Figure 7.49 a comparison of the pressure standard deviation is shown. It can be seen that significant pressure fluctuations are observed for all the powders, but the peaks differ in shape, size and location for the three powders. The standard deviation curve for the large particles differs much from the two other powders. The reason for the wide peak of large fluctuation may be the low bed expansion for this powder.

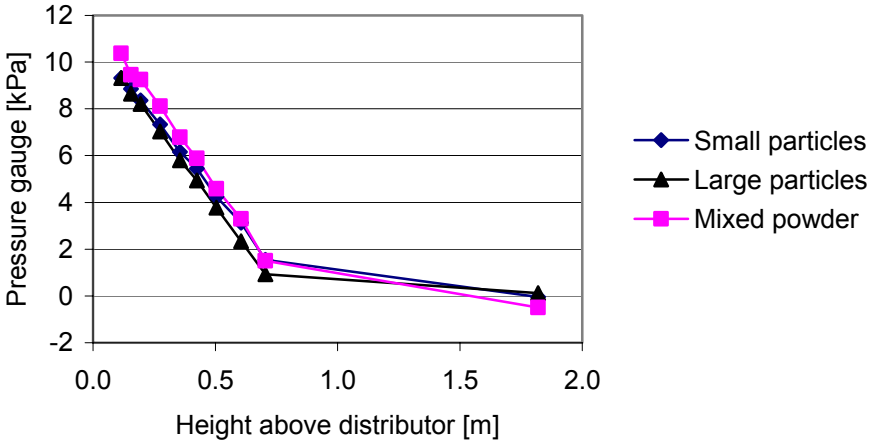

Figure 7.48: Pressure as a function of vertical position, superficial velocities 0.133 m/s and 0.21 m/s.

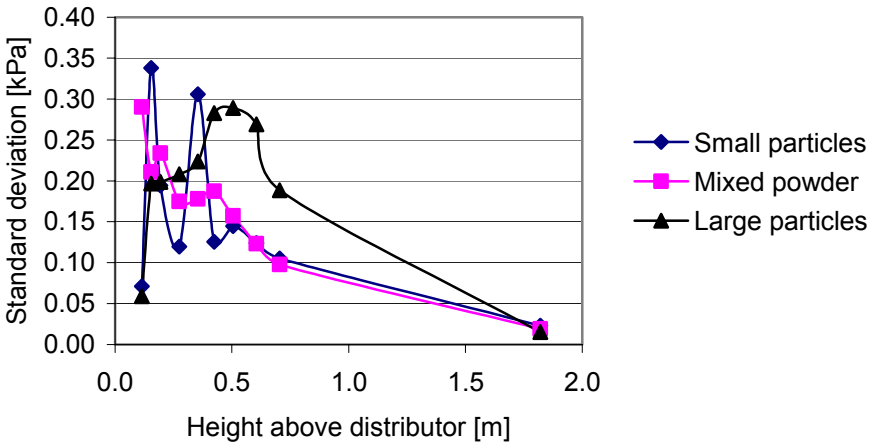

Figure 7.49: Standard deviation as a function of vertical position, superficial velocities 0.133 m/s and 0.210 m/s.

7.7 Summary

A lab-scale fluidized bed with cross-section area 0.25x0.25 m^2 and height 2.0 m has been constructed and built. Experiments are performed using spherical glass particles with three different particle size distributions. The mean particle diameters for these three powders are 154 μm, 322 μm and 480 μm, respectively. The initial bed height is 0.75 m in all the experiments. The particle sizes for the small particle powder and the large particle powder are 100-200 μm and 400-600 μm respectively. The powder with mean particle diameter of 322 μm is a mix containing of 50 volume % of each of the two other powders. It is found that the mixed powder attained a bulk density higher than the two other powders. This agrees well with observations performed by Fedor and Landel (1979) and Gera (2004). It was found that the mixed powder has about equal properties to the powder with the smallest particle sizes.

Bubble velocities, bubble pierced length and bubble frequencies are measured at heights 0.39 m, 0.55 m and 0.71 m above the air distributor. For all the three powders, the bubble velocities increase from height 0.39m to 0.55 m, and decrease a little from 0.55 m to 0.71 m. Mean bubble pierced length increase with height in the bed. The reduction in bubble velocities from height 0.55 m to 0.71 m may be due to increasing wall effects when the bubble sizes increase.

Bubble size as a function of bubble velocity is compared to empirical equations. The comparisons show that the small particle powder and the mixed powder give results somewhere between the empirical equation for Geldart A and Geldart B particles. The large particle powder gives a good agreement with the equation for Geldart B particles.

Bubble frequency increases from wall towards the centre of the bed. The small particle powder gives a higher bubble frequency than the mixed powder especially for superficial velocity 0.09 m/s. Bubble velocities, bubble pierced length and bubble frequency increase with increasing superficial velocity in all radial positions.

The total bubble gas flow is calculated from local mean bubble gas flow times the area. The total bubble gas flow at height 0.55 m and 0.71 m is compared to the total inserted gas flow, and it is found that for the small particle powder and the mixed powder most of inserted gas leaves within the bubbles. For the large particle powder most of the inserted gas penetrates through the bed outside the bubbles.

Pressure is measured at ten levels in the bed. The pressure drop over the particle bed is highest for the mixed powder and lowest for the large particle powder. The mixed powder has the highest bulk density and the highest specific particle area. The drag increases with specific area and increasing drag gives increasing pressure drop.

8. Computational validation and study of 3-D bubbling bed

A computational study of a 3-D bubbling bed is performed. In this chapter the results from the computational study are presented and compared to experimental results presented in Chapter 7. In addition to bubble velocity, bubble pierced length, bubble frequency and pressure drop the computational study also includes gas velocity, particle velocity and void fraction calculations. These parameters can not be compared directly to the experimental data, but the parameters can be used to explain some of the discrepancies in bubble behaviour obtained in the different simulations. This will give an indication about which of the simulated cases that give the most realistic results with respect to the experimental data and observations.

8.1 Computational set-up and conditions

A three-dimensional Cartesian co-ordinate system is used to describe the fluidized bed. The grid is uniform in all direction. Computational set-up is given in Table 8.1. Simulations with glass particles have been run with both one and multiple solid phases in order to study the particle size distribution's influence on calculated bubble behaviour.

The experimental set-up has a height of 2.0 m and an initial particle height of 0.75 m. This work is focused on the flow behaviour in the dense bed, and in order to reduce the computer time the computational set-up has a height of 1.2 m.

The simulated bubbles are defined as void fractions higher than 0.65. This definition is used because it is observed from the experiments that parts of the bubbles can include high fractions of solids. Also from the simulations with the two dimensional bed (Chapter 5) it was observed that in the periphery of the bubbles the particle concentration is about 0.35. Another reason for using a rather low void fraction in the definition of bubbles is that bubbles might occupy only a part of the control volume, and the mean void fraction for the control volume will then be lower than the void fraction in a bubble but significantly higher than the mean void fraction in the bed. A disadvantage of using void fraction 0.65 is that the code may detect too many small bubbles.

Bubbling fluidized beds need rather long time to obtain quasi-steady state. In the cases applied in this work, the bubble frequency has been 1-3 bubbles per second. In the experimental study bubble velocity, bubble pierced length and bubble frequency were averaged over 10 or 20 minutes. In the computational study the results are averaged over 20 or 30 seconds due to long computational simulation time. The bubbles vary much in size and velocities, and when the simulation time is short this may influence the mean values of bubble behaviour rather much and cause discrepancies between simulations and experiments.

In Chapter 5 simulations with glass particles in a two dimensional bed were performed with three different drag models. It was shown that Ergun's drag model gave the most realistic bubble velocities and that Gibilaro's drag model gave the best agreement with the experiments regarding bubble size and bed expansion. In the simulations of the three dimensional bed the Ergun drag model is used as default, but in some cases the Gibilaro drag model is used.

Table 8.1: Computational set-up

Bed design:			
Height: Cross section area: Initial bed height:	1.2 m (0.25x0.25) m^2 0.75 m		
One phase Particle mean diameter:	Small particles 154 μm	Mixed powder 322 μm	Large particles 480 μm
Two phases			
Particle distribution:		154 μm (50 %) 480 μm (50%)	
Three phases			
Particle distribution:		122 μm (24.7%) 250 μm (36.2%) 514 μm (39.1%)	
Superficial gas velocity:	0.090 m/s 0.133 m/s	0.090 m/s 0.133 m/s	0.210 m/s
Grid resolution: Horizontal grid size Vertical grid size	 10.0 mm 10.0 mm		
Initial conditions: Gas phase shear viscosity Initial void fraction Max. volume fraction of solids Freeboard pressure Solid density Gas density	 $1.8 \cdot 10^{-5}$ Pa·s 0.60 0.64356 101325.0 Pa 2485 kg/m^3 1.2 kg/m^3		

In the experimental work it was observed that bubbles in a fluidized bed can vary significantly in size and shape. Figure 8.1 shows a plot of computational bubble pierced length as a function of bubble velocity. The simulation is performed with small particles, superficial velocity 0.133 m/s and Ergun's drag model. The corresponding experimental case is shown in Figure 8.2. The computational bubble pierced length varies from 1 cm to 20 cm and about half of the bubbles have a pierced length equal to or lower than 5 cm. The size of the experimental bubbles is also concentrated around 1 to 20 cm, but for the experimental bubbles a higher part of the bubbles have a pierced length higher than 5 cm. The simulation time is 30 seconds whereas the experimental time is 10 minutes for the corresponding case. The bubble size distribution and the mean bubble pierced length may change if simulation time is increased.

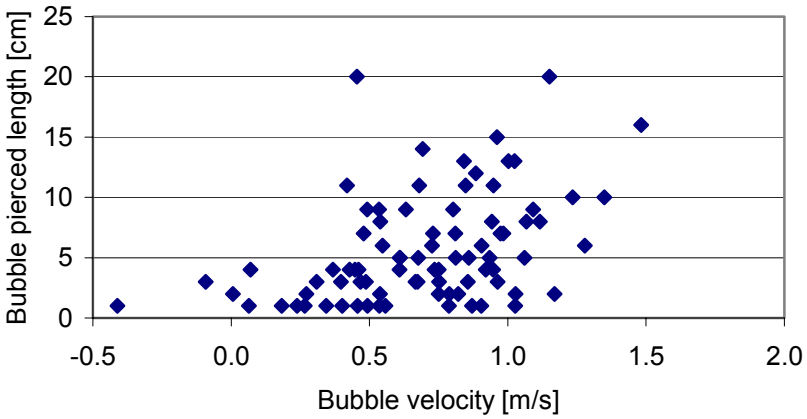

Figure 8.1: Computational bubble pierced length as a function of bubble velocity. Superficial velocity is 0.133 m/s, particle diameter 100-200 µm.

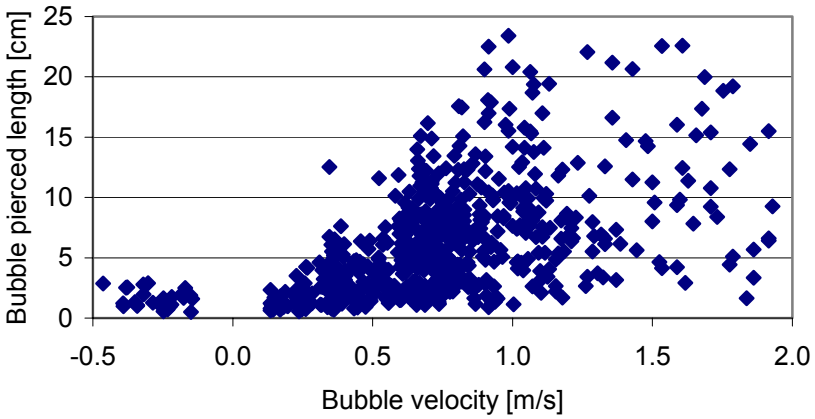

Figure 8.2: Experimental bubble pierced length as a function of bubble velocity. Superficial velocity is 0.133 m/s, particle diameter 100-200 µm.

8.2 100-200 µm glass particles

The particle size distribution of this powder is given in Chapter 7, and the mean particle size is 154 µm. The simulation time is 30 s, and the simulations are performed with one particle phase. The comparisons between experimental and computational results are performed at heights 0.39 m, 0.55 m and 0.71 m above the air distributor.

8.2.1 Bubble velocity

In Figure 8.3 the comparisons of computational and experimental results for superficial gas velocity 0.09 m/s are shown. The simulations are performed with Erguns drag model and a 'switch' to plastic regime. The results show that there is good agreement between computational and experimental bubble velocities, but at all levels the computational velocities are somewhat lower than the experimental velocities. The computational velocities do not give a smooth curve. This indicates that the simulation time might be too short for

registration of bubble behaviour. However, 3-D simulation is very CPU sensitive. The figure also shows that the computational bubble velocities increase from height 0.39 m to 0.55 m and decrease again between height 0.55 m and 0.71 m. The same trend is also observed from the experiments.

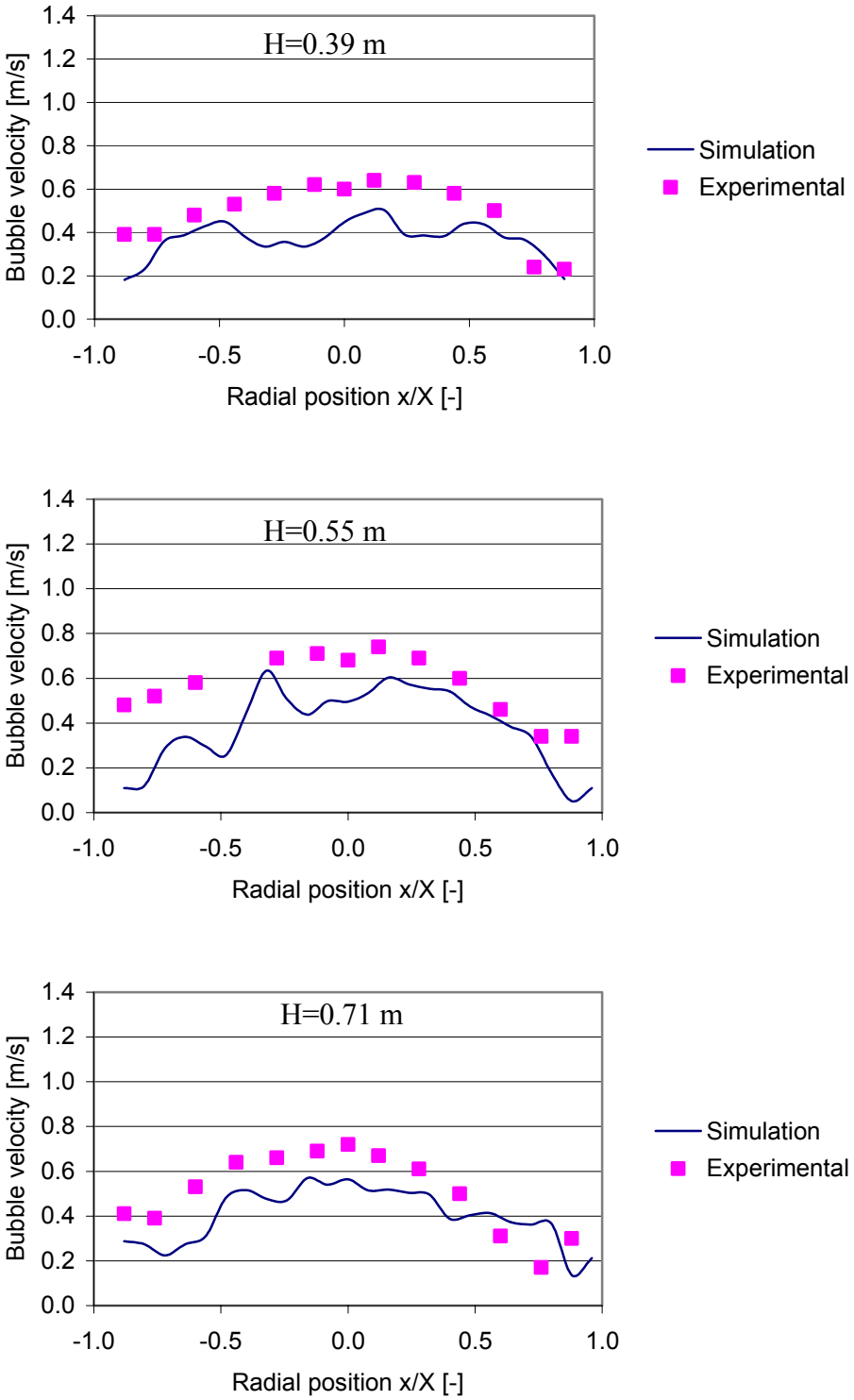

Figure 8.3: Comparison of experimental and computational bubble velocities at different heights. Superficial velocity is 0.09 m/s

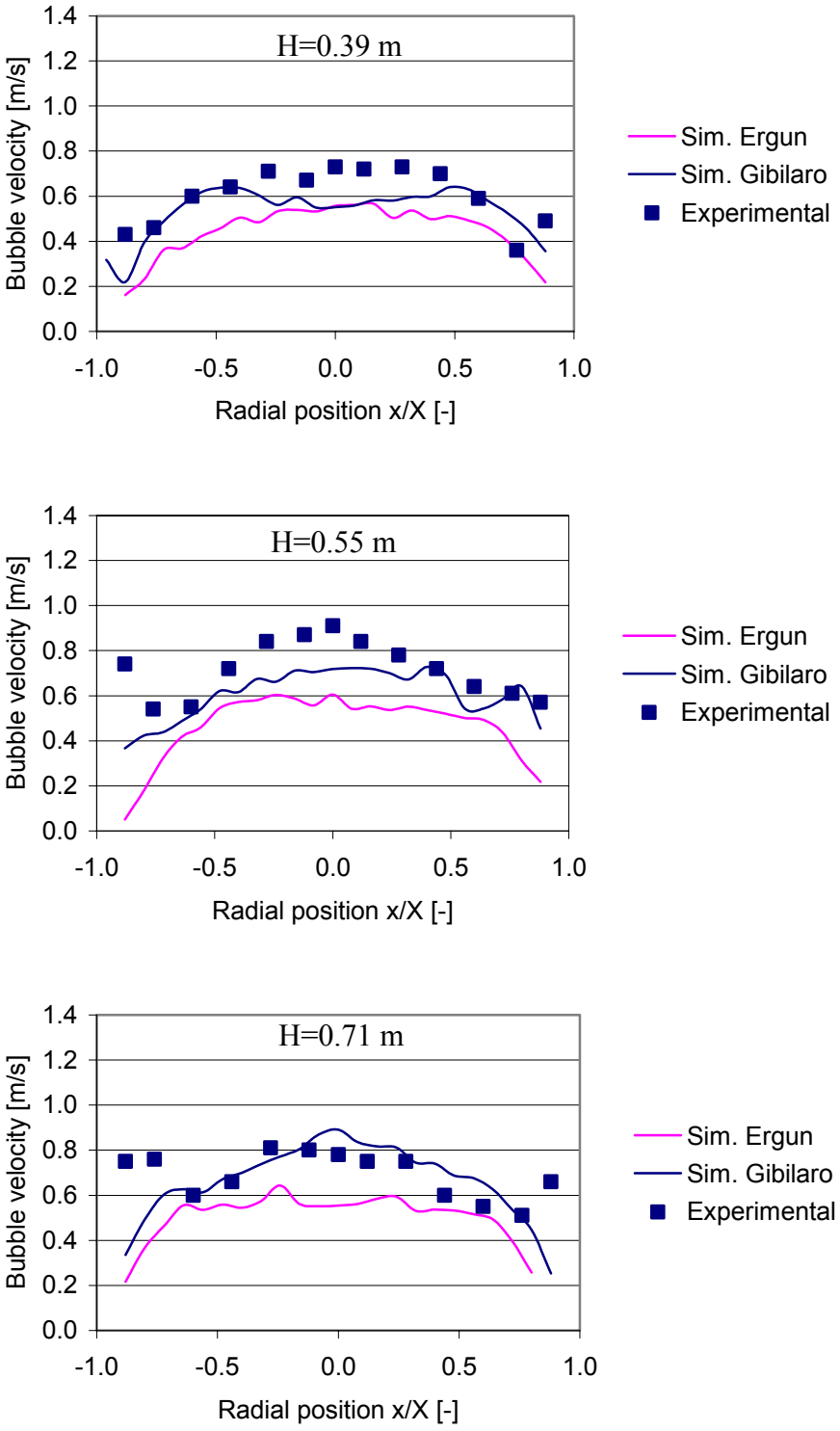

Figure 8.4: Comparison of experimental and computational bubble velocities at different heights. Superficial velocity is 0.133 m/s

In Figure 8.4 computational and experimental bubble velocities for superficial velocity 0.133 m/s are compared. The simulations are performed with the Ergun and the Gibilaro drag models. In the simulation with the Gibilaro drag model the bubble velocity increases with height in the bed, and the results from this simulation agree rather well with the experimental data. Compared to the experiments the Ergun drag model gives too low bubble velocities at all the radial positions. For this case it can also be seen that the computational bubble velocities change insignificantly with height. For both cases the largest discrepancies are located close to the walls. The velocity profiles are rather smooth, which indicates that 30 s might be sufficient simulation time for the superficial velocity 0.133 m/s.

8.2.2 Bubble pierced length

Figure 8.5 shows a comparison of computational and experimental mean bubble pierced length as a function of radial position. The simulation is performed with superficial gas velocity of 0.090 m/s. The experimental bubbles increase significantly with increasing height above the distributor. The same tendency is not observed for the computational bubbles. The computational bubble sizes differ only randomly from each other at the three levels. The simulated bubbles have a lower bubble pierced length than the experimental bubbles at all radial positions.

Figure 8.6 shows a comparison of the experimental and computational bubble pierced length at three different heights. The simulations are performed with superficial velocity 0.133 m/s and with Ergun's and Gibilaro's drag models. The simulations with Ergun's drag model give the largest bubbles. Comparison of the computational bubble pierced length at the three levels shows that there is no significant increase in bubble size as a function of bed height. The computational results using Ergun's drag model agree rather well with the experimental results at height 0.39 m above the distributor. The discrepancies between computational and experimental bubble size increase with height in the bed. At all three levels the experimental bubbles are larger than the computational bubbles. The largest discrepancies are observed close to the walls.

8.2.3 Bubble frequency

Figure 8.7 shows a comparison of computational and experimental bubble frequencies for superficial velocity 0.09 m/s. The results from the simulation agree well with the experiments near the walls. The discrepancies are considerable in the centre of the bed.

The simulations with superficial velocity 0.133 m/s are performed with Ergun's and Gibilaro's drag model. The computational bubble frequencies are compared against the experimental data in Figure 8.8. The two drag models give about the same bubble frequency profile. The results from the simulations agree well with the experimental data at height 0.39 m. The discrepancies between computational and experimental bubble frequencies increase with increasing height in the bed.

In most positions the computational mean bubble frequency, velocity and size are lower than the experimental data. This indicates that in the calculations a higher part of the inserted gas penetrates through the bed outside the bubbles.

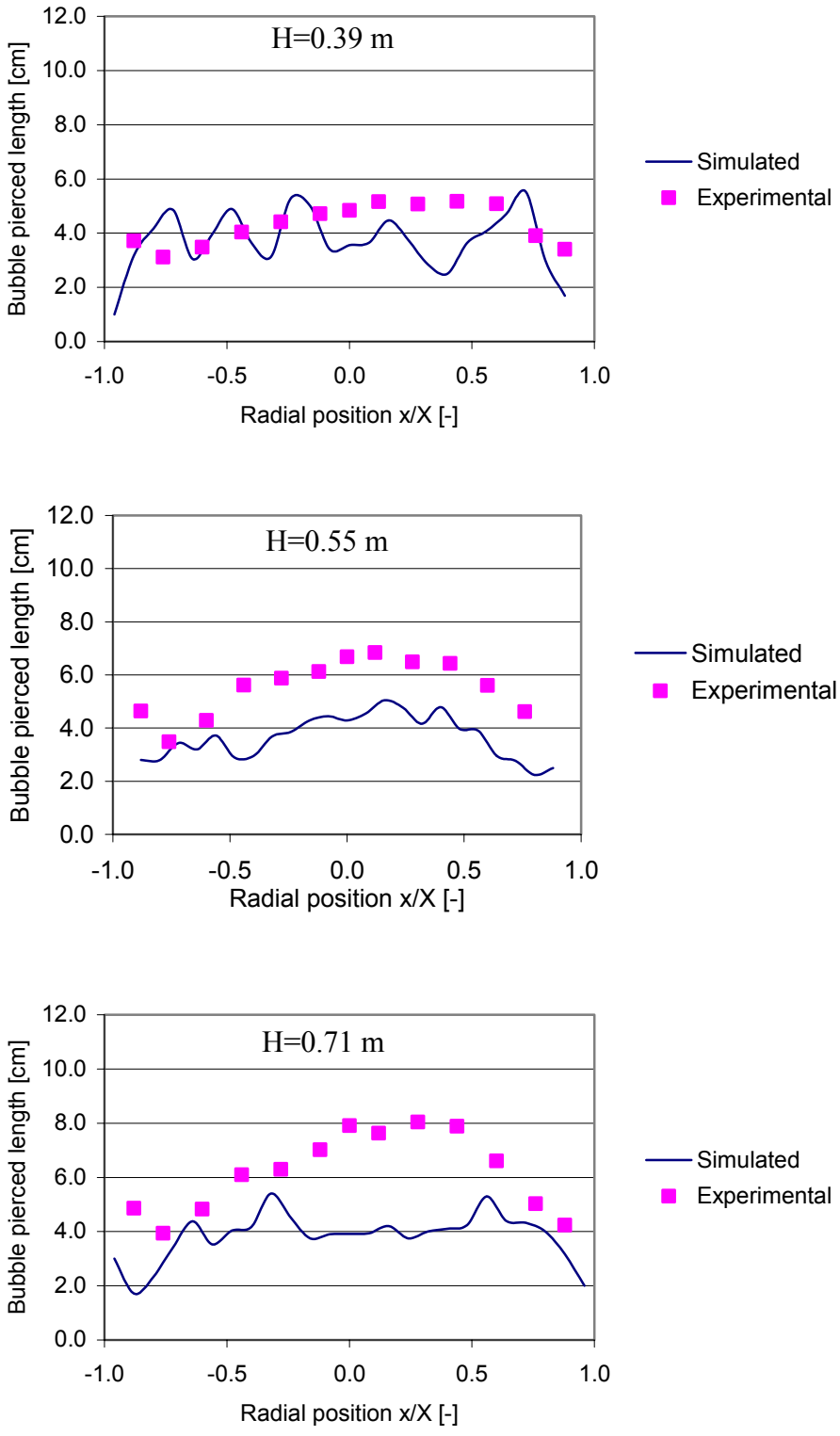

Figure 8.5: Comparison of experimental and computational bubble pierced length at different heights above the air distributor. Superficial velocity is 0.09 m/s.

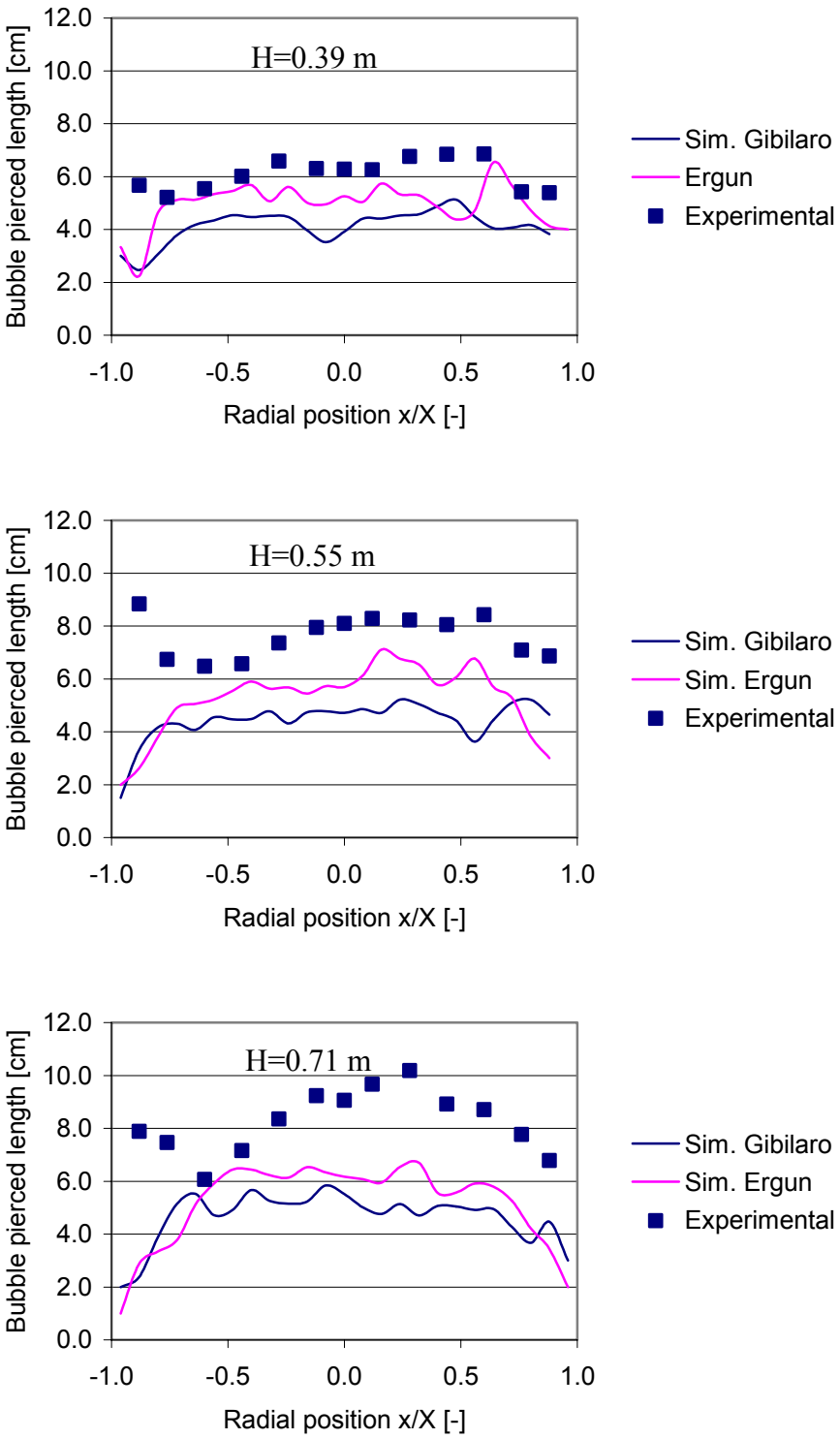

Figure 8.6: Comparison of experimental and computational mean bubble pierced length at different heights. Superficial velocity is 0.133 m/s.

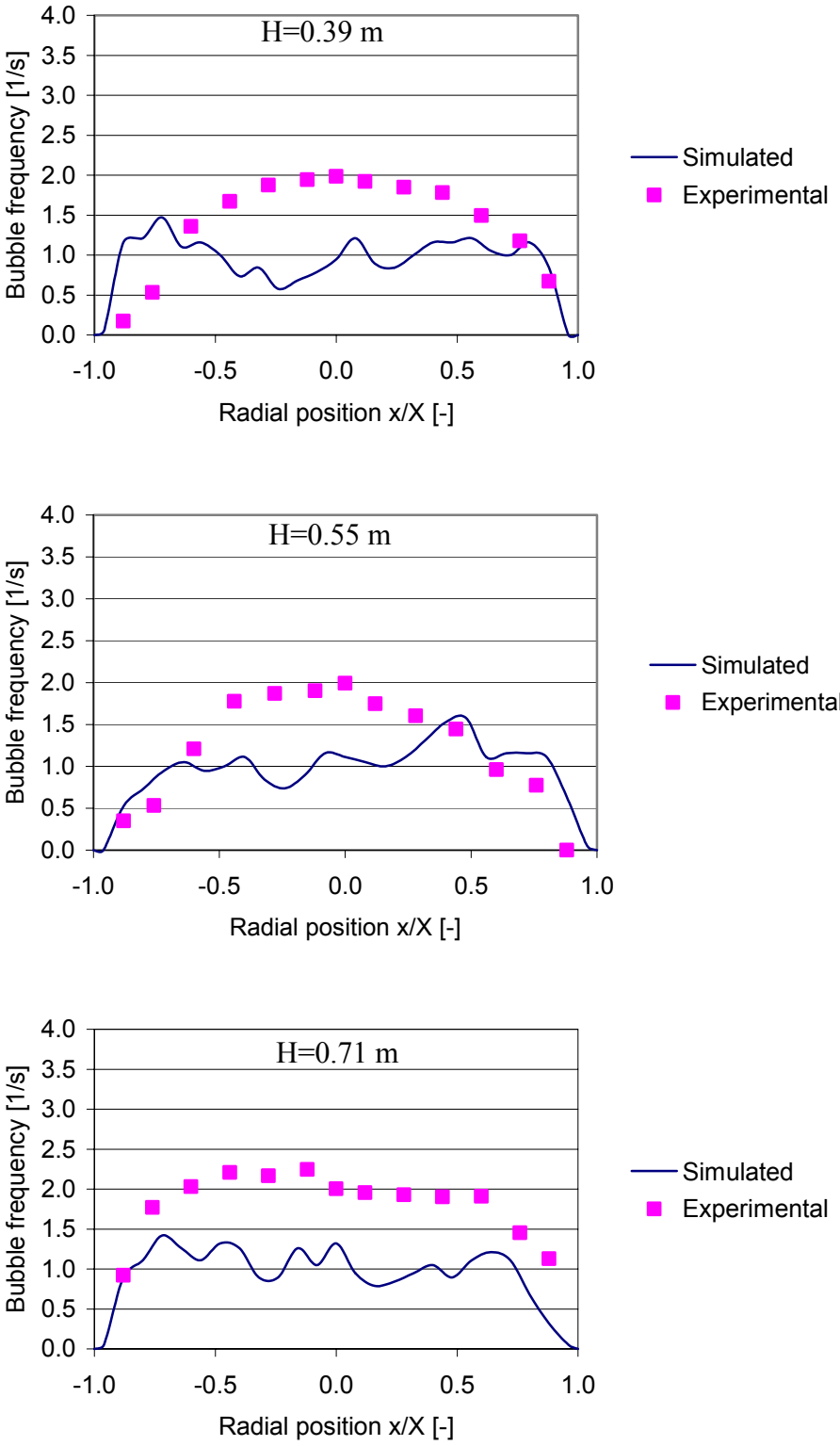

Figure 8.7: Comparison of computational and experimental bubble frequency at different heights. Superficial velocity is 0.090 m/s.

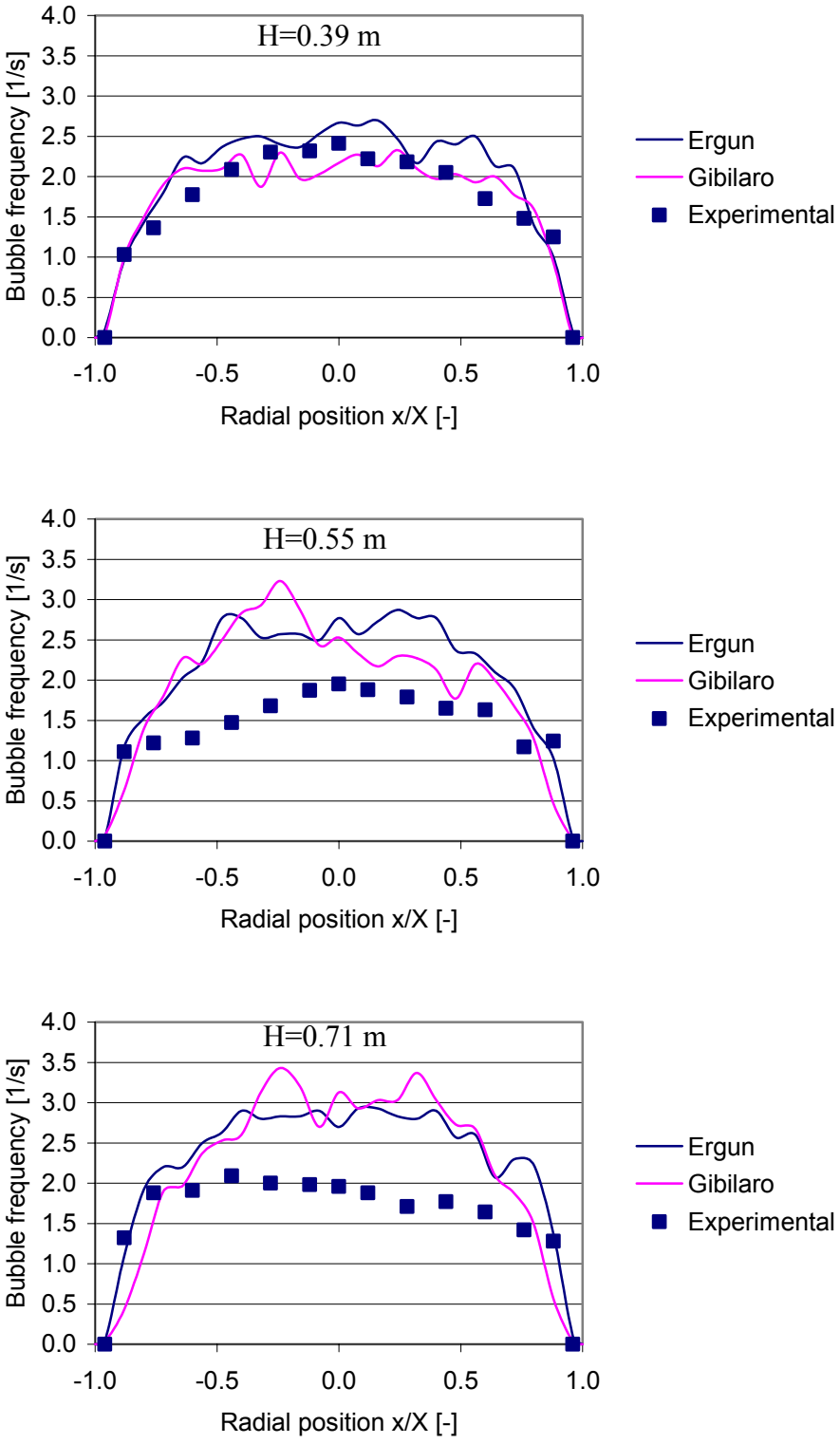

Figure 8.8: Comparison of computational and experimental bubble frequency at different heights. Superficial velocity is 0.133 m.

8.2.4 Pressure drop

In Figures 8.9 and 8.10 comparisons of experimental and computational pressure drops as a function of height for the superficial velocities 0.090 m/s and 0.133 m/s respectively are shown. The results from the simulations with Ergun's drag model agree well with the experimental data. Compared to the experimental data, Gibilaro's drag model gives too high pressure at all the vertical positions. The total pressure drop over the bed is however about the same as the experimental pressure drop.

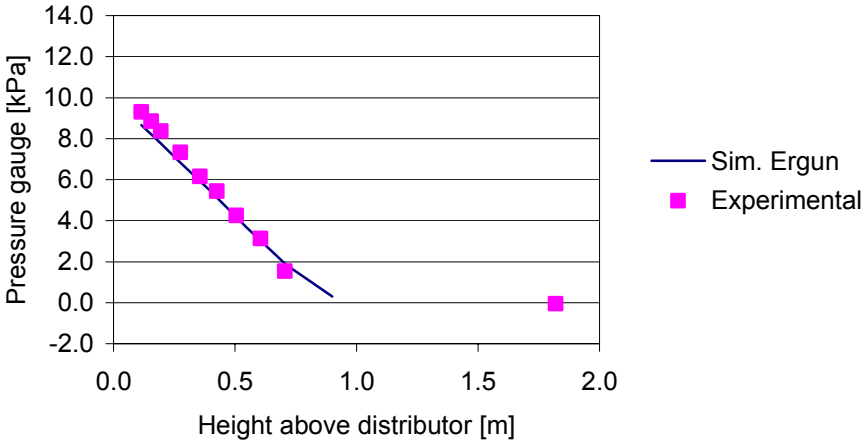

Figure 8.9: Comparing experimental and computational pressure drop. Superficial velocity is 0.090 m/s.

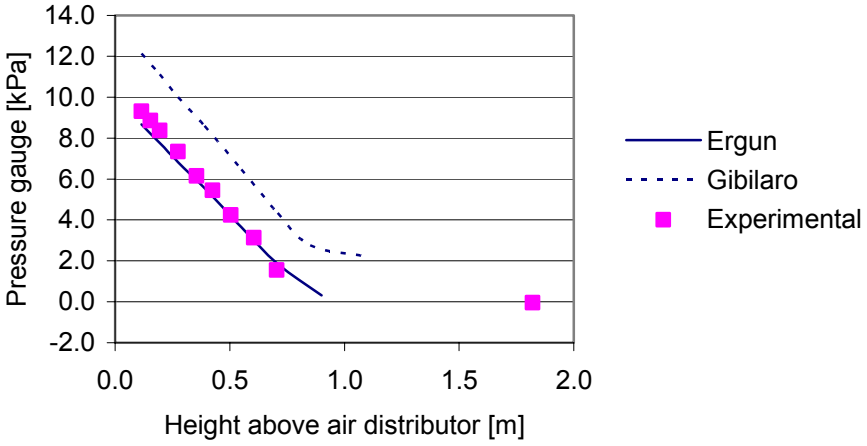

Figure 8.10: Comparing experimental and computational pressure drop. The superficial velocity is 0.133 m/s.

In Figure 8.11 a comparison of experimental and computational pressure fluctuations at different heights in the bed is shown. The comparison is performed for the superficial velocity 0.133 m/s. The computational oscillations agree well with the experimental data both in size and frequency at height 0.275 m, 0.425 m and 0.505 m above the air distributor. At height 0.355 m the measured pressure fluctuations are significantly larger than the computational fluctuations. Also at this level the frequency of the computational fluctuations agree well with the experimental observations.

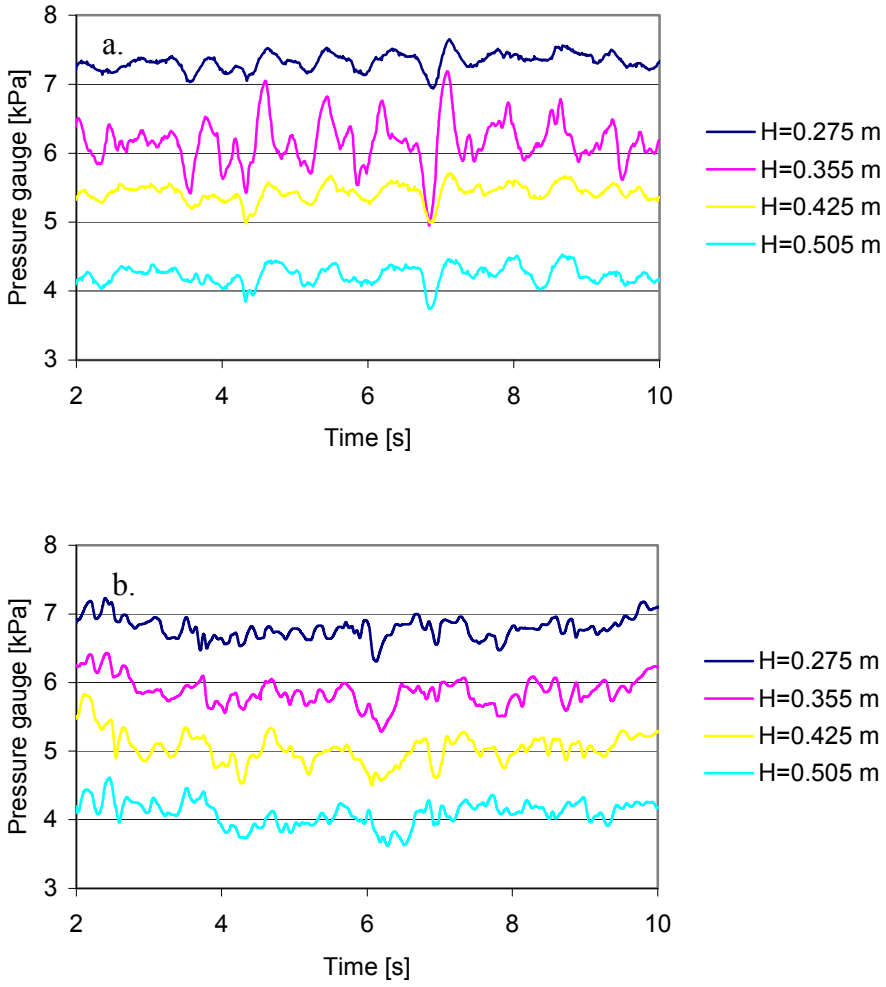

Figure 8.11: Comparison of a) experimental and b) computational pressure fluctuations at different heights in the bed. The superficial velocity is 0.133 m/s and the Ergun drag model is used.

8.2.5 Gas velocity, particle velocity and void fraction

Figures 8.12 and 8.13 show the gas velocity, particle velocity and void fraction for particles with mean diameter of 154 μm and superficial velocity of 0.133 m/s. The calculated minimum fluidization velocity for the small particles is 0.020 m/s. The results shown in Figures 8.12 and 8.13 are obtained from simulations with the Ergun and the Gibilaro drag model respectively. The velocities and void fractions from the simulation with the Ergun drag model change rather little with height in the bed. The simulation with the Gibilaro drag model gives

significant increase in velocities and void fractions with increasing height in the bed. The Ergun drag model gives the highest void fractions in all positions of the bed. This indicates that the Ergun drag model gives higher bed expansion than the Gibilaro drag model. This is also the conclusion from the simulations of the two dimensional bed discussed in Chapter 5.

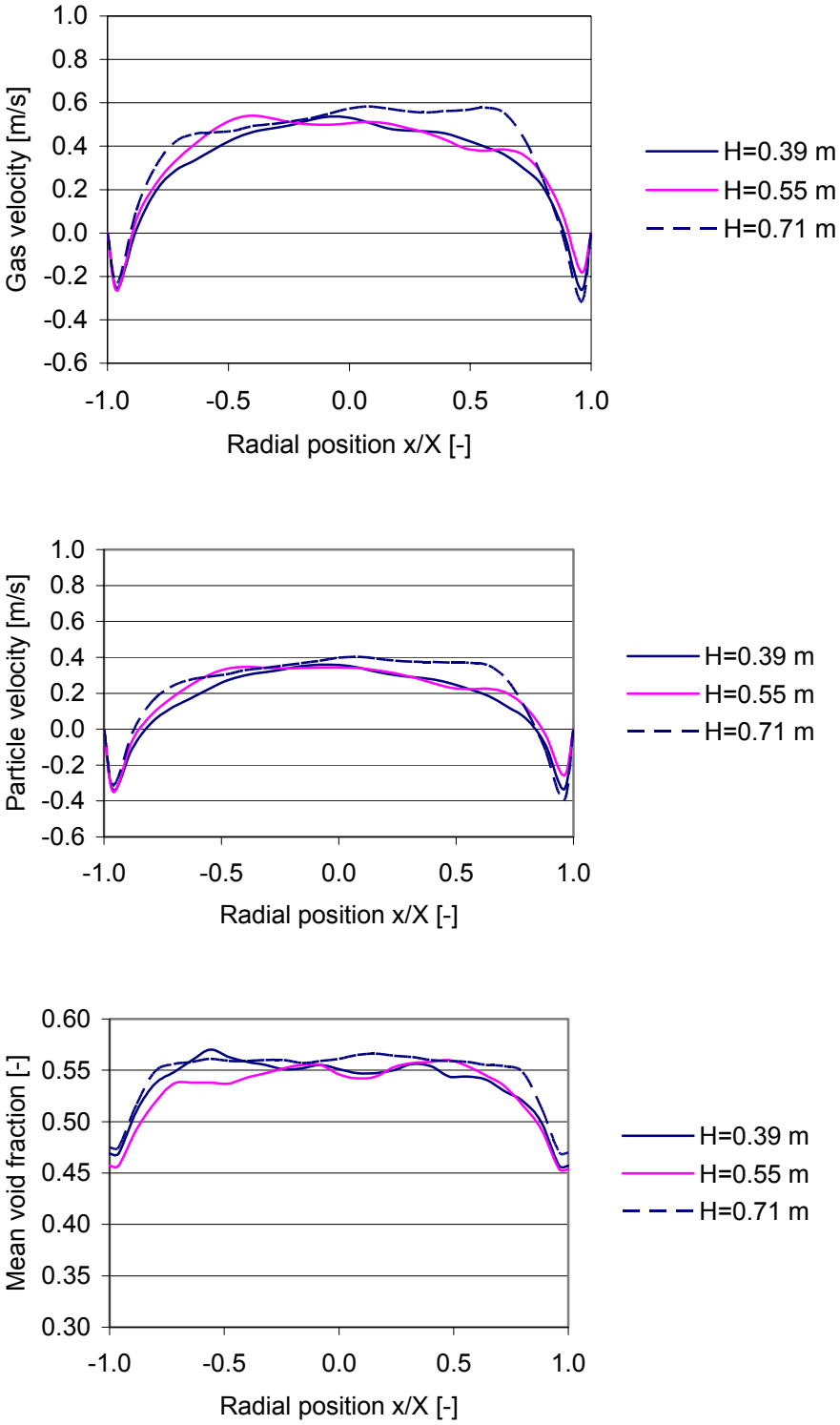

Figure 8.12: Mean gas velocity, particle velocity and void fraction as a function of radial position. Mean particle diameter is 154 μm, superficial velocity is 0.133 m/s, Ergun drag model.

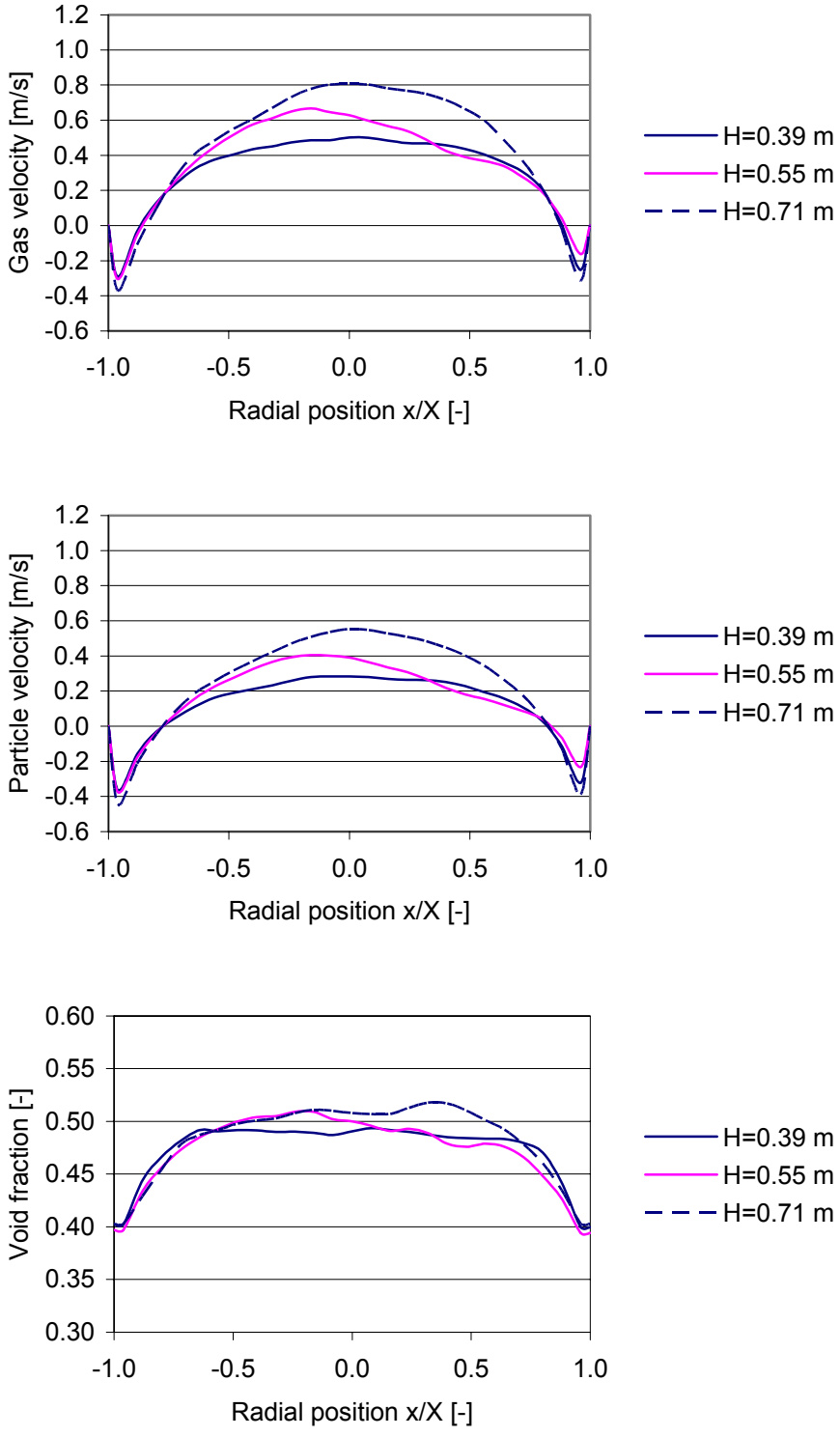

Figure 8.13: Mean gas velocity, particle velocity and void fraction as a function of radial position. Mean particle diameter is 154 μm, superficial velocity is 0.133 m/s, the Gibilaro drag model.

Both the models give a relatively high bed expansion for the case used here. The gas and particle velocity profiles have the same shape. The gas velocity is about 0.20 m/s higher than the particle velocity. This means that the particles have a high velocity and that the condition of the bed is close to a turbulent fluidized bed, where instead of bubbles, turbulent motion of solid clusters and voids of gas of various sizes and shapes are observed. The figures also show that the velocity and void fraction curves are smooth and symmetrical. This indicates that the simulation time is sufficient for calculation of these parameters. The gas and particle velocities are negative close to the walls. According to theory discussed in Chapter 2, solids are dragged up the bed behind the bubbles and drift downwards in parts of the bed. The down-flow of particles can be so fast that it overcomes the up-flow of gas in the emulsion. This can result in a net negative gas velocity in some radial positions

8.3 400-600 µm glass particles

The simulations with this powder are performed with one particle phase with a mean diameter of 480 µm and a superficial velocity of 0.210 m/s. Erguns drag model and a 'switch' to plastic regime are used. The simulation time is 30 s.

8.3.1 Bubble velocity

In Figure 8.14 a comparison between computational and experimental bubble velocities is shown. The computational velocities agree well with the experimental data in most of the radial positions at height 0.39 m. At height 0.55 m the largest discrepancies are located in the centre. The computational bubble velocity decreases significantly from height 0.55 to 0.71 m. An insignificantly small bed expansion is observed for this powder. At height 0.71 m the bubbles are so close to the top of the bed that the computational bubble velocity might be very much influenced by the gas velocity and the bubble eruption. This is further discussed in section 8.3.5. The computational bubble velocity as a function of radial position does not give smooth profiles. This indicates that the simulation time is too short. Also in the experimental study it was not succeeded obtaining symmetrical velocity profiles for this powder.

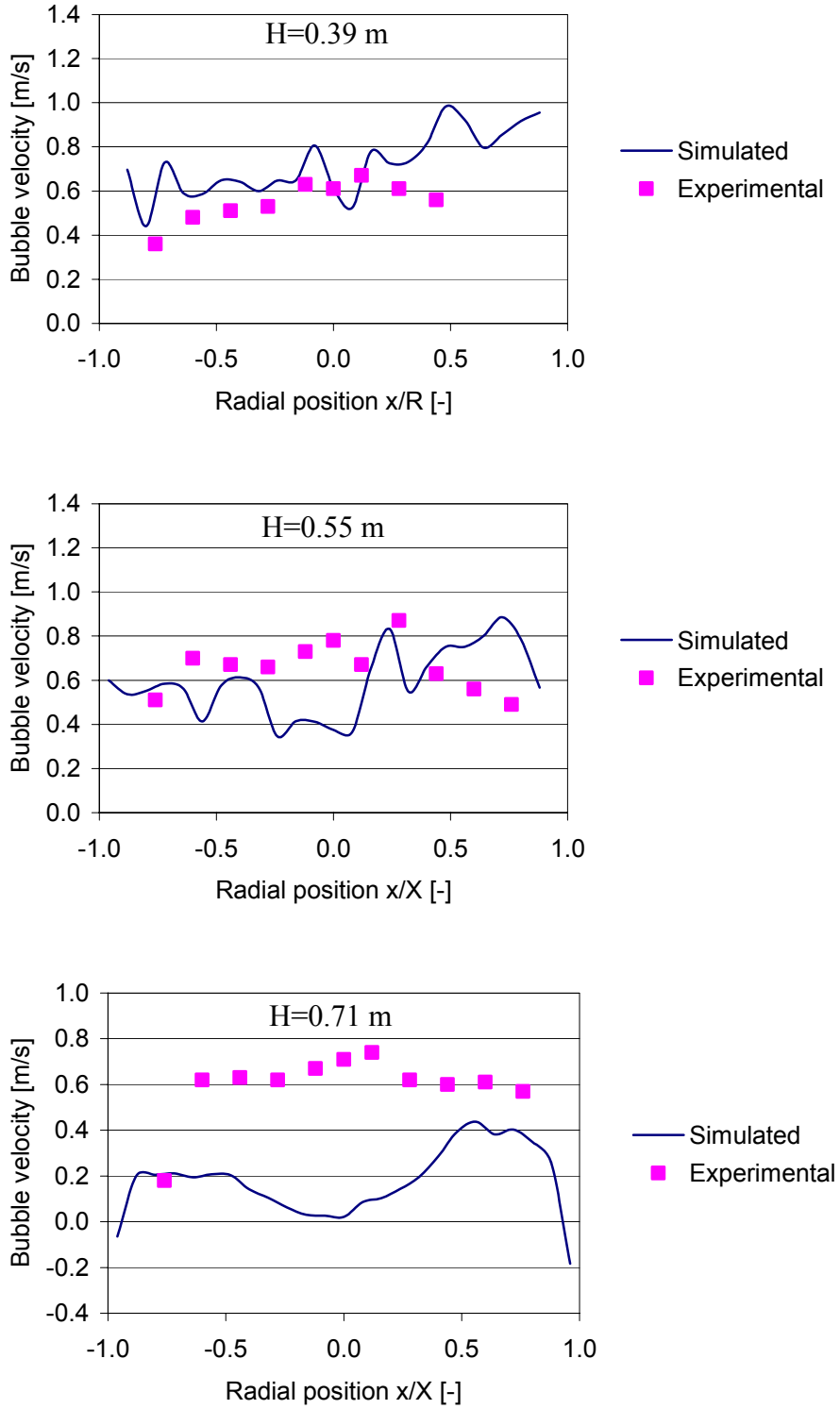

Figure 8.14: Comparison of experimental and computational bubble velocities at height 0.39 0.55 m and 0.71 m. The superficial velocity is 0.210 m/s

8.3.2 Bubble pierced length

Figure 8.15 shows the bubble pierced length as a function of bubble velocity. It can be seen from the figure that bubble velocity increase with increasing bubble size. The same observation is done in the experimental studies. The figure also shows that few of the computational bubbles have a pierced length higher than 5 cm and that the highest bubble pierced length detected at this level is 7 cm. For the corresponding experimental case, half of the bubbles have a pierced length above 5 cm.

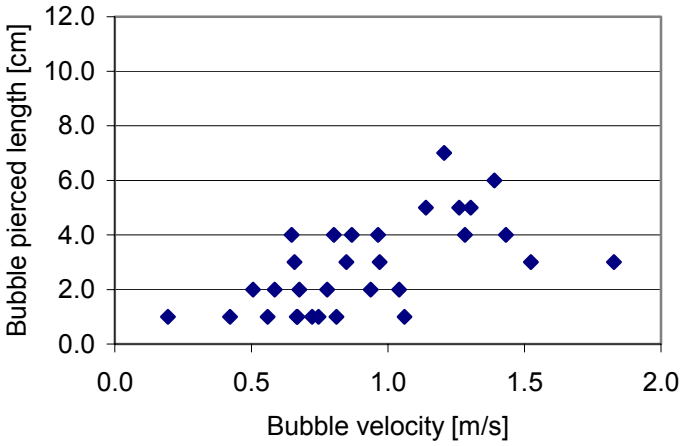

Figure 7.15: Bubble pierced length as a function of bubble velocity at height 0.39 m above the air distributor. Superficial velocity=0.210 m/s.

In Figure 7.16 a comparison of experimental and computational bubble size at different heights is shown. The experimental bubbles have a higher mean bubble pierced length than the computational bubbles at all positions. The computational bubble pierced length decreases considerably from height 0.55 to 0.71 m. The reason for this might be that at height 0.71 m the bubbles are close to the surface where the bubbles erupt.

8.3.3 Bubble frequency

In Figure 8.17 the simulated bubble frequencies are compared to experimental data. The simulations give rather low bubble frequencies at height 0.39 m and 0.55 m. At these levels the discrepancies between experimental and computational bubble frequencies are significant, especially in centre of the bed. The bubble frequencies increase considerably from height 0.55 to 0.71 m. The frequency at height 0.71 m might be affected of that bubbles erupt or are about to erupt at this level.

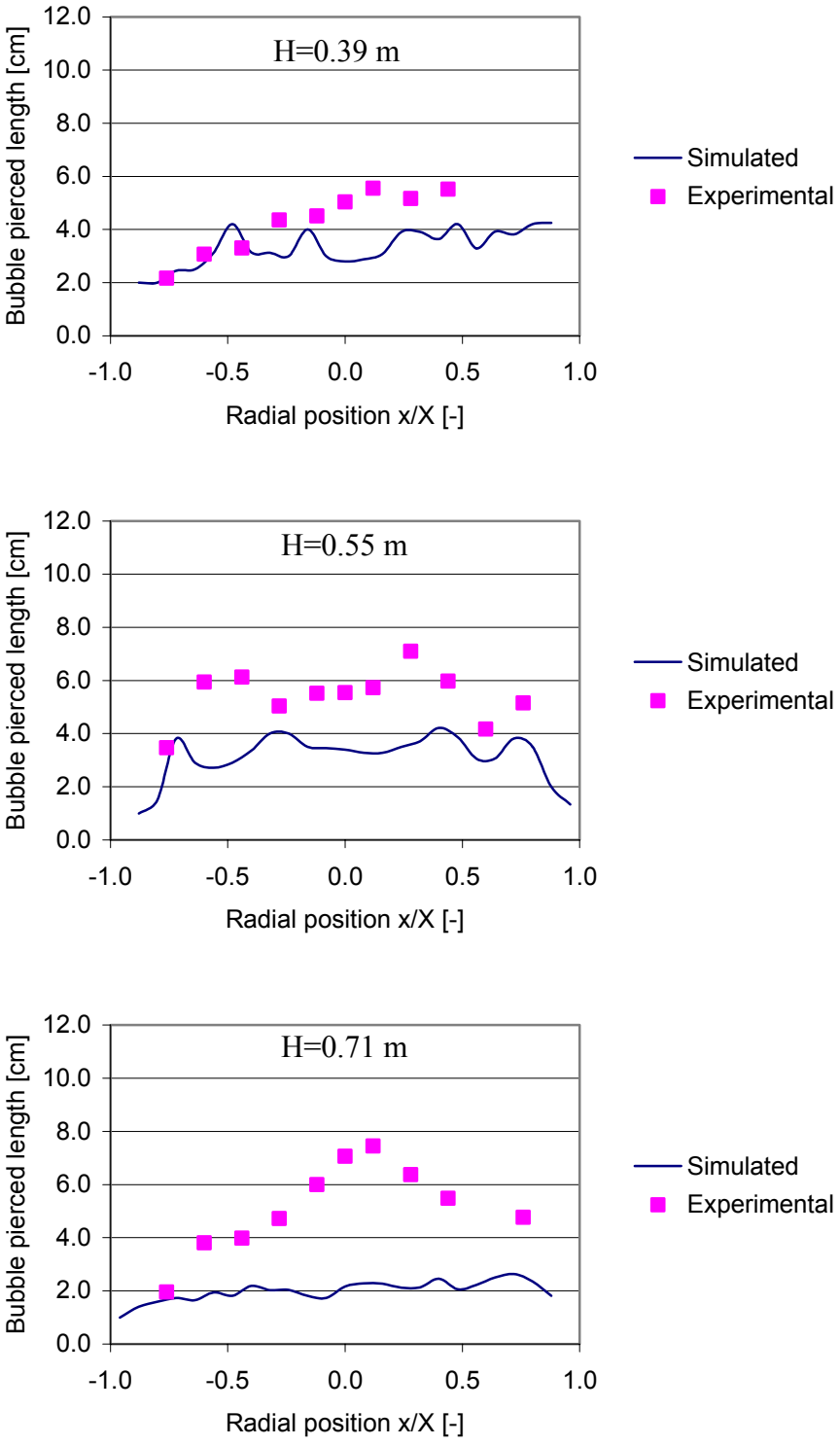

Figure 8.16: Comparison of experimental and computational mean bubble pierced length at different heights. Superficial velocity is 0.210 m/s.

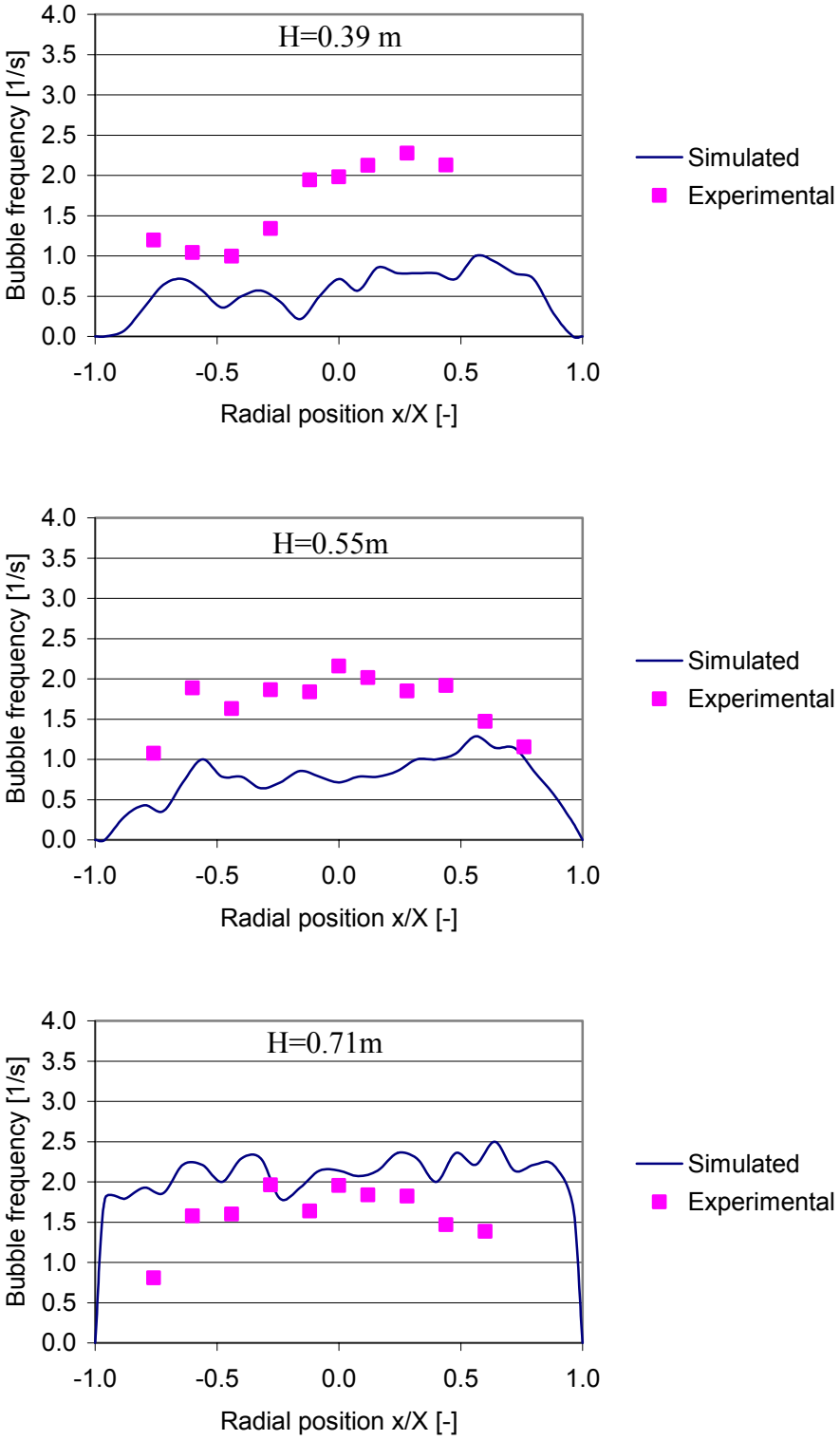

Figure 8.17: Comparison of computational and experimental bubble frequency. The superficial velocity is 0.210 m/s.

8.3.4 Pressure drop

Computational pressure is compared against measurements in Figure 8.18. It can be seen that the simulation gives a lower pressure than the experiment at all vertical positions. The discrepancies between computational and experimental pressure increase with increasing height in the bed. The total pressure drops over the particle bed are about 8 and 9 kPa for the simulation and experiment respectively.

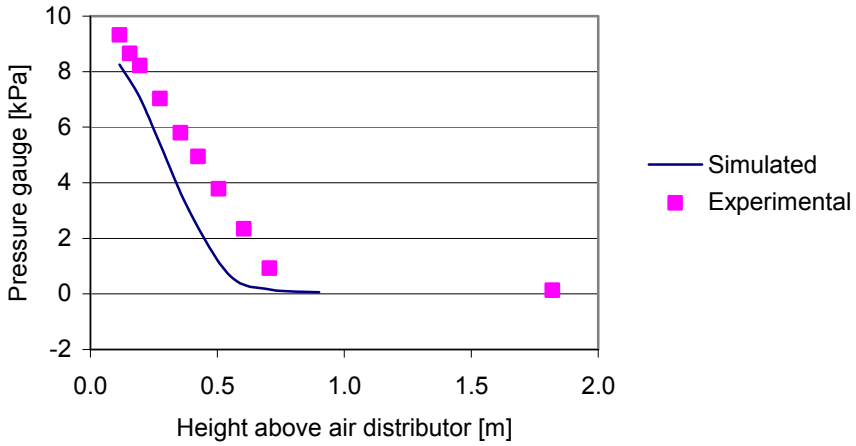

Figure 8.18: Comparing experimental and computational pressure drop. The superficial velocity is 0.210 m/s.

8.3.5 Gas velocity, particle velocity and void fraction

In Figure 8.19 the profiles for the gas velocity, particle velocity and void fraction are shown. The calculated minimum fluidization velocity for this powder is 0.190 m/s and is very close to the superficial velocity. It can be seen from the void fraction that there are no significant bed expansion in this case. Also from the experimental study a very low bed expansion was observed. The bubble sizes increases with the excess of gas velocity. The simulation predicted rather small bubbles compared to the experimental data. The experimental minimum fluidization velocity is influenced by the particle size distribution. The simulation is performed with one particle phase and the excess gas velocity is based on the mean particle size. The experimental excess gas velocity might therefore be higher than the calculated excess gas velocity and this can explain why the simulation gives smaller bubbles than the experiment.

The gas and the particle profiles are smooth but not symmetrical around the centre axis. The highest velocities and void fractions are located to the right of the centre. This indicates that a longer simulation time should be used to get a better radial distribution of bubbles.

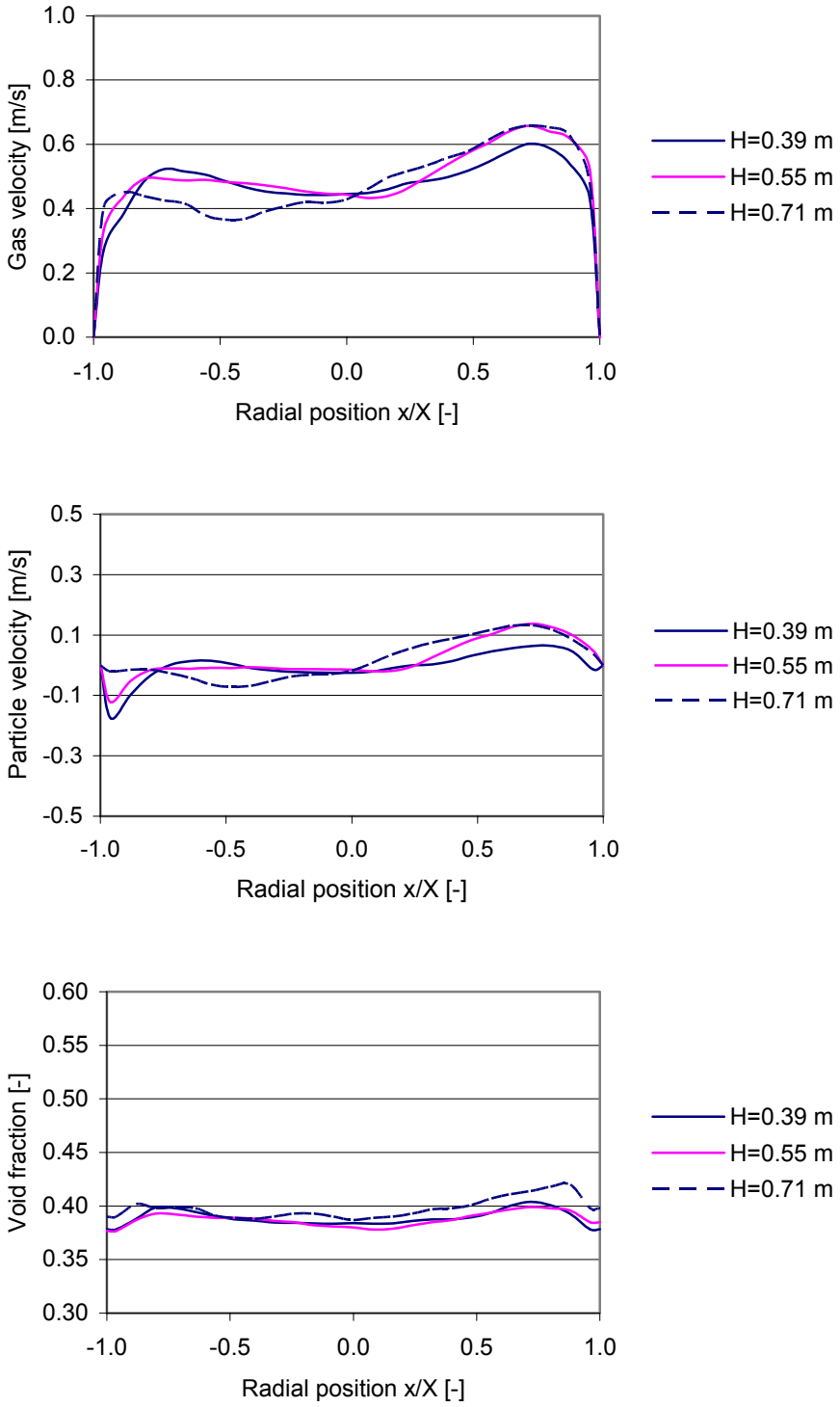

Figure 8.19: Mean gas velocity, particle velocity and void fraction as a function of radial position. Mean particle diameter is 480 μm, superficial velocity is 0.210 m/s, the Ergun drag model.

8.4 Mixed glass particles

The mixed powder has a particle size distribution of 322±161 μm which indicates that the spreading of the distribution is large and that the powder might behave significantly different from mono-sized particles with diameter 322 μm. Hence a particle size distribution by using more than one particle phase is included. The mixed powder has a higher maximum packing than each of the two powders that the mixture is composed of. Minimum fluidization velocity is expected to increase with increasing particle diameter, Gidaspow (1994). The experiments showed that the mixed powder had about the same fluidization velocity as the small particle powder. This observation means that the mixed powder has a lower fluidization velocity than should be expected for mono-sized particles with diameter 322 μm.

8.4.1 Bubble velocity

In the simulations with one particle phase including switch to plastic regime close to minimum fluidization, no bubbles were detected for the superficial velocity 0.090 m/s. The theoretical minimum fluidization velocity can be calculated from Erguns equation. The minimum fluidization velocity for particles with diameter 322 μm is calculated to be 0.085 m/s. For Geldart B particles bubbles are expected to form as soon as the velocity exceeds minimum fluidization velocity. The ratio between superficial velocity and minimum fluidization velocity is 0.090/0.085=1.06. This ratio may be too small to obtain bubbles. Excess air velocity is the difference between superficial velocity and minimum fluidization velocity. Bubbles increase in size with increasing excess air. By using superficial velocity 0.090 m/s, the bubbles might be so small that they are not detected as bubbles. The grid volume used in the simulation is 1 cm^3 and bubbles smaller than that can not be detected.

Simulations with three particle phases including a switch to plastic regime do not give results. The simulations with superficial velocity 0.09 m/s are therefore performed without a switch to plastic regime. The simulations are performed with one and three particle phases and with Gibilaro's drag model. Bubbles are detected in the simulation with one particle phase but unphysical high solid volume fractions are obtained in parts of the bed. The simulation with 3 particle phases and without plastic regime works well, but also for this case rather high packing is observed at some locations in the bed. In Figure 8.20 the comparisons of computational and experimental bubble velocities are shown at height 0.39 m, 0.55 m and 0.71 m above the air distributor. Compared to the experimental data, the simulation with one particle phase gives rather high velocities at height 0.39 and 0.55 m. At height 0.71 m the bubble velocity is very low. Due to the unphysical high packing this level might be very close to the surface of the bed.

The results from the simulation with three particle phases agree better with the experimental data at all levels. However the bubble velocity profile for this case differs from the experimental bubble velocity profile. At all levels the bubble velocity is low in the centre. The bubble velocity decreases rather much from height 0.55 m to 0.71 m.

Figure 8.21 shows a comparison between gas velocity and bubble velocity at height 0.71 m for the two simulations. For the simulation with one particle phase, it can be seen that the gas and bubble velocities differ insignificantly from each other in most of the radial positions. This indicates that the level is very close to the surface of the bed. The simulation with three

particle phases gives larger differences between bubble velocities and gas velocities. But also for this case it is obvious that the bubble velocities are very much influenced by the gas velocities and that the location is close to the surface.

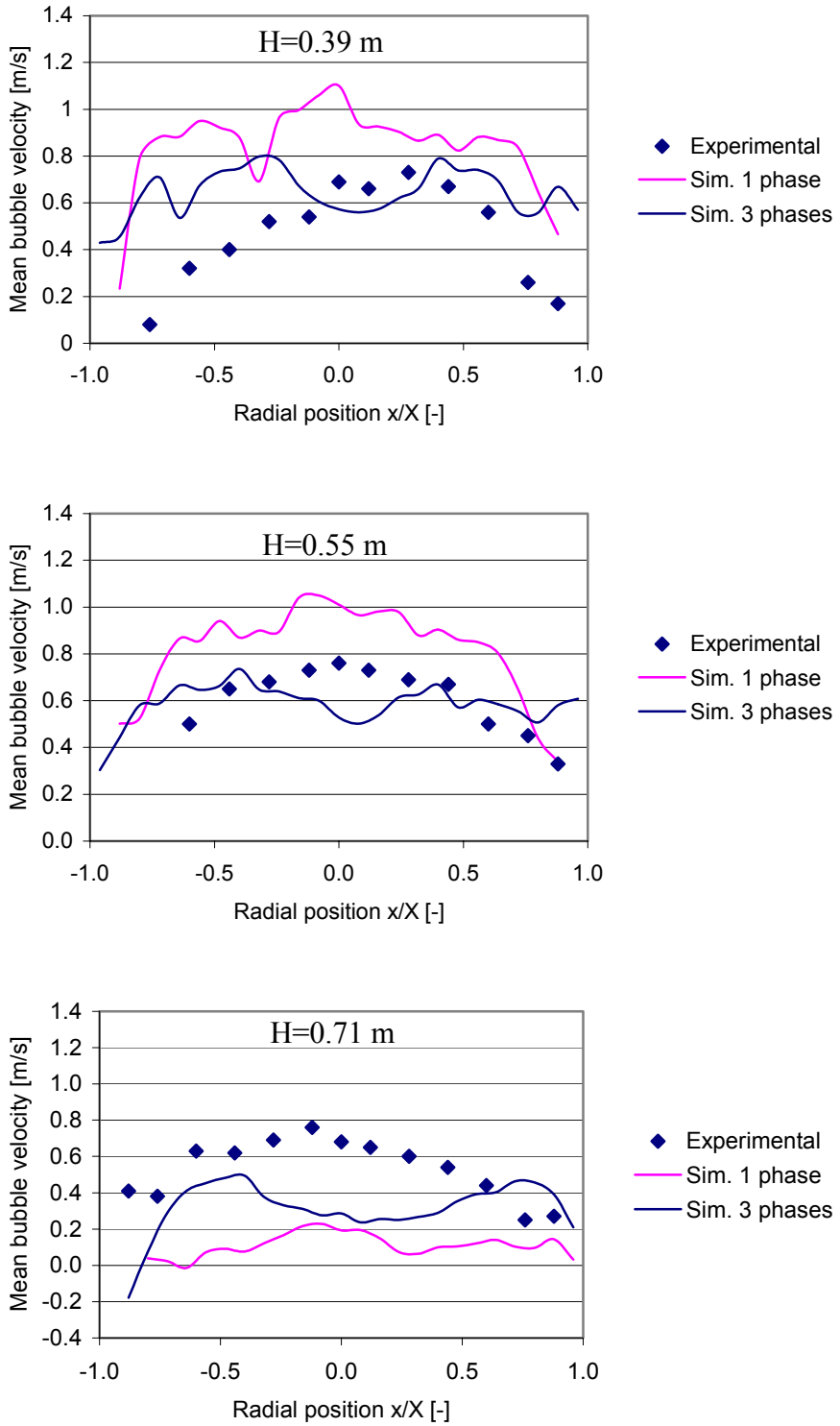

Figure 8.21: Comparison of experimental and computational bubble velocities at different heights. Superficial velocity is 0.090 m/s. Gibilaro drag model is used in the simulations.

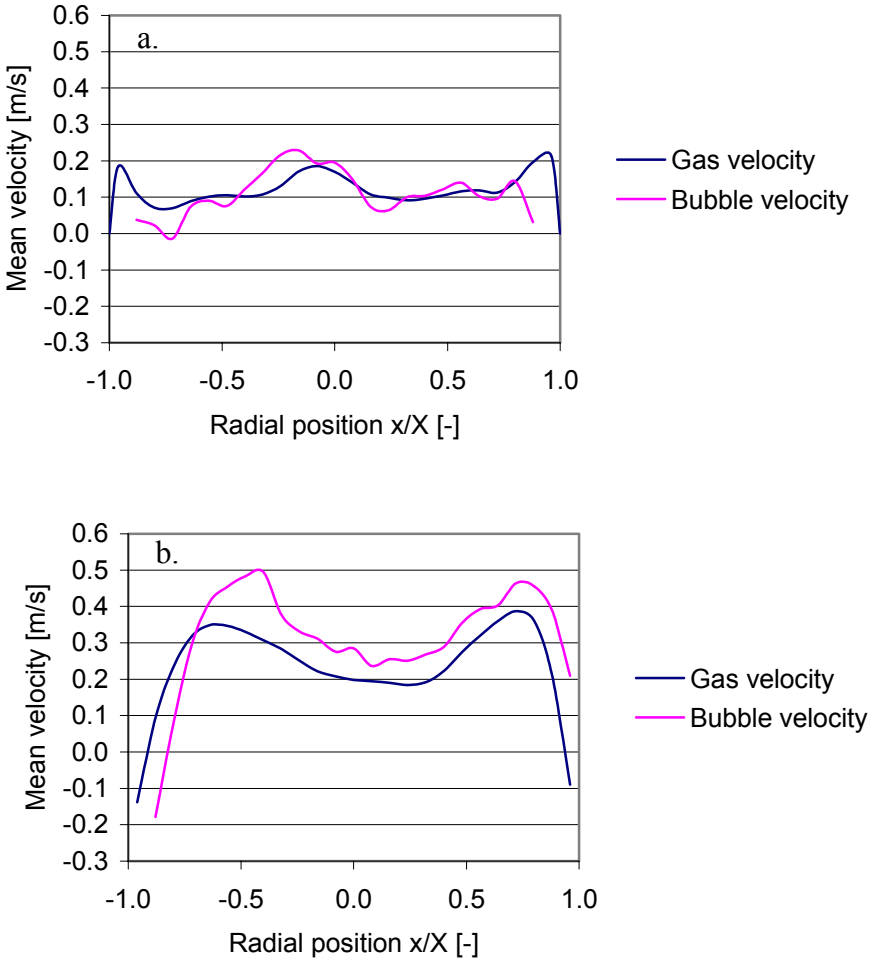

Figure 8.22: Comparison of gas and bubble velocities at height 0.71 m. a) Simulation with 1 particle phase. b) Simulation with three particle phases. The superficial velocity is 0.090 m/s.

The simulations of the mixed powder should be performed with multiple particle phases to take into consideration the influence of particle size distribution on flow behaviour. Four different simulations have been performed with superficial velocity 0.133 m/s and the simulation conditions are given in table 8.2.

Tabel 8.2: Specification of different case studies.

	Case 1	Case 2	Case 3	Case 4
Number of solid phases	1	2	1	3
Drag model	Ergun	Ergun	Gibilaro	Gibilaro
Stresses, solid pressure	Viscous regime with a switch to plastic regime	Viscous regime with a switch to plastic regime	Viscous regime	Viscous regime

Figure 8.23 shows the bubble formations obtained from the different computational conditions. The data is given at time 10 s and the location is in the centre of the bed. Case 1 gives rather small bubbles and the bubbles are only slightly increasing with increasing height in the bed. By studying Case 2 it can be seen that there are no clear bubbles in the lower part of the bed. The explanation to this might be that the two particle phases are not well mixed and the large particles can be found in the bottom of the bed and the small particles in the top of the bed. The inlet air penetrates through the large particle phase and bubbles are not formed until the air reach the small particle phase. At this level the small particles are fluidized and voids of gas are formed. The top of the bed looks very much like a turbulent fluidized bed. A turbulent fluidized bed is described as a bed where the surface disappears and a turbulent motion of solid clusters and voids of gas of various sizes and shapes can be observed, Kunii and Levenspiel (1991).

Case 3 gives a considerably lower bed expansion than the other cases. The bubbles seem to increase with height in the bed. In the corresponding case performed with three particle phases, Case 4, small bubbles are formed near the air inlet, and the bubbles increase in size with increasing height in the bed. Small bubbles can also be seen in the higher part of the bed, and this will reduce the value of the mean bubble pierced length. The bubbles obtained from Case 4 seem to move towards the centre of the bed with increasing height.

In regions with high solid packing, the dominant stress generation is mostly due to multi-particle contact or the frictional effect. The frictional stresses are included in the plastic regime and substitute the kinetic and collisional stresses when the solid volume fraction is high. By including the frictional solid stresses, the compaction of solids around the bubble interface is reduced. This again leads to an increase of gas flow through the bubble boundary into the emulsion phase and smaller bubbles are predicted. Case 1 and Case 4 give the most realistic results, and these simulations are used in the further study.

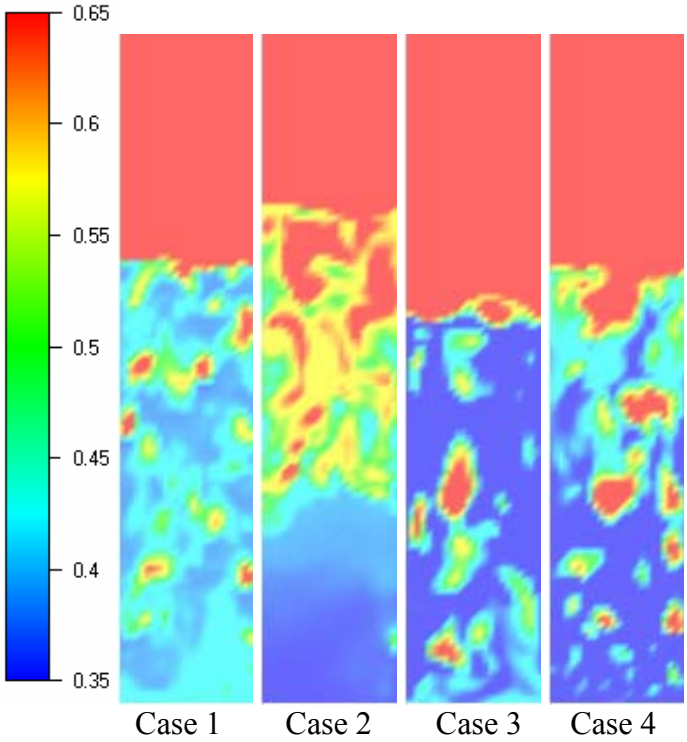

Figure 8.23: Comparison of bubble formation obtained from four different simulations at time 10 s and location in the centre of the bed.

In Figure 8.24 comparisons of computational and experimental bubble velocities at different heights are shown. The results from the simulation with three particle phases agree rather well with the experimental data at height 0.39 m and 0.55 m. At height 0.71 m the computational bubble velocities are lower than the experimental velocities. The bubble velocities obtained from simulation with one particle phase and plastic regime included agree well with the experimental data at all the three heights.

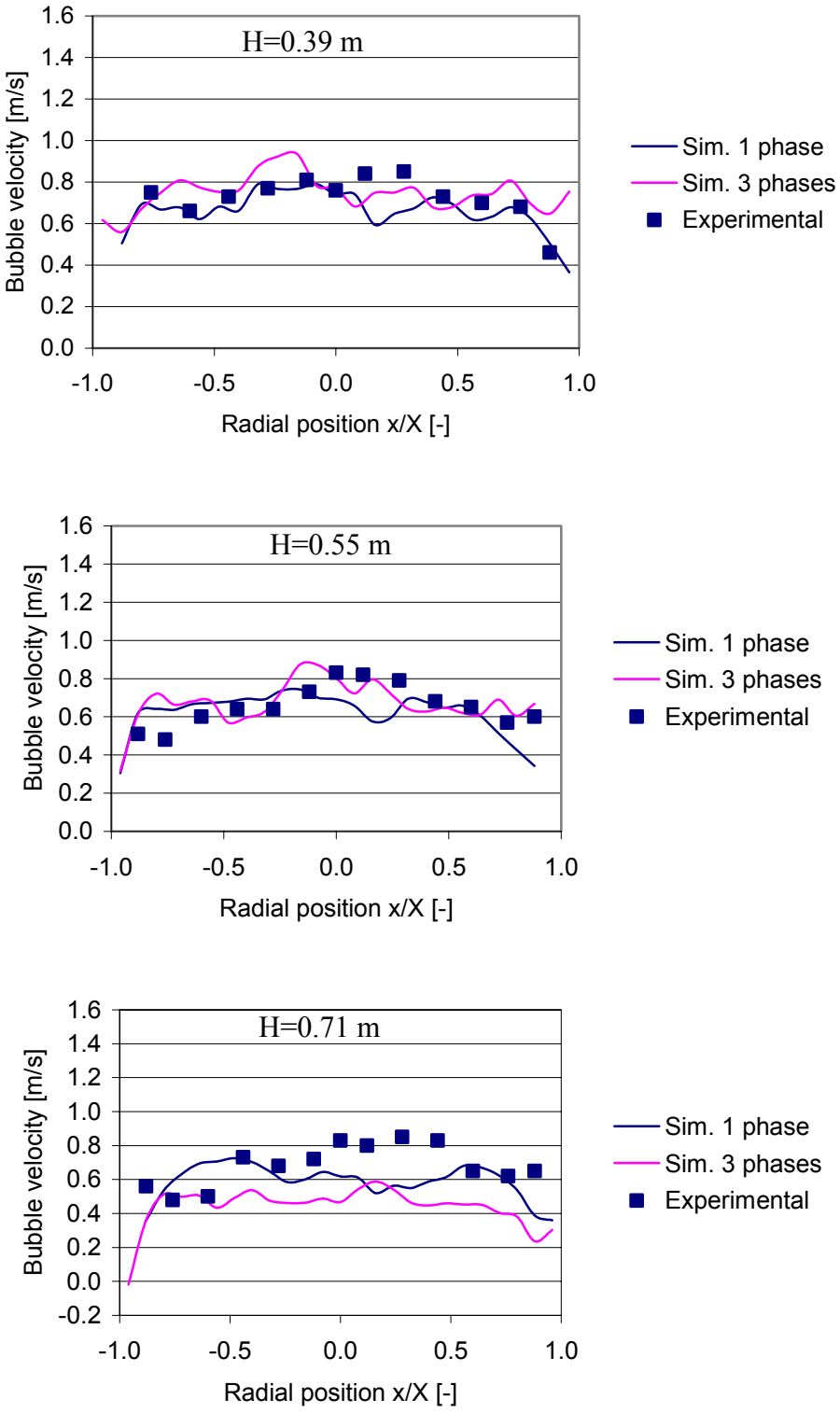

Figure 8.24: Comparison of experimental and computational bubble velocities at different heights. Superficial velocity is 0.133 m/s.

8.4.2 Bubble pierced length

Figure 8.25 shows the computational bubble pierced length as a function of bubble velocity. The simulation is performed with three particle phases and superficial velocity 0.09 m/s. It can be seen that most of the simulated bubbles have a pierced length lower than 5 cm.

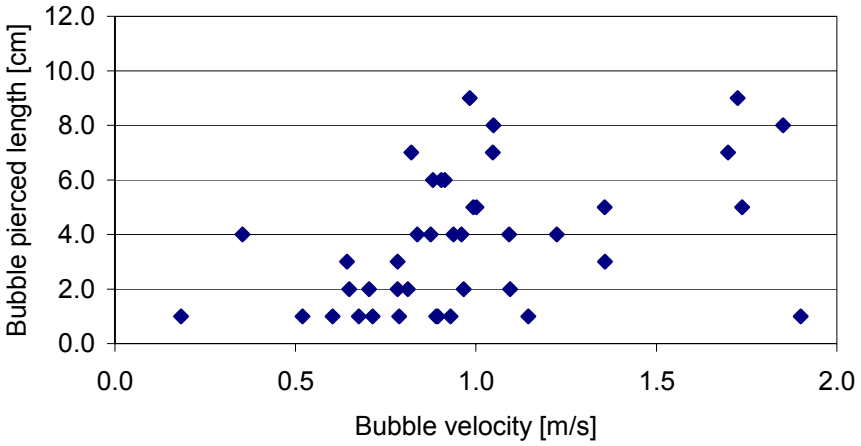

Figure 8.25: Bubble pierced length as a function of bubble velocity. The superficial velocity is 0.09 m/s. Three particle phases and the Gibilaro drag model are used.

Computational data from simulations with one and three particle phases are compared against experimental data in Figure 8.26. The simulations with one and three solid phases give no significant differences in bubble sizes at height 0.39 m. At height 0.55 m it can be seen that the two simulations give about the same bubble size in the centre of the bed and that the simulation with three solid phases gives larger bubbles near the walls. At these two levels the computational results agree rather well with the experimental results. The simulations give smaller bubbles than the experiments in the centre of the bed and larger bubbles near the walls. In the simulations with one particle phase the bed expansion is much lower than in the experiments. At height 0.71 m the bubbles are close to the surface of the bed and about to erupt. This may be the reason that the computational bubble pierced length has decreased considerably from height 0.55 m to height 0.71 m. When using three particle phases the simulation gives a higher bed expansion and it can be seen from the figure that this simulation agrees well with the experiment towards the walls. Rather big discrepancies can be observed in the centre of the bed.

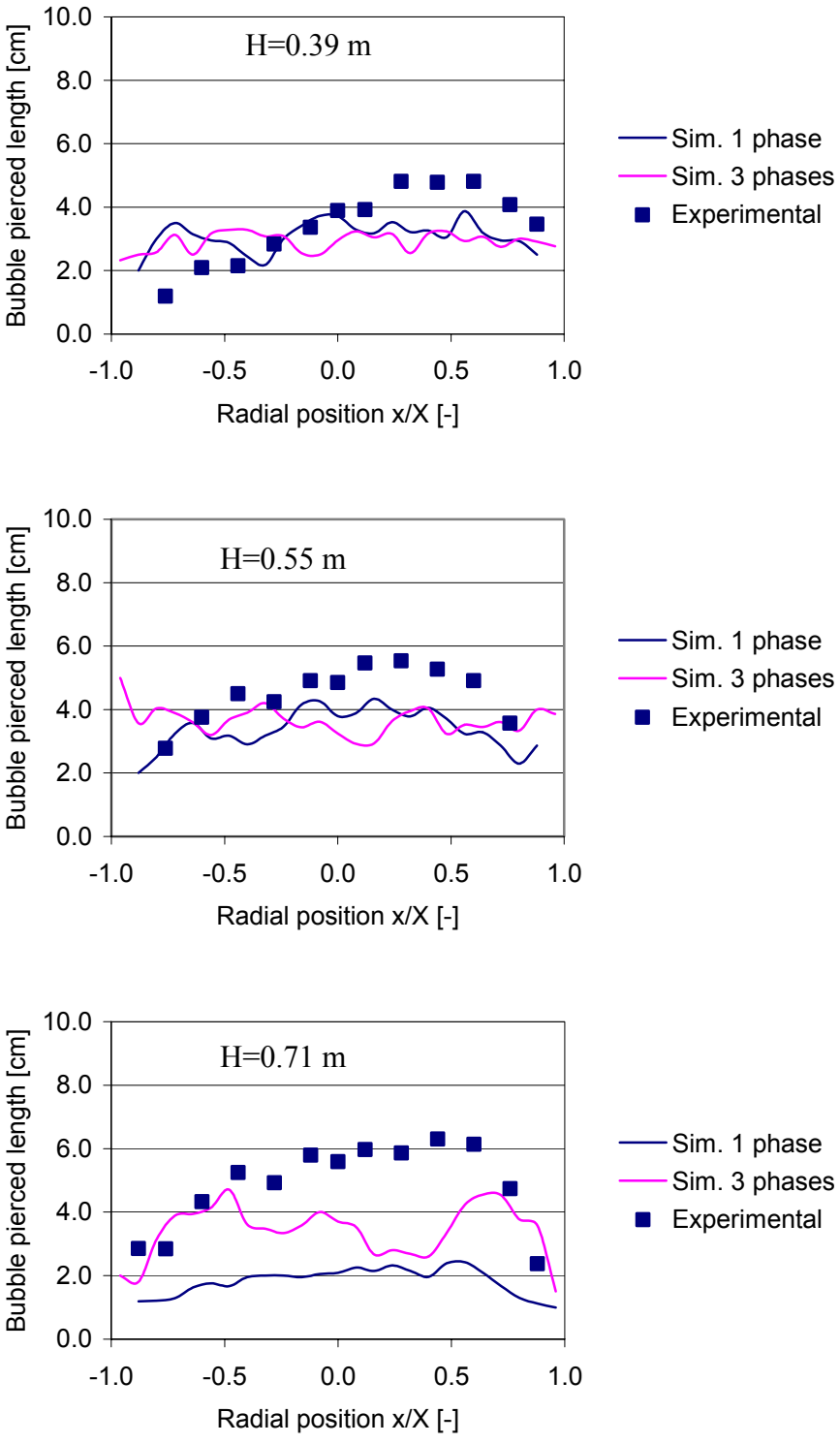

Figure 8.26: Comparison of experimental and computational mean bubble pierced length at different heights. Superficial velocity is 0.090 m/s.

Figure 8.27 shows the bubble pierced length as a function of bubble velocity for superficial velocity 0.133 m/s. Also for this case about half of the bubbles have a bubble pierced length between 1 and 5 cm but also rather large bubbles are calculated. It can be seen from the figure that the bubble velocity increases with increasing bubble size.

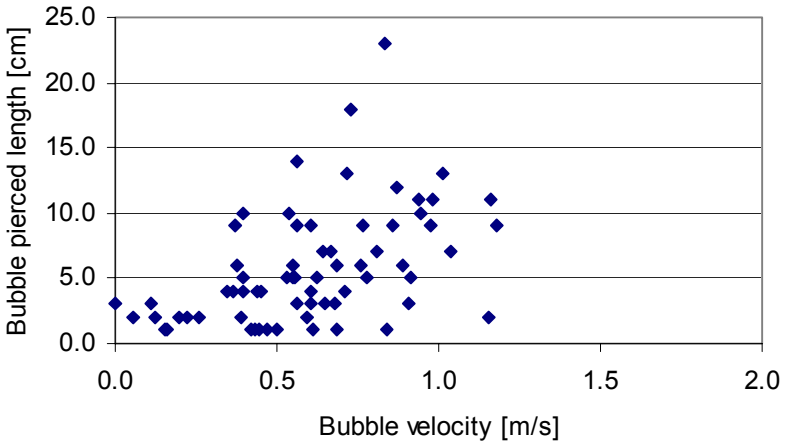

Figure 8.27: Bubble pierced length as a function of bubble velocity. Superficial velocity is 0.133 m/s.

In Figure 8.28 the computational results are compared against the experimental results. The simulation with 1 particle phase and a switch to plastic regime gives small bubbles compared to the experimental bubbles at all heights. The simulation with three particle phases gives somewhat larger bubbles than the simulation with one phase. No increase in bubble size with increasing height in bed can be observed for the two cases, and the discrepancies between computational and experimental bubble size increases with height in the bed.

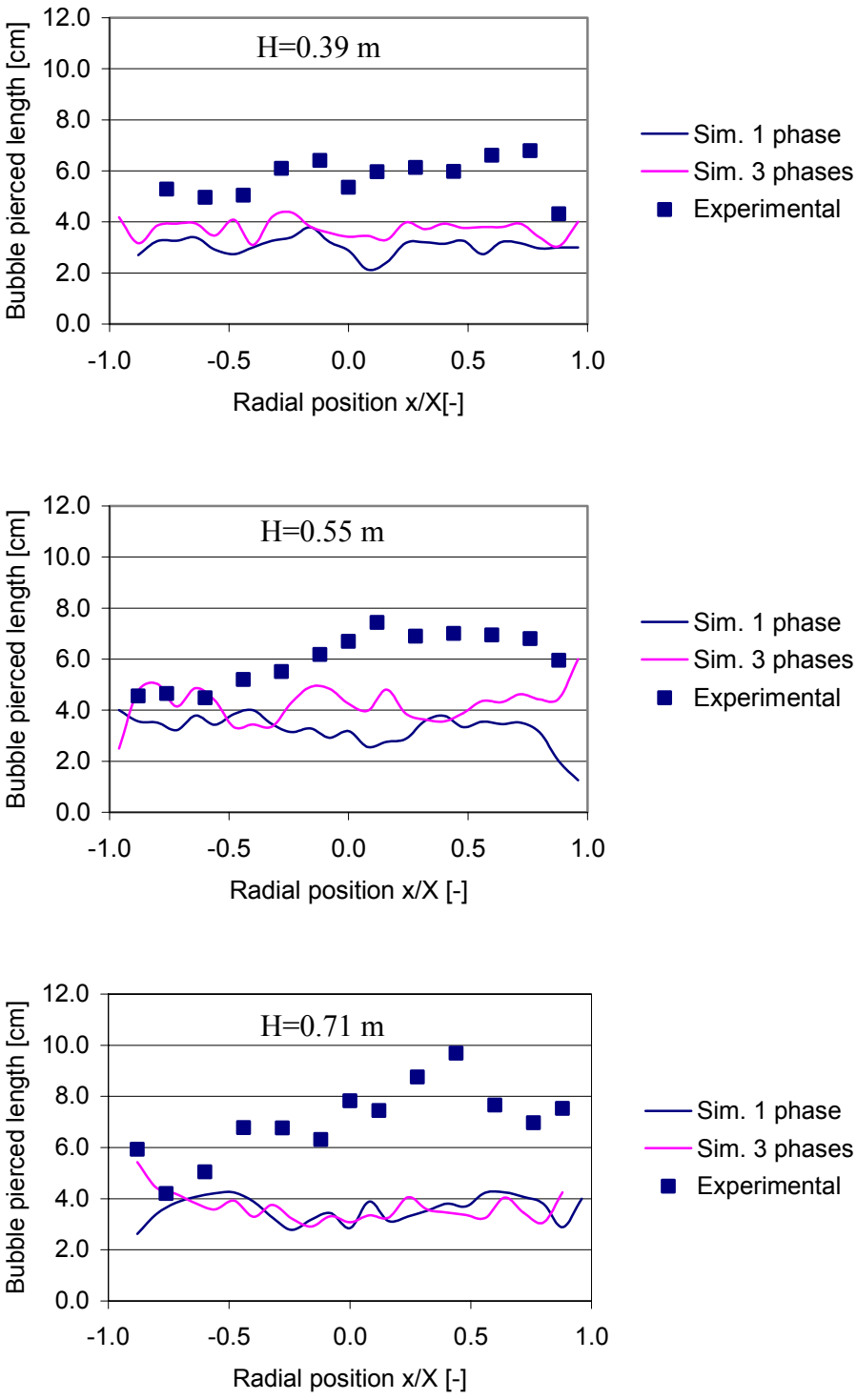

Figure 8.28: Comparison of experimental and computational mean bubble pierced length at different heights. Superficial velocity is 0.133 m/s.

8.4.3 Bubble frequency

Figure 8.29 shows the computational bubble frequencies compared against the experimental data. The simulations agree rather well with the experiment at height 0.39 m and 0.55 m above the air distributor. At height 0.71 m the simulation with 1 particle phase gives a too low

bubble frequency at all the radial position. The simulation with three particle phases gives too high bubble frequency in some radial positions at this level.

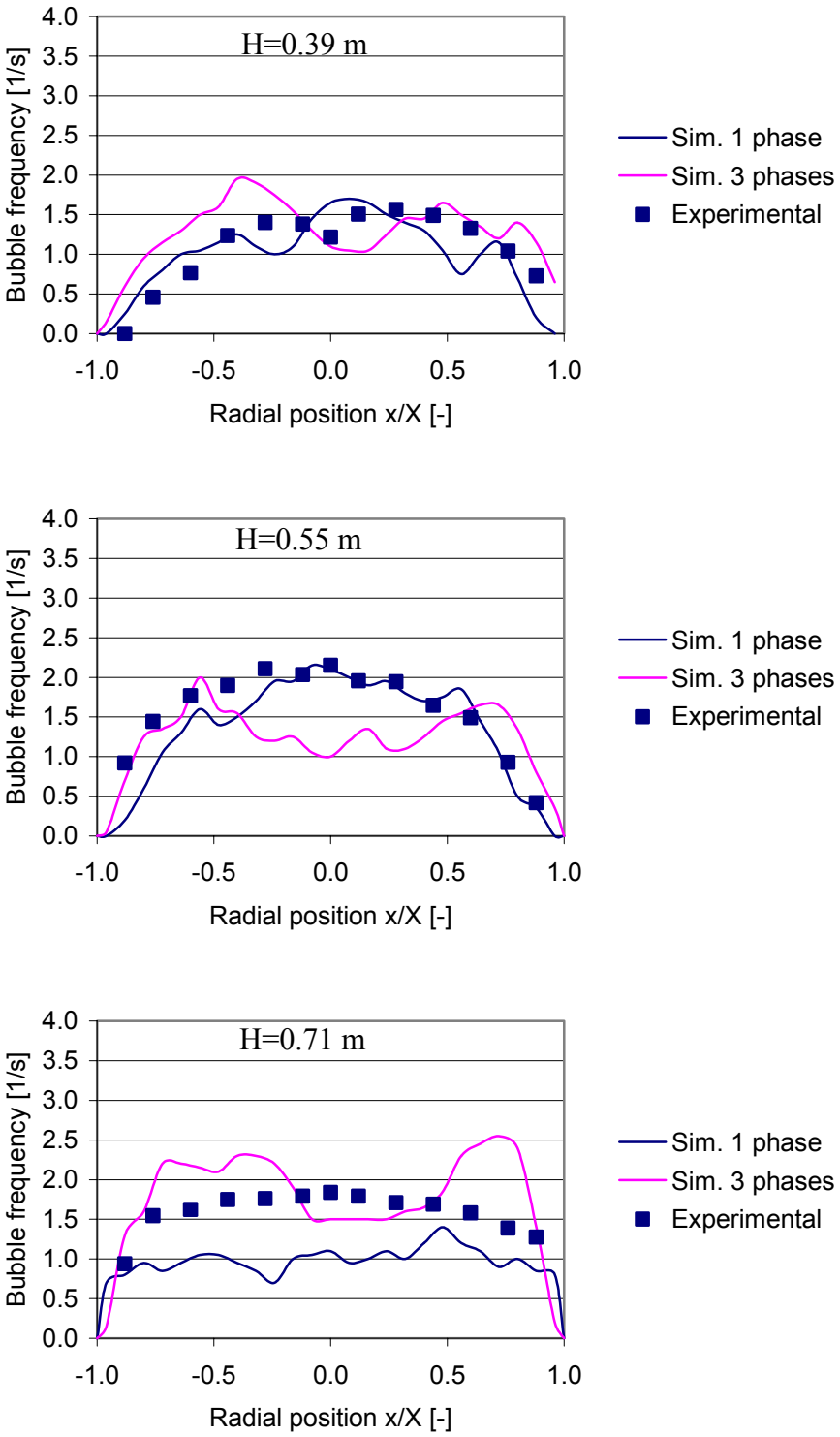

Figure 8.29: Comparison of computational and experimental bubble frequency at different heights. Superficial velocity is 0.090 m/s.

Figure 8.30 shows the comparison of computational and experimental bubble frequencies for superficial velocity 0.133 m/s. The simulation with one solid phase and plastic regime included gives a bubble frequency profile that differs much from the experimental profile.

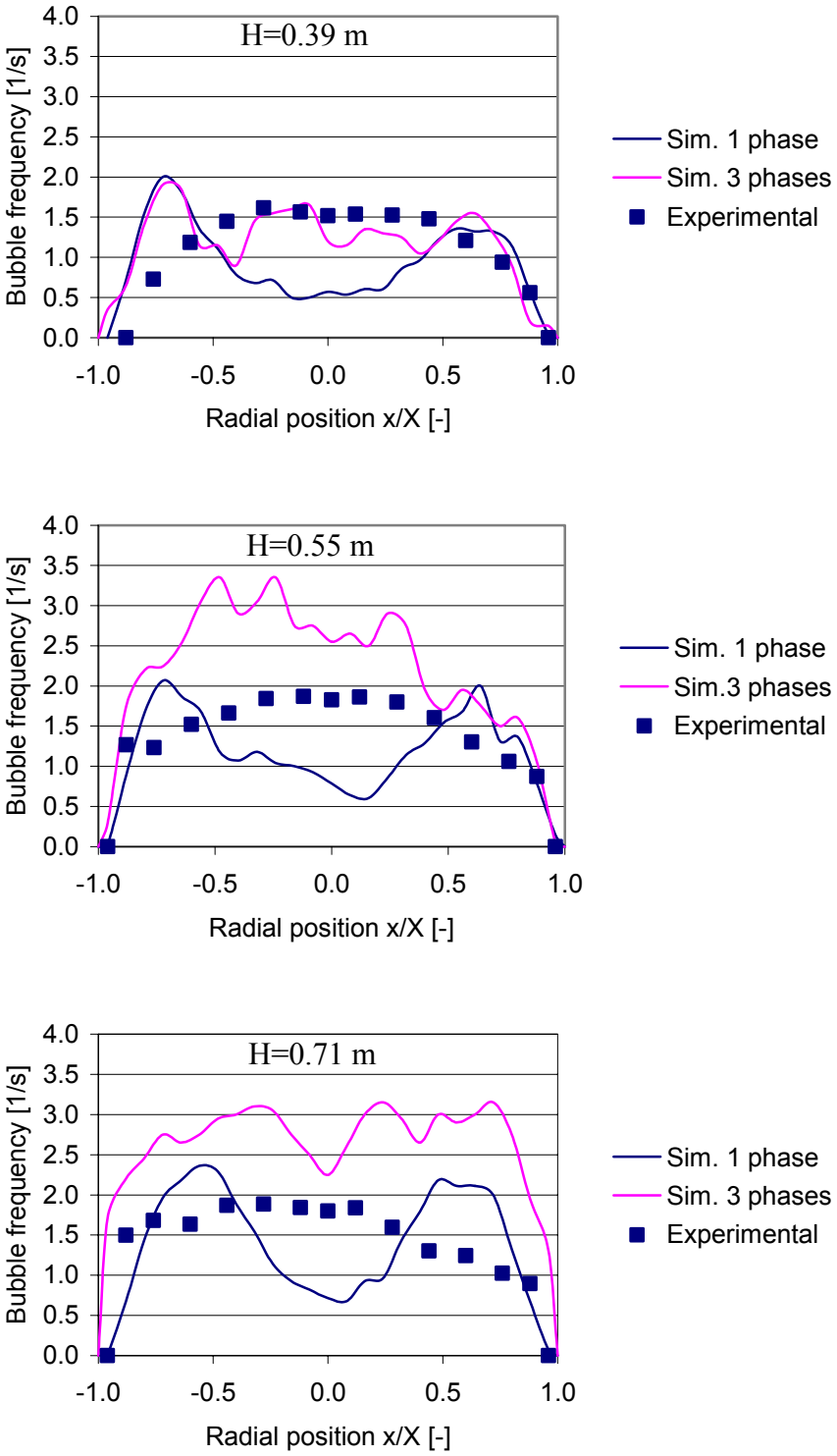

Figure 8.30: Comparison of computational and experimental bubble frequency at different heights. Superficial velocity is 0.133 m/s.

The bubble frequency is low in centre area and high bubble frequency can be observed at each side of the centre. It can be seen that the peaks are closer to the centre at height 0.71 m than at height 0.55 m. According to theory discussed in chapter 6, bubbles are formed close to the walls and moves against the centre with increasing height in the bed. For this case most of the bubbles should reach the centre of the bed at height about 0.50 m. The simulation with three particle phases gives good agreement with the experiment at height 0.39 m. The discrepancies increase with height in the bed.

At most positions the simulations give higher bubble frequencies than the experiments. This may be due to the high ratio of small particles that are detected. The high bubble frequencies are only obtained for the mixed powder and superficial velocity 0.133m/s.

8.4.4 Pressure drop

In Figure 8.31 a comparison of the computational and experimental pressure is shown for the superficial velocity 0.09 m/s. Simulations with one and three particle phases give about similar pressure curves. The computational pressure agrees well with the measured pressure. It seems however that the simulated pressure curves get a flat profile from height 0.71 m above the air distributor whereas the experimental data show a pressure drop of about 2 kPa from height 0.71 m to the top of the bed.

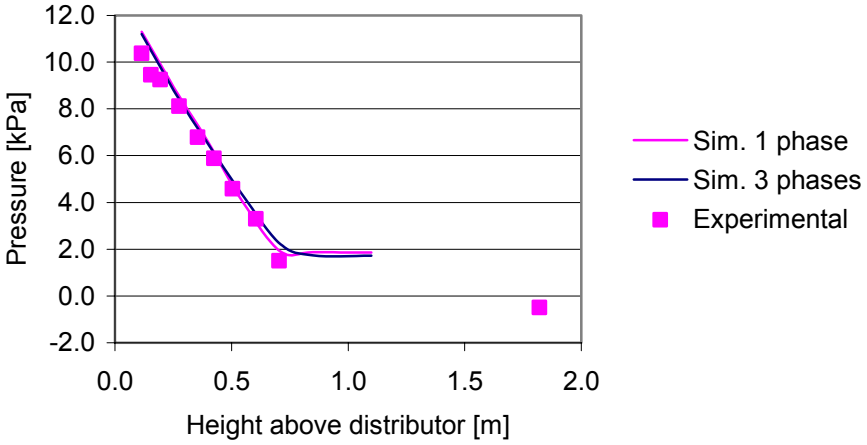

Figure 8.31: Comparing experimental and computational pressure drop. Superficial velocity is 0.090 m/s.

Comparison of computational and experimental pressure for superficial velocity 0.133 m/s is given in Figure 8.32. The computational pressure from the simulation with one particle phase agrees well with the experimental pressure in all vertical positions. The pressure curve obtained from the simulation with three particle phases is parallel to the experimental pressure curve below height 0.71 m. That indicates good agreement between computational and experimental pressure drop over the bed. The computational pressure is however higher than the measured pressure in all vertical positions.

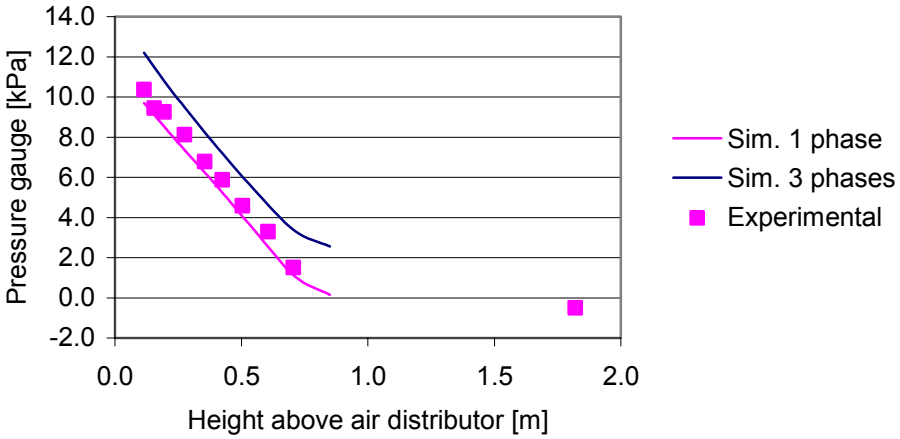

Figure 8.32: Comparing experimental and computational pressure drop. The superficial velocity is 0.133 m/s.

8.4.5 Gas velocity, solid velocity and void fraction

In Figure 8.33 and 8.34 the gas velocity, particle velocity and void fraction profiles for mixed powder and superficial velocity 0.133 m/s are shown for one and three particle phases respectively. The simulation with one particle phase gives rather low void fractions, but the mean void fractions exceed the minimum void fractions in all the radial positions. The solid velocities are low compared to the gas velocities. Both of these observations indicate that the bed expansion is low. Gas velocity, particle velocity and void fraction change insignificantly with height in the bed.

In the simulation with three particle phases the void fractions increase significantly with height in the bed. The mean void fraction is rather low at height 0.39 m but except for a small area close to the walls, the mean void fractions exceed the minimum void fraction. The gas and particle velocities increase from the walls to about the radial positions ±0.75, and in the rest of bed the velocity profiles are rather flat. The particle velocities are about 0.2 m/s lower than the gas velocities. In a small area in the centre the gas and particle velocities decrease from height 0.71 m to 0.55 m. This might be a consequence of bubbles erupting in the centre.

From the study of the mean gas velocities, particle velocities and void fractions for the mixed powder it can be seen that both the simulation conditions give realistic results. The problem with high packing can be solved by including the plastic regime or by including a particle size distribution in the calculations.

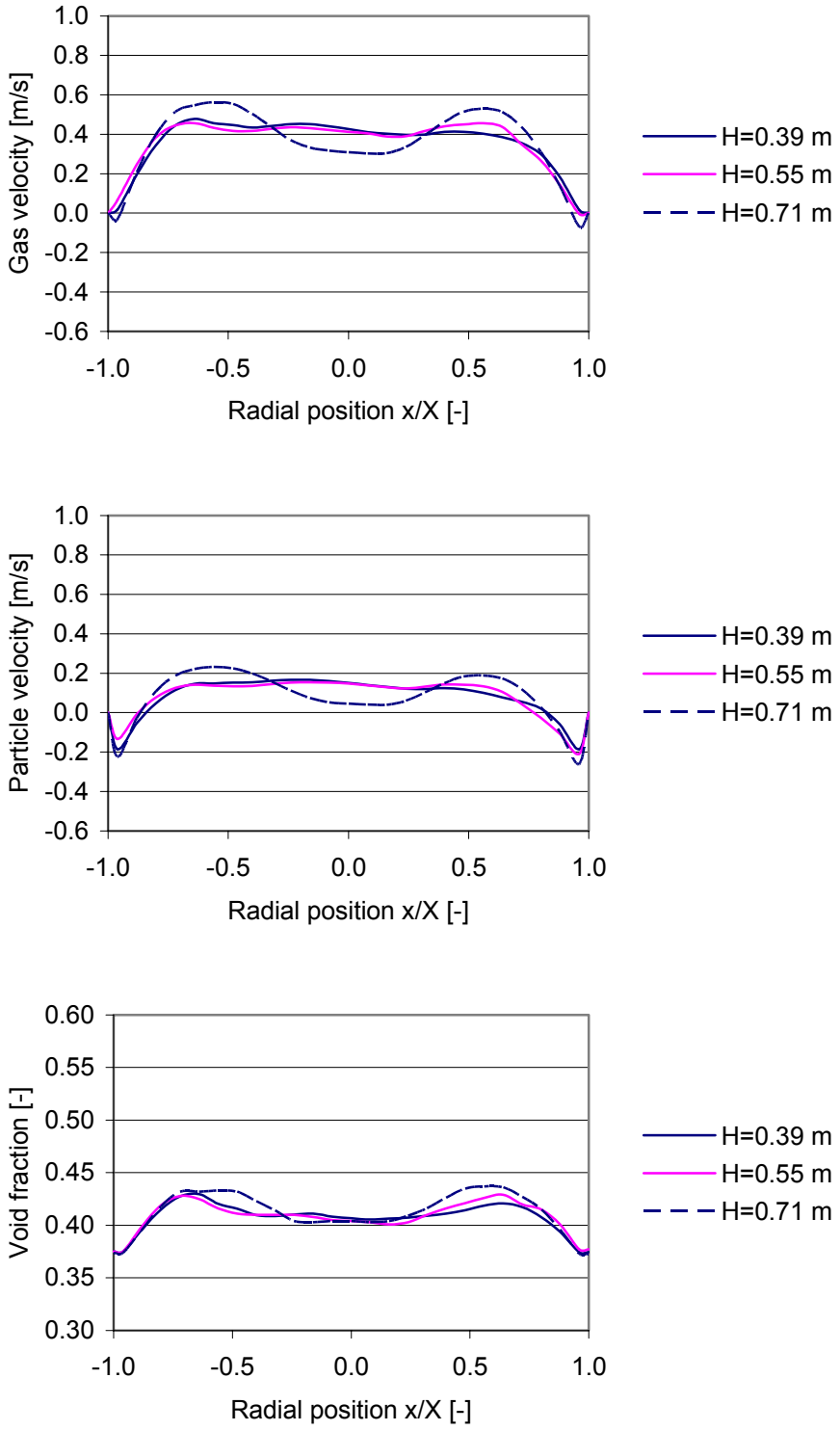

Figure 8.33: Mean gas velocity, particle velocity and void fraction as a function of radial position. The simulation is performed with 1 particle phase and the superficial velocity is 0.133 m/s.

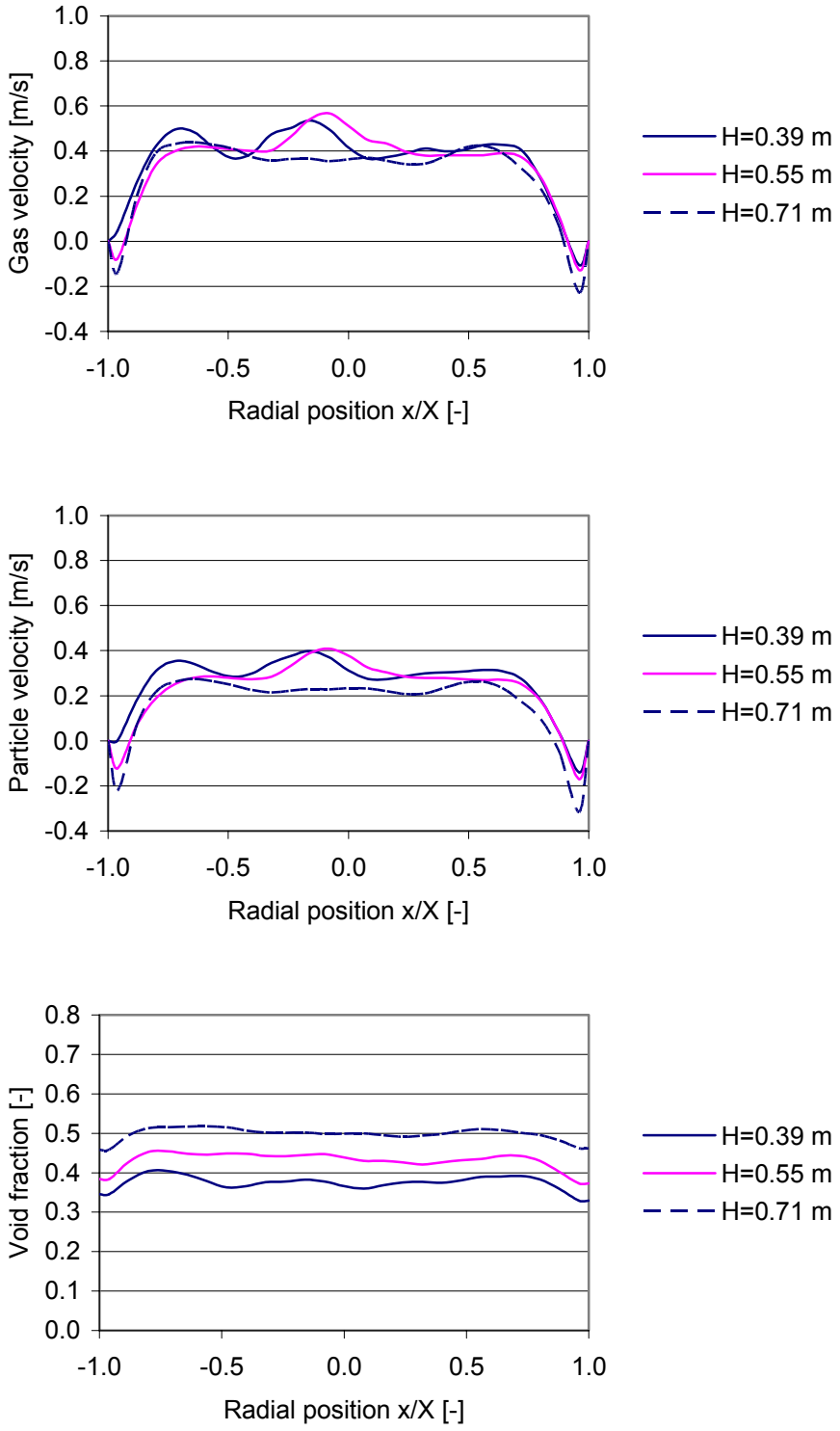

Figure 8.34: Mean gas velocity, particle velocity and void fraction as a function of radial position. The simulation is performed with 3 particle phases. Superficial velocity is 0.133 m/s.

8.5 Summary

A computational study of bubble behaviour in a 3-dimensional fluidized bed has been performed. The simulations with the small particle powder and the large particle powder are performed with one particle phase and a switch to plastic regime at about minimum fluidization. It is found that by including plastic regime in the calculations, the simulations with the Ergun drag model and the Gibilaro drag model give about the same bubble behaviour. The Ergun drag model gives the best agreement with the experiments regarding bubble sizes, whereas the Gibilaro drag model gives the most realistic bubble velocities. Simulations with the mixed powder are performed with one and two particle phases and the plastic regime included and with one and three particle phases without a 'switch' to the plastic regime. At low superficial gas velocity no bubbles were detected when the plastic regime was included.

The computational results are compared to the experimental data. Simulations with low excess gas velocity give rather low bubble frequencies compared to the experimental data. The simulations with superficial gas velocity 0.133 m/s give higher bubble frequencies than the experiments. All the simulations give lower bubble pierced length than the experiments. For most of the simulations the bubble frequencies increase with height above the distributor whereas the mean bubble pierced length change rather little as a function of vertical position. A study of the bubbles in the centre of the bed at time 10 s was performed for the mixed powder. The conclusion of this was that simulation with one phase and plastic regime included give rather small bubbles in all radial positions. By including two solid phases and the plastic regime, no bubbles were created in the lower part of the bed and rather large bubbles were observed in the upper part of the bed. In the simulations without plastic regime and three particle phases the tendency was that the bubble pierced length increased with increasing height in the bed. But for this case also small bubbles were observed at the higher levels, and this may cause the rather low mean bubble pierced length at these positions.

The three powders that are used in this study, are classified within the Geldart group B powders, and it should be expected that bubbles coalescence and that the bubble size increase with increasing height in the bed. The small particle powders are close to Geldart A particles, and for group A particles the bubbles are expected to grow quickly to a few centimetres and stay at that size as a result of the equilibrium between coalescence and splitting. The experimental data showed however an increase in bubble size as a function of height in the bed. The computational bubble frequencies and bubble sizes agree rather well with the experimental data at height 0.39 m and the discrepancies increase with increasing height above the air distributor.

The simulations with one particle phase and including the plastic regime give rather small discrepancies between computational and experimental bubble velocities. The computational bubble velocities are somewhat lower than the experimental bubble velocities. The same are observed for simulations with three particle phases and without plastic regime. The simulations with one particle phase and without plastic regime differ significantly from the corresponding simulations with three solid phases and give rather high bubble velocities compared to the experimental observations.

In the simulations the bubbles were defined as void fractions higher than 0.65. This means that rather small bubbles might be detected and that the mean bubble frequencies get higher than the experimental frequencies. From the plots of the computational bubble pierced length as a function of bubble velocities it was found that 50% or more of the bubbles were smaller than 5 cm. A considerably lower part of small bubbles are detected in the experiments. The bubble velocities increase with bubble size, and when a lot of small bubbles are included in the calculations, the mean bubble pierced length will decrease and the mean bubble velocity will decrease. This might be one reason for the discrepancies between computational and experimental results.

Computational and experimental pressure drop over the bed were compared. The simulations with one particle phase and including plastic regime give very good agreement with the experimental data for the small particle powder and the mixed powder. The Ergun drag model gave the best agreement. The computational pressure obtained from the simulations with the large particle powder differs rather much from the experimental data especially in the upper part of the bed. The difference in total pressure drop over the bed, however, is rather small. The simulations without the plastic regime gave good agreement with the experiments for the case with low superficial velocity. For the case with higher velocity, the simulations gave a higher pressure than the experiments at all the vertical positions.

A study of the computational void fractions and gas and solid velocities showed that simulations with one particle phase and without a switch to the plastic regime give unphysical low void fractions. Corresponding simulations with three particle phases give significantly higher void fractions and give rather good agreement with the experimental bubble behaviour. Still a rather high packing can be observed in parts of the bed. This may possibly be solved by using more than three particle phases. The problem by increasing the number of particle phases is the increase in required CPU time.

High packing is not a problem in the simulations including the plastic regime. The frictional solid stresses in the plastic regime results in smaller bubbles and lower bubble rise velocity due to increased leakage of gas through the bubble boundary. Simulations with two particle phases, however, do not give realistic results when the plastic regime is included.

9. Conclusions and recommendations

The objective of this work is to get a better understanding of bubble behaviour in fluidized beds. Experimental and computational studies have been performed on two and three dimensional geometries.

9.1 Conclusions

The FLOTRACS code proposed by Mathiesen et al. (2000 a,b) was used to calculate bubble behaviour in fluidized beds. The model was modified to improve its use in dense particle systems. Second order differencial scheme and the flux limiters Van Leer, Superbee and Minmod were included in the code. It was focused on the ability to handle dense packing of solids and a solid volume fraction correction equation used in MFIX was adopted. The routine accounts for the effect of solid pressure so that the computations are stabilized in closed packed regions.

At high solid volume fraction, sustained contacts between particles occur and the resulting frictional stresses might be accounted for in the description of the solid phase stress. Frictional stresses or the plastic regime were included in the code. When the solid volume fraction exceeds a critical packing the frictional stresses compensate the kinetic and collisional stresses. The solid pressure and frictional stresses in the plastic regime are described by empirical equations. Empirical equations should always be used with care.

In Chapter 5, experimental and computational studies of bubble behaviour in a two dimensional fluidized bed with a central jet have been performed. A video camera was used in experimental detection of bubble size and bubble velocity. The purpose of these studies was to verify the calculation of bubble formations on a simple well-defined model. Glass particles classified as Geldart B particles and PMMA particles classified as Geldart A particles were used in this study.

The simulations with glass particles were performed with one and three particle phases, with various values of the coefficient of restitution and with different drag models. Computational results from simulations with one and three particle phases were compared. For the current flow conditions the two cases gave no significant differences in bubble formations. The simulations with three particle phases gave slightly lower bubble velocities and agreed better with the experimental data. Further simulations were performed with three particle phases.

Simulations were performed with the Ergun, the Gibilaro and the Syamlal & O'Brien drag models. The computational results were compared to the experimental data. The Ergun and Syamlal & O'Brien drag models agreed well with the experiments according to bubble velocity. The Syamlal & O'Brien drag model gave an unsymmetrical first bubble and no continuous bubble formation. The Gibilaro drag model agreed well with experiments according to bubble size and bubble shape, but the model gave significantly higher bubble velocities than the experiments. The Ergun drag model gave the most realistic bubble behaviour and this model was used in the further simulations.

According to earlier studies, the coefficient of restitution has an important effect on bubble behaviour when the solid volume fraction is close to maximum packing. The plastic regime was included in FLOTRACS to avoid unphysical high packing. When the solid concentration exceeded critical packing, the plastic regime was controlling the flow and the effect of varying the coefficient of restitution was found to be insignificant. Corresponding simulations performed without the plastic regime showed that when the coefficient of restitution was decreased the particles became closer packed in the densest regions and the bubble size increased.

Geldart group A particles, PMMA, were used in order to study in what way different discretization schemes influenced the bubble behaviour. These particles fluidized very easily and gave a high bed expansion. High packing was not critical for these particles and simulations with the Ergun and the Gibilaro drag models gave about the same results. In the study of bubble behaviour in the two dimensional bed, it was found that the computational bubble velocities became higher than the experimental velocities. In the simulations performed with PMMA the Gibilaro drag model gave the lowest bubble velocities and this model was therefore used in the further simulations.

Simulations were performed with first and second order discretization schemes (SOU) and with the flux limiters Superbee, Van Leer and Minmod. The computational results were compared to experimental data. The first order scheme (FOU) gave unphysical pointed bubbles probably due to numerical diffusion. FOU also gave significantly higher bubble velocities than the experiments. SOU without flux limiter gave the most realistic bubble shape and bubble velocity, but SOU without a flux limiter can generate oscillations around sharp gradients and may give unphysical solutions. The comparison of the different flux limiters showed that all the flux limiters gave rounded bubbles and that the simulation with Superbee gave the most realistic bubble velocity.

In Chapter 6, a computational study of bubble behaviour in cylindrical fluidized beds was performed by using the MFIX code described by Syamlal (1993). A selection of computational results was compared to the experimental data from Werther and Molerus (1973).

A grid resolution test was performed for a fluidized bed with diameter 0.1 m and height 1.0 m. The intension was to find an optimum mesh that could be used in computational studies of larger fluidized beds. 3-D simulations were performed with different grid resolutions in angular, radial and axial direction in order to study the grid resolution influences on the numerical results. It was found that 20x200x18 was the coarsest grid that could be used without losing information. Simulations were also performed using 2-D Cartesian and 2D axis-symmetrical coordinates. Comparison of the results from the 2-D and 3-D simulations showed that 2-D Cartesian co-ordinates can be used to model the bed with good accuracy.

Fluidized beds with diameters of 0.1, 0.2, 0.45 and 1.0 m were simulated using 2-D Cartesian coordinates. The height of the beds was 1.0 m and the initial particle height was 0.5 m for all the beds. Void fraction as a function of height was studied. The mean void fractions changed significantly as a function of height for the 0.2 and 0.45 m beds, less for the 0.10 m bed and just insignificantly for the 1.0 m bed.

Void fraction as a function of radial position was calculated at two vertical positions in the bed, one close to the air distributor and one in the upper part of the particle bed. Void fraction profiles indicated the location of bubbles in the bed. The bubbles were expected to move towards the centre of the bed with increasing height. The void fraction profiles changed significantly between the two heights. The tendency was that the area of high void fraction moved against the centre with increasing height in the bed. The beds with diameter 0.1 m and 0.2 m attained a more laminar void fraction profile than the larger beds. The reason may be that the wall effects became less important when the bed diameter was increased.

Wall and coalescence effects influence the flow pattern and it cannot be assumed that bubble behaviour in a 2-D bed is the same as in a 3-D bed with the same particles. Simulations with 3-D cylindrical coordinates were performed for the 0.1 and 0.2 m beds. The bubble frequency profiles obtained by the 3-D simulations differed from the 2-D simulations. Bubble frequencies as a function of radial position were compared to experimental data. Experimental and computational results agreed rather well. Mean bubble pierced length and mean bubble rise velocity at the axis as a function of height above the distributor are calculated and compared to experimental data. These comparisons were performed for the 0.10 m bed. The calculated mean local pierced length and local mean bubble rise velocity agreed well with the experimental data in the lower part of the bed, whereas the discrepancies were significant in the top of the bed. This may be due to a significantly higher bed expansion in the experiments than in the simulations.

Large industrial beds require a high number of grids and long CPU time. Scaling down from large to smaller beds can be useful. Scaling includes use of dimensionless numbers which are kept constant during scaling. Scaling down is a way of reducing mesh and the CPU time. The 0.20 m and 0.45 m beds were scaled down and simulated on a 0.10 m bed. Scaling parameters proposed by Fitzergald and Crane (1980) were used in the simulations. The results of the simulations showed that the scaling down performed in the way it has been done here, gave unrealistic and smeared results. This may be due to the control volume size compared to the particle sizes and to the fact that change of particle properties may change the bubble behaviour in the fluidized bed.

An experimental study of bubble behaviour in a three dimensional fluidized bed was performed in Chapter 7. A lab-scale 3-D fluidized bed was constructed and a fibre optical probe was used to measure bubble behaviour. A data processing program was developed in Labview to analyse the raw data from the measurement system. Spherical glass particles with three different particle size distributions were used in the experiments. The experimental results were analysed and discussed.

It was found that by mixing two powders with different particle size distribution, the mixed powder attain a bulk density higher than the two original powders. The mixed powder attained very equal properties to the powder with the smallest particle sizes. According to the Geldart classification of particles, all the three powders were classified as group B particles. When the smallest particles and the mixed powder were fluidized, the beds expanded significantly before bubbles appeared. High bed expansion is typical for Geldart A particles. This indicates that flow behaviour is influenced of particle size distribution and that particle classification cannot be based only on mean particle size. The large particle bed expanded insignificantly

before bubbles appeared, and the minimum bubble velocity was very close to the calculated minimum fluidization velocity as expected for Geldart B particles.

For all the three powders, mean bubble pierced length increased with height in the bed. The tendency was also that bubble velocities increased with height in the bed. In the upper part of the bed, however, the bubble velocities decreased with height due to increasing wall effects when the bubble sizes increased. Bubble size as a function of bubble velocity was compared to empirical equations developed by Kunii and Levenspiel (1991). The comparisons showed that the small particle powder and the mixed powder gave results somewhere between the empirical equation for Geldart A and Geldart B particles. The result obtained from the large particles agreed well with the equation for Geldart B particles.

Bubble frequency increased from the wall towards the centre of the bed. The small particles gave a higher bubble frequency than the mixed powder especially for the lowest superficial velocity. Bubble velocity, bubble pierced length and bubble frequency increased with increasing superficial velocity.

The total bubble gas flow was calculated from local mean bubble gas flow times the area and compared to the total inserted gas flow. It was found that for the small particles and the mixed powder most of the inserted gas left with the bubbles. The experiments with large particles were performed with a low excess gas velocity and it was found that most of the inserted gas penetrates through the bed outside the bubbles.

Pressure was measured at ten levels in the bed. The pressure drop over the particle bed was highest for the mixed powder and lowest for the large particle powder. The mixed powder has the highest bulk density and the highest specific particle area. The drag increases with specific area and increasing drag will give increasing pressure drop.

In Chapter 8, a computational study of bubble behaviour in the three dimensional fluidized bed was performed. The simulations with the small and large particle powder were performed with one particle phase and a switch to plastic regime at about minimum fluidization. When including plastic regime in the calculations, the simulations with the Ergun and the Gibilaro drag model gave about the same bubble behaviour. Ergun's drag model gave the best agreement with experiments regarding bubble sizes, whereas the Gibilaro drag model gave the most realistic bubble velocities.

The mixed powder has a wide particle size distribution and according to the results from the experimental study, this powder should be simulated with multiple particle phases. Simulations with multiple particle phases and a switch to plastic regime gave unrealistic flow behaviour due to segregation of the particle phases. In simulations with one particle phase and low superficial velocity no bubbles were detected. This may be due to the low theoretical excess gas velocity. Simulations of the mixed powder and low superficial gas velocity were therefore performed with 3 particle phases and without a switch to plastic regime.

The computational results were compared to the experimental data. Simulations with low excess gas velocity gave rather low bubble frequencies compared to the experimental data. The simulations with high excess gas velocity gave higher bubble frequencies than the experiments. For most of the simulations the bubble frequencies increased with height above the distributor. The computational bubble frequencies agreed well with the experimental data

at the lower position in the bed, and the discrepancies increased with increasing height above the air distributor.

All the simulations gave a lower bubble pierced length than the experiments. The mean bubble pierced length changed insignificantly as a function of vertical position. For Geldart group B powders bubbles coalescence and it should be expected that the bubble size increase with increasing height in the bed. For Geldart A particles the bubbles are expected to grow quickly to a few centimetres and stay at that size as a result of the equilibrium between coalescence and splitting. The experimental data showed an increase in bubble size as a function of height in the bed. The computational bubble sizes agreed well with the experimental data at the lower position in the bed, and the discrepancies increased with increasing height above the air distributor.

The simulations with one particle phase and including the plastic regime gave rather small discrepancies between computational and experimental bubble velocities. The computational bubble velocities were somewhat lower than the experimental bubble velocities. The same were observed for simulations with three particle phases and without plastic regime.

In the simulations the bubbles were defined as void fractions higher than 0.65. The consequence was that rather small bubbles might be detected in all positions in the bed and that the mean bubble frequencies became higher than the experimental frequencies. From the plots of the computational bubble pierced length as a function of bubble velocities it was found that 50% or more of the bubbles were smaller than 5 cm. A considerably lower part of small bubbles were detected in the experiments. The bubble velocities increase with bubble size, and when a lot of small bubbles are included in the calculations, the mean bubble pierced length and the mean bubble velocity will decrease. This might be one reason for the discrepancies between computational and experimental results. Another reason might be that by including the frictional solid stresses, the compaction of solids around the bubble interface is reduced. This again leads to an increase of gas flow through the bubble boundary into the emulsion phase and smaller bubbles are predicted.

In the experimental study bubble velocity, bubble pierced length and bubble frequency were averaged for 10 or 20 minutes. In the computational study the results were averaged for 20 or 30 seconds due to long simulation time. Detected bubbles varied much in size and velocities, and the short simulation time may influence the mean values of bubble behaviour significantly and cause discrepancies between simulations and experiments.

Computational and experimental pressure drop over the bed were compared. The simulations with one particle phase and including plastic regime agreed well with the experimental data for the small particle powder and the mixed powder. The Ergun drag model gave the best agreement. The computational pressure obtained from the simulations with the large particles differed rather much from the experimental data especially in the upper part of the bed. The total pressure drop over the bed, however, agreed well with the experimental data. The simulations without the plastic regime gave good agreement with the experiments for the case with low superficial velocity. For the case with higher velocity, the simulations gave a higher pressure than the experiments in all the vertical positions.

A study of the computational void fractions and gas and solid velocities was performed. It was found that the problem with high packing can be solved by including the plastic regime. Simulations with three particle phases without a switch to plastic regime gave reasonable void fractions, but a high packing was observed in parts of the bed. This may possibly be solved by using more than three particle phases. The problem by increasing the number of particle phases is the increase in required CPU time.

9.2 Recommendations for further work

Future research should include extended experimental study of bubble behaviour in fluidized beds. The objective should be to verify the influence of particle size distribution on bubble behaviour in a fluidized bed.

The study should be performed on mono sized powders and mixtures of two or more mono sized powders. Corresponding studies of bubble behaviour should be performed in 2-D and 3-D fluidized beds

The results from the experimental study should be used to verify and improve the CFD model on a simple well-defined system.

An extended study of drag models should be performed to find a drag model or a combination of drag models that could be used with good accuracy for all types of particles and flow conditions.

The packing problem should be solved in a way that can be used for all flow conditions. The solid pressure used in the plastic regime is a function of void fraction and the actual solid fraction. It is desirable to study whether the solid pressure in the plastic regime also should be expressed by variables like particle properties and superficial velocity.

An extended study of the influence of frictional stresses on the bubble behaviour should be performed. The CFD model should be capable of handling multiple solid phases for 2-D and 3-D geometries also when the frictional stresses are included in the code.

The influence of coefficient of restitution should be studied for different flow conditions.

Chemical reaction, heat and mass transfer should be included in the CFD code. This should be done to improve the application of the model to chemical reactors.

A preliminary computational work on scaling of bubbling fluidized beds have been performed. This work should be extended to also include experimental work. The objective should be to obtain scaling parameters that can be adapted to the CFD code.

Bibliography

Aguillón, J., Shakourzadeh, K. and Guigon, P. (1996), Hydrodynamic behaviour of circulating fluidized bed with secondary air injection, *Proceedings of the Fifth International Conference on Circulating Fluidized Beds,* pp. 146-151, Beijing, China.

Bagnold, R.A. (1954), Experiments on a Gravity-Free Dispersion of Large Solid Spheres in a Newtonian Fluid Under Shear. *Proc. of Roy. Soc.,* **A225**, pp. 49-63.

Bokkers, G.A., van Sint Annaland, M., Kuipers, J.A.M. (2004), Mixing and segregation in a bidiperse gas-solid fluidised bed: a numerical and experimental study, *Powder Technology,* **140**, pp. 176-186.

Carnahan, N.F., Starling, K.E. (1969), Equation of State for Nonattracting Rigid Spheres, *Journal of Chemical Physics,* **51**(2), pp. 635-636.

Chapman, S., Cowling, T.G. (1970), The Mathematical Theory of Non-Uniform Gases. Third edition, Cambridge Univ. Press.

Chiesa, M., Mathiesen, V., Melheim, J.A., Halvorsen, B. (2004), Numerical simulation of particulate flow by Eulerian-Lagrangian and Eulerian-Eulerian approach with application to a fluidized bed, *Computers & Chemical Engineering,* **29**, pp. 291-304.

Crowe, C., Sommerfeld, M., Tsuji, Y. (1998), Multiphase Flows with Droplets and Particles, CRC Press LLC.

Deardorff, J.W. (1971), On the Magnitude of Subgrid Scale Eddy Coefficient. *Journal of Computational Physics,* Vol. 7, pp.120-133.

Di Felice, R. (1994), The voidage function for fluid-particle interaction systems, *Int. Journal Multiphase Flow,* **20**(1), pp. 153-159.

Ding, J., Gidaspow, D. (1990), Bubbling fluidization model using kinetic theory of granular flow. AIChE, **36**(4), pp. 523-538.

Ergun, S. (1952), Fluid Flow Through Packed Columns, *Chemical Engineering Progress*, **48**(2), pp. 89-94.

Fedor, R.F., Landel, R.F. (1979), An empirical method of estimating the void fraction in mixtures of uniform particles of different size, *Powder Technology*, **23**, pp. 225-231.

Fitzgerald, T.J., Crane, S.D. (1980), Proceedings of the Sixth International Conference on Fluidized bed Combustion, **3**, pp. 815, Atlanta, GA.

Geldart, D. (1973), Types of Gas Fluidization, *Powder Technology*, **7**, pp 285-295.

Geldart, D. (1986), Gas Fluidization Technology, John Wiley & Sons Ltd.

Gera, D., Gautam, M., Tsuji, Y., Kawaguchi, T., Tanaka, T. (1998), Computer simulation of bubbles in large-particle fluidized beds, *Powder Technology*, **98**, pp. 38-47.

Gera, D., Syamlal, M., O'Brien, T.J. (2004), Hydrodynamics of particle segregation in fluidized beds*, International Journal of Multiphase Flow*, **30**, pp. 419-428.

Gibilaro, L.G., Di Felice, R., Waldram, S.P. (1985), Generalized Friction Factor and Drag Coefficient for Fluid-Particle Interaction, *Chemical Engineering Science,* **40(10)**, pp. 1817-1823.

Gidaspow, D., Huilin, L. (1998), Equation of State and Radial Distribution Functions of FCC Particles in a CFB. *AIChE,* **44(2)**, pp. 279-293.

Gidaspow, D., Huilin, L., Manger, E. (1996), Kinetical Theory of Multiphase Flow and Fluidization: Validation and Extension to Binary Mixtures. XIXth International Congress of Theoretical and Applied Mechanics. Kyoto, Japan.

Gidaspow, D. (1994), Multiphase Flow and Fluidization. Academic Press, Boston

Gidaspow, D. Lin, C., Seo, Y.C. (1983), Fluidization in Two-Dimensional Beds with a Jet. Part I. Experimental porosity distribution, *Ind. Chem. Fundam.,* **22**(2), pp. 187-193.

Gidaspow, D., Syamlal, M., Seo, Y.C. (1986), Hydrodynamics of Fluidization: Supercomputer Generated vs. Experimental Bubbles, *Journal of Powder and Bulk Solids Tech.,* **10**(3), pp. 19-23.

Glicksman, L.R., Hyre, M., Woloshun, K. (1993), Simplified Scaling Relationship for Fluidized Beds, *Powder Technology*, **112**, pp. 34-45.

Goldschmidt, M.J.V., Beetstra, R., Kuipers, J.A.M. (2001a), Comparison of the Kinetic Theory of Granular Flow with 3-D hard-sphere discrete particle simulations, *Chemical Engineering Science.*

Goldschmidt, M. J. V., Kuipers, J. A. M., van Swaaij, W. P. M. (2001b), Hydrodynamic modelling of dense gas-fluidised beds using the kinetic theory of granular flow: effect of coefficient of restitution on bed dynamics. *Chemical Engineering Science*, pp. 571-578.

Guenther, C., Syamlal, M., (2001) The effect of numerical diffusion on simulation of isolated bubbles in a gas- solid fluidized bed, *Powder Thecnology*, **116**, pp. 142-154.

Halow, J.S., Fasching, G.E., Nicoletti, P. (1990), Preliminary Capacitance imaging experiments of a fluidized bed, Advances in fluidization engineering, *AIChE,* **86,** pp. 41-50.

Halow, J.S., Fasching, G.E., Nicoletti, P., Spenik, J.L. (1993), Observations of a fluidized bed using capacitance imaging, *Chemical Engineering Science,* **48**(4), pp. 643-659.

Halow, J.S., Nicoletti, P. (1992), Observation of fluidized bed coalescence using capacitance imaging, *Powder Technology*, **69,** pp. 255-277.

Halvorsen B., Guenther, C., O'Brien, T., Mathiesen, V. (2003), CFD calculation for scaling of a bubbling fluidized bed, AIChE , November 2003, San Francisco.

Halvorsen, B., Mathiesen, V. (2002a), CFD Modelling and simulation of a lab-scale Fluidised Bed, *Modeling, Identification and Control*, **23**(2), pp. 117-133.

Halvorsen, B., Mathiesen, V. (2002b), A comparison of first and second order spatial scheme for simulation of a bubbling fluidised bed, *Advances in Fluid Mechanics IV*, Wit Press, pp. 569-578.

Herbert, P. M., Gauthier, T. A., Briens, C. L. and Bourgougnou, M.A.(1994) Application of fiber optic reflection probes to the measurement of local particle velocity and concentration in gas-solid flow, *Powder Technology*, **80**, pp 243-252.

Hirsch C. (1990), Numerical computation of internal and external flows, Volume 2-C*omputational Methods for Inviscid and Viscous Flows*,John Wiley & Sons Ltd, Chichester, pp. 536-550.

Hoomans, B.P.B., Kuipers, J.A.M., Van Swaaij, W.P.M. (1998), The influence on particle properties on pressure signals in dense gas-fluidised beds: A computer simulation study. *World Congress on Particle Technology*, Brighton, UK.

Horio, M., Østergaard, V.K., Sørensen, A. (1986)

Hrenya, C.M., Sinclair, J.L. (1997), Effects of particle-phase turbulence in gas-solid flows. *AIChE*, **43**, pp. 853-869.

Huilin, L., Gidaspow, D. (2003b), Hydrodynamics of binary fluidisation in a riser: CFD simulation using two granular temperatures, *Chemical Engineering Science* **58**, pp. 3777-3792.

Huilin, L., Wenti, L., Rushan, B., Lidan, Y., Gidaspow, D. (2000), Kinetic theory of fluidized binary granular mixtures with unequal granular temperature, *Physica A* **284**, pp. 265-276.

Huilin, L., Yurong, H., Gidaspow, D. (2003a), Hydrodynamic modelling of binary mixture in a gas bubbling fluidized bed using the kinetic theory of granular flow, *Chemical Engineering Science* **58**, pp. 1197-1205.

Huilin, L., Yurong, H., Gidaspow, D., Lidan, Y.,Yukun, Q. (2003c), Size segregation of binary mixture of solids in bubbling fluidized beds, *Powder Tecnology* **134**, pp. 86-97

Ibsen, C.H. (2002), An experimental and Computational Study of Gas-Particle Flow in Fuidised Reactors, Ph.D. Thesis, Aalborg University, Esbjerg.

Jenike, A.W. (1987), A Theory of Flow of Particulate Solids in Converging and Divering Channels Based on a Conical Yield Function, *Powder Technology*, **50**, pp. 229-236.

Jenkins, J.T., Savage, S.B. (1983), A theory for the rapid flow of identical, smooth, nearly elastic, spherical particles. *Journal of Fluid Mechanics*, Vol. 30, pp. 187-202.

Jenkins, J.T., Cowin, S.C. (1979), Theories for Flowing Granular Materials, Mech. Applied to Transport of Bulk Materials, *Ap. Mech.Div. of ASME*, **31**, pp. 79-89.

Johnson, P.C., Jackson, R. (1987), Frictional-collisional constitutive relations for granular materials, with application to plane shearing, *Journal of Fluid Mechanics*, **176**, pp 67-93.

Johnsson, F., Vrager, A., Leckner, B. (1999), Solid flow pattern in the exit region of a CFB-furnace – influence of exit geometry, *15th International Conference on Fluidised bed Combustion,* Savannah.

Kuipers, J. A. M. ,van Duin, K. J., van Beckum, F. P. H.,van Swaaij, W. P. M, (1993), Computer simulation of the hydrodynamics of a two-dimensional gas-fluidized bed. *Computers chemical Engineering,* **17**(8), pp. 839-858.

Kuipers, J. A. M. ,van Duin, K. J., van Beckum, F. P. H.,van Swaaij, W. P. M, (1992), A numerical model of gas fluidized beds. *Chemical Engineering Science,* **47**(8), pp. 1913-1924.

Kunii, D., Joshida, K., Hiraki, I. (1967), The behaviour of freely bubbling fluidized bed, Proseedings of the International Symposium on Fluidization, pp. 652.

Kunii, D., Levenspiel, O. (1991), Fluidization Engineering, Second edition, Butterworth-Heineman series in chemical engineering.

Laux, H. (1998), Modeling of dilute and dense dispersed fluid-particle flow, Ph.D. Thesis, NTNU Trondheim, Norway.

Lebowitz, J.L. (1964), Exact Solution of Generalized Percus-Yevick Equation for a Mixyure of Hard Spheres, *The Physical Review*, **133**(4A), pp. A895-A899.

Lischer, J., Louge, M.Y. (1991), Optical fiber measurements of particle concentration in dense suspensions: Calibration and Simulation, *Applied. Optics*, **30(8)**.

Lun, C.K.K., Savage, S.B. (1987), A Simple Kinetic Theory for Granular Flow of Rough, Inelastic, Spherical Particles, *Journal of Applied* Mechanics **54**, pp. 47-53.

Lun, C.K.K., Savage, S.B., Jeffrey, D.J., Chepurniy, N. (1984), Kinetic Theory for Granular Flow: inelastic particlesin Couette flow and slightly inelastic particles in a general flowfield, *Journal of Fluid Mechanics* **140**, pp. 223-256.

Ma, D. and Ahmadi, G., 1986. An equation of state for dense rigid sphere gases, *Journal of Chemical Physics*, Vol 84, No. 6, pp. 3449-3450

Manger, E. (1996), Modelling and simulation of gas/solid flow in curvilinear coordinates. Ph.D. thesis, Telemark Institute of Technology, Norway.

Mathiesen, V, Arastoopour, H., Hjertager, B.H. (1999), Experimental and Computational Study of Multiphase Gas/Particle Flow in a CFB Riser, *AIChE Journal* **45**(12) pp. 2503-2518.

Mathiesen, V, Solberg, T, Hjertager, B.H. (2000a), Prediction of gas/particle flow including a realistic particle size distribution. *Powder Technology* **112**, pp. 34-45.

Mathiesen,V., Solberg,T., Hjertager, B.H. (2000b). An experimental and computational study of multiphase flow behavior in a circulating fluidized bed. *Int. Journal of Multiphase Flow* **26**(3), pp. 387-419.

Militzer, J., Shakourzadeh, K. (1991), Solid Particle Velocity Measurement System, Manual for VECTOR, Canada.

Nieuwland, J.J., van Sint Annaland, M., Kuipers, J.A.M., van Swaaij, W.P.M. (1996), Hydrodynamic Modeling of Gas/Particle Flows in Riser Reactors, *AIChE* **42**(6), pp. 1569-1582.

Pain, C. C., Mansoorzadeh, S., de Oliveira C. R. E. (2001a) A study of bubbling and slugging fluidised beds using the two-fluid granular temperature model. *International Journal of Multiphase Flow*, **27**, pp. 527-551.

Pain, C. C., Mansoorzadeh, S., de Oliveira C. R. E., Goddard, A. J. H. (2001b) Numerical modelling of gas-solid fluidized beds using the two fluid approach. *International Journal for numerical methods in fluids*, **(36)**, pp. 91-124.

Patankar, N. A., Joseph, D. D. (2001), Lagrangian numerical simulation of particulate flows. *International Journal of Multiphase Flow,* **27,** pp. 1685-1706.

Patankar, N. A., Joseph, D. D. (2001a), Modeling and numerical simulation of particulate flows by the Eulerian-Lagrangian approach. *International Journal of Multiphase Flow,* **27,** pp. 1659-1684.

Patankar, S.V. (1980), Numerical Heat Transfer and Fluid Flow, Hemisphere Publishing Corporation, New York, pp. 80-85.

Patil, D.J., van Sint Annaland, M., Kuipers, J.A.M. (2005a), Critical comparison of hydrodynamics models for gas-solid fluidized beds-Part I: bubbling gas-solid fluidized beds operated with a jet, *Chemical Engineering Science*, **60** (1), pp. 57-72.

Patil, D.J., van Sint Annaland, M., Kuipers, J.A.M. (2005b), Critical comparison of hydrodynamics models for gas-solid fluidized beds-Part II: freely bubbling gas-solid fluidized beds, *Chemical Engineering Science*, **60** (1), pp. 73-84.

Pita, J.A., Sundaresan, S. (1993), Developing Flow of a Gas-Particle Mixture in a Vertical Riser, *AIChE Journal* **39**(4), pp. 541-552.

Prichett, J.W., Blake, T.R., Garg, S.K. (1978), A Numerical Model of Gas Fluidized Beds, *AIChE Sympositum Series 176*, **74**, pp. 134-148.

Pugsley, T., Tanfara, H., Malcus, S., Cui, H., Chaouki, J., Winters, C. (2003), Verification of fluidized bed electrical capacitance tomography measurements with fibre optic probe, *Chemical Engineering Science* **58**, pp. 3923-3934.

Rensner, D., Werther, J. (1992), Estimation of the effective measuring volume of single fiber reflection probes for solid concentration measurement, Preprints of the 5th European Symposium Particle Characterization (PARTEC 92), **(107).**

Rice, R. B., Jovanovic, Z., Harner, R., Cocco, R. (2003), In-Situ analysis of Bubble Hydrodynamics in a Fluidized Bed Reactor, *AIChE, Advances in Particle Technology*, **60aa**

Rowe, P.N. (1961), Drag Forces in a Hydraulic Model of Fluidized Bed-PartII, *Trans. Instn. Chem*., **39**, pp. 175-180.

Sabéri, S., Shakourzadeh, K., Bastoul, D., Militzer, J. (1995), Bubble size and velocity measurement in gas-liquid systems: Application of fibre optic technique to pilot plant scale, *The Canadian Journal of Chem.Eng*. **73,** pp. 253-257

Samuelsberg, A., Hjertager, B.H. (1996), An experimental and numerical study of flow patterns in a circulating fluidized bed reactor, *Int. Journal of Multiphase Flow*, **22**(3), pp. 575-591.

Schaeffer, D.G. (1987) Instability of Evolution Equations Describing Incompressible Granular Flow, *J.Differ. Eqs*., **66**, pp. 19.

Sinclair, J.L., Jackson, R. (1989), Gas-Particle Flow in Vertical Pipe with Particle-Particle Interactions, AIChE Journal **35**(9), pp. 1473-1486.

Syamlal, M. (1998), High Order Discretization Methods for the Numerical Simulation of Fluidized Beds. *AIChE, Fluidization and Fluid Particle Systems,* **94(318)**, pp. 53-57.

Syamlal, M. (1998), MFIX Documentation Numerical Technics, Topical Report 1998, DOE/MC/31346.

Syamlal, M., O'Brien, T.J. (1987), A Generalized Drag Correlation for Multiparticle Systems, Morgantown Energy Technology Center, DOE Report.

Syamlal, M., Rogers, W., O'Brien, T.J. (1993), MFIX Documentation Theory Guide, Morgantown Energy Technology Center, DOE/METC-94/1004.

Tayebi, D., Svendsen, H.F., Grislingås, A., Mejdell, T., Johannessen, K. (1999), Dynamics of fluidized-bed reactors. Development and application of a new multi-fiber probe, *Chemical Engineering Science* **54** (13-14), pp. 2113-2122.

van Wachem, B. G. M., Schouten, J. C., Krishna, R., Van den Bleek, C. M. (1998), Eulerian Simulations of Bubbling Behaviour in Gas-Solid Fluidised Beds, *Computers chem. Eng.* **22**, pp. S299-S306.

van Wachem, B. G. M., Schouten, J. C., Van den Bleek, C. M., Krishna, R., Sinclair, J. L. (2001b), Comparativ Analysis of CFD Models of Dense Gas-Solid Systems. *AIChE*, **47(5)**, pp. 1035-1051.

van Wachem, B. G. M., Schouten, J. C., Van den Bleek, C. M., Krishna, R., Sinclair, J. L. (2001a), CFD Modeling of Gas-Fluidized Beds with a Bimodal Particle Mixture Systems. *AIChE*, **47(6)**, pp. 1292-1302.

Weber, A. (1995), Using the VECTOR Probe for Velocity Measurements, COMPETT-APR Reinland-Pfalz, Industrial Placement Programme.

Wen, C.Y., Yu, Y.H. (1966), Mechanics of Fluidization, *Chemical Engineering Progress*, **62**, pp. 100-111.

Werther, J., Molerus, O. (1973a), The local structure of gas fluidized beds -I. A statistically based measuring system. *Int. Journal of Multiphase flow*, **1**, pp. 103-122

Werther, J., Molerus, O. (1973b), The local structure of gas fluidized beds -II. The spatial distribution of bubbles. *Int. Journal of Multiphase flow*, **1**, pp123-138.

Witt, P. J., Perry, J. H., Schwarz, M. P. (1996), CFD Modeling of Fluidized Beds. *CRC* New Technologies for Power Generation from Low-Rank Coal, Mulgrave, Vic., Australia.

Yasuna, J.A., Moyer, H.R., Elliott, S., Sinclair, J.L. (1995), Qantitative predictions of gas-particle flow in vertical pipe with particle-particle interactions, *Powder Technology* **84**, pp. 23-34.

Zevenhoven, R., Järvinen, M. (2001), CFB reactors, CFD and particle/turbulence interactions. 4th International Conference on Multiphase Flow, New Orleans (LA) USA

Zhang, Y., Reese, J.M. (2003), The drag force in two-fluid models of gas-solid flows, *Chemical Engineering Science,* **58**, pp. 1641-1644.

Publications

This thesis

Halvorsen, B., Mathiesen, V. (2005), Experimental and computational study of bubble behaviour in fluidized beds*, 29th Annual Conference of the South African Society for Numerical and Applied Mathematics*, 30. March - 1 April, Stellenbosh, South Africa.

Chiesa, M., Mathiesen, V., Melheim, J.A., Halvorsen, B. (2005), Numerical simulation of particulate flow by Eulerian-Lagrangian and Eulerian-Eulerian approach with application to a fluidized bed, *Computers & Chemical Engineering,* **29**, pp. 291-304.

Halvorsen B., Guenther, C., O'Brien, T., Mathiesen, V. (2003), CFD calculation for scaling of a bubbling fluidized bed, AIChE , November 2003, San Francisco.

Halvorsen, B., Mathiesen, V. (2001), CFD Modelling and simulation of a lab-scale Fluidised Bed, *42 nd Conference on Simulation and Modelling* pp. 327-344, Porsgrunn, Norway.

Halvorsen, B., Mathiesen, V. (200a2), CFD Modelling and simulation of a lab-scale Fluidised Bed, *Modeling, Identification and Control*, **23**(2), pp. 117-133.

Halvorsen, B., Mathiesen, V. (2002b), A comparison of first and second order spatial scheme for simulation of a bubbling fluidised bed, *Advances in Fluid Mechanics IV*, Wit Press, pp. 569-578.

For future work

Loyd, C.A., Du Plessis, J.P., Halvorsen, B.M. (2004), On closure modelling of volume averaged equations for flow through two-dimensional arrays of squares, *Advances in Fluid Mechanics V*, Wit Press, pp. 85-93.